Aus dem
Helmholtz-Zentrum München
Comprehensive Pneumology Center (CPC)

Regulation of PA200 in lung cancer

Dissertation
zum Erwerb des Doctor of Philosophy (Ph.D.) an der Medizinischen Fakultät der
Ludwig-Maximilians-Universität München

vorgelegt von
Ayşe Seda Yazgılı

aus
Istanbul/Türkei

Jahr
2024

Mit Genehmigung der Medizinischen Fakultät der
Ludwig-Maximilians-Universität München

Erstes Gutachten:	Prof. Dr. Silke Meiners
Zweites Gutachten:	PD Dr. Claudia Staab-Weijnitz, Ph.D.
Drittes Gutachten	Prof. Dr. Amanda Tufman
Viertes Gutachten:	PD Dr. Farkhad Manapov

Dekan: Prof. Dr. med. Thomas Gudermann

Tag der mündlichen Prüfung: 09.02.2024

Affidavit

LMU LUDWIG-MAXIMILIANS-UNIVERSITÄT MÜNCHEN

Dean's Office Medical Faculty
Faculty of Medicine

Affidavit

Yazgılı, Ayşe Seda

Surname, first name

Beatson Institute for Cancer Research, Switchback Rd, Bearsden, G611BD Glasgow

Address

I hereby declare, that the submitted thesis entitled

Regulation of PA200 in lung cancer

is my own work. I have only used the sources indicated and have not made unauthorised use of services of a third party. Where the work of others has been quoted or reproduced, the source is always given.

I further declare that the dissertation presented here has not been submitted in the same or similar form to any other institution for the purpose of obtaining an academic degree.

Glasgow, 05.09.2023

Place, Date

Ayşe Seda Yazgılı

Signature doctoral candidate

Confirmation of congruency

LMU LUDWIG-MAXIMILIANS-UNIVERSITÄT MÜNCHEN

Dean's Office Medical Faculty
Doctoral Office

Confirmation of congruency between printed and electronic version of the doctoral thesis

Doctoral candidate:	Ayşe Seda Yazgılı
Address:	Beatson Institute for Cancer Research, Switchback Rd, Bearsden, G611BD Glasgow

I hereby declare that the electronic version of the submitted thesis, entitled

Regulation of PA200 in lung cancer

is congruent with the printed version both in content and format.

Glasgow, 05.09.2023
Place, Date

Ayşe Seda Yazgılı
Signature doctoral candidate

Table of Contents

Summary

In this thesis, I focused on investigating the role of PA200, a proteasome activator, which is found to be overexpressed in non-small cell lung cancer (NSCLC) (Javitt et al., 2023; Welk, 2018). To understand its function, I generated CRISPR/Cas9 PA200 knock-out cell lines (A549 and NCI-H1299), validated the efficiency of gene editing, and confirmed PA200 protein depletion. Through analyses of proteasome/immunoproteasome expression and redistribution, I observed alterations in the dynamics, activation, and distribution of proteasome complexes in the absence of PA200. Notably, these effects differed between the two NSCLC cell lines.

To gain deeper insights into the functional relevance of PA200, I established and optimized fundamental cancer biology assays, including proliferation, invasion, and migration assays. The results demonstrated a distinct impact of PA200 depletion on proliferation and metabolism rates in the two cell lines. Moreover, the absence of PA200 led to decreased invasion and migration abilities, albeit to different extents in the two cell lines. These findings raised the possibility of PA200's involvement in the epithelial-to-mesenchymal transition (EMT). To investigate this, I examined well-established EMT markers and observed that PA200 indeed plays a role in EMT, but the response is context-dependent, considering the divergent responses of the two NSCLC cell lines to PA200 knock-out. Building upon these findings, *in vivo* experiments were conducted in collaboration with the lab of Georgios Stathopoulos to validate the impact of PA200 depletion on tumour size. The results confirmed that the absence of PA200 reduces tumour size. Our animal model system did not, however, allow for the analysis of the metastatic behaviour of PA200-depleted lung carcinoma cell lines.

To gain insights into the differential effects of PA200 in the two NSCLC cell lines, global changes in RNA expression were determined by RNA sequencing. The data revealed diverse regulatory patterns at the RNA level following PA200 knock-out in the two NSCLC cell lines. Additionally, immunoprecipitation experiments with subsequent mass spectrometry (MS) analyses were conducted to identify PA200 interactors. Surprisingly, the main interactors of PA200 were found to be non-proteasome-associated proteins. Subsequent experiments using MS analysis of different fractions of native gels provided evidence for the existence of proteasome-independent presence of PA200 in the cells. Moreover, employing urea lysis of the TSDG-lysed cell pellets allowed me to detect PA200 in the insoluble fractions, which primarily consisted of DNA, RNA, and their interactor proteins. These findings support the notion that

PA200 can interact with insoluble components of the cells such as DNA and RNA interactors within the cellular context.

In conclusion, this research elucidated the multifaceted roles of PA200 in NSCLC, highlighting its impact on proteasome dynamics, cellular functions, EMT, tumour growth, and interactions with various proteins. The context-dependent effects observed in the two NSCLC cell lines shed light on the complexity of PA200-mediated processes and provide a foundation for further investigations.

Zusammenfassung

In dieser Arbeit konzentrierte ich mich auf die Untersuchung der Rolle von PA200, einem Proteasomaktivator, der bei nicht-kleinzelligem Lungenkrebs (NSCLC) überexprimiert ist (Javitt et al., 2023; Welk, 2018). Um seine Funktion zu verstehen, habe ich CRISPR/Cas9 PA200-Knockout-Zelllinien (A549 und NCI-H1299) generiert, die Effizienz der Depletion validiert und auf RNA und Proteinebene bestätigt. Die Depletion von PA200 führte zu einer veränderten Dynamik, Aktivierung und Verteilung von Proteasom-Komplexen. Bemerkenswerterweise unterschieden sich diese Effekte zwischen den beiden NSCLC-Zelllinien.

Um tiefere Einblicke in die funktionelle Relevanz von PA200 zu gewinnen, habe ich verschiedene biologische Tests etabliert und optimiert, darunter Proliferations-, Invasions- und Migrationstests. Die Ergebnisse zeigten deutliche Auswirkungen der PA200-Depletion auf die Proliferations- und Stoffwechselraten in den beiden Zelllinien. Darüber hinaus führte das Fehlen von PA200 zu einer verminderten Invasion und Migration, wenn auch in unterschiedlichem Ausmaß in den beiden Zelllinien. Diese Ergebnisse ließen die Möglichkeit einer Beteiligung von PA200 am Übergang vom Epithel zum Mesenchym (EMT) vermuten. Die Analyse von EMT-Markern legt nahe, dass PA200 tatsächlich eine Rolle bei der EMT spielt, dies jedoch kontextabhängig ist, wenn man die unterschiedlichen Reaktionen der beiden NSCLC-Zelllinien berücksichtigt. Weitergehend wurden in-vivo Maus-Experimente durchgeführt, um den Einfluss der PA200-Depletion auf die Tumorgröße zu validieren. Die Ergebnisse bestätigten, dass das Fehlen von PA200 das Wachstum der Tumorzellen in der Maus verringert.

Um Einblicke in die Auswirkung einer PA200 Depletion in den beiden NSCLC-Zelllinien zu gewinnen, wurde eine Transkriptomanalyse mittels RNA-Sequenzierung durchgeführt. Die Daten zeigten unterschiedliche regulatorische Muster auf RNA-Ebene in den beiden NSCLC-Zelllinien nach PA200-Knockout.

Darüber hinaus wurden Immunpräzipitationsexperimente zur Identifizierung von PA200-Interaktionspartnern durchgeführt und Massenspektrometrie zur Analyse der assoziierten Proteine eingesetzt. Überraschenderweise wurde festgestellt, dass es sich bei den

Interaktionspartnern von PA200 meist um nicht Proteasom-assoziierte Proteine handelt. Nachfolgende Experimente deuten auf die Existenz einer Proteasom-unabhängigen Fraktion von PA200 in den Tumorzellen. Dies wurde mittels Nachweis von PA200 in unlöslichen Proteinfraktionen, die hauptsächlich aus DNA, RNA und ihren Interaktorproteinen bestanden, bestätigt. Diese Ergebnisse stützen die Annahme, dass PA200 im zellulären Kontext mit unlöslichen Komponenten wie DNA- und RNA interagieren kann.

Zusammenfassend trägt dieses Forschungsprojekt dazu bei die zelluläre Funktion von PA200 bei NSCLC besser zu verstehen und validiert PA200 als Onkogen für Lungentumorzellinien. Die in den beiden NSCLC-Zelllinien beobachteten kontextabhängigen Effekte geben Aufschluss über die Komplexität PA200-vermittelter Prozesse und bieten eine Grundlage für weitere Untersuchungen.

1 Introduction

1.1 Lung cancer

Lung cancer stands as one of the most prevalent malignancies worldwide and remains a prominent cause of cancer-associated mortality, with an estimated 2.20 million new cases and 1.79 million deaths reported annually (Cancer, 2020; Thai et al., 2021). Striking progress and notably enhanced outcomes for numerous patients have been attainable due to significant improvements in comprehending disease biology, predictive biomarkers, and treatment refinements (Howlader et al., 2020). Furthermore, public health initiatives aimed at decreasing smoking rates have resulted in enhanced survival rates and a decrease in the occurrence of lung cancer in high-income nations (Jemal et al., 2010; Ng et al., 2014; Siegel et al., 2020). Significantly, men are experiencing a more rapid decline in lung cancer incidence due to the historical pattern of slower adoption and cessation of tobacco use among women (Siegel et al., 2020). Nonetheless, instances of new lung cancer cases persist in low-income nations where access to healthcare is limited, and initiatives to encourage smoking cessation are not as prevalent (Jemal et al., 2010; Ng et al., 2014). Intriguingly, lung cancer is not solely confined to smokers, as evidenced by the latest research from the Swanton Lab, indicating a link between air pollution-induced lung inflammation and the activation of cells harbouring cancer-causing mutations (Swanton et al., 2022).

Lung cancer presents a wide spectrum of clinicopathological characteristics, displaying significant diversity (Travis, Brambilla, Nicholson, et al., 2015). Within lung cancer diagnoses, non-small cell lung cancer (NSCLC) and small-cell lung cancer (SCLC) comprise 85% and 15% of cases, respectively (Figure 1.1 A) (Singal et al., 2019). In accordance with NSCLC classification, adenocarcinomas constitute the most prevalent subtype of lung cancer, closely followed by squamous-cell carcinomas (Figure 1.1 B) (Bray et al., 2015; Travis, Brambilla, Nicholson, et al., 2015). Notably, the occurrence of squamous-cell carcinomas has exhibited a significant decrease, attributed to declining smoking rates within high-income countries and changes in cigarette content (Alberg et al., 2013).

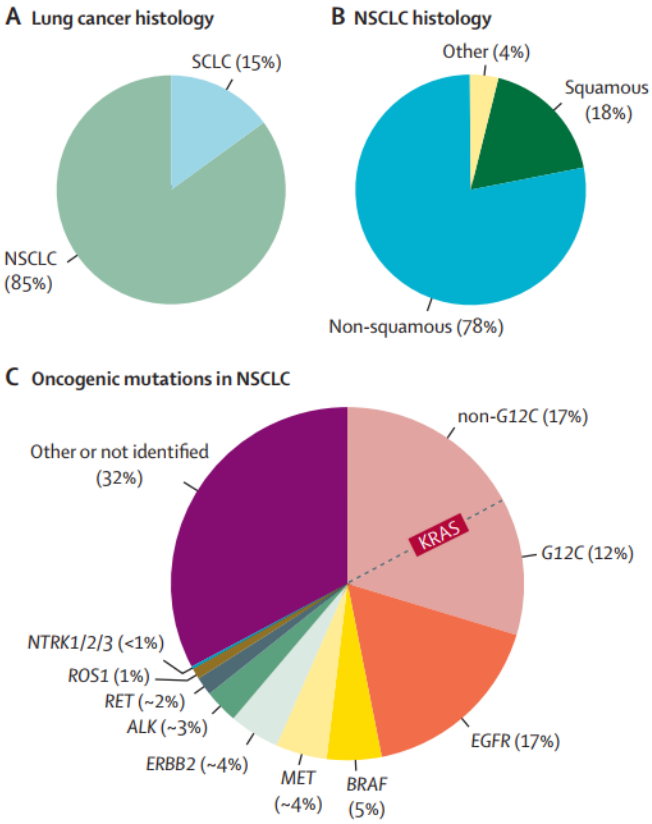

Figure 1.1: Lung cancer classification. Lung cancers are classified into two main types: SCLC and NSCLC. The latter is subtyped into A) squamous and non-squamous according to histology. B) The NSCLC is driven by several different mutations (Singal et al., 2019). The image is taken from a recent review (Thai et al., 2021).

1.1.1 Small-Cell Lung Cancer (SCLC)

SCLC is a high-grade neuroendocrine carcinoma that typically develops in smokers who are still smoking or have quit, and it has a very poor prognosis (Rudin et al., 2021). The WHO's pathological categorization system identifies only two subtypes of SCLC: SCLC (80% of cases) and combined SCLC (20% of cases) which has an additional non-small-cell carcinoma component (Travis, Brambilla, Nicholson, et al., 2015). The occurrence of SCLC often mirrors the prevalence of smoking, albeit with an approximate 30-year delay (Huang et al., 2015). This establishes SCLC as one of the malignancies displaying the most robust epidemiological associations with tobacco use. Over the course of the last thirty years, SCLC incidence in the USA has decreased in parallel with cigarette smoking prevalence (Breitling et al., 2020). Only 2% of SCLC cases occur in never-smokers who have never smoked more than 100 cigarettes in their whole lives (Varghese et al., 2014). However, a Korean population-based study showed a link between air pollution and another recent study showed increased SCLC cases with

increased radon exposure in never-smokers (Lamichhane et al., 2017; Rodríguez-Martínez et al., 2022). The majority of SCLC cases exhibit concurrent inactivation of the tumour suppressors p53 and RB proteins which are the products encoded by TP53 and RB1 genes, respectively (George et al., 2015). This simultaneous inactivation of tumour suppressors diverges from the principal oncogenic drivers commonly found in various other solid tumours, particularly NSCLC, wherein activating oncogenic mutations play a crucial role in the initiation of carcinogenesis (Rudin et al., 2021). Furthermore, alterations may also influence SCLC tumourigenesis in the immune microenvironment and lung stroma (Huang et al., 2015). These insights are further corroborated by comprehensive DNA and RNA sequencing investigations involving larger cohorts of primary tumours and models derived from patient samples and circulating tumour cells (CTCs) (George et al., 2015; Peifer et al., 2012; Udagawa et al., 2018). In the context of SCLC, the most prevalent sites for metastasis include the contralateral lung, the brain, the liver, the adrenal glands, and the bone is the most typical locations (Rudin et al., 2021). This pattern of metastatic dissemination is notably associated with the abundance of CTCs in SCLC (Hou et al., 2012). The scarcity of samples for histological diagnosis and subsequent study has been a persistent issue in SCLC research. The lack of tumour material may be lessened by the capacity to separate CTCs from SCLC patients' blood (Hodgkinson et al., 2014).

1.1.2 Non-Small Cell Lung Cancer (NSCLC)

NSCLC is histologically classified into squamous cell carcinoma (SCC), which typically develops close to a central bronchus, while non-squamous NSCLC begins in lung epithelial cells of the core bronchi to terminal alveoli (Paradigms, 2017). The majority of the mutations in NSCLC are found in KRAS (29%), EGFR (17%), BRAF (5%), MET (4%), and ERBB2 (4%) genes (Figure 1.1 C) (Thai et al., 2021). The WHO identified three main forms of NSCLC are adenocarcinoma, squamous cell carcinoma, and large cell (Travis, Brambilla, Burke, et al., 2015; Travis, Brambilla, Nicholson, et al., 2015).

Adenocarcinomas develop from cells that typically release mucus and other chemicals and account for about 40% of lung malignancies, making them the most prevalent kind of NSCLC (Travis, Brambilla, Burke, et al., 2015). While it is the most common form of lung cancer observed in individuals who have never smoked, this subtype of lung cancer predominantly impacts individuals who are currently smoking or have a history of smoking (American Cancer Society, 2019). In contrast to other types of lung cancer, this variant is more frequently

diagnosed in women rather than men, and it has a higher propensity to occur in younger people. Adenocarcinoma typically develops in the outer regions of the lung and is more likely to be discovered early on.

Squamous cell carcinomas account for 25% to 30% of lung malignancies and are typically caused by cells in the airway epithelium that line the lungs (Duma et al., 2019). These tumours often originate in the central regions of the lungs, near major airways, and they are commonly linked to a history of smoking, particularly in the bronchial region (American Cancer Society, 2019).

Large cell tumours comprise between 5-10% of all lung malignancies. Their prevalence is decreasing due to more advanced immunophenotyping methods that accurately classify poorly differentiated squamous cell carcinomas and adenocarcinomas (Duma et al., 2019). Large cell carcinoma can potentially arise in any region of the lung. It often exhibits rapid growth and has a tendency to metastasize, posing challenges for effective treatment (American Cancer Society, 2019).

1.1.2.1 Treatment in NSCLC

The treatment options in the non-metastatic NSCLC are surgery, neoadjuvant, and adjuvant chemotherapy, depending on the cancer stage. Previously, for-early-stage NSCLC, the surgical resection of a single lobe (lobectomy) or limited resection was accepted as the ideal practice (Duma et al., 2019). However, early-stage NSCLC surgery continues to be challenging and patient-specific. On the other hand, neoadjuvant chemotherapy may be advantageous in treating micrometastases early, staging the tumour more conservatively, enabling total resection, and improving tolerability (Duma et al., 2019). Nevertheless, the impact of neoadjuvant therapy remains uncertain, and existing studies have not demonstrated a survival benefit from preoperative treatment (Felip et al., 2010; Gilligan et al., 2007). A recent review discusses the targeted therapy in NSCLC in detail and notes that neoadjuvant immunotherapy for NSCLC has shown exceptional pathological response rates without any rise in postoperative morbidity (Aguado et al., 2022). Furthermore, individuals with early-stage lung cancer are advised to undergo adjuvant chemotherapy, as studies have revealed that distant metastases are the leading cause of recurrence after potentially curative surgery. The use of molecularly targeted drugs and immunotherapy in the early stages of NSCLC is gaining popularity. Despite numerous trials utilizing EGFR and anaplastic lymphoma kinase (ALK) inhibitors following surgical resection, these studies did not demonstrate a significant

improvement in progression-free survival (PFS) or overall survival (OS) (Goss et al., 2013; Kelly et al., 2015).

While treating advanced-stage lung cancer, the histological cell type, genetic mutation profile, and performance status must be considered. EGFR mutations and ALK rearrangement testing should be performed on all patients with histologically diagnosed cancer (Lindeman et al., 2013). Including additional genes (i.e., ERBB2, MET, BRAF, KRAS, and RET) for labs performing next-generation sequencing panels and ROS1 testing for all adenocarcinoma patients are important new recommendations (Lindeman et al., 2018). For patients with advanced-stage disease, molecular targeted therapy is typically the initial treatment of choice if they possess well-identified driver mutations. On the other hand, for patients who do not have EGFR mutations or ALK rearrangements or for those with unknown mutation status, the standard approach involves systemic cytotoxic chemotherapy (Gridelli et al., 2015).

1.2 Hallmarks of cancer

The hallmarks of cancer were first introduced by Hanahan & Weinberg in 2000. The list initially consisted of six hallmarks (Hanahan & Weinberg, 2000). The hallmarks included evading apoptosis, self-reliance in growth signals, lack of sensitivity to anti-growth signals, invasion and metastasis, infinite capacity for replication, and angiogenesis (Hanahan & Weinberg, 2000) (Figure 1.2 A). After 11 years, four new hallmarks were added: metabolism deregulation, immune evasion, tumour-promoting inflammation, and genome instability and mutation (Hanahan & Weinberg, 2011) (Figure 1.2 B). The hallmarks of the cancer list gained four new members in 2022: plasticity, epigenetic reprogramming, polymorphic microbiomes, and senescence based on another decade-old research (Figure 1.2 C) (Hanahan, 2022). This subsection will introduce the following hallmarks in more detail: metabolic rewiring, tissue invasion and metastasis, immune evasion, and tumour-promoting inflammation, as they will be investigated in the course of this thesis.

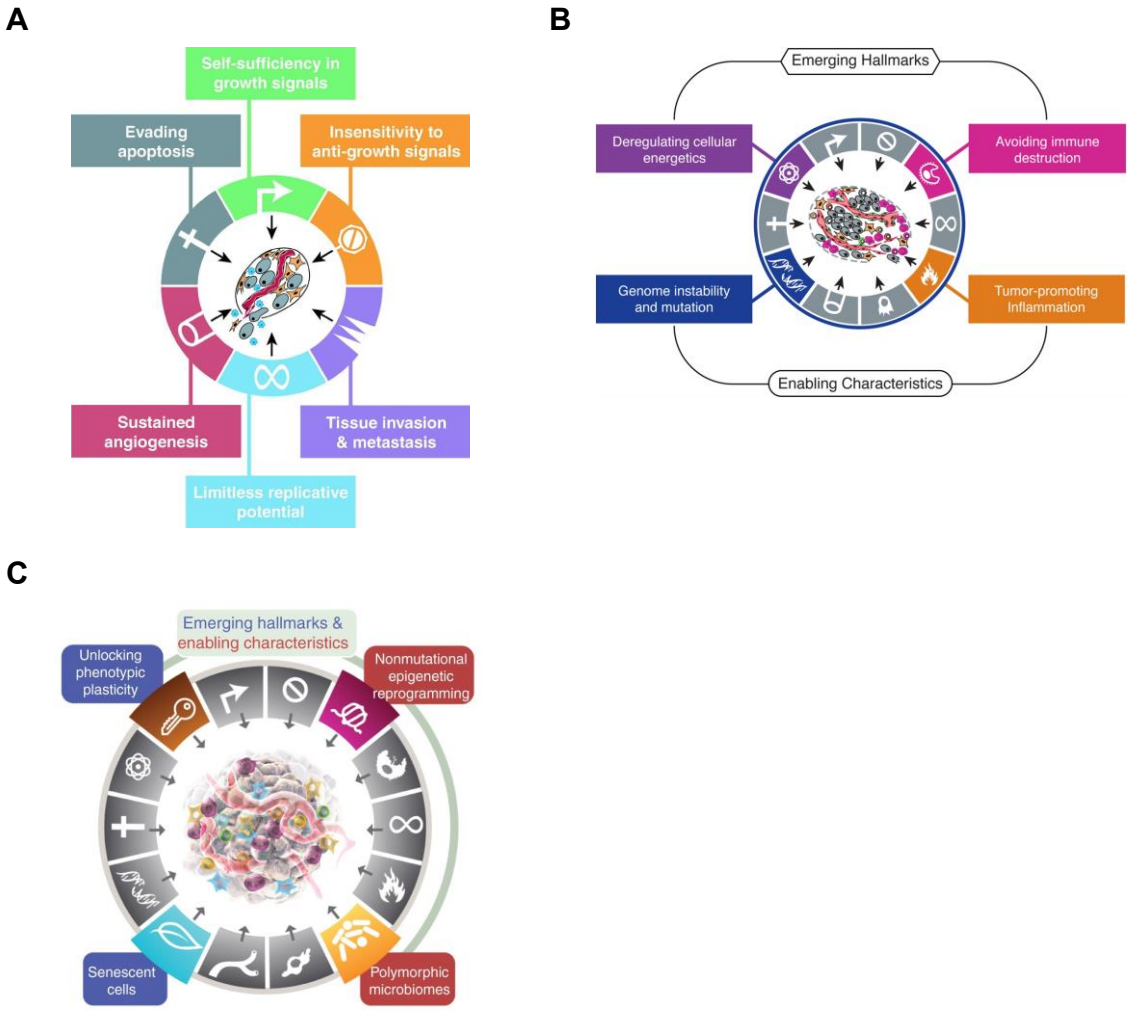

Figure 1.2: Hallmarks of cancer over the years. A) The term “hallmarks of cancer” was first introduced with six characteristics (Hanahan & Weinberg, 2000). **B)** Changes in the metabolism, immune evasion, tumour-promoting inflammation, and genome instabilities further added to the hallmarks of the cancer list (Hanahan & Weinberg, 2011). **C)** In the recent review in 2022, four more hallmarks made it to the list: plasticity, epigenetic reprogramming, microbiome, and senescence (Hanahan, 2022). This figure is adapted from the cited reviews above.

1.2.1 Deregulation of cellular energetics

Otto Warburg initially noted a reprogramming of energy metabolism as a cancer-related trait in the 1920s (Warburg et al., 1927). This phenomenon is now often referred to as "the Warburg effect." Although the amount of ATP produced by aerobic glycolysis is around 18 times lower, glycolytic intermediates can be redirected into biosynthetic pathways to create amino acids, nucleosides, and other components necessary for cell proliferation (Beyoğlu & Idle, 2021). Therefore, some cancer-related mutations make it possible for cancer cells to digest nutrients in a fashion that promotes proliferation rather than effective energy generation (Vander Heiden

et al., 2009). While glucose is a well-known fuel for cancer growth, amino acids also play a significant role in the development of the disease (Lieu et al., 2020). For instance, while glutamine is classified as a nonessential amino acid because of the presence of endogenous glutamine biosynthesis pathways, it becomes essential in cancer cells due to the rapid consumption of glutamine by transformed cells, which surpasses the rate of glutamine biosynthesis (Zhang et al., 2017). Glutamine has a variety of roles in cellular metabolism in addition to contributing to the biosynthesis of nucleotides, intermediates of the tricarboxylic acid (TCA) cycle, glutathione (GSH), and other non-essential amino acids (Yoo et al., 2020). Thus, glutamine deficiency inhibits cancer progression and, in some malignancies, even triggers cell death (L. Chen & H. Cui, 2015; Qing et al., 2012; Yoo et al., 2020). This metabolic dependence on glutamine by malignant cells has been called glutamine addiction (Wise & Thompson, 2010). Fetal calf serum (FCS) provides hormones, minerals, trace elements, lipids, and components for attachment, spreading, stabilization, and detoxification to cells (Gstraunthaler, 2003). Therefore, serum-free conditions can also rewire the metabolism. For example, in prostate cancer cells, serum deprivation triggers oxidative stress adaption (White et al., 2020), whereas serum deprivation sensitizes the cells to cisplatin treatment in cervical and ovarian cancer cell lines (Senichkin et al., 2018).

1.2.2 Invasion and metastasis

Hanahan and Weinberg stated that "stimulating invasion and metastasis" is a characteristic of cancer (Hanahan & Weinberg, 2011). Metastases still continue to be an essential characteristic of cancer malignancy, with the invasion of adjacent tissue and seeding in distant sites accounting for more than 90% of cancer patients' fatalities (Fares et al., 2020; Steeg, 2006). For metastasis to occur, the cancer cells must leave their primary site, travel through the circulation, tolerate blood vessel pressure, adapt to new biological conditions in a secondary site, and avoid a lethal fight with immune cells in order to generate metastases (Maitra, 2019; Massagué & Obenauf, 2016). Transdifferentiated epithelial cells acquire the capacity to invade, withstand stress, and spread through a process known as epithelial-to-mesenchymal transition (EMT) (Hanahan & Weinberg, 2011). Epithelial cells are immobile and firmly attached to one another and the surrounding extracellular matrix (ECM) (Fouad & Aanei, 2017). EMT is responsible for the reversible biochemical changes that enable a particular epithelial cell to develop a mesenchymal phenotype and confers epithelial cells with epithelial-mesenchymal plasticity, which is essential for the spread of cancer and other diseases (Fares et al., 2020; Ye

& Weinberg, 2015). Several molecular mechanisms are activated to start the EMT process (Figure 1.3). These consist of synthesizing ECM-degrading enzymes, activating transcription factors, expressing particular cell-surface proteins, and reorganizing cytoskeletal proteins (Kalluri & Weinberg, 2009). Furthermore, several signalling molecules induce EMT such as HGF, EGF, FGF, and TGF-β (Adamczyk-Gruszka et al., 2022; Farajihaye Qazvini et al., 2019; Kalluri & Weinberg, 2009; Liu et al., 2017; Nawshad et al., 2005).

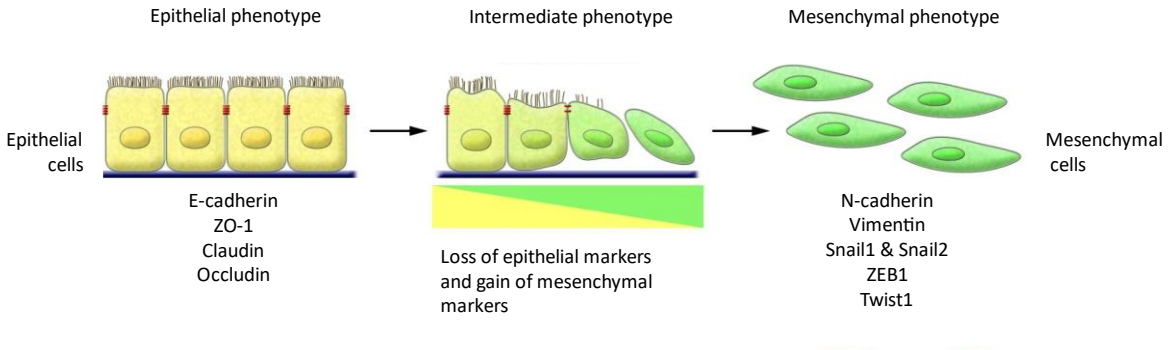

Figure 1.3: Epithelial-to-mesenchymal transition process. An EMT is distinguished by the functional transformation of differentiated epithelium cells into mobile, ECM component-secreting mesenchymal cells. The list includes the epithelial and mesenchymal cell markers used in this study. The figure is adapted from a previous review (Kalluri & Weinberg, 2009).

1.2.3 Immune evasion

Hanahan and Weinberg added immune evasion to the hallmarks of the cancer list in 2011 (Hanahan & Weinberg, 2011). The immune system acts as a potent inhibitor of tumour development and progression, at least in some types of cancer that are not caused by viruses. Effective anti-cancer immune responses require a series of steps to be repeated (Chen & Mellman, 2017; Kim & Chen, 2016). The process begins with the release of neoantigens from dead cancer cells upon tumour formation. Dendritic cells (DCs) capture these neoantigens and transport them to the nearest draining lymph node (DLN). Using MHC-I and MHC-II molecules, DCs present the acquired antigens to T cells, triggering activation of effector T cells. Within the DLN, cancer-specific T cells recognizing the antigen express essential cell adhesion molecules and chemokine receptors for migration and infiltration into the tumour. Subsequently, these cells traverse the bloodstream to reach the tumour tissue. The MHC-I-antigen complex presented by the cancer cells is later recognized and bound by the T cell receptor (TCR) of CD8+ T cells as they infiltrate into the tumour. Cytotoxic T cells can kill malignant tumour cells that express tumour neoantigens (Raskov et al., 2021). Immunotherapy supports the immune system's ability to combat cancer (Steven et al., 2016; Waldman et al.,

2020). Of the therapy options, immune check point inhibitors show effectiveness only in some tumours. The responsive subtypes are now known as “hot” tumours, while the unresponsive ones are called “cold” tumours (Kim & Cho, 2022). For tumours to be classified as "hot," they must first undergo successful antigen recognition, T cell activation, and T cell infiltration into the tumour. However, a malfunction at the beginning of the cancer-immune cycle occurs in "cold" tumours, distinguished by immunological non-infiltration, and most cold tumours do not react to immune checkpoint inhibitors. Therefore, it may be hypothesized that immunological checkpoint inhibitor reactivity is a common characteristic of this kind of immune infiltration and is primarily influenced by antigen identification and T-cell migration to the tumour (Havel et al., 2019; McGranahan et al., 2016; van Rooij et al., 2013).

1.2.4 Tumour-promoting inflammation

Another immune system-related hallmark of cancer, tumour-promoting inflammation, was added in 2011 (Hanahan & Weinberg, 2011). Inflammation plays a role in fostering various hallmark characteristics within the tumour microenvironment. This is achieved through the release of bioactive molecules, including growth and survival factors, enzymes that modify the extracellular matrix to support angiogenesis, invasion, and metastasis, as well as proangiogenic factors. Additionally, inflammation provides signals that trigger the activation of programs such as EMT and other processes that facilitate hallmark traits (DeNardo et al., 2010; Grivennikov et al., 2010; Qian & Pollard, 2010). Furthermore, inflammation can promote the transformation of early neoplasia into advanced malignancies and is sometimes visible at the earliest stages of neoplastic evolution (de Visser et al., 2006; Qian & Pollard, 2010). Since many cancers lack apoptotic cell death, necrotic cell death may be more relevant and immunostimulatory (Galluzzi et al., 2018; Weinlich et al., 2017). For instance, tumour cell necrosis may result in local and systemic anti-tumour immunity even when the antigens presented in dying and remaining tumour cells are not entirely shared (Snyder et al., 2019). Additionally, cancer cells nearby may be actively mutated by chemicals released by inflammatory cells, particularly reactive oxygen species, which speeds up the development of their genetic makeup into states of increased malignancy (Grivennikov et al., 2010). Understanding how inflammation promotes tumour growth is crucial for at least two reasons: by inhibiting inflammation, malignancies can be detected earlier, and it can be understood how metastatic seeds spread once they have become established far away (Greten & Grivennikov, 2019).

1.3 The proteasome system

1.3.1 The constitutive proteasome (c20S)

The proteasome, around 700 kDa protein complex, is found in the cytoplasm and the nucleus of all eukaryotic cells. The proteasome is an evolutionarily conserved protease complex composed of 28 subunits. Its structure is barrel-shaped and consists of four stacked, heptameric rings that exhibit symmetry. The outer rings are formed by seven subunits (α1–7) each, while the inner rings are composed of seven subunits (β1–7) each. These inner rings collectively seal the entry port of the core proteasome, ensuring controlled protein degradation and preventing unregulated protein destruction (Figure 1.4) (Groll et al., 2000; Groll et al., 1997).

Within the interior chamber of the barrel structure, the catalytically active sites are located on three distinct beta subunits, specifically referred to as β1/PSMB6, β2/PSMB7, and β5/PSMB5. These subunits each feature an N-terminal threonine residue that functions as the active centre, initiating a nucleophilic attack on the peptide bonds of the unfolded protein substrate. The substrate binding pockets within these β1, β2, and β5 subunits dictate their cleavage preferences, resulting in diverse activities targeting acidic residues (caspase-like activity), basic residues (trypsin-like activity), as well as large hydrophobic amino acids (chymotrypsin-like activity), among other amino acid types (Arciniega et al., 2014; Groll et al., 1997; Huber et al., 2012).

The presence of the ring-like subunits around the 20S core particle confines its accessibility, resulting in limited activity when the 20S proteasome is in its closed configuration. Consequently, the 20S proteasome struggles to effectively degrade large and folded proteins (Groll et al., 2000) (Groll et al., 2000). However, emerging evidence suggests that the 20S core particle can still target partially or fully unfolded proteins for degradation (Aiken et al., 2011; Pickering et al., 2010; Wang et al., 2020). Moreover, recent findings indicate that uncapped 20S proteasomes are capable of breaking down native proteins featuring intrinsically disordered regions (IDRs) or proteins entirely composed of disordered regions (van der Lee et al., 2014). These intrinsically disordered proteins (IDPs) contain elements with signalling and regulatory functions associated with processes like oncogenesis and growth regulation (Dyson & Wright, 2005). Notably, the 20S proteasome exhibits resilience in oxidative conditions, contrasting with the relatively less stable 19S-capped 20S proteasome complexes (Livnat-Levanon et al., 2014).

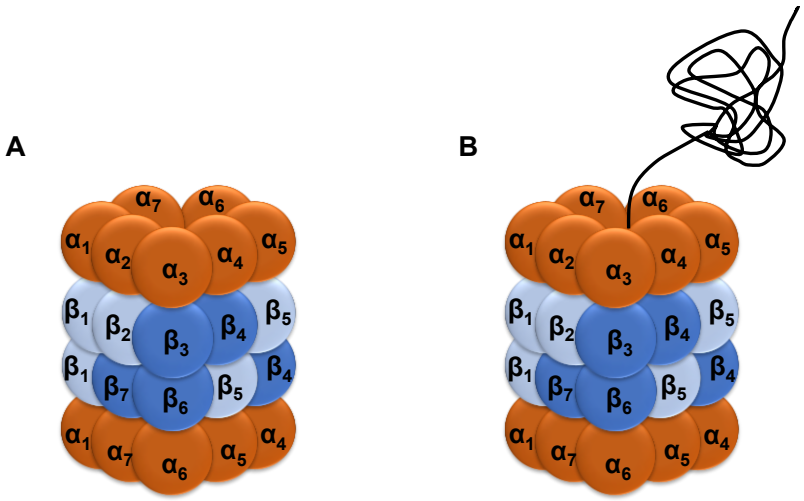

Figure 1.4: Cartoon representation of the constitutive proteasome. A) The two α-rings (orange) and two β-rings (light and dark blue), in a symmetric α1-7β1-7β1-7α1-7 conformation, form the 20S core particle. The β1, β2, and β5 (coloured light blue) subunits are catalytically active. Without an activator, the α-rings of the 20S core particle are in a closed conformation. **B)** To be degraded, the substrates enter the 20S core particle via the α-ring gate centre (Dahlmann, 2016)**.**

The thymus expresses another catalytic subunit, β5t/PSMB11, which is involved in the positive selection of $CD8^+$ T lymphocytes (Murata et al., 2007; Nitta et al., 2010). The testis is one tissue where the α4s/PSMA8 subunit is explicitly expressed, which adds to the diversity of cellular 20S proteasome particles (Kniepert & Groettrup, 2014; Uechi et al., 2014).

Structural investigations of 20S proteasomes have demonstrated that the N-termini of the 20S particle functions as gatekeepers, obstructing the entrance to the proteolytic chamber. This arrangement serves to prevent uncontrolled protein entry and degradation by the 20S proteasomes (Groll et al., 2000; Groll et al., 1997; Huber et al., 2012; Schrader et al., 2016). The activation of 20S proteolysis involves at least a partial opening of this gate, allowing the admission of partially folded or unfolded proteins (Kish-Trier & Hill, 2013). Consequently, approximately 20% of cellular proteins, primarily those with excessive disordered regions, are potentially susceptible to degradation by 20S proteasomes (Baugh et al., 2009; Kumar Deshmukh et al., 2019).

Table 1.1: The nomenclature of the 20S core subunits

Subunit	Gene symbol	Name
α	PSMA1	*proteasome 20S subunit alpha 1*
	PSMA2	*proteasome 20S subunit alpha 2*
	PSMA3	*proteasome 20S subunit alpha 3*
	PSMA4	*proteasome 20S subunit alpha 4*
	PSMA5	*proteasome 20S subunit alpha 5*
	PSMA6	*proteasome 20S subunit alpha 6*
	PSMA7	*proteasome 20S subunit alpha 7*
	PSMA8	*proteasome 20S subunit alpha 8*
β	PSMB1	*proteasome 20S subunit beta 1*
	PSMB2	*proteasome 20S subunit beta 2*
	PSMB3	*proteasome 20S subunit beta 3*
	PSMB4	*proteasome 20S subunit beta 4*
	PSMB5	*proteasome 20S subunit beta 5*
	PSMB6	*proteasome 20S subunit beta 6*
	PSMB7	*proteasome 20S subunit beta 7*
	PSMB11	*proteasome 20S subunit beta 11*

1.3.2 The immunoproteasome (i20S)

While all cell types constitutively express the standard proteasome, cells of hematopoietic origin contain an additional set of proteasomes with unique catalytic subunits (Groettrup et al., 2001). The three catalytically active sites in this so-called immunoproteasome are the only structural differences between the immuno- and the standard proteasomes. The term "immunosubunits" originated from the location of the genes low molecular mass protein 2 (LMP2/β1i) and low molecular mass protein 7 (LMP7/β5i) in the MHC class II genomic region (Ortiz-Navarrete et al., 1991; Yang et al., 1992). These subunits integrate into the immunoproteasome instead of their homologous counterparts β1 and β5, for example, after INF-γ stimulation (Akiyama et al., 1994; Früh et al., 1994; Groettrup et al., 2001). Later, a third low molecular mass protein 10 (LMP10/ MECL-1/β2i) was discovered to be the replacement for the standard β2 subunit (Groettrup et al., 2010; Groettrup, Kraft, et al., 1996).

However, non-immune cells can also express immunosubunits upon the secretion of pro-inflammatory cytokines like interferon (IFN) or tumour necrosis factor (TNF) (Angeles et al., 2012). Upon stimulation by interferons (IFNs), specific regulatory factors such as interferon regulatory factor-1 (IRF-1) and signal transducers and activators of transcription-1 (Stat-1) play

a role in orchestrating the expression of three immunosubunits (Brucet et al., 2004; Chatterjee-Kishore et al., 1998; Foss & Prydz, 1999; Namiki et al., 2005). Notably, type I IFNs can also lead to the upregulation of the immunoproteasome, although higher doses are necessary compared to the upregulation achieved by IFN-γ (Freudenburg et al., 2013a, 2013b; Shin et al., 2006). Immune cells exhibit elevated baseline immunoproteasome expression in comparison to non-immune cells, likely due to sustained activation of intracellular signalling pathways (McCarthy & Weinberg, 2015). In studies involving mice, it was observed that mice lacking either Type I or Type II IFN receptors displayed modest decreases in mRNA levels for β1i and β5i in their thymus and spleens, while another study found that the expression of immunoproteasome proteins in the spleens of mice lacking IFN-γ was comparable to that of wild-type mice (Barton et al., 2002; Lee et al., 1999). However, immunoproteasome subunit mRNA and protein expression are significantly decreased in $STAT1^{-/-}$ mice spleens, indicating that non-phosphorylated STAT1 is at least partly responsible for basal immunoproteasome expression rather than IFN-γ signaling (and phosphorylated STAT1) (Barton et al., 2002; Lee et al., 1999; McCarthy & Weinberg, 2015).

In contrast to the conventional subunits β1, β2, and β5, the immunosubunits possess distinct cleavage preferences due to structural alterations in the substrate-binding pockets of their active sites (Huber et al., 2012). For instance, when β1 is replaced with LMP2, there is a notable reduction in post-acidic cleavage activity. Consequently, a pool of peptides with predominantly hydrophobic C-termini is generated. These peptides more closely align with the binding requirements of MHC class I molecules, as compared to antigens produced by the standard proteasome. This alteration in cleavage specificity highlights the role of immunosubunits in generating peptides suitable for MHC class I antigen presentation (Groettrup et al., 2001).

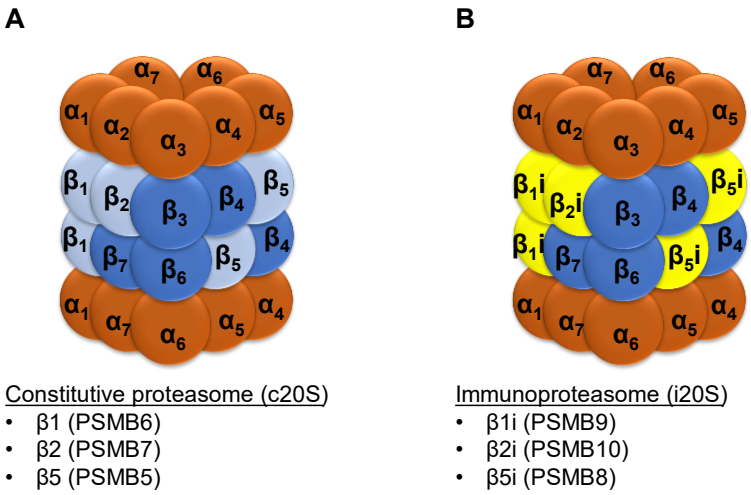

Figure 1.5: Cartoon representation of the differences between constitutive proteasome and immunoproteasome. A) The two α-rings (orange) are in a symmetric α1-7 orientation and have two β-rings (light and dark blue) in a β1-7 conformation in between. The gene name of the catalytically active subunits (light blue) is mentioned below in brackets (Dahlmann, 2016). **B)** The immunoproteasome shares similarities in structure; however, the catalytically active sites differ. The β1- β2- β5 subunits are replaced with β1i- β2i- β5i (yellow), respectively. The gene name of the catalytic subunits (yellow) of immunoproteasomes is mentioned below in brackets.

MHC class I antigen presentation shows only minor abnormalities in mice lacking LMP2, LMP7, or MECL-1 (Basler et al., 2006; Fehling et al., 1994; Van Kaert et al., 1994). In contrast, mice lacking all i20S subunits exhibit a deficiency in MHC class I epitope presentation, reminiscent of the immunological phenotype observed in LMP7-deficient mice (Eleanor Z Kincaid et al., 2012). Moreover, the i20S proteasome plays a role in maintaining and shaping the CD8+ T-cell repertoire throughout the immune response to intracellular infections (Yang et al., 1992; Zaiss et al., 2008). Additionally, i20S contributes to the suppression of regulatory cell induction while fostering the development of pro-inflammatory T-helper type 1 (Th1) and type 17 (Th17) cells (Bockstahler et al., 2020; Goetzke et al., 2021; Khalid W Kalim et al., 2012). Moreover, monocytes and T cells stimulate the production of the cytokines IL-23 and IL-2 (Muchamuel et al., 2009). When it comes to degrading oxidized proteins in an ATP- and ubiquitin-free way, i20S has been proven to be more effective than its conventional equivalent (Abi Habib et al., 2020; Pickering et al., 2010). The idea is supported by the fact that the mTOR pathway increases i20S expression to halt the accumulating of misfolded or damaged proteins (Eleanor Z. Kincaid et al., 2012). Furthermore, it has been demonstrated that i20S expression alters the quantity of transcription factors that control essential signalling pathways (Çetin et al., 2021; de Verteuil et al., 2014).

Table 1.2: The nomenclature of the i20S catalytically active subunits

c20S catalytically active subunits	**i20S catalytically active subunits**		
Gene Symbol	*Gene Name*	*Protein Name*	*Aliases*
PSMB7	PSMB8	*proteasome 20S subunit beta 8*	β5i, LMP7
PSMB6	PSMB9	*proteasome 20S subunit beta 9*	β1i, LMP2
PSMB5	PSMB10	*proteasome 20S subunit beta 10*	β2i, MECL-1, LMP10

1.3.3 Proteasome Activators

Multiple proteasome activators have been identified, including the 19S regulator, PA28αβ, PA28γ, and PA200 (Figure 1.4 A). These proteins attach to the 20S proteasome's alpha rings and open the gate to the proteolytic chamber, making it easier to degrade proteins and peptides. These regulators can form singly or doubly capped complexes by attaching either one end of the 20S molecule or both. For example, the most studied proteasome activator, 19S, was found to attach either one end (26S) or both ends of the catalytic core (30S) and work in an ATP- and ubiquitin-dependent way (Figure 1.4 B). Alternatively, PA28αβ, PA28γ, and PA200 attach to the proteasome and enable an ATP- and ubiquitin-independent protein degradation (Figure 1.4 C). Additionally, these activators can create complexes with mixed regulators attached to one 20S catalytic core.

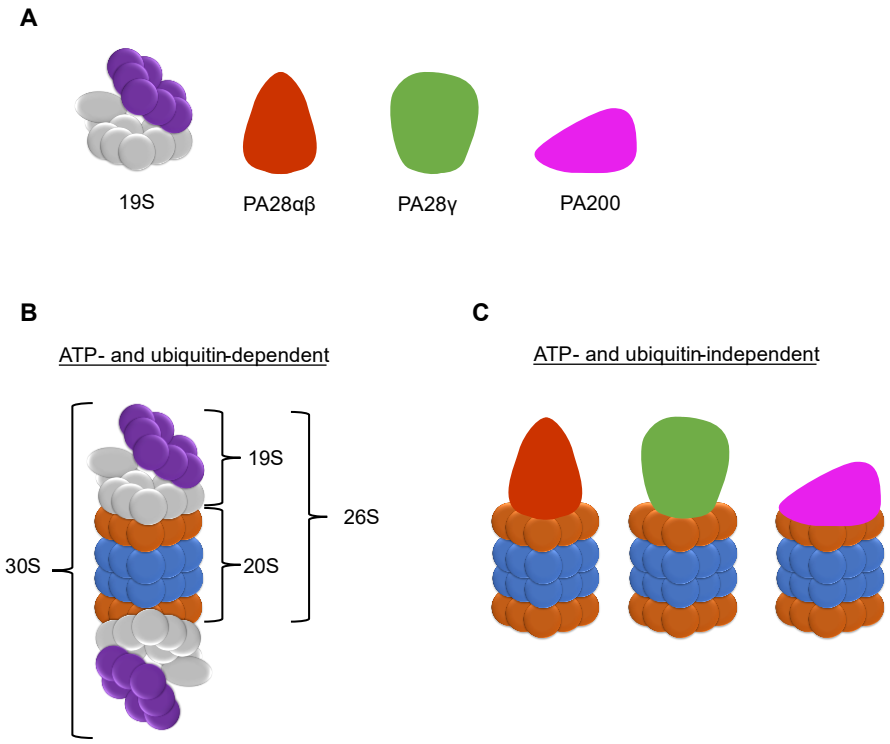

Figure 1.6: Cartoon representation of proteasome complexes. The proteasome has four different **A)** activators identified so far. These proteins bind and activate the catalytic core (20). They can be separated depending on their dependency on ATP and ubiquitin. 19S binds to 20S and works in a **B)** ATP- and ubiquitin-dependent fashion. Three activators, PA28αβ, PA28γ, and PA200, work in a **C)** ATP- and ubiquitin-independent manner.

1.3.3.1 The 19S activator

As previously mentioned, 19S binds to the 20S core either at one or both ends and forms 26S and 30S, respectively. The 26S proteasome, which mediates ubiquitin-dependent substrate degradation, is at the centre of the ubiquitin-proteasome system (Ciechanover, 2005). 19S-bound complexes make up most of the cell's proteasome complexes together with free 20S proteasomes (Fabre et al., 2013). 19S is made of a structure that resembles a base and a lid (Bard et al., 2018). The base of the 19S contains four non-ATPase subunits (RPN1, RPN2, RPN10, and RPN13) and a ring of six ATPases (RPT1-RPT6) with ubiquitin-binding features(Tanaka, 2009). The lid comprises nine non-ATPase subunits and is primarily involved in the deubiquitylation of substrates by the RPN11, UCH37, and UBP6/USP14 (Lander et al., 2013). The ATPases play a crucial role in facilitating binding between the 20S core and the 19S regulatory particle, leading to conformational changes and substrate unfolding essential for the activation of the 26S proteasome (Eisele et al., 2018; Finley et al., 2016; Matyskiela et al., 2013; Navon & Goldberg, 2001). Extensive studies involving knockout mouse models have demonstrated the indispensability of most 19S subunits for both cell and organismal survival

(Bedford et al., 2008; Sitaraman et al., 2019; Ugun-Klusek et al., 2018). Cell type-specific knockouts of individual 19S subunits have further elucidated the causal relationship between these subunits and specific pathophysiological conditions such as neurodegeneration and acute lung injury (Tanaka et al., 2012). Moreover, the assembly of 26S proteasome complexes requires specific chaperones to facilitate the formation of the complex from the 20S core and the 19S regulator (Funakoshi et al., 2009; Kaneko et al., 2009; Murata et al., 2009; Roelofs et al., 2009). Notably, in mammals, p28/PSMD10 and p27/PSMD9 have been identified as activating assembly factors, promoting the assembly of the 26S complex (Kaneko et al., 2009; Lu et al., 2017). In contrast, Proteasomal ATPase-Associated Factor 1 (PAAF1) and S5b/PSMD5 appear to inhibit the formation of the 26S complex (Levin et al., 2018; Park et al., 2005; Shim et al., 2012). These intricate regulatory mechanisms ensure the proper assembly and functioning of the 26S proteasome complex in cells.

1.3.3.2 PA28α/β

The PA28α/β proteasome activator is exclusive to higher eukaryotic organisms and is constructed from seven 28 kDa subunits, termed PSME1 (α) and PSME2 (β) (Fort et al., 2015; Wang et al., 2020). These subunits, often induced by interferon (IFN), exhibit co-regulation with the immunoproteasome, suggesting their involvement in the presentation of MHC I antigens (Cascio, 2014; Rechsteiner et al., 2000). Within mammals, PA28 consists of four PA28α and three PA28β subunits, a composition that enhances proteasome activity more effectively than homomeric PA28α or PA28β complexes (Huber & Groll, 2017; Realini et al., 1997). Unlike the 19S regulator, they work in an ATP and ubiquitin-independent manner and are wide enough to accommodate small proteins and disordered polypeptides (Stadtmueller & Hill, 2011). PA28αβ is found in the cytoplasm of cells from numerous organs, but it is most abundant in immunological tissues (Rechsteiner et al., 2000). The PA28αβ complexes preferentially bind with the immunoproteasome and activate all catalytically active subunits on the 20S in vitro (Fabre et al., 2015; Realini et al., 1997). Further studies showed that IFN-γ stimulation increases the expression of PA28α and PA28β subunits, as well as the formation of PA28αβ complexes (Murata et al., 2001; Tanahashi et al., 1997). The PA28αβ complex has been hypothesized to take part in antigen processing and to be crucial for MHC class I antigen presentation acting in concert with the immunoproteasome (Dick et al., 1996; Groettrup, Soza, et al., 1996; Preckel et al., 1999; Stohwasser et al., 2000) However, investigations involving double knockout animals lacking PA28α and PA28β subunits have revealed only minor

alterations in MHC I antigen presentation and disease progression upon viral induction. This suggests that PA28α/β might not be universally vital for generating MHC I antigenic peptides but instead influences the processing of specific epitopes (Murata et al., 2001; Respondek et al., 2017; Yamano et al., 2008).

1.3.3.3 PA28γ

PA28γ, also known as PSME3, shares close genetic similarities with PA28αβ. However, it forms a distinct complex with seven subunits, each having a molecular weight of 28 kDa, creating a homoheptameric structure, and its primary location is within the cell nucleus (Fort et al., 2015; Realini et al., 1997; Stadtmueller & Hill, 2011). Although PA28γ is capable of interacting with both the 20S and 26S proteasome components, the majority of its presence in the nuclear environment is as independent complexes or as part of structures not directly associated with the proteasome. This suggests that PA28γ might perform functions beyond its established role in proteasome activation. This situation raises the possibility that PA28γ might have roles unrelated to proteasome activity or that these unattached PA28γ complexes could act as a reservoir that can swiftly join the proteasome when required for activation (Welk et al., 2016). PA28γ knock-out mice develop slower and are prone to premature ageing. However, they are viable and fertile, indicating that PA28γ is not necessary for survival (Fort et al., 2015; Murata et al., 1999). Recent studies found the involvement of PA28γ in NF-κB and transforming growth (TFG) -β signalling (Ali et al., 2013; Jiao et al., 2020; Sun et al., 2016; Xie et al., 2019; Xu et al., 2016). It is essential for maintaining protein homeostasis upon oxidative stress, proteotoxic stress following proteasome suppression, genotoxic stress during DNA repair, and autophagy regulation (Dong et al., 2013; Jiang et al., 2019; Levy-Barda et al., 2011; Pickering et al., 2010; Welk et al., 2016; Zhang et al., 2015). Recent findings from mammalian cryo-EM structures demonstrate that PA28γ activates the trypsin-like catalytic site of the 20S proteasome through an allosteric mechanism and might be involved in the degradation of the DNA and RNA binding proteins (Thomas & Smith, 2022).

1.3.3.4 Proteasome Activator 200 (PA200)

I participated in crafting a recently published review on PA200, where I held the position of the first author (Yazgili et al., 2022). In this part of the thesis, certain portions of the PA200 review were rephrased to establish a strong foundational understanding of PA200.

1.3.3.4.1 The structure of PA200

PA200 (protein name), also referred to as PSME4 (gene name), is a monomeric protein with a molecular weight of 200 kDa. It interacts with both the catalytic core (20S) and the 26S proteasome complexes, leading to the activation of their proteolytic capabilities towards peptides (Ustrell et al., 2002). PA200 is highly conserved in mammals and has homologs in plants (*Arabidopsis thaliana*), yeast (*Saccharomyces cerevisiae*), and worms (*Caenorhabditis elegans*), but not in Arachne or *Drosophila melanogaster* (Fort et al., 2015).
Although the structural similarities between human PA200 and yeast PA200, known as Blm10, are preserved, the sequence similarity between the two is only 17% (Savulescu & Glickman, 2011; Toste Rego & da Fonseca, 2019). Using PA200 isolated from bovine testes, the initial PA200/20S structure was documented in 2005, achieving a resolution of 23 Å (Ortega et al., 2005). The 20S alone, 20S-singly capped or 20S-doubly capped with PA200, formed at a ratio of 5:4:1. PA200 was characterized as an asymmetric, hollow, dome-like structure attached to all exterior alpha subunits of the 20S (apart from α7) as a monomer (Ortega et al., 2005; Yazgili et al., 2022). In addition, the 20S gate was reported to open up upon PA200 binding; however, due to the low resolution of the structures, no possible entry sites were observed in the earliest structure (Figure 1.7).

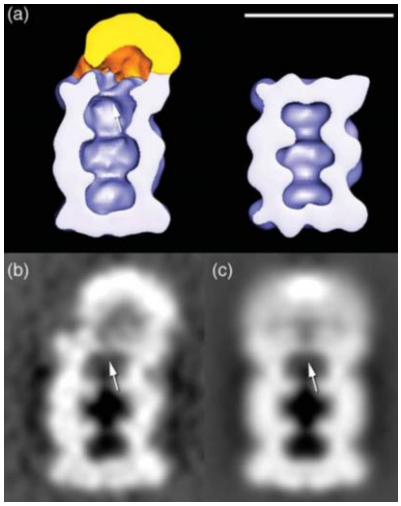

Figure 1.7: Earliest structure of PA200-20S proteasome complexes. a) Isosurface representations cut through the middle of the PA200-20 S complex (left), and the 20 S proteasome (right) shows only the end where PA200 (gold) is bound (arrow), opening the gate to the internal cavities of the 20 S, in contrast, the free end of the 20 S proteasome blue) is closed. **b)** corresponds to the view in a), and a cylindrical average around the central axis **c)**, indicating the decreased density at the end of the 20 S bound to PA200. The image is taken from the first PA200 structure paper (Ortega et al., 2005).

A recent structure of human PA200 and entirely *in vitro* reconstituted human 20S was published in late 2019 (Toste Rego & da Fonseca, 2019). In this study, five proteasome assembly chaperones that aided the 20S in vitro assembly were used to express all the alpha (α) and beta (β) subunits utilizing a baculovirus expression method. To co-express human PA200, a third baculovirus was introduced. This recombinant PA200/20S complex's high-resolution cryo-EM analysis revealed a dome-like structure comparable to the previous PA200, resulting from helical repetitions and binding to the 20S proteasome (Figure 1.8 A). The high-resolution analysis of PA200's interaction with the alpha subunits revealed that PA200 linked to 20S via two anchor points, one near the α1– α2 interface and the other one at the α5– α6 interface. When PA200 was bound, α5 and α7 moved to the interior of the PA200 dome, and α3 shifted to have a bigger ring opening. The catalytically active β-subunits underwent allosteric effects as a result of these modifications, with the β2 active site broadening and the β1 and β5 sites narrowing. By binding PA200 to recombinantly expressed 20S, these structural modifications of the catalytic centres were followed by an increase in trypsin-like (T-L) activity (β2), a decrease in chymotrypsin-like (CT-L) activity (β5), and a decrease in caspase-like (C-L) activity (β1) *in vitro*. The PA200 and PA200-20S complex's most recent cryo-EM structure, measuring 3.75 Å and 2.72 Å, respectively, was published in 2020 (Guan et al., 2020). This study used commercially available 20S standard proteasomes to complex recombinantly

expressed human PA200, which produced a variety of doubly- or singly-capped PA200/20S complexes. The 20S α-subunits were similarly rearranged following the PA200 attachment, but no rearrangement was seen on the unbound alpha rings. Although the authors did not specify any allosteric alterations to the catalytically active beta sites, the *in vitro* activity assay showed a roughly 3-4–fold increase in CT-L activity. The other two active sites, however, were not examined. While limiting the direct access to 20S but partially opening the 20S entrance pore, PA200 rests directly on the α -rings of 20S in both recent structures. Only unstructured protein chains or peptides would be permitted through the PA200 gate due to the PA200 dome's narrow opening.

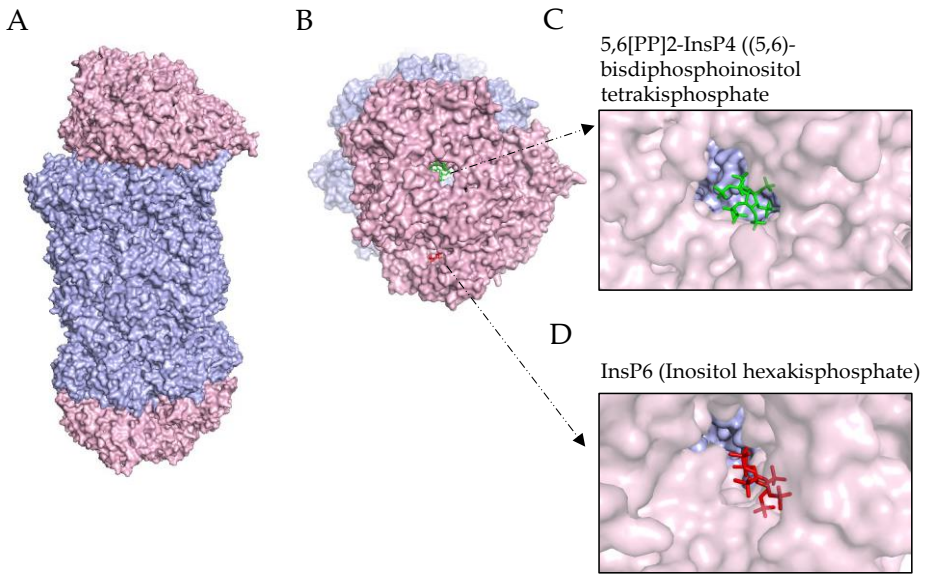

Figure 1.8: Structure of PA200. A) General view of the complex proteasome structure with PA200 attached to both ends (the 20S (blue), PA200 (pink), PDB ID: 6REY) **B)** Two negatively charged molecules sit on top of PA200 **C)** (5,6)-bisdiphosphoinositol tetrakisphosphate (5,6[PP]2-InsP4) and **D)** Inositol hexakisphosphate (InsP6). The image is taken from a recent review of PA200 (Yazgili et al., 2022).

Two positively charged grooves outside PA200 were identified by the high resolution of PA200/20S complexes and serve as potential substrate entrance sites (Figure 1.8 B). Two negatively charged densities, (5,6)-bisdiphosphoinositol tetrakisphosphate (5,6[PP]2-InsP4) and inositol hexakisphosphate (InsP6), however, blocked these channels (Figure 1.8 C and D, respectively). These extremely negatively charged small signalling molecules may be used to fine-tune substrate entrance via PA200. InsP6 played a role in folding, ternary interactions, and structural stabilization in earlier structures (Macbeth et al., 2005; Scaiola et al., 2020). RNA editing (Macbeth et al., 2005), mRNA transcription (Okamura et al., 2018), RNA export (Folkmann et al., 2011), DNA repair (Byrum et al., 2004; Hanakahi & West, 2002), and

modulation of histone deacetylases (HDAC) activity (Marcum & Radhakrishnan, 2019) have all been linked to InsP6. In addition, InsP6 plays a role in UV radiation resistance and serves as a glue to bind Cullin-RING ligase (CRL) and COP9 signalosome (CSN) together (Lin et al., 2020). The substantial abundance of InsP6 in the nucleus is consistent with its regulatory role on numerous nuclear pathways (Brehm et al., 2007). Regarding the InsP4 function, not much is known. Evidently, no PA200 structure is available right now without these molecules. Hence, their purposes may only be hypothesized. Given that PA200 is also found in the nucleus, InsP6 may interact with PA200 and modify its activity, possibly serving as an inhibitor. The structural information thus sheds light on the possibilities that PA200 binding could (1) hinder the access of bulky and positively charged substrates, (2) enhance its preference for negatively charged substrates, and (3) elevate its catalytic efficiency for ubiquitinylated substrates when forming hybrid complexes with 26S (Yazgili et al., 2022).

The structure from Toste Rego et al. shows that upon PA200 binding to the 20S, the 20S alpha subunit gate opens, and the proteolytic sites are rearranged, facilitating the proteolytic processing of peptide substrates (Toste Rego & da Fonseca, 2019). PA200's potential to activate specific active sites, however, remains debatable. PA200 promotes peptide hydrolysis of all 20S active sites, primarily the C-L activity, according to early biochemical data using PA200 and 20S isolated from bovine testes (Ustrell et al., 2002). Later, Blickwedehl et al. reported increased C-L activity connected to cell PA200 expression (Blickwedehl et al., 2008). In contrast, the structural results from Toste Rego et al. showed that the C-L and CT-L activities decreased. However, the T-L active site was activated in an in vitro reconstituted PA200/20S complex (Toste Rego & da Fonseca, 2019). Later, Guan et al. found that red blood cell-isolated human 20S and recombinant human PA200 increased CT-L activity by 3–4 times (Guan et al., 2020). An in vitro experiment using cell extracts and added recombinant human PA200 revealed activation of the C-L and suppression of the T-L activities, according to a new study (Javitt et al., 2023). Recent research found enhanced activity for all 20S catalytic subunits when recombinant human PA200 was introduced, further compounding the issue (Zivkovic et al., 2022).

1.3.3.4.2 The function of PA200

A potential nuclear localization signal in PA200/PSME4 suggests its nuclear localization (Ustrell et al., 2002). In cytoplasmic, microsomal, and nuclear extract crosslinking experiments, PA200 was found in each subcellular fraction (Fabre et al., 2013). However, the

subcellular localization may change according to the type of cell. In several experiments, genomic DNA and PA200 were colocalized (Blickwedehl et al., 2007; Qian et al., 2013). In SH-SY5Y neuroblastoma cells, a CHIP seq analysis discovered that PA200 was connected to several gene promoters' transcription start sites (Douida et al., 2020).

PA200 is linked to several processes, including DNA damage repair (Blickwedehl et al., 2008; Blickwedehl et al., 2007), mitochondrial stress responses (Douida et al., 2020), response to proteasome inhibition (Welk et al., 2016), glutamine sensitivity of cancer cells (Blickwedehl et al., 2012), myofibroblast differentiation (Welk et al., 2019), and possibly a reduction in MHC class I antigen presentation in lung cancer (Javitt et al., 2023). Most of these studies investigated the potential functional implications of PA200 depletion in various cell types using acute silence of PA200. The knockdown of PA200 is often well tolerated by the cells at baseline but seems crucial in response to stress. Cancer cells exposed to ionizing radiation had a lower chance of surviving, and silencing of PA200 was linked to enhanced genomic instability and glutamine depletion sensitivity (Blickwedehl et al., 2008; Blickwedehl et al., 2007; Blickwedehl et al., 2012). However, when bred with p53-deficient animals, embryonic stem cells derived from PA200 knockout mice did not exhibit altered mortality or increased sensitivity to genotoxic stress (radiation of bleomycin) (Khor et al., 2006). In neuroblastoma cells, stable silencing of PA200 led to a metabolic switch from oxidative phosphorylation to glycolysis and increased intracellular ROS levels (Douida et al., 2021). In the same neuroblastoma cell line, ChIP-seq results showed that PA200 binds to the promoters of genes involved in cell cycle progression and death in response to mitochondrial stress, further supporting the idea that PA200 regulates mitochondrial function (Douida et al., 2020). Cells with low expression of PA200 were more susceptible to rotenone-induced cellular death (Douida et al., 2020). In contrast, the knockdown of PA200 in primary human lung fibroblasts stimulated myofibroblast development and shielded them from staurosporine-induced death (Welk et al., 2019). As opposed to this, mice lacking PA200 did not exhibit a different response to pulmonary fibrosis caused by bleomycin (Welk et al., 2019). This study indicates a differential role of PA200 across different cell types and possibly between mice and humans. The downregulation of PA200 in endothelial cells by miRNA-29b was linked to increased oxidative stress and endothelial dysfunction in a rat model (F. Wang et al., 2017). However, this effect was not linked to the modulation of PA200 and could instead be the result of additional and/or alternate targets of miRNA-29b. Knockdown of the PA200/PSME4 gene in hepatocellular carcinoma reduced mTOR phosphorylation and inhibited in vitro cell

proliferation (Ge et al., 2022). It is yet unclear how PA200 stimulates mTORC1 activation at the molecular level.

One of the consistent findings on PA200 function refers to its part in developing sperm cells. The ubiquitous genetic reduction of PA200 led to male infertility in mice (Khor et al., 2006), and this finding was supported by a separate PA200 KO model (Qian et al., 2013). Given that PA200 is mainly expressed in testes, it has been hypothesized that PA200 preferentially binds to a specialized type of proteasome, the spermatoproteasome, in which a gamete-specific α4s subunit substitutes the α4 isoform of constitutive proteasomes. To test this hypothesis, the spermatoproteasomes (s20S) were co-immunoprecipitated with α4s antibodies from bovine testes. The results showed that PA200 was enriched 2-fold in the spermatoproteasomes compared to the constitutive proteasome. However, when immunoprecipitation was carried out using the PA200 antibody, the levels of s20S and c20S were comparable, indicating that PA200 did not favour one 20S type over the other. Although PA200 appeared to have a role in s20S, the authors concluded that it does not work as an exclusive activator during germ cell development since 19S is coupled to α4s more (Zivkovic et al., 2022). In comparison to spermatogonia (SPG), PA200 binding to 20S was found to be at least 10-fold higher in spermatids (SPTs) and Sertoli (SER) cells, indicating a specialized role for PA200 in these cells (Zivkovic et al., 2022).

Qian et al. proposed the potential involvement of PA200 in the degradation of core histones associated with acetylation in response to DNA double-strand breaks (Qian et al., 2013). Their study revealed significant abnormalities in the early-stage elongated spermatids' core histone ablation in the testes of PA200 KO mice (Qian et al., 2013). They observed in vitro binding of acetylated histones to recombinant bromodomains from mouse PA200 and its yeast counterpart, Blm10, through pulldown experiments. The authors also demonstrated that bovine PA200 facilitated the in vitro degradation of acetylated histones by 20S proteasomes. This notion was reinforced by Mandemaker et al., who observed elevated histone levels in UV-exposed HeLa cells upon PA200 silencing (Mandemaker et al., 2018). Another recent study by Jiang et al. suggested that PA200 influences the stability of histone modifications H3K4me3 and H3K56ac in processes related to ageing and transcription (Jiang et al., 2021). However, the new cryo-EM structures of human recombinant PA200 did not corroborate the presence of a bromodomain in PA200, casting some limitations on these findings. Moreover, the positively charged histidine residues in PA200's entrance pores might not favour the binding of acetylated histones (Guan et al., 2020; Qian et al., 2013; Toste Rego & da Fonseca, 2019). Recent research by Douida et al. further suggested that PA200's role likely extends beyond the degradation of

acetylated histones (Douida et al., 2020). Their CHIP seq experiment in a neuroblastoma cell line indicated that PA200's genomic DNA binding only partially overlapped with the presence of H3K27ac marks. The mechanisms underlying the transcriptional regulation of PA200 expression are not well elucidated. Several studies have indicated that proteasome inhibitor therapy can trigger the transcriptional activation of PSME4, possibly as part of an auto-regulatory feedback loop (Meiners et al., 2003; Sha & Goldberg, 2014). Notably, research by Welk et al. demonstrated a two-fold upregulation of PSME4 within 24 hours following treatment with the proteasome inhibitor bortezomib. This upregulation was also observed upon decreased assembly of the 26S proteasome due to the silencing of the 19S component Rpn6 (Welk et al., 2016). Through in silico analysis of the PSME4 promoter, a conserved binding site for Nrf1 near the transcriptional start point was identified (Welk et al., 2016). Additionally, our research group revealed the transcriptional activation of PA200 in response to treatment with transforming growth factor beta (TGF-β) (Welk et al., 2019). The same study found that when basal stem cells differentiated into airway epithelial cells, PA200 was downregulated (Welk et al., 2019). One study suggested that the microRNA-29b binds to the 3' UTR of PA200 in the context of post-transcriptional control of PA200 (Jagannathan et al., 2015), but additional evidence is lacking. The fast assembly of PA200 into the 20S or 26S proteasome complexes at the level of the proteasome complex has been shown in response to acute proteasome inhibition (Welk et al., 2016). These findings imply that free PA200 exists and that it can be quickly recruited to the 20S and 26S proteasomes to create single- or double-capped PA200/20S or hybrid PA200/26S complexes (Welk et al., 2016). It has also been noted that PA200 forms PA200-20S-19S proteasome complexes when exposed to radiation in Hela cells (Blickwedehl et al., 2008). Structures of the complexes PA200-20S-PA28 and PA200-20S-19S were also documented in a recent BioRxiv publication (Zhao et al., 2021). The presence of PA200 in both the 20S and 26S complexes was confirmed by crosslinking experiments, which show that PA200 occupies the cytoplasm and nucleus in almost equal amounts (Fabre et al., 2013). It accounts for less than 5% of the cell's total proteasome fraction (Fabre et al., 2014). Another recent paper revealed that PA200 could bind to 20S complexes containing immunoproteasome subunits (Javitt et al., 2023). In their findings, the authors propose that the binding of PA200 to the immunoproteasome might exert a negative regulatory influence on the specific activities of the immunoproteasome responsible for generating MHC class I antigenic peptides. PA200 dysregulation in disease

To identify the functions of PA200, many studies used cancer lines previously (Blickwedehl et al., 2008; Blickwedehl et al., 2012; Douida et al., 2020; Ustrell et al., 2002). Our group showed the first direct evidence of the dysregulation of PA200 in the disease. Welk et al. showed that PA200 is upregulated in the myofibroblast in the fibrotic lung tissues of idiopathic pulmonary fibrosis function, and PA200 is involved in the activation of the myofibroblast (Welk et al., 2019). Recently, Javitt et al. showed that PA200 is upregulated in NSCLC, and its expression level corresponds to the responsiveness to immune checkpoint inhibition (Javitt et al., 2023). In our recent review, we have extensively discussed the dysregulation of PA200 in diseases (Yazgili et al., 2022). Interestingly, our literature survey found that PA200/PSME4 gene expression is increased in various cancers (Table 1.3) and cardiovascular diseases, whereas it is decreased in infection, environmental stress, neurodevelopment, and neurodegeneration. Therefore, considering its dysregulation in cancer, finding the significance of PA200 might serve as a potential therapeutic to target proteasome complexes with PA200 selectively. Our recent review of the protein discussed the PA200 dysregulation in diseases.

Table 1.3: An overview of PA200/PSME4 gene regulation in cancer. (Taken from (Yazgili et al., 2022))

Context	Disease	PA200/PSME4 Expression	Reference
Cancer	Multiple myeloma	↑ (loss of miR-29b)	(Jagannathan et al., 2015)
	Multiple myeloma	↑	(Yu et al., 2022)
	Gastric cancer	↑	(Guo et al., 2021)
	Oesophageal squamous cell carcinoma	↑	(Tong et al., 2012)
	Esophageal Adenocarcinoma	↑	(Maag et al., 2017)
	Oral squamous cell cancer (OSCC)	↑	(Farah et al., 2016)
	Hepatocellular carcinoma	↑	(Ge et al., 2022)
	Non-small lung cancer	↑	(Sanchez-Palencia et al., 2011)
	Lung cancer	↑	(Abdueva et al., 2010)
	Transitional cell carcinoma of the kidney	↑	(Jones et al., 2005)
	Osteosarcoma	↓	(Jones et al., 2012)

1.4 The proteasome as a therapeutic target in lung cancer

The proteasome, a widely recognized target for cancer therapy, serves as the primary protein degradation mechanism within cells, breaking down essential regulators of cell growth, migration, and survival. The discovery of diverse alternative proteasome activators has added intricacy to the role of the proteasome. The engagement of proteasome activators with the 20S

proteasome core units allows for swift, precise, and localized adjustments to proteasomal activity, ensuring the cell can dynamically respond to its specific requirements (Coux et al., 2020; Meiners et al., 2014). This idea proposes that any dysregulation of proteostasis in disease will be associated with adaptive changes in proteasome function and alternative complex formation. However, there is little known about how alternative proteasome activators are regulated and how they interact with the 20S proteasome core complex in response to specific cellular stimuli or during disease pathogenesis.

Numerous clinical trials have investigated the effectiveness of proteasome inhibitors in treating lung cancer (Manasanch & Orlowski, 2017). These substances successfully limit protein degradation in the cell and efficiently inhibit the proteasome's catalytic activities, which impede cell development and cause apoptosis (Meiners et al., 2008). While these inhibitors, such as bortezomib, carfilzomib, and ixazomib, have demonstrated encouraging outcomes in myeloma, their effectiveness for solid tumours, such as lung cancer, is constrained by their noticeable cytotoxic side effects as a result of their broad suppression of general cellular protein breakdown. Proteasomes are a class of different complexes that differ in their associated proteasome activators but share the 20S proteasome as their common proteolytic core (Figure 1.9 A) (Meiners et al., 2014; Stadtmueller & Hill, 2011). Each of these different proteasome complexes has a distinct function in regulating cellular activity. Pathological developments may be aided by or caused by any of the dysfunctional proteasome complexes (Tanaka et al., 2012). Proteasome inhibitors impede cell growth and trigger cell death by deactivating the catalytic core of the 20S subunit, effectively halting protein degradation across all proteasome complexes within the cell (Figure 1.9 B) (Meiners et al., 2008; Morozov & Karpov, 2018). Nevertheless, research has shown that when catalytic proteasome activity is inhibited, there is a swift mobilization of proteasome activators like PA28 and PA200 to associate with the 20S and 26S complexes (Welk et al., 2016). Therefore, possible alternative proteasome inhibitors can be generated and selectively target one subset of proteasome complexes (Figure 1.9 C).

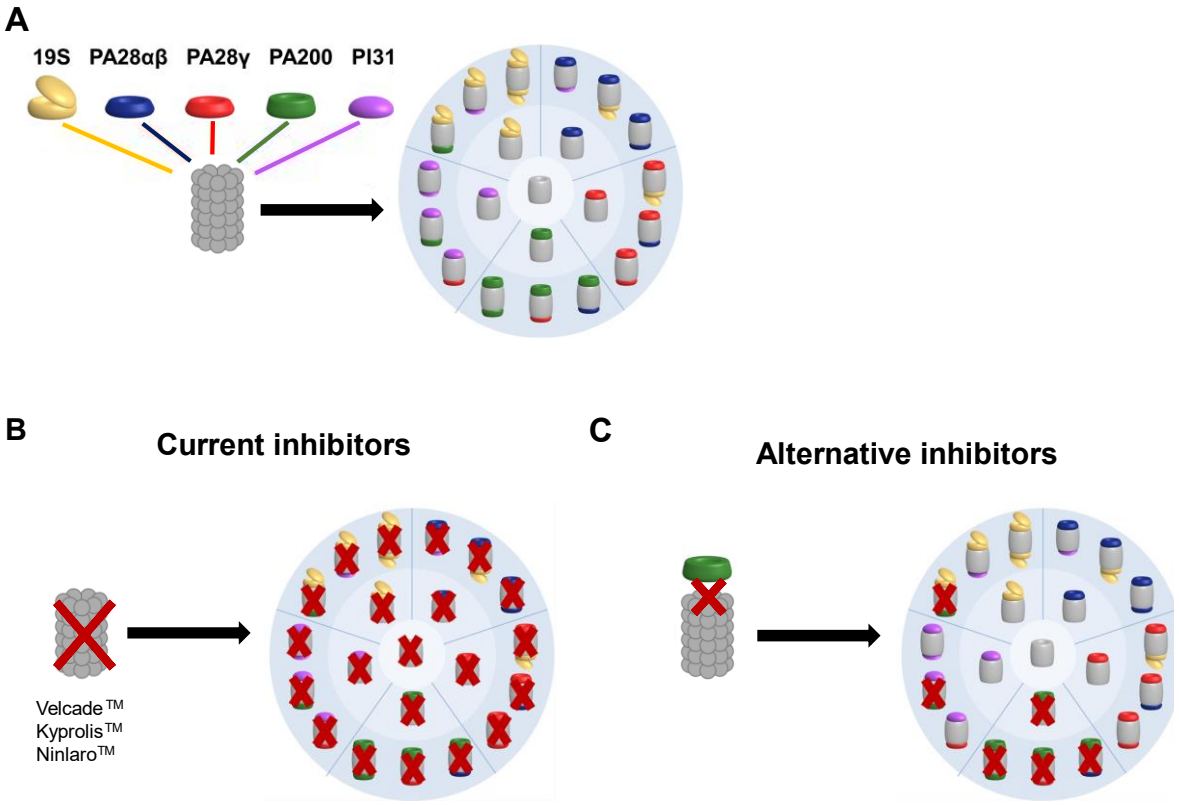

Figure 1.9: Selective inhibitors may potentially target cellular subsets of the proteasome complexes. (A) The 20S catalytic core is present in all proteasome complexes in the cell but combines with alternate proteasome regulators. **(B)** Current 20S core inhibitors inhibit the catalytic activity, which results in a general inhibition of all proteasome complexes. **(C)** The alternative inhibitors, in theory, can target PA200/proteasome complexes more efficiently and selectively for lung cancer therapy. (Adapted from (Meiners et al., 2014))

Previously, we observed an upregulation of PA200 protein levels in the tumour tissues of lung cancer patients compared to their healthy tissues (Welk, 2018). Furthermore, recent research also observed an increase in PA200 levels in lung cancer and focused on the regulatory function of PA200 in immune evasion (Javitt et al., 2023). Our in-depth review of PA200 extensively explored the recent progress in comprehending its functions, structural attributes, and association with diverse diseases (Yazgili et al., 2022). Notably, it highlighted a growing gap in our understanding of PA200 biology, particularly in the context of lung cancer. Therefore, in this study, we aimed to better characterize the function of PA200 in PA200-depleted human non-small cell lung cancer (NSCLC) cell lines as a model to understand its dysregulation in this disease.

2 Aims

The first study on the dysregulation of PA200 in disease showed that patients with idiopathic pulmonary fibrosis had elevated levels of PA200 in their lungs (Welk et al., 2019). A recent study found that PA200 is more abundantly expressed in immunotherapy-resistant "cold" cancers and counter-regulates the production of MHC class I antigenic peptides by inhibiting the immunoproteasome in lung cancer (Javitt et al., 2023). Therefore, finding and validating inhibitors of the PA200/proteasome complex for treating lung cancer will create a new perspective for cutting-edge therapeutic approaches to inhibit other proteasome complexes. The specific aims of this study were:

1. *Generation and validation of PA200 depleted non-small cell lung cancer (NSCLC) cell lines*

The first objective of this project was to generate PA200-deleted human lung cancer cells (A549 and NCI-H1299) using CRISPR/Cas9 technology.

2. *Characterization of the PA200 knock-out cells in vitro*

The changes in the proteasome landscape were studied in the PA200 knock-out cell lines. The engineered cells were further profiled for their phenotypic and functional alterations, including growth, survival, and invasion capacities.

3. *Identifying the role of the PA200 in tumour formation in vivo*

The PA200 deficient human cells were analyzed in a non-orthotopic typic flank tumour model in mice to monitor how PA200 presence affects primary tumour development in vivo and the development of metastases.

4. *Analyzing the cell-autonomous response upon PA200 depletion in vitro*

The changes in the RNA levels upon PA200 depletion were assessed by RNA sequencing. The PA200 interactome was identified by immunoprecipitation of the protein and LC-MS/MS collaboration with the Helmholtz Zentrum München core facility.

3 Materials

3.1 Antibodies

3.1.1 Primary antibodies

Rb: Rabbit, **Ms**: Mouse, **Gt**: Goat, **mAb**: Monoclonal, **pAb**: Polyclonal

Target	Catalog Number	Host & Type	Application	Working Dilution	Company
Claudin-1 (D5H1D)	13255	Rb mAb	Western Blotting	1:1000	Cell Signaling Technology
CSL4	ab181108	Rb mAb	Western Blotting	1:1000	Abcam
E-Cadherin (24E10)	3195	Rb mAb	Western Blotting	1:1000	Cell Signaling Technology
EIF5B	ab89016	Ms pAb	Western Blotting	1 µg/µl	Abcam
Erf3/GSPT1 + eRF3B/GSPT2	ab256471	Rb mAb	Western Blotting	1:1000	Abcam
GAPDH (HRP-linked)	14C10	Rb mAb	Western Blotting	1:80000	Cell Signaling Technology
Integrin β3 (ITGB3)	D7X3P	Rb mAb	Western Blotting	1:1000	Cell Signaling Technology
Lmp2 (Psmb8)	ab3328	Rb pAb	Western Blotting	1:1000	Abcam
Lmp7 (Psmb9)	ab3329	Rb pAb	Western Blotting	1:1000	Abcam
MECL-1 (Psmb10)	ab190790	Rb mAb	Western Blotting	1:1000	Abcam
N-Cadherin (D4R1H)	13116	Rb mAb	Western Blotting	1:1000	Cell Signaling Technology
Nucleolin	ab134164	Rb mAb	Western Blotting	1:10000	Abcam
PA200	NBP1-22236	Rb pAb	Western Blotting Immunoprecipitation	1:5000 3 µl	Novus Biologicals
Pa28α	ab155091	Rb mAb	Western Blotting	1:1000	Abcam
Pa28α	ab155091	Rb mAb	Western Blotting	1:1000	Abcam
Pa28β	sc-23642	Gt pAb	Western Blotting	1:1000	Santa Cruz
Pa28γ	sc-136025	Ms mAb	Western Blotting	1:1000	Santa Cruz
Slug (C19G7)	9585	Rb mAb	Western Blotting	1:1000	Cell Signaling Technology
Snail (C15D3)	3879	Rb mAb	Western Blotting	1:1000	Cell Signaling Technology
Vimentin (D21H3)	5741	Rb mAb	Western Blotting	1:1000	Cell Signaling Technology
ZEB1 (D80D3)	3396	Rb mAb	Western Blotting	1:1000	Cell Signaling Technology
ZO-1 (D7D12)	8193	Rb mAb	Western Blotting	1:1000	Cell Signaling Technology
α1-7 (MCP231)	ab22674	Ms mAb	Western Blotting	1:1000	Abcam
β-Actin (HRP-linked)	A3854	Ms mAb	Western Blotting	1:80000	Sigma-Aldrich
β-Catenin (D10A8)	8480	Rb mAb	Western Blotting	1:1000	Cell Signaling Technology

3.1.2 Secondary Antibodies

Rb: Rabbit, **Rt**: Rat, **Hs**: Horse

Target	Catalog Number	Host	Application	Working Dilution	Company
Anti-goat IgG HRP-linked	61-1620	Rb	Western Blotting	1:40000	Thermo Fisher Scientific
Anti-Mouse IgG (H+L)-Alexa Fluor 488	415-545-166	Rt	Immunofluorescence	1.5 mg/ml	Jackson ImmunoResearch
Anti-mouse IgG HRP-linked	7076	Hs	Western Blotting	1:40000	Cell Signaling Technology
Anti-rabbit IgG HRP-linked	7074	Hs	Western Blotting	1:40000	Cell Signaling Technology
Protein A (HRP Conjugate)	12291S	-	Western Blotting	1:20000	Cell Signaling Technology

3.2 Oligonucleotides

All quantitative real-time polymerase chain reaction (qRT-PCR) primers were procured from Eurofins, Germany.

3.2.1 qRT-PCR Primers

FW: Forward primer, **RV**: Reverse Primer

Target Gene	Target Species		Sequence 5'-3'
AC007255.1	human	FW	GTCTTGTTCTGCTACCCTCCA
		RV	GCTCCACATTCACTTTCCATA
AC007785.1	human	FW	AAACTGACCCTCCTTCTT
		RV	CTCCTTGGCTCCTATACTC
AC104041.1	human	FW	CCGCCTTGCAGTTTGATCTC
		RV	ACTCCCACCCGAATATTGCG
AC139722.1	human	FW	GATGGCTCAGAAGGCAGAAC
		RV	GCCGACCACACCAGATACTT
ADAM23	human	FW	ACATCAACCAAGACTCGGAAAG
		RV	TTTGGAGCCGAAGGCTTCAAT
AL031283.2	human	FW	AAGCAAGGTATGCGTCAGGG
		RV	GGGATACGCAGCAGAGAGTC
AL139220.2	human	FW	TGTGCCTCTTTTGGTCCACTT
		RV	ATTAGGGAAGCCAGAGCCAAC
AP001972.3	human	FW	AAGGAGAAGAGGCAGACCCT
		RV	GGACGCACTCAAACCTACGA
AP002893.1	human	FW	TGGCTTTCTCCCCATTGTCG
		RV	TGGCTCAGTTCCCTCCCTTA
B-catenin	human	FW	CATCTACACAGTTTGATGCTGCT
		RV	GCAGTTTTGTCAGTTCAGGGA
BMP4	human	FW	TAGCAAGAGTGCCGTCATTCC
		RV	GCGCTCAGGATACTCAAGACC
CASC19	human	FW	TTGGAGTGCCTGGGTTAGA
		RV	CTGTCCTTGCCAGTGTCTT
claudin 2 (CLDN2)	human	FW	ATCGCTCCAACTACTACGATGC

		RV	TGAACTCACTCTTGACTTTGGGA
collagen, type IV, alpha 1 (COL4A1)	human	FW	GGACTACCTGGAACAAAAGGG
		RV	GCCAAGTATCTCACCTGGATCA
E-Cadherin (CDH1)	human	FW	ATTTTTCCCTCGACACCCGAT
		RV	TCCCAGGCGTAGACCAAGA
EPAS1	human	FW	TTGCTCTGAAAACGAGTCCGA
		RV	GGTCACCACGGCAATGAAAC
ITGB3	human	FW	CATGAAGGATGATCTGTGGAGC
		RV	AATCCGCAGGTTACTGGTGAG
LGR6	human	FW	ACACAACCGCATCTGGGAAAT
		RV	CGTTCCAGCTAAGATCCAGGG
LINC01127	human	FW	GCTTTTCTCGCTATGCTGCC
		RV	GTTTGCCATTTGGGTGGTCC
LINC01748	human	FW	ACCCCACCCTCAAAGAAACA
		RV	AGGGCAATCAGATTCAGCCG
N-Cadherin (CDH2)	human	FW	AGCCAACCTTAACTGAGGAGT
		RV	GGCAAGTTGATTGGAGGGATG
NPAS2	human	FW	GATGGCTTCATTATCGCAGTGA
		RV	CGACGGTAAATGCCCAAGG
Occludin	human	FW	ACAAGCGGTTTTATCCAGAGTC
		RV	GTCATCCACAGGCGAAGTTAAT
PPARGC1A	human	FW	TCTGAGTCTGTATGGAGTGACAT
		RV	CCAAGTCGTTCACATCTAGTTCA
PRICKLE1	human	FW	TTTGCTTGCTTACCAGAGGAAA
		RV	ACTGGCAATACCGTACCTCAT
PSMB8	human	FW	AGTACTGGGAGCGCCTGCT
		RV	CCGACACTGAAATACGTTCTCCA
PSMB9	human	FW	CGTTGTGATGGGTTCTGATTCC
		RV	GACAGCTTGTCAAACACTCGGTT
PSMB10	human	FW	TGCTGCGGACACTGAGCTC
		RV	GCTGTGGTTCCAGGCACAAA
PSME1	human	FW	CAAGGTGGATGTGTTTCGTG
		RV	TGCTCAAGTTGGCTTCATTG
PSME2	human	FW	GCAAACAGGTGGAGGTCTTC
		RV	GTCAGCCAGATTGAGGGAGT
PSME3	human	FW	TAGCCATGATGGACTGGATGG
		RV	CCTTGGTTCCTTGGAAGGCT
PSME4	human	FW	ATTTGGAGTTACCCTGGAGACC
		RV	GCAGCTTTTCACGAGTGTTTTG
RPL19	human	FW	TGTACCTGAAGGTGAAGGGG
		RV	GCGTGCTTCCTTGGTCTTAG
SLC8A1-AS1	human	FW	CAGTCGTGTTCGTCGCACTT
		RV	GCTGCCCGTGACGTTACCTAT
SNAIL1	human	FW	ACTGCAACAAGGAATACCTCAG
		RV	GCACTGGTACTTCTTGACATCTG
SNAIL2	human	FW	CGAACTGGACACACATACAGTG
		RV	CTGAGGATCTCTGGTTGTGGT
TGFA	human	FW	AGGTCCGAAAACACTGTGAGT
		RV	AGCAAGCGGTTCTTCCCTTC
TWIST1	human	FW	GTCCGCAGTCTTACGAGGAG
		RV	GCTTGAGGGTCTGAATCTTGCT
Vimentin (VIM)	human	FW	TGCCGTTGAAGCTGCTAACTA
		RV	CCAGAGGGAGTGAATCCAGATTA
ZEB1	human	FW	TTACACCTTTGCATACAGAACCC
		RV	TTTACGATTACACCCAGACTGC
ZEB2	human	FW	GCGATGGTCATGCAGTCAG

		RV	CAGGTGGCAGGTCATTTTCTT
Zo-1	human	FW	ACCAGTAAGTCGTCCTGATCC
		RV	TCGGCCAAATCTTCTCACTCC

3.2.2 Primers for PCR and Sanger sequencing

Application	**Species**		**Sequence 5´- 3´**
PCR	Human	FW	ATCTGCAAGAGAGATGCAGCC
	Human	RV	AGGTTTGAGCAGCAGCAAGA
Sanger Sequencing	Human	RV	TGGATGGGGAAAGCAAAACCC

3.3 Cell culture

3.3.1 Human cell lines

Cell line	**Origin**	**Specification**
A549	Human adenocarcinoma, alveolar epithelial basal cell	DSMZ, ACC 107
NCI-H1299	Lung large cell carcinoma, derived from metastatic lymph node	Gift from Dr. Georgios Stathopoulos's Lab

3.3.2 Media formulations for cell lines

Cell line	Media formulations	Catalog number	Company
A549	DMEM/F-12 (1:1) (1x) 10% FBS 100 U/mL Penicillin/Streptomycin	31330-038 S0615 15140-122	Thermo Fisher Scientific Sigma-Aldrich Thermo Fisher Scientific
NCI-H1299	RPMI-1640 Medium 10% FBS 100 U/mL Penicillin/Streptomycin	R08758-500ML S0615 15140-122	Sigma-Aldrich Sigma-Aldrich Thermo Fisher Scientific
A549	**(w/o L-glutamine)** DMEM/F-12 (1:1) (1x) 10% FBS 100 U/mL Penicillin/Streptomycin	 21331-020 S0615 15140-122	 Thermo Fisher Scientific Sigma-Aldrich Thermo Fisher Scientific
NCI-H1299	**(w/o L-glutamine)** RPMI-1640 Medium 10% FBS 100 U/mL Penicillin/Streptomycin	 R0883-500ML S0615 15140-122	 Sigma-Aldrich Sigma-Aldrich Thermo Fisher Scientific

3.4 Treatments

Stimulation	Solvent	Stock concentration	Company
hTGFβ-1	4 mM HCl + 1 mg/mL BSA	100 µg/ml	PeproTech
hIFN-β	0.1% BSA	500000 U/ml	Abcam, Cambridge
hIFN-γ	0.1% BSA	100 µg/ml	PeproTech
Bortezomib	DMSO	2.6 mM	Millenium Pharmaceuticals

3.5 Enzymes

Enzymes	Company
DNase 2 U/µL	Peqlab
M-MLV Reverse Transcriptase	Sigma-Aldrich
Phusion HF DNA Polymerase	New England Biolabs

3.6 Kits

Kits	Company
LightCycler 480 SYBR Green I Master	Roche Diagnostics
Pierce BCA Protein Assay Kit	Thermo Fisher Scientific
Proteasome-Glo™ Assay	Promega
Roti-Quick RNA Extraction Kit	Carl Roth
peqGOLD Total RNA Kit	VWR
DNeasy Blood & Tissue Kit	Qiagen
QIAquick Gel Extraction Kit	Qiagen

3.7 Markers

Markers	Company
Protein Marker IV (10-245 kDa)	AppliChem

Peqlab peqGOLD DNA-ladder 100 bp Plus	VWR

3.8 Purified Proteins

Purified Proteins	Company
Human 20S Standard Proteasome (BML-PW8720-0050)	Enzo Life Sciences
Human 20S Immunoproteasome (E-370-025)	Boston Biochem
PA200	Dr. Marijke Jansma, HMGU

3.9 Buffer recipes

All solutions were formulated using Milli-Q® water unless specified otherwise. These buffers were frequently used in our lab and were previously described elsewhere (Meul, 2021; Welk, 2018).

Buffer	Reagent	Final Concentration
0.1 M Phosphate buffer pH 8	Na_2HPO_4 NaH_2PO_4	93.2 mM 6.8 mM
5x Native loading buffer	Tris Glycerol Bromophenol blue	250 mM 43.5 % (v/v) 0.05% (w/v)
6x Laemmli buffer	Tris Glycerol SDS Bromophenol blue DTT	300 mM 50 % (v/v) 6% (w/v) 0.01 % (w/v) 600 mM
8x TBE Buffer	Tris Boric acid EDTA-Na2	89 mM 89 mM 2 mM
MTT dissolving reagent	Isopropanol Triton X-100 HCl	- 10% (v/v) 0.0074% (v/v)
Native gel running buffer	Tris Boric acid EDTA $MgCl_2$ ATP DTT	89 mM 89 mM 2 mM 5 mM 2 mM 1 mM
OK Lysis Buffer	Tris/HCl (pH 7.5, 100 mM) DTT (1 M) MgCl2 (1 M) Glycerol (87%) ATP Digitonin (5%) cOmplete® protease inhibitor PhosphoStop phosphatase inhibitor	50 mM 2 mM 5 mM 10% (v/v) 2 mM 0.05% (v/v) 1x 1x
PBST washing buffer	NaCl KCl Na_2HPO_4 KH_2PO_4 Tween-20	137 mM 2.7 mM 10 mM 2 mM 1 % (v/v)
Phosphate buffered saline (PBS) pH 7.4	NaCl KCl	137 mM 2.7 mM

	Na_2HPO_4 K_2HPO_4	10 mM 2 mM
Proteasome activity overlay assay reaction buffer	Tris pH 7.5 ATP $MgCl_2$ DTT Suc-LLVY-AMC	50 mM 1 mM 10 mM 1 mM 0.05 mM
Proteasome Reconstitution Buffer pH 7.5	HEPES EDTA	25 mM 0.5 mM
RIPA lysis buffer pH 7.5	Tris/HCl pH 7.5 NaCl IGEPAL Sodium deoxycholate SDS cOmplete® protease inhibitor PhosphoStop phosphatase inhibitor	50 mM 150 mM 1 % (v/v) 0.5 % (w/v) 0.1 % (w/v) 1x 1x
SDS PAGE running buffer	Tris Glycin SDS	25 mM 192 mM 0.1 % (w/v)
Solubilization buffer	Na_2CO_3 SDS β-mercaptoethanol	66 mM 2 % (w/v) 1.5 % (v/v)
TSDG buffer pH 7.0	Tris pH 7.0 NaCl $MgCl_2$ EDTA DTT NaN_3 Glycerol	10 mM 10 mM 1.1 mM 0.1 mM 1 mM 1 mM 10 % (v/v)
Urea Lysis Buffer	Urea Thiourea DTT SDS	8 M 2 M 50 mM 0.1%
Western blot transfer buffer	Tris Glycine Methanol	25 mM 192 mM 10 % (v/v)

3.10 Reagents

These products were frequently used in our lab and were previously described elsewhere (Meul, 2021; Welk, 2018).

Reagents	**Solvent**	**Stock concentration**	**Company**
4’,6-Diamidin-2-phenylindol (DAPI)	PBS	1 M	Sigma-Aldrich
6x DNA Loading Dye	-	6x	Thermo Fisher Scientific
Activity-based probe LW124	DMSO	2.5 µM	Prof. Dr. H. Overkleeft, University of Leiden, Netherlands
Activity-based probe MV151	DMSO	50 µM	Prof. Dr. H. Overkleeft, University of Leiden, Netherlands

Activity-based probe MVB127	DMSO	25 µM	Prof. Dr. H. Overkleeft, University of Leiden, Netherlands
Alt-R® CRISPR-Cas9 crRNA	H_2O	100 µM	IDT
Alt-R® CRISPR-Cas9 tracrRNA	H_2O	100 µM	IDT
Adenosine triphosphate (ATP)	-	-	Roche Diagnostics
Bovine serum albumin (BSA)	-	-	AppliChem
Collagen G (L7213-100ML)	-	-	Sigma-Aldrich
cOmplete™ protease inhibitor cocktail	H_2O	25x	Roche
Dithiotreitol (DTT)	H_2O	1 M	Life Technologies
Dynabeads™ Protein A	-	-	Thermo Fisher Scientific
First Strand Buffer	-	5x	Life Technologies
Fluorescent Mounting Medium	-	-	Dako
Lipofectamine® CRISPRMAX™ Cas9 Transfection Reagent	-	-	Thermo Fisher Scientific
Luminata™ Classico Western HRP Substrate	-	-	Merck Millipore
Luminata™ Forte Western HRP Substrate	-	-	Merck Millipore
Matrigel® Basement Membrane Matrix (356234)	-	-	Corning
M-MLV RT Buffer	-	-	Thermo Fisher Scientific
Nuclease-Free Water	-	-	Ambion, Thermo Fisher Scientific
Nucleotide Mix	-	10 mM	Promega
Opti-MEM Reduced Serum Medium	-	-	Thermo Fisher Scientific
Penicillin/Streptomycin	-	-	Thermo Fisher Scientific
Random Hexamers	-	250 µM	Promega
RNAsin RNAse Inhibitor	-	40 U/µL	Promega
Roti-Block	-	10x	Carl Roth
Succinyl-leucine-leucine-valine-tyrosine-aminomethylcoumarine (Suc-LLVY-AMC)	DMSO	2 mM	Bachem
SuperSignal West Atto Ultimate	-	-	Thermo Fisher Scientific
SuperSignal West Extended Duration Substrate	-	-	Thermo Fisher Scientific
SuperSignal West Femto	-	-	Thermo Fisher Scientific
SuperSignal West Pico	-	-	Thermo Fisher Scientific
SYBR Safe	-	-	Thermo Fisher Scientific
Thiazolyl Blue Tetrazolium Bromide	PBS	3 mg/ml	Sigma-Aldrich
Trypsin (0.25 % EDTA)	-	-	Thermo Fisher Scientific

3.11 Chemicals

These chemicals were frequently used in our lab and were previously described elsewhere (Meul, 2021; Welk, 2018).

Product	**Company**
Boric acid	AppliChem
Bromophenol blue	AppliChem
Citric acid monohydrate	AppliChem
Dithiotreitol (DTT)	Life Technologies
DMSO	Carl Roth
EDTA	AppliChem
Ethanol	AppliChem
Glycerol	AppliChem
Glycine	AppliChem
IGEPAL	Sigma-Aldrich
Isopropanol (p. A.)	AppliChem

Magnesium acetate	Sigma-Aldrich
Magnesium chloride	AppliChem
Methanol (p. A.)	AppliChem
Potassium chloride	AppliChem
Potassium phosphate monobasic	AppliChem
Sodium azide	AppliChem
Sodium chloride	AppliChem
Sodium citrate tribasic dihydrate	AppliChem
Sodium deoxycholate	AppliChem
Sodium phosphate dibasic	AppliChem
Sodiumdodecylsulfate (SDS)	AppliChem
Thiazolyl Blue Tetrazolium Bromide	Sigma-Aldrich
Tris	AppliChem
Triton X-100	Life Technologies
Tween-20	AppliChem
Xylene	AppliChem
β-Mercaptoethanol	AppliChem

3.12 Consumables

Product	**Company**
25 Culture-Inserts 2 well for self-insertion	ibidi
6/24/96 well plates	TPP
96 well plates, white, for luminescence detection	Berthold Technologies
Cell culture dishes (6 cm, 10 cm, 15 cm)	Nunc
Cell culture flasks (75 cm^2, 175 cm^2)	Nunc
Cryovials 1.5 ml	Greiner Bio-One
Falcon tubes (15 mL, 50 mL)	BD Bioscience
Glass pasteur pipettes	VWR International
Microplate 96-well, PS, flat bottom (for BCA assay)	Greiner Bio-One
NuPAGE Novex 3-8 % Tris-Acetate Gel 1.5 mm (10 & 15 well)	Thermo Fisher Scientific
PCR plates, white, 96 well	Biozym Scientific
Pipet tips	Biozym Scientific
PVDF membrane	Bio-Rad
SafeSeal reaction tubes (0.5 mL, 1.5 mL, 2.0 mL)	Sarstedt
Sealing foil for qPCR plate	Kisker Biotech
Serological pipettes Cellstar 2, 5, 10, 25 and 50 mL	Greiner Bio-One
Super RX Fuji medical X-ray film	Fujifilm Corporation
Syringes (10 mL, 20 mL, 50 mL)	Neolab
Whatman blotting paper 3 mm	GE Healthcare

3.13 Devices

Technical device	**Company**
-20 °C freezer MediLine LGex 410	Liebherr
-80 °C freezer	Eppendorf
-80 °C freezer U570 HEF	New Brunswick
Analytical scale XS20S Dual Range	Mettler-Toledo
Autoclave DX-45	Systec
Autoclave VX-120	Systec
Cell culture work bench Herasafe KS180	Thermo Fisher Scientific
Centrifuge MiniSpin plus	Eppendorf

Centrifuge Rotina 420R	Hettich
Centrifuge with cooling, Micro220R	Hettich
CO_2 cell incubator BBD6620	Thermo Fisher Scientific
Dry ice container Forma 8600 Series, 8701	Thermo Fisher Scientific
DynaMag-2	Thermo Fisher Scientific
Film developer Curix 60	AGFA
Gel imaging system ChemiDoc MP	Bio-Rad
Gel imaging system ChemiDoc XRS+	Bio-Rad
iBright™ CL1500 Imaging System	Invitrogen
Ice machine ZBE 110-35	Ziegra
Light Cycler LC480II	Roche Diagnostics
Liquid nitrogen cell tank BioSafe 420SC	Cryotherm
Liquid nitrogen tank Apollo 200	Cryotherm
Magnetic stirrer KMO 2 basic	IKA
Mastercycler gradient	Eppendorf
Mastercycler Nexus	Eppendorf
Milli-Q® Advantage A10 Ultrapure Water Purification System	Merck Millipore
Milli-Q® Integral Water Purification System for Ultrapure Water	Merck Millipore
Mini Centrifuge MCF-2360	Schubert & Weiss Omnilab
Nalgene Freezing Container (Mister Frosty)	Omnilab
pH meter InoLab pH 720	WTW
Plate centrifuge 5430	Eppendorf
Plate reader Sunrise	Tecan
Plate reader TriStar LB941	Berthold Technologies
Power Supply Power Pac HC	Bio-Rad
Refrigerator Profi Line	Liebherr
Research plus pipettes	Eppendorf
Roll mixer	VWR International
Scale XS400 2S	Mettler-Toledo
Shaker Duomax 1030	Heidolph
Thermomixer compact	Eppendorf
Vacuum pump NO22AN.18 with switch 2410	KNF
Vortex mixer	IKA
Water bath Aqua Line AL 12	Lauda

3.14 Software

Software	**Company**
GraphPad Prism 9	GraphPad Software
Image Lab	Bio-Rad
ImageJ	National Institutes of Health
LightCycler® 480 SW 1.5	Roche Diagnostics
Magellan Software	Tecan
Microsoft Office Professional Plus 2010	Microsoft
PyMol	Schrödinger
Qupath-0.3.2	Queen’s University Belfast
Tristar MicroWin 2000	Berthold Technologies
Zen Blue	Carl Zeiss Meditec

4 Methods

4.1 Cell culture

4.1.1 Maintenance of human cell lines

Human NSCLC cell lines A549 were obtained from DSMZ, and NCI-H1299 were a gift from the lab of Dr. Georgios Stathopoulos. The cell lines were cultured as monolayers in 10 cm^2 or 15 cm^2 cell culture dishes at 37 °C and 5% CO_2 in a humidified incubator. A549 cells were grown in the DMEM/F12 medium, while NCI-H1299 cells were cultured in the RPMI-1640 medium. Both media were supplemented with 10% fetal bovine serum (FBS) (Sigma) and 100 U/mL penicillin/streptomycin (Gibco, Thermo Fisher Scientific). For serum deprivation, 1% FBS medium was added to the mediums instead of 10% FBS. They were passaged at a ratio according to their growth rate.

4.1.2 Cell harvest

4.1.2.1 Trypsinization

The cell culture medium was removed, and the cells were rinsed once with PBS. Subsequently, trypsin was added to the cells, and the plates were placed in a 37 °C, 5% CO2 humidified incubator for 5 minutes. The trypsinization process was halted by adding the respective medium supplemented with 10% FBS, leading to cell detachment. The cells were then collected by centrifugation at 1500 rpm for 5 minutes. After discarding the medium, the cells were washed once with PBS and subjected to another round of centrifugation under the same conditions. Finally, the PBS was removed, and the resulting cell pellets were stored at -20 °C until further use.

4.1.2.2 Scraping

The medium was aspirated, and cells were washed once with ice-cold PBS. Later, the cells were detached by scraping in ice-cold PBS on ice. The cells were collected and pelleted by centrifugation for 5 min at 1500 rpm, and after PBS was aspirated, the pellets were stored at -20 °C until further use.

4.1.1 Generation of PA200 knock-out NSCLC cell lines via CRISPR/Cas9

Low passage number cells were used to generate PA200 knock-out A549 and NCI-H1299 cells (passage 4 and passage 5, respectively). Defrosted cells were incubated either with DMEM F12 medium + 10% FBS+ 1% Pen/Strep (A549) or RPMI-1640 medium + 10% FBS+ 1% Pen/Strep (H1299). The cells were harvested when they reached 80% confluency. 250.000-300.000 cells were counted and seeded into the 6-well plate. After 24 hours, cells were 70% confluent and ready for transfection. For the transfection, Lipofectamine™ CRISPRMAX™ Transfection Reagent, Invitrogen™ TrueCut™ Cas9 Protein v2, Hs.Cas9.PSME4.1.AB (crRNA, IDT) and tracRNA (IDT) were used. 1 µl tracRNA (100 µM) and 1 µl crRNA (100 µM) were diluted in 98 µl TE Buffer and annealed at 95°C for 5 minutes according to the manufacturer's protocol to generate sgRNA. For transfection, transfection mixes A and B were prepared in microcentrifuge tubes, as indicated in Table 4.1 below.

Table 4.1: Composition of transfection mixes A and B (per well in a 6-well plate).

Transfection Mix A		**Transfection Mix B**	
Opti-MEM™ I Medium	125 µl	Opti-MEM™ I Medium	125 µl
gRNA (crRNA:tracrRNA) (5`GAGCTGATTTGGAGTTACCC`3)	6250 ng	CRISPRMAX™ Reagent	7.5 µl
Cas9 nuclease	1200 ng	-	-
Cas9 Plus™ Reagent	12.5 µl	-	-

Transfection mix B was allowed to incubate at room temperature for 1 minute. It was then added to transfection mix A and further incubated for 10 minutes under the same conditions. Subsequently, the resulting complex was added dropwise to the cells. The cells were incubated at 37°C for 48 hours. Following the incubation period, the cells were collected and 50 cells were seeded onto 15 cm dishes containing the respective medium supplemented with 20% FBS instead of the usual 10% FBS, aiming to promote growth stimulation. After 2 weeks, colonies were picked with trypsin-incubated cloning disks and transferred to 24-well (one colony per one well). To avoid contamination, the cloning disks were removed the next day with sterile forceps. When the cells became confluent, they were harvested, and 2:3 of the cells were transferred to 6-well plates. 1:3 of the cells were pelleted to monitor the transfection via protein expression level. Cells possibly not-edited (wild type) and cells possibly edited (knock out) were transferred to 10 cm dishes according to PA200 presence or not, respectively. When cells became confluent, they were transferred to a 15 cm^2 dish. A small portion of these cells was then pelleted for DNA sequencing. When the cells reached 80% confluency in the 15 cm^2

dishes, they were frozen with 90% FBS and 10% DMSO to be used when the DNA sequencing showed successful editing.

4.1.2 Treatment of cells

4.1.2.1 TGFβ-1 treatment

300.000 A549 cells and 200.000 NCI-H1299 cells were seeded into 10 cm dishes containing 1% FBS medium. This seeding was done with the purpose of synchronizing the cell cycles over a 24-hour period. On the following day, the existing medium was substituted with either medium supplemented with 1% FBS or medium supplemented with 1% FBS along with TGF-β1 (at a concentration of 5 ng/ml, Catalog Number: 100-21-10UG). These two conditions were referred to as the control and treatment conditions, respectively. Cells were harvested 72 h later by the scraping method. ¾ of the pellet was used for protein isolation, and ¼ of the pellet was used for RNA isolation.

4.1.2.2 Interferon treatment

1.5 million A549 cells and 1 million NCI-H1299 cells were plated in 10 cm dishes and allowed to grow for 24 hours in a medium supplemented with 10% FBS. On the subsequent day, the existing medium was removed, and cells were treated with standard medium, medium containing IFNβ (at a concentration of 100 U/ml, Catalog Number: ab7147575), or medium containing IFNγ (at a concentration of 10 ng/ml, Catalog Number: #300-02-100 µg). Following 24 hours of treatment, cells were detached using trypsin. Upon harvesting, the cell pellet was divided, with 2/3 of it allocated for protein isolation and the remaining 1/3 designated for RNA isolation.

4.1.3 Cell proliferation assay

The daily proliferation rate of different cell types was assessed using the established methodology outlined in previous studies (Meul et al., 2020; Sullivan et al., 2015). Briefly, to initiate the assay, 30.000 A549 cells and 40.000 NCI-H1299 cells were seeded into separate wells of 6-well plates a day prior to the experiment. On the subsequent day, the initial cell count for each cell line on day 1 was determined by counting control wells. Subsequently, the cells

were cultured for an additional 3 days, and on day 4, the final cell count was recorded. The rate of cell division per day was calculated utilizing the formula:
Proliferation Rate (Doublings per day) = log2 (Final cell count (day 4)/Initial cell count (day 1))/3 (days)

4.1.4 MTT assay

Cellular metabolic activity was assessed using the MTT (3-(4,5-dimethylthiazol-2-yl)-2,5-diphenyltetrazolium bromide) assay, which relies on the reduction of MTT to a purple insoluble formazan product by NAD(P)H-dependent cellular oxidoreductases (Mosmann, 1983). The cells were cultured in 24-well plates, and to each well, 200 µL of a 3 mg/mL thiazolyl blue tetrazolium bromide solution (Sigma) in PBS was added to achieve a final concentration of 0.5 mg/mL. The cells were then incubated for 1 hour at 37 °C. Wells containing only the medium without cells were included as blanks. After incubation, the medium was removed, and the formazan crystals were solubilized using 500 µL of MTT dissolving reagent. The absorbance of the resulting solution was measured at 570 nm using a SunriseTM plate reader (TECAN).

4.1.5 Colony formation assay

A colony formation assay was employed to evaluate the capacity of individual cells to develop into colonies (Franken et al., 2006). In 6-well plates, 100 NCI-H1299 and 200 A549 cells were seeded per well. The culture medium was refreshed on day 3 and day 7 of the experiment. On day 10, the cells were washed with PBS and then fixed using 4% formaldehyde for 15 minutes at room temperature. Following fixation, the colonies were stained with 1% crystal violet dye, photographed, and subsequently quantified.

4.1.6 Migration and invasion assay with Boyden chamber

For analysis of cellular migration, 600 µl 10% FBS medium was used as a chemoattractant and added to 24-well plates. Boyden chambers were inserted into the wells, and 100.000 NCI-H1299 cells in 0% FBS medium were added to the upper side. After a 24-hour period, the culture medium was removed, and the cells were treated with 4% formaldehyde at room temperature for 15 minutes on both sides. Following fixation, the cells were subjected to

staining with 1% crystal violet solution for 15 minutes at room temperature. Excessive dye was washed off with water, and chambers were left to dry until imaging with Axio Observer.Z1/7.

4.1.7 Wound healing assay

Ibidi 2 well silicone inserts assessed cellular wound healing capacity. First, the inserts were put into the 24-well plate (1 insert/well). A549 (28.000 cells/insert side) and NCI-H1299 (20.000 cells/insert side) cells were seeded to both sides of the inserts. The next day, the silicone material was lifted, and 1 ml medium was added. Cells were incubated in the live cell imaging microscope (Axio Observer.Z1/7) at 37°C and 5% CO_2 for 48h or until the 500 µm gap closed. Images from different time points are calculated using the Wound Healing Tool macro on ImageJ. (Carpentier G., 2012) (*Wound Healing Tool*, 2022).

4.1.8 Spheroid formation and matrix invasion

Spheroids were generated using low attachment U-bottom 96-well plates. A total of 5.000 A549 cells were seeded in each well with 100 µl of medium and centrifuged briefly for 2 minutes at 1000 rpm to establish initial cell-cell contact. The cells were then incubated for 72 hours under standard conditions of 37°C and 5% CO2. After this incubation period, the spheroids were gently collected into 1.5 ml Eppendorf tubes and allowed to settle on the tube's bottom for 5 minutes on ice.

Simultaneously, a collagen G matrix gel was prepared. Solution A was created by combining 1M HEPES buffer (pH= 7-7.5) and 0.7M NaOH in equal proportions. Subsequently, solution A was mixed with 20% FBS (PAA) in 10× PBS (pH = 7.4) in a 1:1 ratio to create solution B (pH = 7.90–8.05). For the final gelation step, collagen G and solution B were mixed in a 4:1 ratio, as previously described (Burgstaller et al., 2013). To create a collagen G+Matrigel matrix, a mixture of collagen G matrix gel and Matrigel was prepared in a 1:1 ratio, resulting in a total volume of 200 µl. All steps were carried out on ice using pre-chilled materials to prevent premature gel formation. The spheroids were then transferred into the matrix mixture using 40 µl of medium. To ensure the integrity of the spheroids and minimize bubble formation within the matrix, the tips of the yellow pipette tips were modified by cutting. Subsequently, 40 µl of the spheroid-matrix mixture was dispensed into each well of a 24-well plate, with this process repeated four times to create technical replicates. Typically, each well contained 2-4 spheroids. The plates were subsequently placed in an incubator set at 37°C and 5% CO2,

allowing the gel matrices to solidify over a period of 5 hours. After this solidification period, 1 ml of medium (pre-warmed to 37°C) was gently added to each well to prevent detachment of the matrices. Following the 5-hour solidification, the spheroids were imaged using a live cell imaging microscope (Axio Observer.Z1/7) under conditions of 37°C and 5% CO2. The cells were then subjected to an incubation period of 72 hours under the specified conditions, after which they were imaged once more.

4.2 Animal experiments

The PhD students Georgia Giotopoulou and Sabine Behrend carried out injections and scoring. Harvesting was jointly done by Ayse Seda Yazgili, Georgia Giotopoulou, Sabine Behrend, and Lilith Trassl.

4.2.1 Study Approval

Experiments were designed and approved *a priori* by ROB-55.2-2532.Vet_02-20-197 (approval numbers) and were conducted according to Directive 2010/63/EU (http://eur-lex.europa.eu/legal-content/EN/TXT/?qid=1486710385917&uri=CELEX:32010L0063).
SCID mice are purchased from Charles River (NOD.CB17-Prkdcscid/NCrCrl (strain code 394), https://www.criver.com/products-services/find-model/nod-scid-mouse?region=3671) SCID refers to a mouse model in which the SCID mutation (Severe Combined Immunodeficiency) was combined with a NOD (non-obese diabetic, non-obese diabetic) genotype. T and B cell lymphocyte development is hampered in SCID homozygous animals. Additionally, the NOD background leads to impaired natural killer (NK) cell activity. Male and female animals are used for the experiments to keep the number of animals as small as possible. The sexes were evenly distributed to the respective experimental groups (Table 4.2). The animals were used in the experiment at the age of six to eight weeks at a weight of 20-25 g and were also housed in groups during the experiments. The sample size was determined before conducting the experiment through a power analysis using G*power software. The experimental procedures were randomized across different cages.

4.2.2 Subcutaneous injection of genetically engineered cells

The acclimatized mice were anaesthetized with 1-2% isoflurane and immobilized on a warm plate for the procedure. The injection site (region: flank to the lower back, approx. 2x3 cm) was shaved to ensure safe subcutaneous injection of the tumour cells under visibility and disinfected. Then, $3x10^6$ million PA200 WT or PA200 KO cells in 150 µl body-temperature PBS were injected subcutaneously (Table 4.2). The injection was applied with a 27G cannula (diameter 0.4 mm). After injection, the animals continue to be warmed with a red-light lamp (about 1 m from the mouse) or in a cage without bedding on a warming plate at 39°C and observed until they fully arouse from anaesthesia (about 1 hour until the normal activity is observed). The animals are then placed in the cage and remain there in groups. The procedure takes about five to ten minutes.

Table 4.2: Mice used for PA200 WT or KO cell subcutaneous injection.

	A549		NCI-H1299	
Gender	**WT**	**PA200 KO**	**WT**	**PA200 KO**
Female	4	6	6	9
Male	6	9	4	6

4.2.3 Scoring of the mice

For weighing, the animals are placed from the cage into a weighing pan on the scale. After this, the tumour size was measured using callipers by placing the animals on the cage lid. The three vertical dimensions of the tumour (δ1, δ2, and δ3) were measured twice a week, and the tumour volume was calculated using the formula $\pi * \delta1 * \delta2 * \delta3 / 6$, as outlined in previous studies (Giopanou et al., 2017; Stathopoulos et al., 2010). Tumour size and weight were determined every two days while the experiments were ongoing. The conditions of the endpoint of the experiments were as follows: either the tumour reached 150 mm^3 or after 10 weeks post-subcutaneous injection (TVA approval number ROB-55.2-2532.Vet_02-20-197).

4.2.4 The endpoint of the mouse experiment

Mice were planned to be sacrificed once their tumour burden reached the maximal size, the primary tumour had necrosis or 10 weeks after the injection. The necrosis occurred on the primary tumours and was visible by eye, and information was given by the animal caretakers. Lethal anaesthesia was induced by an intraperitoneal injection of ketamine (250 mg/kg body

weight) and xylazine (10 mg/kg body weight). The injection was made with a 27G cannula (diameter 0.4 mm). The depth of the anaesthesia is checked using the intertoe reflex. After the animals become unconscious, they are observed for at least 3 minutes until they stop breathing completely. The lungs were removed to ensure death, and the carcasses were disposed. This method of killing was used for the purpose of organ harvesting, to rule out lung damage or organ bleeding, which is necessary for the following examinations of the lung tissue.

4.3 Protein biochemistry

4.3.1 Protein extraction from cell pellets

4.3.1.1 Native protein extracts

4.3.1.1.1 TSDG cell lysis

This method is a standard practice in our lab and was previously described elsewhere (Meul, 2021; Welk, 2018; Yazgili et al., 2021). Briefly, frozen cell pellets were thawed and dissolved in TSDG buffer, which was supplemented with 1x cOmpleteTM protease inhibitor cocktail (Roche) and 1x PhosSTOP phosphatase inhibitor cocktail (Roche Diagnostics). The volume of the lysis buffer was adjusted to match the size of the cell pellet. The process of lysing the cells involved disrupting the cell membrane through a series of 7 freezing-thawing cycles using liquid nitrogen. Subsequently, the cell extracts underwent centrifugation at 15000 rpm and 4°C for a duration of 20 minutes to remove cellular debris and achieve clear cell lysates. These cleared cell lysates were then stored at a temperature of -20°C until they were ready for further use. It's important to note that the TSDG cell lysis method was exclusively employed in the immunoprecipitation of PA200.

4.3.1.1.2 OK cell lysis

This method is a standard practice in our lab and was previously described elsewhere (Meul, 2021; Welk, 2018; Yazgili et al., 2021). Briefly, frozen cell pellets were thawed and subsequently dissolved in an OK buffer. This buffer was supplemented with 1x cOmpleteTM protease inhibitor cocktail (Roche) and 1x PhosSTOP phosphatase inhibitor cocktail (Roche Diagnostics). The volume of the lysis buffer was adjusted to match the size of the cell pellet. Following this, the cells underwent lysis on ice for a duration of 20 minutes, with intermittent

vortexing during the process. The supernatants were collected by centrifuging the lysates at 15000 rpm and 4°C for a period of 20 minutes. The collected samples were then stored at a temperature of -20°C until they were ready for further use.

4.3.1.2 Denatured protein extracts

4.3.1.2.1 Ripa Lysis

This method is a standard practice in our lab and was previously described elsewhere (Meul, 2021; Welk, 2018). Briefly, to obtain denatured protein extracts, the RIPA lysis buffer was used. Frozen cell pellets were dissolved in an amount of RIPA buffer and adjusted according to the size of the cell pellet. This RIPA buffer was supplemented with 1x cOmpleteTM protease inhibitor cocktail (Roche) and 1x PhosSTOP phosphatase inhibitor cocktail (Roche Diagnostics). The cell lysis process was carried out on ice and lasted for 20 minutes, with periodic vortexing during this period. Subsequently, the lysates underwent centrifugation at 15,000 rpm and 4°C for 20 minutes to remove cellular debris. The resulting cleared cell lysates were then stored at -20°C until they were ready to be used for further experiments.

4.3.1.2.2 Urea Lysis

Urea lysis was applied to recover the insoluble proteins after the isolation with TSDG lysis. After the TSDG lysis was applied, the left-over pellets that contained the insoluble part of the cell were stored at -20°C until further use. These pellets were then dissolved in the same volume of urea lysis buffer (see recipe 3.9), and 6x Laemmli sample buffer was applied (to a final concentration of 1x).

4.3.2 Bicinchoninic acid (BCA) assay

This method is a standard practice in our lab and was previously described elsewhere (Meul, 2021; Welk, 2018). Briefly, the Pierce BCA protein assay kit from Thermo Fisher Scientific was utilized for determining the protein concentrations in the cell lysates. As part of the process, 20 µl of bovine serum albumin at varying concentrations were prepared as standard samples. Initially, the samples of interest were diluted in PBS at a 1:10 ratio, resulting in a total volume of 20 µl. Subsequently, 200 µl of the BCA working solution was added to these samples, which were then incubated at 37 °C for a duration of 30 minutes. To complete the procedure, the absorbance of the samples was measured in triplicate using the Sunrise Plate

Reader, with readings taken at a wavelength of 562 nm. The absorbance values obtained from the standard samples were employed to construct a standard curve, which was used to quantify the protein concentrations of the unknown samples.

4.3.3 SDS gel preparation and Western blot analysis

4.3.3.1 Sample preparation

This method is a standard practice in our lab and was previously described elsewhere (Meul, 2021; Welk, 2018). Briefly, 15 µg protein was used per sample for Western blotting. Protein extracts were diluted to an equal volume with Milli-Q® water, mixed with 6x Laemmli sample buffer (with a final concentration of 1x), and heated at 95 °C for 15 minutes to denature the proteins.

4.3.3.2 SDS gel preparation and electrophoresis

This method is a standard practice in our lab and was previously described elsewhere (Meul, 2021; Welk, 2018). Briefly, polyacrylamide gels (7.5 %, 10 %, 12 %, or 15 % SDS) were prepared by mixing chemicals listed in Table 4.3 and pouring them into the casting equipment (Bio-Rad) for the electrophoretic separation of proteins. After pouring the resolving gel, a layer of isopropanol (250 µl/gel) was added to form a plain interface and eliminate the bubbles. After the gel's complete polymerization, the isopropanol layer was removed and washed with MilliQ® water. Later, stacking gel was poured, and combs were inserted. The percentage of polyacrylamide was selected depending on the protein's molecular weight to be detected.

Table 4.3: Composition of 1.5 mm 7.5 %, 10 %, 12 % and 15 % SDS polyacrylamide gels.

	SDS Resolving Gels				**SDS Stacking Gel**
Chemical	**7.5% Volume (mL/gel)**	**10% Volume (mL/gel)**	**12% Volume (mL/gel)**	**15% Volume (mL/gel)**	**3.6% Volume (mL/gel)**
4x Resolving buffer	2.0	2.0	2.0	2.0	-
4x Stacking buffer	-	-	-	-	1.0
H_2O	4.0	3.3	2.8	2.0	2.52
30% Acryla-mide	2.0	2.7	3.2	4.0	0.48
TEMED	0.012	0.012	0.012	0.012	0.012
10% APS	0.1	0.1	0.1	0.1	0.05

Protein samples and 3-6 µl protein markers were loaded onto SDS gels. Electrophoresis was performed in Bio-Rad gel running chambers at a voltage of 90 V at the first instance until the samples reached the resolving gel, then increased to 120 V.

4.3.3.3 Immunoblotting

This method is a standard practice in our lab and was previously described elsewhere (Meul, 2021; Welk, 2018). Briefly, following electrophoresis, the proteins were transferred from the gel to a polyvinylidene fluoride (PVDF) membrane (Bio-Rad) using the tank method through immunoblotting. To activate the PVDF membrane, it was treated with 100% methanol. The transfer of proteins onto the PVDF membrane was carried out using transfer buffer (1x Transfer buffer + 10% Methanol) at a current of 250 mA for a duration of 90 minutes at 4°C. To prevent non-specific binding, the PVDF membranes were incubated either in Roti®-Block for a minimum of 1 hour or for 10 minutes using an EveryBlot blocking buffer.
Primary antibodies were diluted as per the manufacturer's instructions and then allowed to incubate overnight at a temperature of 4°C. On the following day, the PVDF membrane underwent three washes lasting 15 minutes each with PBST (Phosphate Buffered Saline with Tween). Subsequently, secondary antibodies linked with horseradish peroxidase (HRP) and diluted in PBST were applied for a duration of 1 hour at room temperature. After two rounds of washing the membranes with PBST, chemiluminescent signals were generated using either LuminataTM Classico/Forte reagent (Merck Millipore) or Super Signal (West/Pico/Femto/Atto, Thermo Fisher Scientific). The generated signals were detected using either the iBright (CL1500 Imaging System, Thermo Fisher Scientific) or the ChemiDoc (XRS+ or MP system, Bio-Rad). Densitometric analysis of the detected bands was performed within the linear range using the ImageLab software from Bio-Rad.

4.3.4 Native gel electrophoresis

This method is a standard practice in our lab and was previously described elsewhere (Meul, 2021; Welk, 2018). Briefly, native gel electrophoresis was utilized to analyze intact and active proteasome complexes using the XCell SureLock® Mini-Cell system from Thermo Fisher Scientific, following the method outlined recently (Yazgili et al., 2021). Briefly, 15 µg of protein from OK lysates was diluted with water. The diluted lysates were then mixed with 5x

native gel loading buffer and loaded onto commercially available 3-8% gradient NuPAGE Novex Tris-acetate gels from Life Technologies. The native proteasome complexes were separated over a 4-hour period at 4°C with a voltage of 150 V. After the native gel electrophoresis, an in-gel proteasome activity assay was conducted to assess the chymotrypsin-like (CT-L) activity of the native proteasome complexes. For this assay, the gels were incubated in a reaction buffer at 37°C for 30 minutes. The reaction buffer comprised 50 mM Tris, 1 mM ATP, 10 mM MgCl2, 1 mM DTT, and 0.05 mM Suc-LLVY-AMC, a fluorogenic peptide substrate. The fluorescence generated by the CT-L specific cleavage of the Suc-LLVY-AMC substrate within the active proteasome was detected using the ChemiDoc XRS+ system at an excitation wavelength of 380 nm and an emission wavelength of 460 nm (BioRad). Prior to immunoblotting, the gels were incubated in a solubilization buffer (2% w/v SDS, 66 mM Na2CO3, 1.5% v/v β-Mercaptoethanol) for 15 minutes. This step facilitated the subsequent transfer of proteins using the previously described immunoblotting technique. For the mass spectrometry sample preparation, the samples were loaded to the native gels by leaving one well empty in between. The gel was run in the same conditions and cut right after into 6 fractions. The gel pieces were stored in lo-bind Eppendorf tubes at -20°C.

4.3.5 Proteasome activity assay with luminescent substrates

4.3.5.1 Cell lysates

The activity of the 20S proteasome active sites, specifically chymotrypsin-like (CT-L), caspase-like (C-L), and trypsin-like (T-L), was assessed using the Proteasome-Glo™ Assays (Promega, Fitchburg) in accordance with the manufacturer's instructions and as described previously (Meul, 2021; Welk, 2018). In this procedure, 1 µg of protein lysate from TSDG lysates was mixed with TSDG lysis buffer to achieve equal volumes. The resulting samples were adjusted to a volume of 20 µL with water. Subsequently, the prepared dilutions were transferred to white flat-bottom 96-well plates and combined with 20 µL of the specific active site-targeted substrates: Succinyl-leucine-leucine-valine-tyrosine-aminoluciferin (for CT-L), Z-leucine-arginine-arginine-aminoluciferin (for C-L), or Z-norleucine-proline-norleucine-aspartate-aminoluciferin (for T-L).

As the reactions progressed, the aminoluciferin released by the substrates was converted by luciferase in the reaction buffer, producing luminescent signals. These signals were measured

at 2-minute intervals over a 45-minute period using a Tristar LB 941 plate reader. Each sample was measured in quadruplicate. The values obtained when the luminescent signal reached a plateau were used for the quantification of proteasome activity for each specific substrate.

4.3.5.2 Purified proteasome complexes

First, the purified proteins were diluted according to Table 4.4 with 25 mM HEPES 0.5 mM EDTA pH 7.5 buffer. These working dilutions were used to generate 1 nM 20S proteasome and 1 nM immunoproteasome concentrations by using the same buffer. 10 nM bortezomib was used as a negative control for the proteasome activity. PA200 was added to have the following final concentrations: 1 nM, 2 nM, 4 nM and 10 nM, wherever appropriate. As the assay was planned in quadruplicates, these preparations were done as a master mix. Then, 20 µl/well samples were pipetted to a white flat bottom 96-well plate. The plate was covered with a seal to avoid evaporation, and the samples were incubated at 4°C for 2 hours. After the incubation period, 20 µl of each Proteasome-Glo™ substrate was added to the wells. The released aminoluciferin was measured as indicated above.

Table 4.4: Protein Dilutions

Protein	Stock Concentration	Working Dilution
20S proteasome	1 mg/ml	0.1 mg/ml
Immunoproteasome	3 µM	0.3 µM
PA200	1 mg/ml	0.01 mg/ml

4.3.6 Labelling of active proteasome complexes with activity-based probes (ABPs)

In conjunction with the luminescent proteasome activity assay, activity-based probes (ABPs) were utilized to assess the catalytic activity of distinct 20S active sites within native 20S and assembled 26S proteasome complexes. ABPs, which are irreversible proteasome inhibitors, were employed for their binding affinity to the specific 20S active sites. These ABPs, including MV151 (binding to all 20S active sites), MVB127 (targeting β5/β5i), and LW127 (specific for β1/β1i), are fluorescently labelled, allowing detection through gel-based assays (Verdoes et al., 2006).

This method is a standard practice in our lab and was previously described elsewhere (Meul, 2021; Welk, 2018). Briefly, samples of 7.5 µg protein from OK lysates were diluted in OK lysis buffer (excluding digitonin) to achieve uniform volumes. The samples were incubated with MV151 (5µM), MVB127 (1µM), or LW124 (0.25µM) for one hour at 37 °C in a

thermocycler. Subsequently, 6x Laemmli loading buffer was added, and the samples were loaded onto Mini-PROTEAN TGX Stain-Free Precast Gels (Bio-Rad). Electrophoresis commenced at 90V for 15 minutes, allowing samples to enter the resolving gel, followed by continuing at 120V for 90 minutes. Quantification of active sites in the proteasome was achieved by capturing the site-specific binding of fluorescent activity-based probes using the iBright CL1500 Imaging System (Thermo Fisher Scientific).

Stain-Free imaging technology was employed, which employs a polyacrylamide gel containing a unique trihalo compound covalently linked to tryptophan residues. This compound increases fluorescence upon exposure to UV light, allowing protein detection at concentrations as low as 10-25 ng (Short & Posch, 2011). The trihalo chemical induces immediate fluorescence upon brief photoactivation, enabling rapid protein visualization within the gel. Thus, the stain-free gels underwent a 5-minute activation period, with the distinctive band at around ~48 kDa selected as the loading control. The acquired signal was quantified using ImageJ software.

4.3.7 Immunoprecipitation of PA200

For immunoprecipitation (IP) of PA200, cells were lysed in TSDG buffer under native conditions as described previously to preserve physiological protein-protein interactions. Pre-clearing of the lysates was performed using magnetic Dynabeads coated with Protein A for antibodies raised in rabbits (Thermo Fisher Scientific) on a magnetic rack. 20 µL of Dynabeads were transferred to protein LoBind tubes (Eppendorf) and washed twice with 500 µL phosphate buffer pH 7.4. 200 µg protein lysate (in TSDG buffer + 0.2 % IGEPAL) was incubated with the Dynabeads for 20 minutes at room temperature on a rotator (20 rpm) in a pre-clearing step which allows the saturation of the unspecific binding sites of the Dynabeads with proteins from the cell extracts and thereby reduces unspecific background binding. Alternatively, 200 µg protein was directly used without pre-clearing. In the meantime, 30 µl Dynabeads were washed twice with 100 µL phosphate buffer pH 7.4. Beads were resuspended in 50 µL phosphate buffer pH 7.4 and incubated with 3 µL of the antibody directed against the target protein for 15 minutes at 1250 rpm and room temperature. Afterwards, beads were washed twice with 100 µL TSDG buffer + 0.2 % IGEPAL. 50 µl of the TSDG buffer + 0.2 % IGEPAL was used to resuspend the beads-antibody complexes. Without (w/o) pre-cleared or precleared 200 µg TSDG protein lysates (separated from the beads) were added onto the beads bound to the antibody to a total volume of 250 µl. Samples were incubated with a rotator (20 rpm) for 2

hours at 4 °C. 25 µL per sample of the total mixture was used as input. 25 µl supernatant was collected once the beads had been separated on the magnetic rack. Input and supernatant samples (25 µl) were mixed with 6x loading buffer (5 µl) and heated at 95 °C for 10 min. Beads were washed three (w/o pre-cleared) or five times (pre-cleared) with 500 µL TSDG buffer supplemented with 0.2 % IGEPAL and one final time with TSDG buffer. Co-immunoprecipitated proteins were eluted in 25 µL 1x Laemmli buffer and further denatured for 10 min at 95 °C. Eluted proteins were further analyzed by Western blotting together with the input and supernatant samples or sent to the Research Unit Protein Science (HMGU) for mass spectrometry analysis.

4.4 Histology

The staining was done by the Core Facility Pathology & Tissue Analytics.

4.4.1 Hematoxylin & Eosin and Ki67 staining

Excised tissue specimens were fixed in a 4% (w/v) solution of neutrally buffered formalin, followed by paraffin embedding and sectioning into slices measuring 3 µm in thickness. These sections were subsequently stained using hematoxylin and eosin (HE) staining. The staining procedure was carried out using the HistoCore SPECTRA ST automated slide stainer (Leica, Germany) with ready-made staining reagents (Histocore Spectra H&E Stain System S1, Leica, Germany) in accordance with the instructions provided by the manufacturer. Immunohistochemical staining was performed following standardized protocols on a Discovery Ultra automated stainer (Ventana Medical Systems, Tucson, AZ). Monoclonal rabbit anti-cleaved-Caspase-3 (1:250, #9664S, Cell Signaling, Danvers, USA) or polyclonal rat anti-Ki67 (1:1000, Abcam, Cambridge, UK) antibodies were used as primary antibodies. As secondary antibodies, goat anti-rabbit, biotinylated (1:750) (Vector BA-1000, Burlingame, USA) was applied. Signal detection was achieved using the Discovery® DAB Map Kit (Ventana Medical Systems, Tucson, AZ). The stained tissue sections were then digitally scanned using an AxioScan.Z1 digital slide scanner (Zeiss) equipped with a 20x magnification objective.

4.5 Mass spectrometry analysis

Proteomic analysis by LC-MS/MS, as described in the following section, was performed by

Dr. J. Merl-Pham, Research Unit Protein Science (HMGU) and the methods were previously has been published elsewhere (Gerckens et al., 2021; Hauck et al., 2010; Merl et al., 2012).

4.5.1 Proteomics screen

4.5.1.1 Sample preparation

The method for sample preparation was previously described in detail (Gerckens et al., 2021). Briefly, affinity purification samples were digested using a modified FASP protocol and the protein samples were first subjected to reduction and alkylation using dithiothreitol and iodoacetamide (Grosche et al., 2016; Wiśniewski et al., 2009). Following this, the proteins were diluted to a concentration of 4 M urea and then centrifuged using a 30 kDa filter device (Sartorius). After multiple wash steps employing 8 M urea and 50 mM ammonium bicarbonate, the proteins were enzymatically digested on the filter using Lys-C and trypsin, with an overnight incubation. The resulting peptides were subsequently eluted via centrifugation, acidified with trifluoroacetic acid (TFA), and stored at -20°C.

4.5.1.2 LC-MS/MS measurements

The method for LC-MS/MS measurements was previously described in detail (Gerckens et al., 2021). Briefly, samples were measured on a QExactive HF-X mass spectrometer (Thermo scientific) online coupled to an Ultimate 3000 nano-RSLC (Dionex). Tryptic peptides were automatically loaded on a trap column (300 µm inner diameter (ID) × 5 mm, Acclaim PepMap100 C18, 5 µm, 100 Å, LC Packings) prior to C18 reversed-phase chromatography on the analytical column (nanoEase MZ HSS-T3 Column, 100Å, 1.8 µm, 75 µm x 250 mm, Waters) at 250nl/min flow rate in a 95-minute non-linear acetonitrile gradient from 3 to 40% in 0.1% formic acid. Profile precursor spectra from 300 to 1500 m/z were recorded at 60000 resolution with an automatic gain control (AGC) target of 3e6 and a maximum injection time of 30 ms. Subsequently, TOP15 fragment spectra of charges 2 to 7 were recorded at 15000 resolution with an AGC target of 1e5, a maximum injection time of 50 ms, an isolation window of 1.6 m/z, and normalized collision energy of 28 and a dynamic exclusion of 30 seconds.

4.5.1.3 Quantitative data analysis

The method for quantitative data analysis for LC-MS/MS measurements was previously described in detail (Gerckens et al., 2021). Briefly, the generated raw files were analyzed using MaxQuant 1.6.7.0 (MPI for biochemistry, Martinsried) for label-free quantification applying default settings with the following changes: deamidation (NQ) allowed as variable modification, application of the LFQ algorithm with LFQ ratio count 1, the inclusion of iBAQ method, no second peptide search (Hauck et al., 2010; Merl et al., 2012). Searches were performed against the Swiss-prot human protein database (20432 sequences) with default settings. Results were filtered for a peptide and protein FDR of 0.01. Missing intensity, iBAQ, and LFQ intensity values were imputed in Perseus 1.6.7.0 by replacing them with missing values from normal distribution separately for each column. After imputation, abundance values were used for calculating average enrichment ratios WT/KO for the two different cell types, including statistics by a student's t-test. Candidates were filtered for $p<0.05$ and a fold-change of 1.5.

4.6 Nucleic acid biochemistry

4.6.1 DNA isolation from cell pellets

DNA isolation was carried out using a commercial kit (DNeasy, Qiagen). To initiate the process, cell pellets were suspended in 200 µl of PBS, and 20 µl of Proteinase K was added. Following this, 200 µl of Buffer AL (without ethanol) was introduced, and the mixture was thoroughly mixed. The samples were then subjected to an incubation at 56°C for 10 minutes. After incubation, 200 µl of pure ethanol (96-100%) was combined with the sample and mixed until a uniform solution was achieved. Subsequently, the solution was loaded onto a DNeasy Mini spin column, which was then placed in a 2 ml collection tube. Centrifugation was carried out at a minimum of 6000 x g (8000 rpm) for 1 minute, and the resulting liquid was discarded. To the spin column, 500 µl of Buffer AW1 was added, followed by another round of centrifugation at a minimum of 6000 x g (8000 rpm) for 1 minute after the liquid was discarded. Following this step, 500 µl of Buffer AW2 was introduced, and the samples were centrifuged for 3 minutes at 20,000 x g (14,000 rpm) to facilitate the drying of the DNeasy membrane. The spin columns were then placed within clean 1.5 ml microcentrifuge tubes, and 100 µl of DEPC

water (free from DNase and RNase) was added. After a 1-minute incubation at room temperature, the samples were centrifuged for 1 minute at a minimum of 6000 x g (8000 rpm) to elute the DNA. The concentration of the extracted DNA was subsequently determined using a NanoDrop machine, with DEPC water being used as a blank for calibration.

4.6.2 Polymerase Chain Reaction (PCR) for CRISPR/Cas9 target site amplification

After DNA concentration had been determined, good-quality DNA (with an absorbance A260/A280 ratio of 1.7–1.9) was used. The CRISPR/Cas9 target site was amplified with PCR primers (see 3.2.2) and produced around ~500 bp amplicon. 50 ng DNA samples were mixed with a PCR master mix (Table 4.5), and PCR was performed using the temperature time profile shown in Table 4.6.

Table 4.5: PCR reaction components as a master mix

Component	Final Concentration/Amount	Amount
5x GC Buffer (	1x	10 µl
10 mM dNTP mix	200 µM	1 µl
Forward Primer (10 µM)	1 µM	5 µl
Reverse Primer (10 µM)	1 µM	5 µl
DNA template (25 ng)	50 ng	2 µl
High-fidelity DNA polymerase		0.5 µl
H_2O	Add up to 50 µl	

Table 4.6: PCR temperature and time cycling profile

Repeats	Temperature [°C]	Time [min: sec]
1x	98	03:00
9x	98	00:10
	72	00:15
	72	00:30
26x	98	00:10
	62	00:15
	72	00:30
1x	72	10:00
1x	95	10:00
1x	4	forever

The PCR product was combined with 6x Loading dye (Thermo Fisher Scientific) and introduced onto a 1% TBE agarose gel that contained SYBR Safe (Thermo Fisher Scientific). Electrophoresis was conducted for 30 minutes at 90 V, and the gel was subsequently examined using UV light via the ChemiDoc XRS+ system (Bio-Rad). To prevent sample cross-contamination, an empty well was maintained between the two samples. Bands located around

500 bp were identified and excised from the gel while being illuminated by UV light. A clean, sharp scalpel was employed for this procedure, and the resulting gel pieces were transferred into a 1.5 ml microcentrifuge tube with a known weight. Any excess agarose was removed in order to minimize the size of the gel.

4.6.3 DNA isolation from the agarose gels

Amplified DNA was isolated from the gel with a commercial kit (QIAquick, Qiagen). Briefly, the gel slice was weighed, and 3x volume of Buffer QG to 1 volume of gel was added (e.g., 150 µl buffer to 50 mg of the gel slice). The solution was incubated at 50°C for 10 minutes until the gel slice dissolved completely. One gel volume of isopropanol was added to the sample and mixed (e.g., 50 µl isopropanol to 50 mg of the gel slice). The mixture was transferred to a spin column, and the DNA bound to the column upon 1-minute centrifugation at 17,900 x g. The flow-through was discarded, and 500 µl Buffer QG was added for centrifugation at 17,900 x g for 1 minute. The spin column was then washed with 750 µl Buffer PE and incubated for 5 minutes at room temperature before centrifugation (17,900 x g and 1 minute). To completely dry the membrane, the microcentrifuge tubes were turned 180 degrees and centrifuged again under similar conditions. 20 µl DNase/RNase-free DEPC-water was used to elute the DNA from the columns. The water was added to the centre of the spin column and incubated for 1 minute at room temperature. Samples were then centrifuged, DNA concentration was measured with the NanoDrop machine, and DEPC water was used as blank. Samples were sent to Eurofins for sequencing and the sequencing primer (see 3.2.2).

4.6.4 RNA isolation of cell pellets

For the isolation of total cellular RNA intended for qRT-qPCR, the Roti®-Quick Kit (Carl Roth) was used for phenol-chloroform extraction. The procedure involved the following steps: Initially, cells were lysed in 500 µL of Roti®-Quick 1 solution. After thorough mixing, 600 µL of Roti®-Quick 2 solution was added to the samples and incubated for 10 minutes on ice. Centrifugation was carried out for 15 minutes at 10,000 rpm and 4 °C to achieve phase separation. The upper aqueous phase was gently pipetted by tilting the tube and transferred to a new tube. Subsequently, 500 µL of Roti®-Quick 3 solution was added, and the samples were either incubated at -80 °C for 40 minutes or at -20 °C overnight. RNA was then pelleted by centrifugation for 20 minutes at 13,000 rpm and 4 °C. The supernatant was discarded, and the

RNA pellets were washed twice with 70% (v/v) ethanol. Following drying on ice, the RNA pellet was reconstituted in 25-40 µL of nuclease-free water (Ambion, Thermo Fisher Scientific) based on the initial pellet size. Concentration measurements were performed at a wavelength of 260 nm using the NanoDrop 1000 (Thermo Fisher Scientific).

Additionally, for bulk RNA sequencing, cellular RNA was isolated using an RNA isolation kit (VWR). The procedure involved the following steps: Cell pellets were dissolved in 350 µl of TRK buffer + 2% β-ME and loaded onto a peqGOLD RNA Homogenizer Column placed within a 2 mL Collection Tube. Samples were centrifuged at maximum speed (≥12,000 x g) for 2 minutes, and the flow-through was collected. Ethanol (70%) was added, and the samples were vortexed thoroughly. Subsequently, 700 µl of the mixture was transferred to a peqGOLD RNA Mini Column, followed by centrifugation at 10,000 x g for 1 minute. The filtrate was discarded, and then 500 µl of RNA Wash Buffer I was added, followed by centrifugation at 10,000 x g for 1 minute. The columns were washed once more with 500 µl of 80% ethanol, and centrifugation was carried out at 10,000 x g for 30 seconds each time. Afterwards, the empty columns were centrifuged at maximum speed for 2 minutes to eliminate residual ethanol. The peqGOLD RNA Mini Column was then transferred to clean 1.5 ml microcentrifuge tubes, and 30 µl of nuclease-free water was added to elute the RNA from the columns. Centrifugation at maximum speed for 2 minutes was performed, and RNA concentration was measured using the NanoDrop 1000. The eluted RNA was stored at -80°C until further use.

4.6.5 Reverse transcription of RNA

For the reverse transcription process, RNA ranging from 0.25 to 1 µg was mixed with 9 µL of nuclease-free water, followed by the addition of 2 µL of 250 µM Random Hexamers (Thermo Fisher Scientific). After allowing the mixture to incubate at 70 °C for 10 minutes, the samples were placed on ice. Subsequently, 9 µL of a reverse transcription master mix was introduced, with final concentrations of 1x First Strand Buffer, 10 mM DTT, 0.5 mM dNTPs, 1 U/µL RNAse Inhibitor, and 10 U/µL M-MLV transcriptase. The reverse transcription procedure involved annealing for 5 minutes at 25°C, followed by elongation for 60 minutes at 37°C, which was executed using a Mastercycler Nexus (Eppendorf). The cDNA was subjected to digestion with 1 U of DNase at 37°C for 15 minutes, followed by heat inactivation at 75°C for 10 minutes. The resultant cDNA was then diluted at a 1:5 ratio with nuclease-free water (Ambion, Thermo Fisher Scientific).

4.6.6 Quantitative real-time RT-PCR

Quantitative real-time RT-PCR analysis was carried out using the SYBR Green LC480 system from Roche. A mixture comprising 2.5 µL of both forward and reverse primer dilutions (0.5 µM each) and 5 µL of LC480 SYBR Green I Master mix (Roche) was prepared per well in a 96-well plate format. Additionally, 2.5 µL of cDNA was added to each well. Each sample was measured in duplicate, and the plates were centrifuged for 2 minutes at 1000 rpm prior to initiating the measurements using the standard program outlined in Table 4.7 on the Light Cycler 480 II (Roche). The gene expression levels of the various samples were normalized to the housekeeping gene ribosomal protein L19 (RPL19). The relative gene expression was determined using the ΔΔCT method, with the specificity of the primers verified by analyzing the melting curve.

Table 4.7: Quantitative real-time RT-PCR program

Program	Cycles	Target (°C)	Hold (mm:ss)
Pre-incubation	1	95	05:00
Amplification	45	95	00:10
		60	00:10
		72	00:10
Melting curve	1	95	00:05
		65	01:00
		97	5 acquisitions
Cooling	1	40	00:30

4.6.7 Bulk mRNA sequencing

A total of 1.5 million A549 cells and 1 million H1299 cells were cultured in 15 cm dishes and incubated for 48 hours. Total RNA was isolated utilizing the Total RNA kit (Peqlab, VWR). Subsequently, the samples were dispatched to the Core Facility Next-Generation Sequencing at the Helmholtz Center Munich. The RNA integrity number (RIN) was assessed using the Agilent 2100 Bioanalyzer system, and concentration was quantified using the Qubit 2.0 RNA BR assay (Invitrogen). RNAs with RIN values exceeding 6 were chosen for total RNA sequencing (ribo-depleted), a method that effectively detects essential coding and non-coding transcripts by removing highly abundant rRNA species.

Library preparation for both human and mouse samples involved using the TruSeq stranded total-RNA Library Preparation kit (Illumina) with 1µg of RNA, following the kit's protocol. Following a final quality control step, the libraries were subjected to paired-end sequencing (2x150 bases) on the Hiseq 4000 sequencer (Illumina), targeting a depth of at least 40 million

paired reads per sample. Subsequent to sequencing, initial processing (demultiplexing) of raw data to fastq files was performed using the bcl2fastq v2.20 program from Illumina.

For RNA sequencing file alignment, the STAR tool was employed with the GRCh38/hg38 version. To estimate transcript abundances, the FeatureCounts function within the Subread2 package was utilized in the Unix environment. Initially, the gene-code ReleaseM23 (GRCm38.p6) served as the gene annotation. Subsequently, data underwent filtering, normalization, and differential gene expression analysis using relevant packages within the R programming environment.

limma: (https://bioconductor.org/packages/release/bioc/html/limma.html)

edgeR: (https://bioconductor.org/packages/release/bioc/html/edgeR.html)

4.6.8 Downstream analysis of RNA-seq and Mass Spectrometry data

The downstream analysis for the RNA-seq data and LC-MS/MS was done by using the web tools Enrichr and Reactome pathway browser (Chen et al., 2013; Gillespie et al., 2021; Kuleshov et al., 2016; Xie et al., 2021). Enrichr webtool was used to analyze Gene Ontology (GO) terms (biological process (BP) and molecular function (MF)) and molecular signature database (MSigDB). GO molecular functions encompass actions rather than the entities (such as molecules or complexes) responsible for executing those actions. These functions lack details regarding the specific location, timing, or contextual circumstances in which the actions take place. On the other hand, GO biological processes examine the larger processes carried out by several molecular activities (Mi et al., 2018). Because the biological process is not similar to the pathway analysis, the Reactome pathway browser was used to analyze differentially regulated pathways (Liberzon et al., 2011). Additionally, MSigDB was analyzed to identify defined biological states or activities. According to the RNA-seq results, up- or down-regulated gene sets were uploaded to the above-mentioned web tools. The results were filtered to have $p<0.05$. Only the top 10 regulated terms were included in the figures. The same analysis methods were used for the LC-MS/MS results. In this case

4.7 Statistical analysis

The specific statistical analyses for each panel are provided in the corresponding figure legends. In brief, to assess the significance of differences between wild-type (WT) and PA200 knockout (KO) groups, a two-tailed unpaired t-test was employed. For comparing gene/protein

variations between WT and KOs, ordinary two-way ANOVA with Šídák test was utilized. Treatment disparities between WT and PA200 KOs were examined through multiple unpaired t-tests and the Holm-Šídák method. Statistical significance was denoted in the figures as follows: * for $p < 0.05$, ** for $p < 0.01$, *** for $p < 0.001$, or **** for $p < 0.0001$. The figures display data as mean ± SEM. All statistical analyses were performed using GraphPad Prism software (version 9).

5 Results

5.1 NSCLC cell lines differentially adapt proteasome complexes to PA200 depletion

5.1.1 Generation, validation, and characterisation of PA200 deficient human NSCLC cell lines

CRISPR/Cas9 is a well-known technique used to generate knock-out cell lines via gene editing. As explained in the methods section, crRNA and tracrRNA were annealed to produce sgRNA to target exon 3 of PA200 when combined with Cas9 protein for gene editing (Figure 5.1). After 48h incubation, the cells were diluted and plated to generate single cells clones with or without genomic PA200 editing. Then, after 2-3 weeks, the single cells were grown into clones and carefully transferred for expansion. A small part of the cells was pelleted during this expansion period for further validation.

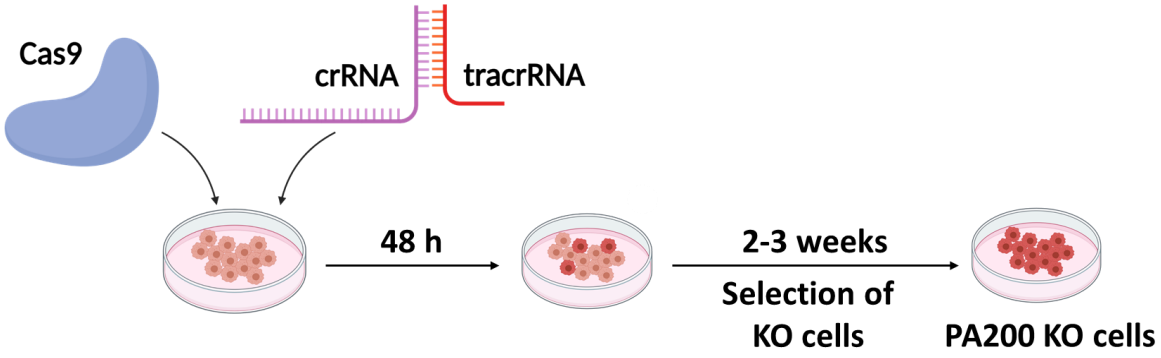

Figure 5.1: CRISPR/Cas9 technology was used to generate PA200 knock-out (KO) NSCLC cell lines (A549 and NCI-H1299). crRNA (IDT) and tracrRNA (IDT) were combined with Cas9 and incubated with the cells for 48h. After 48h, the cells were detached and diluted to generate single-cell clones.

After two weeks, 150 colonies from each cell line were picked, and PA200 protein levels were initially checked for a cost-effective screening. Based on protein expression levels, around 10 clones with or without PA200 were selected and genomic DNA was extracted from the clones. The genomic DNA was then used to amplify exon 3 (guide RNA target site) of PA200 for sequencing analysis. DNA from untreated cells was used as a control template for the Inference of CRISPR Edits (ICE) analysis (*ICE Analysis*, 2019). The ICE analysis is offered by Synthego and analyses the editing of the target exon using Sanger data. ICE analysis is free and only

requires a template sequence (control without any editing) and the sequences of the clones and the gRNA. Once the clones' sequence is aligned with the template sequence, the editing can be easily tracked (Figure 5.2). In this analysis, the clones with 0 bp indel size were identified as wildtype (WT) clones (Figure 5.2 A, C). In contrast, the editing efficiency in the clones was identified according to deletions and shifts of the exon 3 of the PA200 sequence (Figure 5.2 B, D).

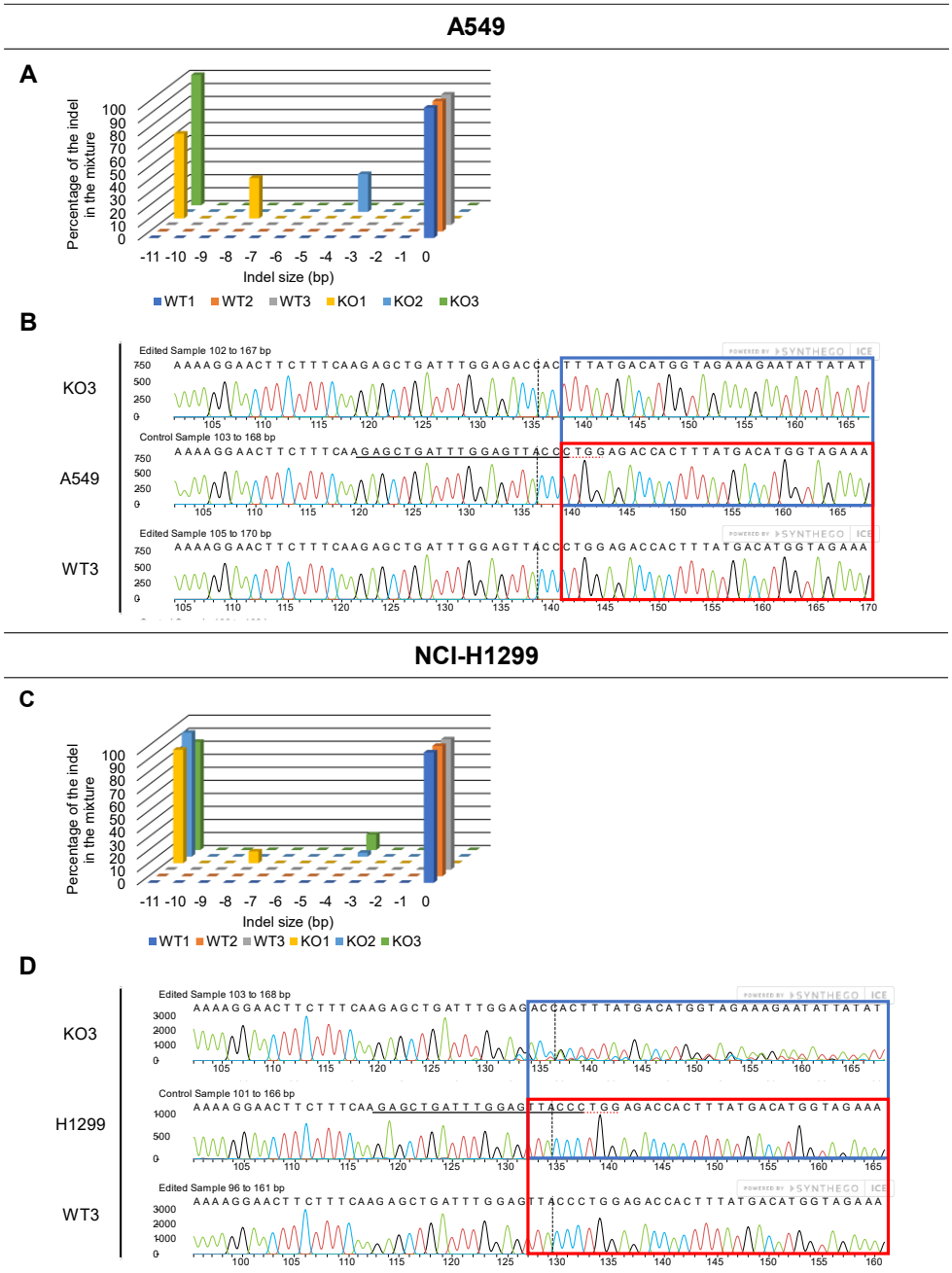

Figure 5.2: Validation of PA200 knock-out cancer cell lines by sequencing. PA200-depleted cell lines generated by CRISPR/Cas9 technology. (A-C) Deletion (indel) sizes and their relative prevalence in the selected clones in A549 cells and NCI-H1299 cell lines, respectively (0 indicates no editing, ICE analysis tool). **(C-D)** Sanger sequencing results were aligned with a non-edited (control) DNA template from A549 and NCI-H1299 (middle). The rectangles show the editing frame in the sequence compared to the non-edited template. The representative KO3 clones show different sequences (blue rectangle), while the WT3 clones do not show any sequence changes (red rectangle). In the control sample, the protospacer neighbouring motif sequence is indicated by a dotted red underline, whereas the guiding target sequence is highlighted in black. Vertical dotted black lines indicate the anticipated cut place.

After confirming the gene editing with the ICE analysis tool, three WT and KO clones were selected from each cancer cell line to be validated on protein and mRNA levels by Western blotting and RT-qPCR analysis, respectively. The clones with edits in the genomic DNA showed no PA200, neither in the protein level (Figure 5.3 A, D) nor in the mRNA level (Figure 5.3 B, E). Additionally, the depletion of PA200 from proteasome complexes was confirmed in native gel analysis (Figure 5.3 C, F). PA200 was mainly associated with the 20S proteasome in both WT clones (Figure 5.3 C, F) but was also found with 26S complexes in the NCI-H1299 WT clones (Figure 5.3 F). In the KO clones of both cell lines, PA200 was absent. The band volume of the PA200 also suggested that the NCI-H1299 WT clones had more PA200 incorporated into the proteasome complexes compared to the A549 WT clones. The different band intensities might be directly related to the abundance levels of the PA200 in two immortalized cell lines. These results show that the editing in the PA200 genomic DNA resulted in the complete functional depletion of PA200 on protein and mRNA levels.

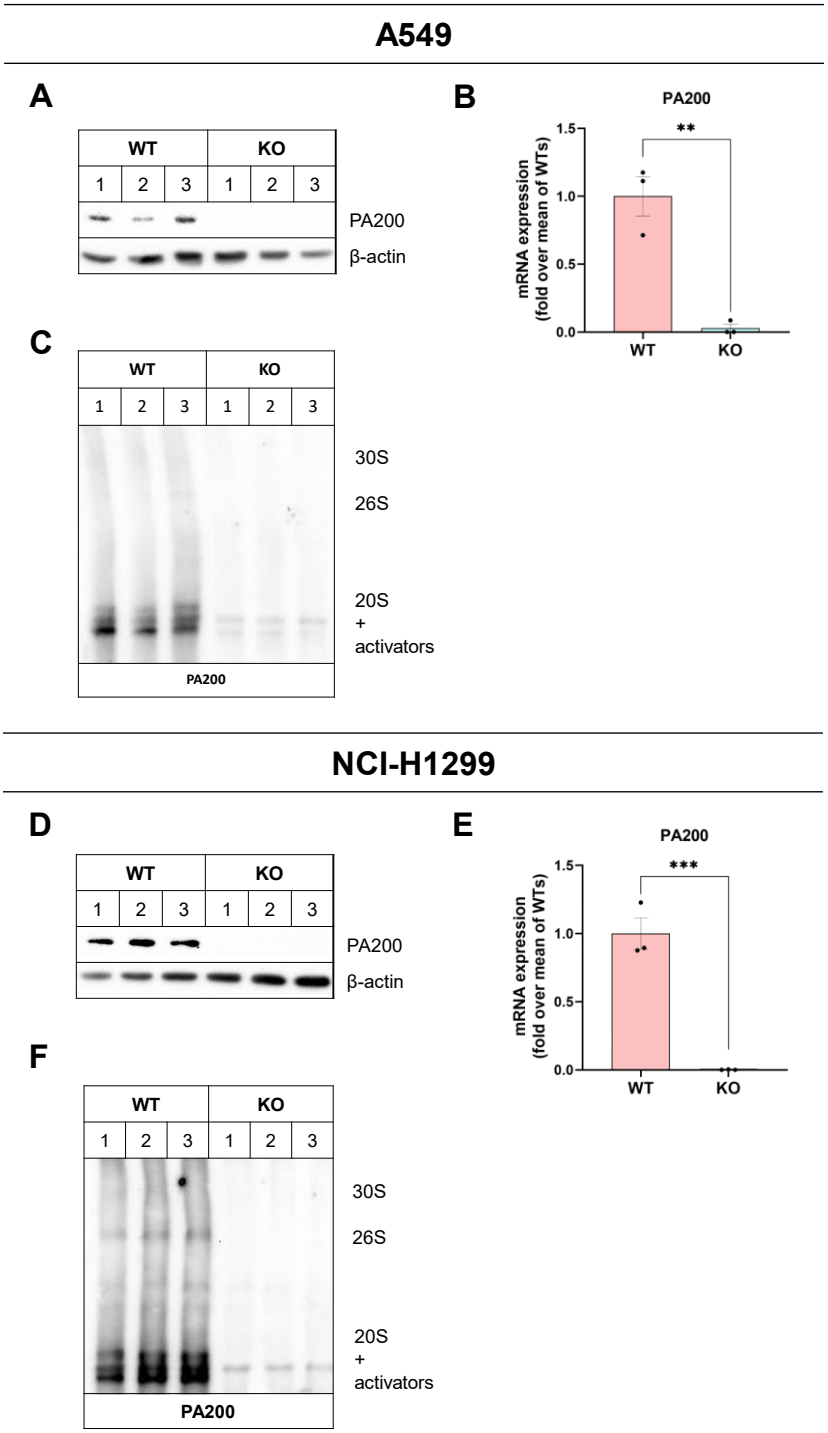

Figure 5.3: Validation of PA200 knock-out cancer cell lines by Western Blotting, RT-qPCR, and native gel. PA200 protein-depleted cell lines were generated by CRISPR/Cas9 technology. **(A, D)** PA200 protein expression levels, **(B, E)** mRNA expression levels and **(C, F)** proteasome distribution levels on the different complexes were validated in the selected colonies in **(A-C)** A549 cells and **(D-F)** NCI-H1299 cell lines, respectively (*p < 0.05, **p < 0.01, ***p < 0.001, two-tailed unpaired t-test, n=3). β-actin served as a housekeeping protein to ensure equal protein loading in Western blotting. RPL19 was used as housekeeping mRNA in the RT-qPCR, the KOs normalised to the WTs, and the ΔΔCt method was used.

Considering PA200 is described as a proteasome activator, we hypothesized that the proteasome activities might be altered upon its deletion. To confirm this hypothesis, proteasome activities and proteasome complex assemblies were determined using native gels. Active proteasome complexes can be separated using native gel electrophoresis. Using fluorogenic peptide, an in-gel activity assay was used to evaluate the CT-L activity of the various complexes (Yazgili et al., 2021). First, the proteins were isolated with OK lysis buffer to keep the integrity of the proteasome complexes. Later, the distribution of active proteasome complexes was measured by immunoblotting the native gel and using an anti-α1-7 antibody to detect 20S proteasomes. Finally, as the in-gel proteasome activity method is only optimised for the CT-L activity, substrate-based activity assays were used to check the activity changes of each catalytically active subunit using chemiluminescence substrates in total cell extracts.

In A549 cell lines, the chymotrypsin-like (CT-L) activity of the 20S significantly increased upon PA200 knock-out (Figure 5.4 A). However, this increase in the CT-L activity was not observed in 26S or 30S complexes. Due to the high variations in the clones, the increase in the 20S complex formation was not significant (Figure 5.4 A). According to the chemiluminescence proteasome activity method, the total CT-L and C-L activities decreased significantly in the KOs, whereas the T-L activity did not change (Figure 5.4 B).

In the NCI-H1299 cell line, the CT-L activity of the 20S decreased, and 30S activity increased significantly in the absence of PA200 (Figure 5.4 C). The in-gel CT-L activity change corresponded to the proteasome distribution. However, only the increase in the 30S complex was observed to be significant (Figure 5.4 C). In contrast to what we observed in the A549 cell lines, the total CT-L and C-L activities significantly increased in the PA200 KOs (Figure 5.4 D).

In addition, we used commercially available purified c20S and i20S to be incubated with recombinantly purified PA200 to understand how PA200 binding affects the dynamics in vitro. PA200-proteasome complexes generated with different concentrations of PA200 (1:1, 1:2, 1:4, and 1:10). Our results showed no significant changes in the total activities of catalytically active subunits with the c20S (Figure 5.4 E). However, we observed a significant activation of the T-L activity of i20S in complex with 10-fold excess in PA200 concentration (Figure 5.4 F).

These results strongly suggest that the absence of the PA200 in the cells affects the proteasome complex activities and complex assemblies' distributions. Of note, PA200 depletion does not result in reduced proteasome activity, as one could have expected from its function as an activator, but differentially activated proteasome complex formation and activities in the two

NSCLC cell lines. In our in vitro activity assays, we also did not observe activation of the 20S using chemiluminescent substrates except for the i20S when combined with 10x excess PA200.

A549

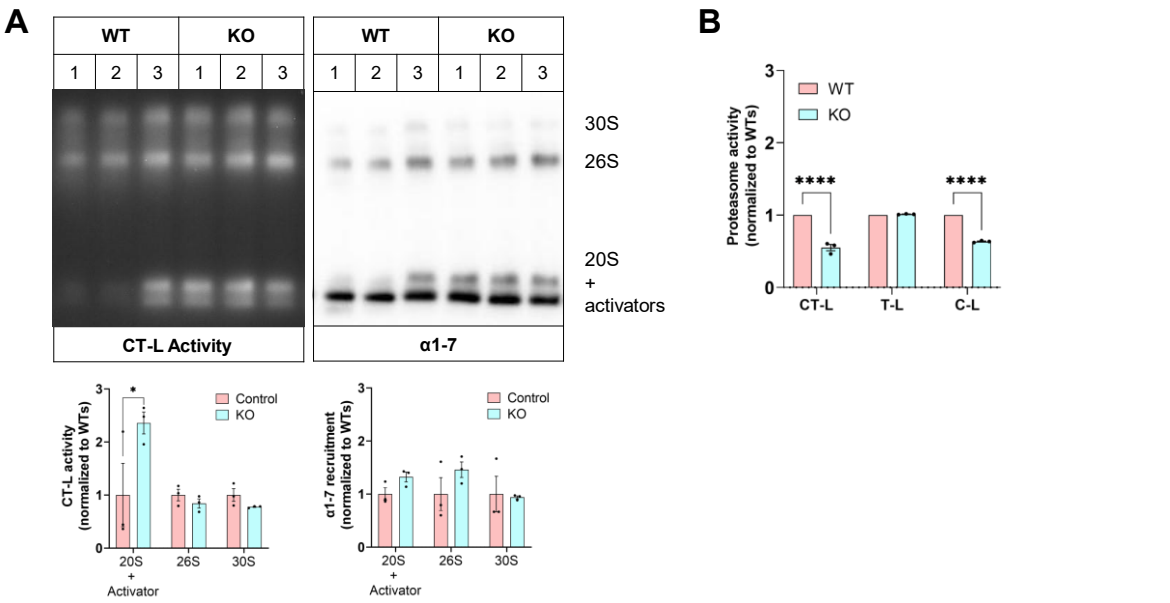

NCI-H1299

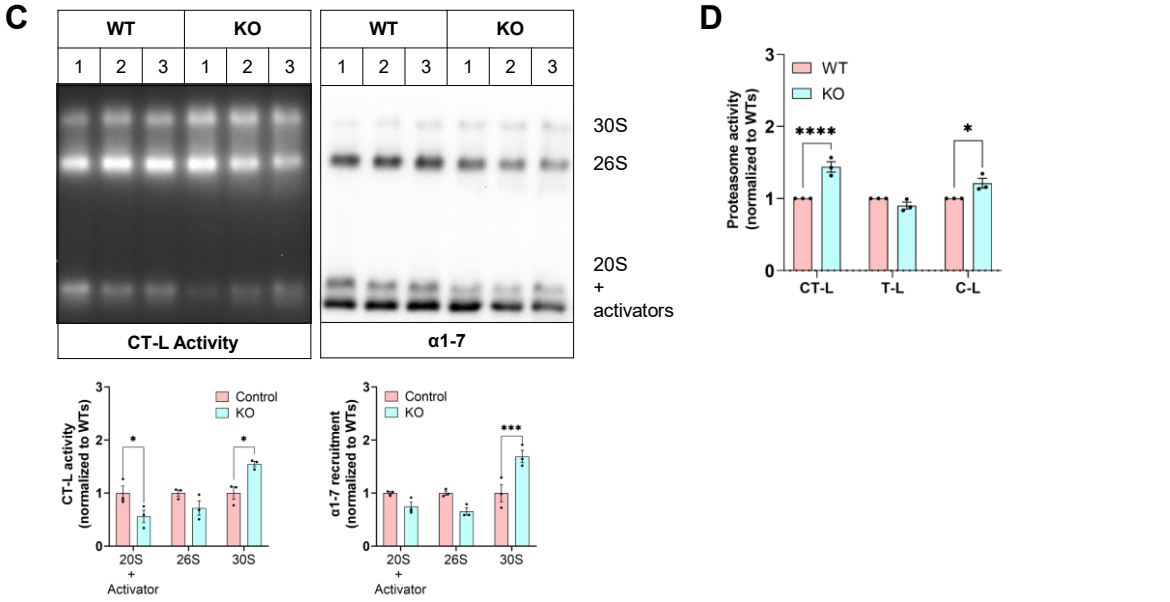

Purified Protein

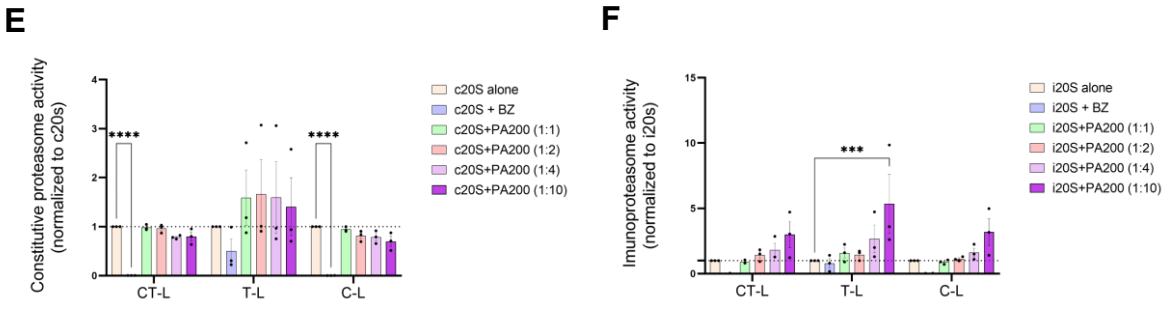

Figure 5.4: Proteasome activity and recruitment response in the absence of PA200 KO are different in two NSCLC cell lines, and the activity of the in vitro complex is different in c20S and i20S. In-gel CT-L proteasome activity was first measured, and the gels were later blotted to observe the distribution of the proteasome complexes in the selected colonies of **(A)** A549 cells and **(C)** NCI-H1299 cells (n=3, different clones). The quantifications are shown below the respective image. Total changes in the proteasome activities were further analysed with chemiluminescence substrates in **(B)** A549 cells and **(D)** NCI-H1299 cells (n=3, different passages). The activity changes in response to the addition of purified PA200 proteins to the purified **(E)** c20S and **(F)** i20S, also analysed with chemiluminescence substrates (n=3, different preparations of PA200 purification with the same protocol). (*$p < 0.05$, **$p < 0.01$, ***$p < 0.001$, **(A-D)** ordinary two-way ANOVA with Šídák's multiple comparisons tests **(E-F)** unpaired t-test, Holm-Šídák method)

5.2 PA200 is involved in the proliferation and metabolism of NSCLC

5.2.1 The absence of PA200 affects the proliferation rate

One of the hallmarks of cancer cells is the change in proliferation, and previously, a significant increase in cell proliferation upon silencing of PA200 in the myofibroblast cells was reported (Hanahan & Weinberg, 2000; Welk et al., 2019). Therefore, we hypothesized that PA200 might also be involved in the proliferation of cancer cells. To examine the proliferation rates, the clones were seeded in a 6-well plate in triplicates (day 0), harvested and counted on day 1 and day 4. The proliferation rates were then determined as described in the methods section and previously (Meul et al., 2020; Sullivan et al., 2015). A549 proliferation rate decreased upon PA200 depletion significantly (Figure 5.5 A). On the other hand, the proliferation rate of the NCI-H1299 PA200 KOs increased but not significantly due to the variety (Figure 5.5 B). These results suggest a potential role of PA200 in cell proliferation; however, its role might depend on the cellular context.

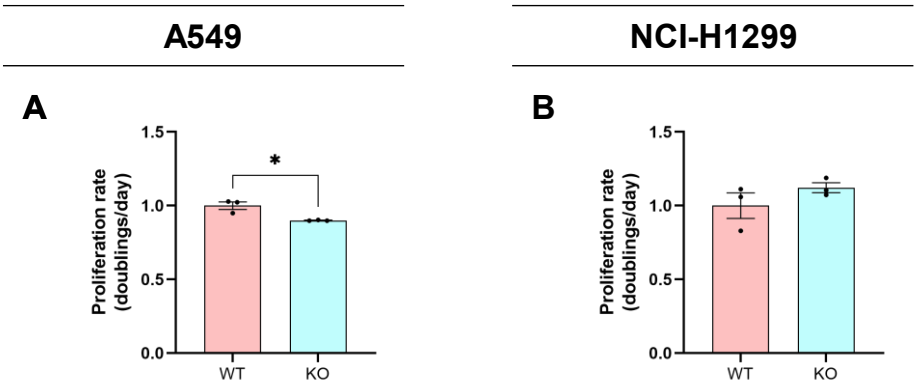

Figure 5.5: Proliferation rate is altered in PA200 KOs. (A) A549 and **(B)** NCI-H1299 pools consisting of 3 WT or 3 PA200 KO clones were seeded and counted on different days to track the doubling time and calculated as explained in the methods part. The data were normalised to the WT. (n=3, different passages, *p < 0.05, two- tailed unpaired t-test).

5.2.2 PA200 is not essential for colony formation capacity

An in vitro cell survival assay based on a single cell's capacity to develop into a colony is known as a clonogenic assay or colony formation assay (Braselmann et al., 2015; Franken et al., 2006). The clonogenic assay is the preferred technique for determining colony-forming capacity following exposure to ionizing radiation, which can also be used to assess the efficacy of other cytotoxic agents. Here, a clonogenic assay protocol was optimised to assess whether the PA200 level changes colony-forming capacity. At the baseline, A549 and NCI-H1299

PA200-depleted cells produced a similar number of colonies as their respective WT controls when seeded with the same cell number (Figure 5.6). This data indicates that the clonal expansion capacity of the two lung cancer cell lines is not altered in the absence of PA200.

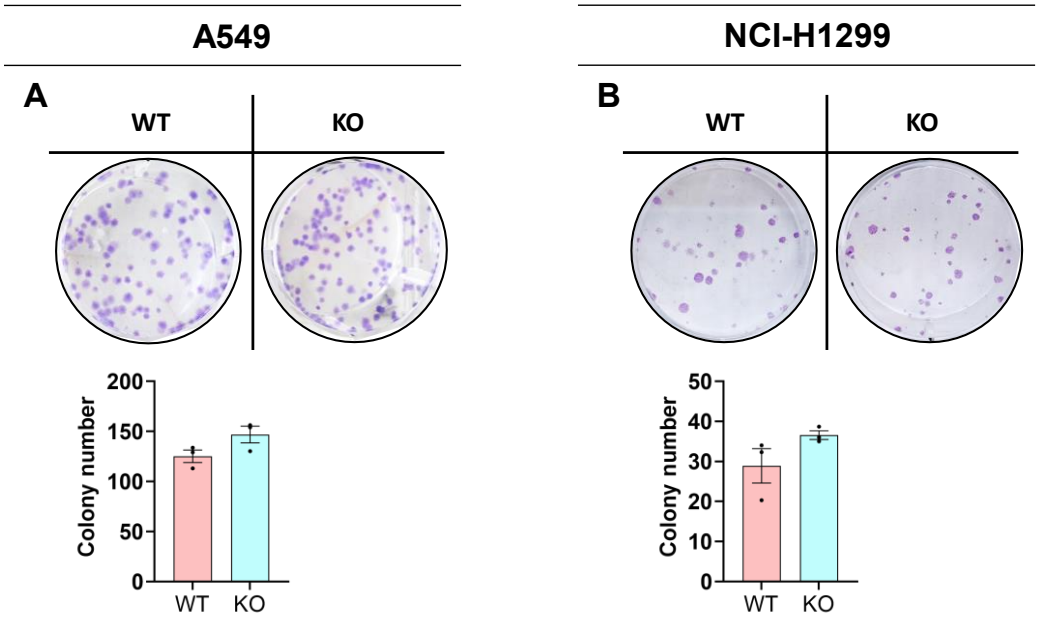

Figure 5.6: Colony formation capacity did not change upon PA200 KO depletion. A clonogenic assay optimised for (A) A549 and **(B)** NCI-H1299 pools of clones. Visible colonies that had at least 50 cells were counted. (n=3, different passages, *p < 0.05, two-tailed unpaired t-test).

5.2.3 Metabolic activity response to PA200 depletion is different in A549 and NCI-H1299

The MTT assay is a colourimetric assay used to assess cellular metabolic activity, which relies on the conversion of a yellow tetrazolium salt (3-(4,5-dimethylthiazol-2-yl)-2,5-diphenyltetrazolium bromide, or MTT) into purple formazan crystals in the metabolically active cells (Slater et al., 1963). Living cells convert MTT to formazan by the presence of NAD(P)H-dependent oxidoreductase enzymes (Berridge & Tan, 1993). Previously, PA200 knockdown was associated with increased sensitivity to glutamine and adaptation to cellular growth conditions (Blickwedehl et al., 2012; Welk, 2018). Therefore, based on the previous findings, we hypothesized that PA200 might be involved in the metabolism changes, which is another hallmark of cancer.

Here, we first tested the effect of serum on metabolic activity in the presence and absence of PA200. Surprisingly, the metabolic activity was differently regulated in A549 and NCI-H1299 cell lines upon PA200 knock-out both under serum starvation (1% FBS) and normal conditions (10% FBS) with or without L-glutamine (Figure 5.7). In A549 cell lines, increased metabolic

activity was observed in all cases upon PA200 depletion. However, the increases were only significant under the following conditions: 1) 1% FBS with L-glutamine and 2) 10% FBS without L-glutamine (Figure 5.7 A). On the contrary, in NCI-H1299 cell lines, the metabolic activity was downregulated upon PA200 depletion (Figure 5.7 B). However, in this cell line, serum starvation was more relevant than the L-glutamine concentration (Figure 5.7 B, upper panel). In addition, under normal serum conditions, the NCI-H1299 KO cells increased their metabolic activity over time with or without L-glutamine. The increase was more pronounced in the medium without L-glutamine (Figure 5.7 B, lower panel) than in other conditions. These results add to the different responses observed between the two NSCLC cell lines upon PA200 depletion.

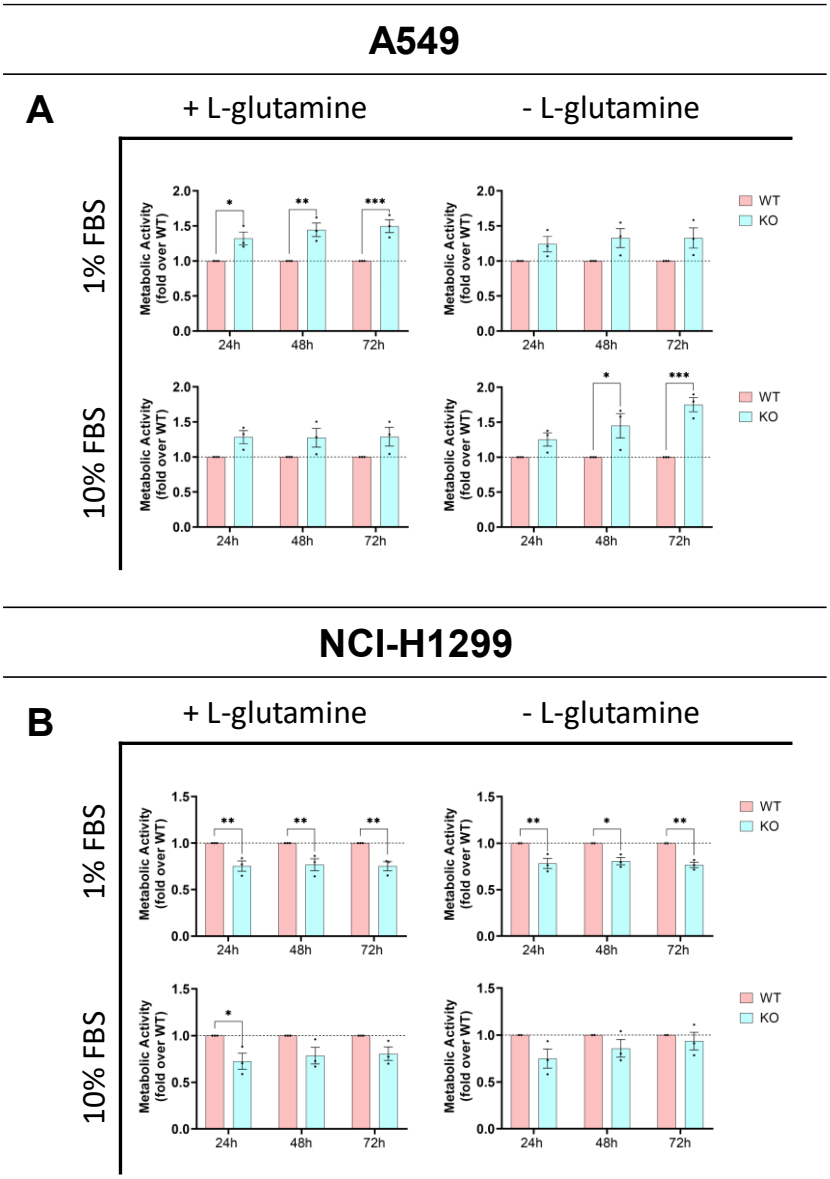

Figure 5.7: Metabolic activity assay (MTT) shows differences between WT and PA200 cells upon serum starvation and L-glutamine addition, but differently in two different NSCLC cell lines. MTT assay was used to determine the metabolic activity rates in **(A)** A549 and **(B)** NCI-H1299 pools of clones. (n=3, different passages, *p < 0.05, **p < 0.01, ***p < 0.001, ordinary two-way ANOVA with Šídák's multiple comparisons test).

5.3 PA200 regulates the invasion and migration capacity of lung cancer cells

5.3.1 Invasiveness and migration are decreased in PA200 KO cell lines

Another hallmark of cancer cells was analysed, i.e., the migration and invasion capacity of WT versus PA200 KOs cells. Initially, Boyden chamber assays were used for migration and invasion assays. Different initial cell numbers, membrane material and concentrations of FBS differences were used during the optimization. However, this method was unreliable for the A549 cells as the cells attached to both sides of the membrane made it impossible to differentiate the non-migrated from the migrated cells. On the other hand, non-migrated NCI-H1299 cells detached easily from the membrane as their attachment strength was less compared to the A549 cells. Therefore, for A549 cell lines, a spheroid formation assay was optimised to track the migrative and invasive capacity (Figure 5.8 A). In this method, the cells were seeded into ultra-low attachment plates (0h) to generate spheroids. The spheroids were then embedded into a collagen G and Matrigel mixture and imaged at 72h and 144h in the gel (Figure 5.8 B). The initial projected area of the KO spheroids embedded in the mixture was bigger than the WTs (Figure 5.8 C, left panel). However, after 72h, the invasion percentage, which was calculated as the difference between the spheroid area at time points 72h and 144h, was higher in the WTs compared to the KOs. This date indicates a faster growth of WT spheroids into the extracellular matrix compared to the KOs (Figure 5.8 C, right panel). As mentioned above, the spheroid formation assay did not work with the NCI-H1299 cell lines as they generated fragile spheroids due to their loose attachments. Therefore, the migration level of NCI-H1299 cell lines was assessed with Boyden chambers as described in the methods. The results showed that the number of migrating cells was significantly reduced in the PA200 KOs (Figure 5.8 D, F). These results show that the migration and invasion capacity is reduced upon PA200 depletion in both lung cancer cell lines.

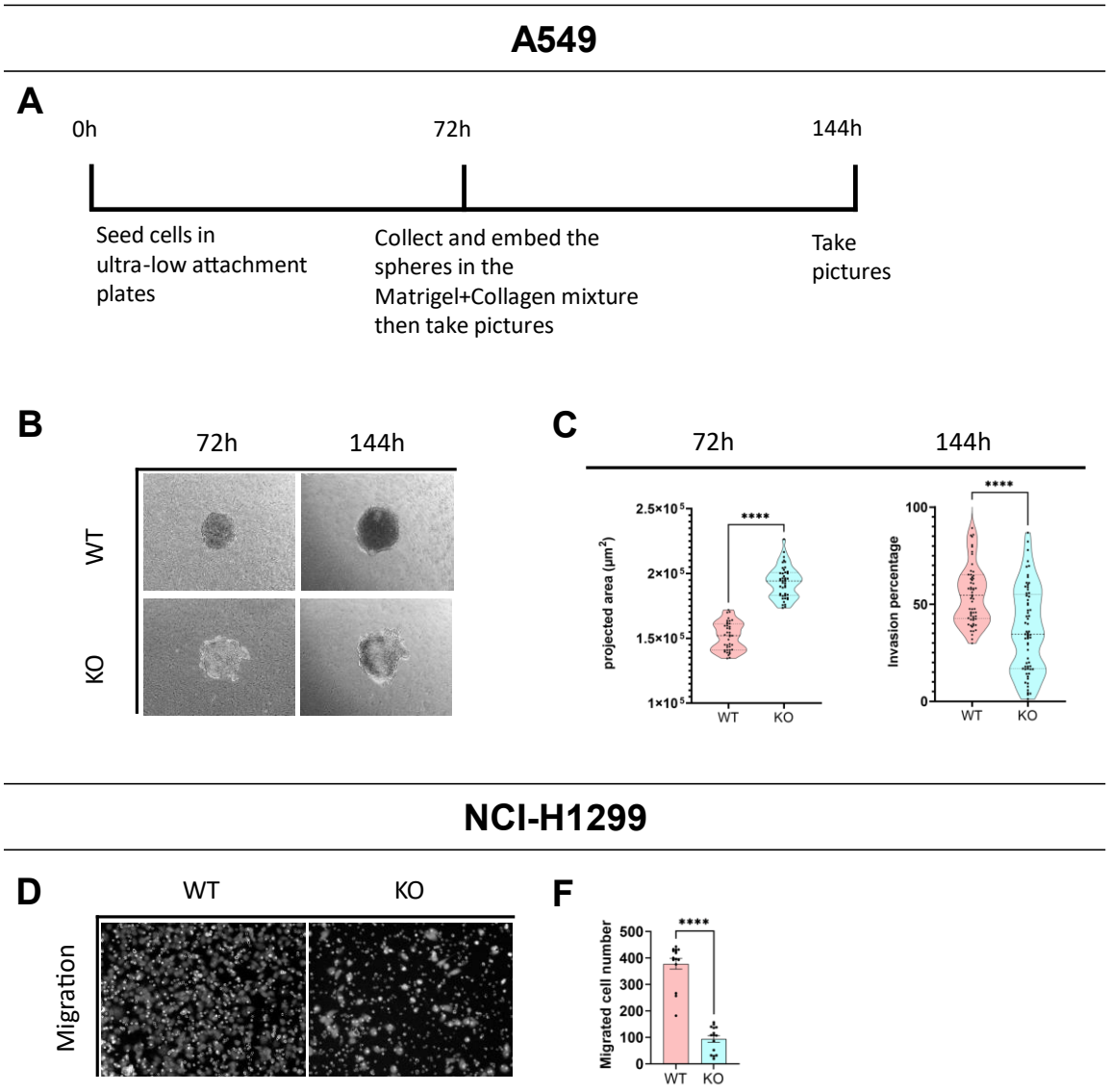

Figure 5.8: PA200 deletion decreases the invasion and migration potential of the NSCLC cell lines. (A) An alternative method of 3D invasion assay to the migration assay with the Boyden chamber was employed for A549 cells, and the PA200 knock-out cells' invasive capacity was examined. **(B)** Representative photos of the spheroids after 72 hours of initial seeding and 72 hours after embedding in the Collagen G+Matrigel membrane. The spheroids' area was calculated twice: once at 72 hours (0 hours after embedding) and once at 144 hours (72 hours after embedding). **(C)** The projected area and the invasion percentage were calculated based on the photos taken. Representative photos of the Boyden chamber migration assay of the NCI-H1299 cells are shown in **(D)** and **(F)** quantified (n=3, different passage, *p < 0.05, **p < 0.01, ***p < 0.001, two-tailed unpaired t-test for C and F).

5.3.2 NCI-H1299 PA200 KO cells have a reduced potential for wound healing

Based on our results that the migration and invasion capacity is decreased in both cell lines upon PA200 KO, the wound healing assay was used further to study cell-cell interaction and migration in both cell lines. This assay used commercially available cell inserts to generate reproducible wound scratches in the confluent cell lawn. Initially, the cells were seeded on the two sides of the inserts, and after 24 hours, the insert was carefully removed. The pictures of the scratch were immediately captured at 0h after washing the detached cells and adding medium. The gap closure was monitored, and images were taken every 20 minutes for 48 hours in a live cell imaging microscope with an incubator. The results show that in A549 PA200 KOs, the wound healing capacity is reduced but not significantly compared to the WT controls over time (Figure 5.9 A and B). However, in NCI-H1299 KOs, the wound healing capacity change was significant and reduced due to PA200 deletion. In addition, the wound was closed entirely in the NCI-H1299 WT cell lines after 48 hours, whereas KO cells could not close the gap after 48 hours (Figure 5.9 C and D). These results suggest that the absence of PA200 interferes with wound healing capacity significantly in NCI-H1299, whereas in A549 cells, the difference is infinitesimal.

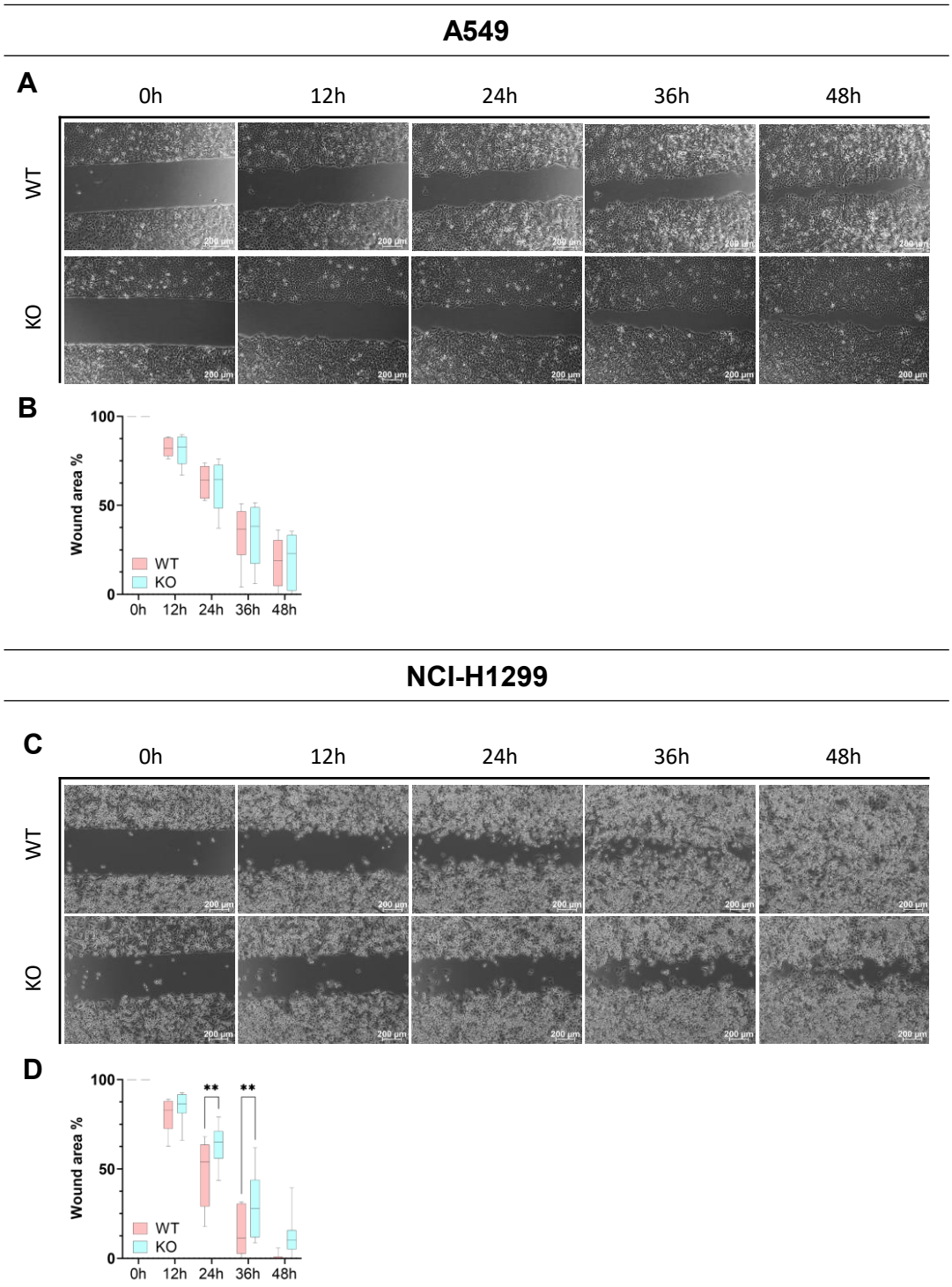

Figure 5.9: PA200 deletion decreases the wound healing potential of NCI-H1299 cells. The wound healing capacity of the stable PA200 knock-out cells was examined in a scratch assay. **(A)** Representative photos of the wound closures of A549 WT and KO cells taken every 12 hours up to 48 hours and **(B)** quantification of wound closure. **(C)** The wound healing capacity was also **(D)** quantified in NCI-H1299 cell lines. **(**Two-tailed unpaired t-test, n=3, different passages**).**

5.3.3 Epithelial to Mesenchymal Transition (EMT) is affected by PA200 deletion

Previously, the regulation of PA200 was investigated in primary human lung fibroblasts (phLF) in response to TGF-β1, a major profibrotic cytokine (Welk et al., 2019). In this study, PA200 increased mRNA and protein levels upon TGF-β1 stimulation in phLF cells, leading to myofibroblast differentiation. Based on this finding, the role of TGF-β in cancer cells which triggers EMT, and our findings on invasion, migration, and wound healing, we hypothesized that PA200 might play a role in this pathway. Therefore, we next studied whether PA200 might regulate the cell status (epithelial or mesenchymal) or its transition (from epithelial to mesenchymal) in response to transforming growth factor-β (TGF-β). For that, we selected well-studied epithelial and mesenchymal markers.

At baseline, depletion of PA200 in A549 cells resulted in upregulation of the epithelial marker genes E-cadherin (E-cad) and Claudin. In contrast, another epithelial marker Occludin was downregulated on the mRNA level (Figure 5.10 A). The mesenchymal marker Twist1 was decreased while Snail2 was increased significantly (Figure 5.10 B). The EMT-associated genes ZEB2 and Integrin-β3 (ITGB3) were significantly decreased (Figure 5.10 C). In contrast to A549 cells, depletion of PA200 in NCI-H1299 cells did not significantly regulate epithelial nor mesenchymal marker gene expression due to high variations in the cell clones (Figure 5.10 D, E). While EMT-associated ITGB3 mRNA levels were significantly decreased, ZEB2 and Col4A1 mRNA levels were increased in NCI-H1299 PA200 KO cells (Figure 5.10 F). These data suggest that the absence of PA200 affects the status of the cell (epithelial or mesenchymal) differently in the two NSCLC cell lines.

To understand the role of PA200 in EMT, we treated the cells with TGF-β for 72 hours and analysed mRNA and protein expression of several EMT marker genes. To synchronize cells, they were cultured under reduced serum condition (1% FBS) for 24 hours before the medium was changed to 1% FBS or 1% FBS + TGF-β (5 ng/ml).

Upon treatment with TGF-β (5ng/ml), the epithelial markers E-cad and Claudin were significantly downregulated in A549 WT cells. However, the downregulation of Claudin was negligibly small in the PA200 KO (Figure 5.10 A). As expected, mRNA levels of mesenchymal markers N-cadherin (N-cad), Vimentin, Snail1 and Snail2 increased in treated cells. The increase was high in the PA200 KOs for N-cad and Snails; however, it was not significant due to the large variance between the clones (Figure 5.10 B). The EMT-inducing effect of TGF-β was less pronounced in NCI-H1299 cells with no downregulation of epithelial markers but

upregulation of several mesenchymal marker genes (Figure 5.10 D, E). In PA200 KO NCI-H1299 cells, the regulation of Claudin and Occludin mRNA levels was opposite to what we observed in A549 KOs (Figure 5.10 A-B, D-E). Interestingly, the ITGB3 mRNA level was re-induced in the A549 PA200 KOs upon TGF-β treatment (Figure 5.10 C), while no change was observed in NCI-H1299 PA200 KOs. The opposite response was observed in ZEB2 mRNA levels.

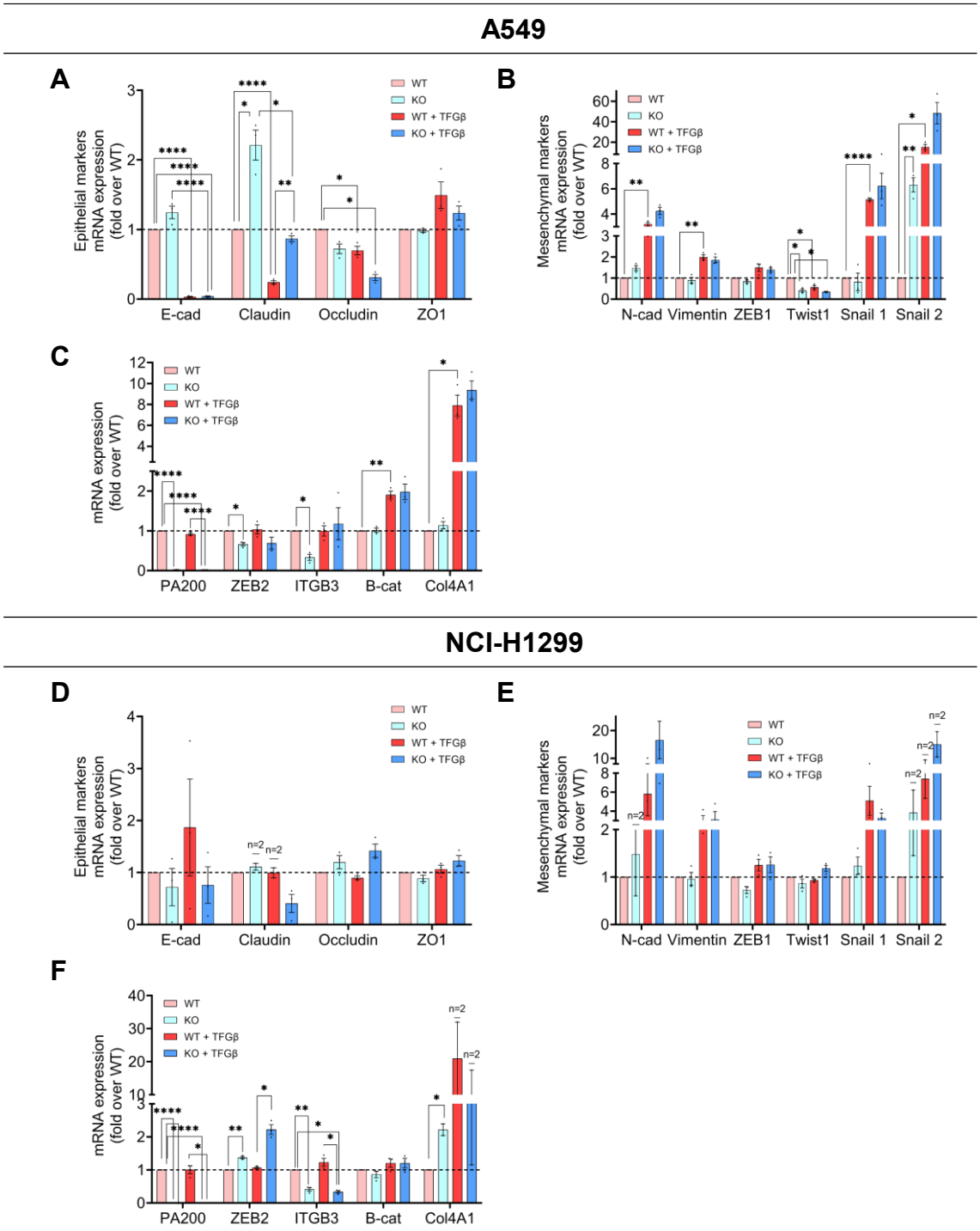

Figure 5.10: PA200 depletion changes the mRNA levels of the genes involved in the EMT and TGF-β signalling. mRNA levels of epithelial and mesenchymal genes and the genes involved in the TGF-β signalling were quantified at baseline and after EMT induction by TGF-β treatment in both cell lines. Data are presented as fold changes of EMT gene expression (**(A, D)** epithelial **(B, E)** mesenchymal) and TGF-β-related signalling **(C, F)** after normalisation to a housekeeping gene (RPL19) and then to the corresponding WT cells according to the ΔΔCt method in **(A-C)** A549 cells and in **(D-F)** NCI-H1299 cells. (*p < 0.05, **p < 0.01, ***p < 0.001, unpaired t-test, Holm-Šídák method, n=3, different passages unless stated otherwise).

Next, protein levels of several EMT markers were analysed by Western blotting (Figure 5.11). The decrease in E-cadherin levels and the increase in the N-cadherin levels in WT TGF-β treated cells indicate a successful epithelial-to-mesenchymal transition. At baseline, both cell lines expressed more E-cad, N-cad, and β-catenin (B-cat) but less ITGB3 protein in PA200 absence. Nonetheless, the response to TGF-β was different in the two cell lines. The epithelial marker, E-cadherin, was hardly detected after the TGF-β treatment in A549 cells. Although decreased after the treatment, E-cad was still strongly expressed together with the mesenchymal marker N-cadherin in the NCI-H1299 KOs. Additionally, the decrease in E-cadherin was only significant in NCI-H1299 WTs, yet the increase of the N-cad was higher in the PA200 KO cells (Figure 5.11 B). In both cell lines, the β-catenin protein was expressed more in the TGF-β treated PA200 KO cells compared to the WTs but reached significance only in the NCI-H1299. Similar to the mRNA response, the ITGB3 protein expression was induced in WT and KO cells of A549 after TGF-β treatment (Figure 5.11 A), while it was not induced in the NCI-H1299 KOs (Figure 5.11 B).

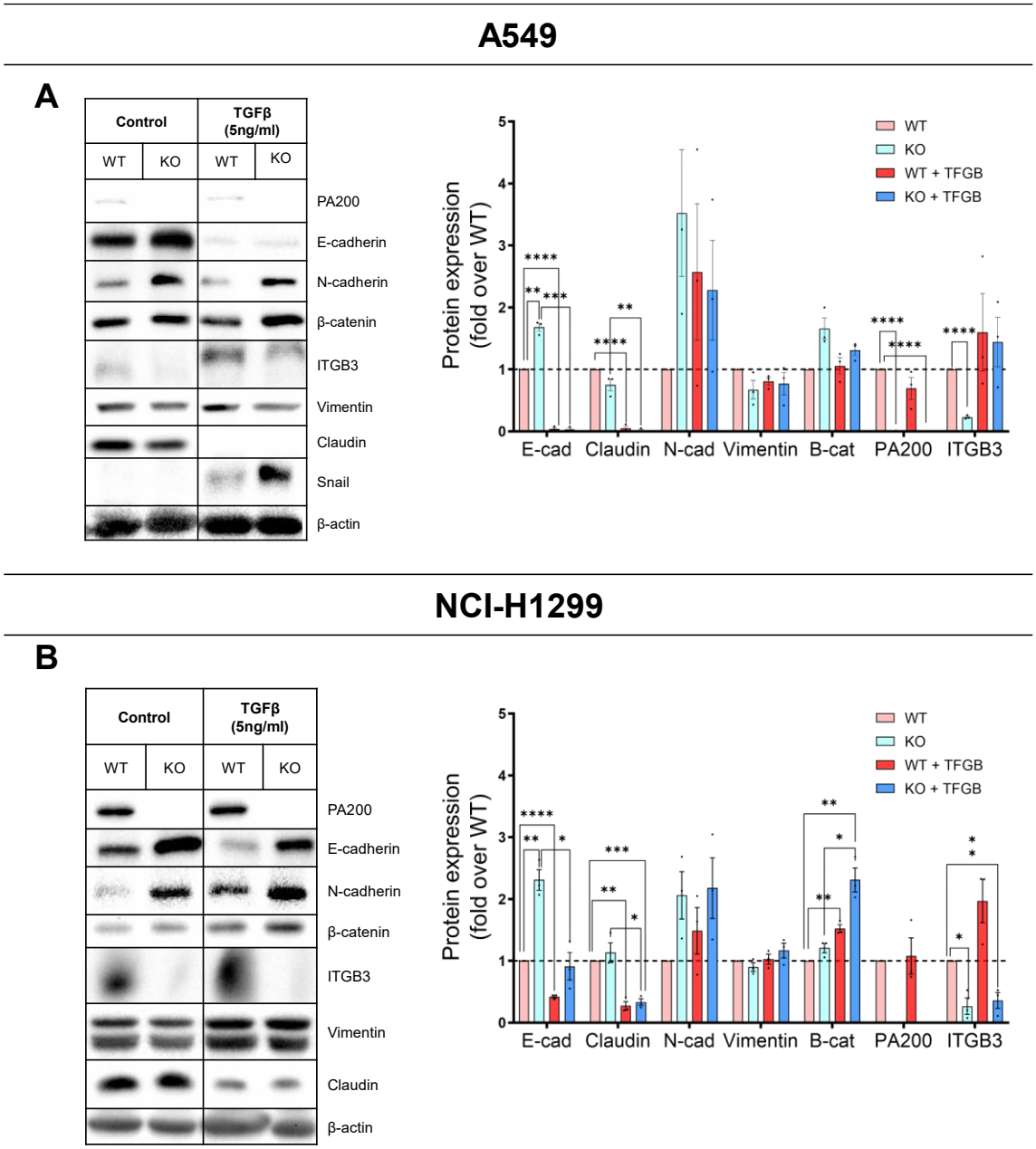

Figure 5.11: Protein levels of EMT and TGF-β signalling markers differ at baseline and upon treatment in A549 and NCI-H1299. Protein levels of epithelial and mesenchymal genes were quantified at baseline and after induction of EMT upon treatment with TGF-β in **(A)** A549 and **(B)** NCI-H1299 cell lines. (*p < 0.05, **p < 0.01, ***p < 0.001, **** p < 0.0001 unpaired t-test, Holm-Šídák method, n=3, different passages).

In conclusion, the regulation of mRNA and protein levels of epithelial, mesenchymal, and TGF-β signalling marker genes showed several differences in A549 and NCI-H1299 cells both at baseline and upon TGF-β treatment. On the mRNA level cells, TGF-β induced EMT more efficiently in the A549 WT cells compared to the NCI-H1299 WT cells. Additionally, the changes in the two transcription factors, Twist1 and ZEB2, were different in the two cell lines. On the protein level, the main difference was observed in the levels of ITGB3 between the cell

lines, similar to the mRNA levels. Interestingly, the increase of the mRNA levels of Claudin was not observed in the A549 PA200 KOs. Furthermore, the two most well-known epithelial (E-cadherin) and mesenchymal marker (N-cadherin) increase upon PA200 deletion, which might indicate induction of a partial EMT state rather than a complete transition. Overall, these data on mRNA and protein levels suggest that PA200 plays a role in EMT, but the level of its involvement might be related to the context of the cell, considering the different responses.

5.4 PA200 regulates the immunoproteasome

Recently, Javitt et al. proposed that PA200 regulates the function of the immunoproteasome (Javitt et al., 2023). They found that the PA200 expression level correlates with the responsiveness of immune checkpoint inhibitors across a variety of cancer types. Furthermore, they elucidated a fostering role of PA200 in the immunosuppressive environment around the tumour, which eliminates anti-tumour immunity by preventing the presentation of MHC class I antigens and reducing tumour inflammation. The proposed mechanism depended on PA200-capped proteasomes reducing the activity of the immunoproteasome. The diminished immunoproteasome activity, in turn, contributed to decreased antigenicity by limiting the diversity of the immunopeptidome, changing the surface HLA presentation, and decreasing cellular inflammation in an IL-6-dependent way. To understand how the immunoproteasome profile changes in the total absence of PA200, we first analyzed the baseline changes and then treated the cells with interferon-β (IFN-β) and interferon-γ (IFN-γ) to stimulate Type I and Type II interferon responses, respectively. Subsequently, we analysed immunoproteasome expression and activity in WT and PA200 KO A549 and NCI-H1299 cells using several biochemical methods. We also included the regulation of PA28αβ activators in our analysis, as this regulator plays a prominent role in antigen presentation and is usually co-regulated with the immunoproteasome (de Graaf et al., 2011)

5.4.1 Depletion of PA200 differentially alters immunoproteasome and PA28 regulator expression in A549 and NCI-H1299 cells

We here investigated whether the depletion of PA200 in the lung cancer cell lines interferes with the expression and activity of the immunoproteasome. Initially, we analysed the overall expression of proteasomal subunits in the different cell lines by Western blotting. PA28β and PA28γ levels were checked to see additional changes in the ATP- and ubiquitin-independent proteasome activators.

In the A549 cell lines, no significant change was observed in the constitutive proteasome (c20S) levels in the PA200 KOs as determined by the detection of α1-7 subunits (Figure 5.12 A, B). However, the immunoproteasome (i20S) - specific subunit levels noticeably differed between the WT and KO cells. These changes were mainly observed in the LMP2 and MECL-1 levels, with LMP2 protein levels being reduced and MECL-1 levels being increased in the KOs. On the other hand, the changes in the PA28β and PA28γ levels were not significant.

In the NCI-H1299 cell lines, we observed that the constitutive proteasome (c20S) and LMP7 levels decreased upon PA200 depletion (Figure 5.12 C, D). Similar to A549 KOs, the LMP2 protein levels significantly decreased in the NCI-H1299 KOs. Interestingly, while MECL-1 upper band intensity was increased in the KOs, the intensity of the lower band was decreased significantly upon PA200 deletion. No significant change was observed in the protein levels of the immunoproteasome-associated proteasome caps, PA28β and PA28γ, in response to PA200 depletion.

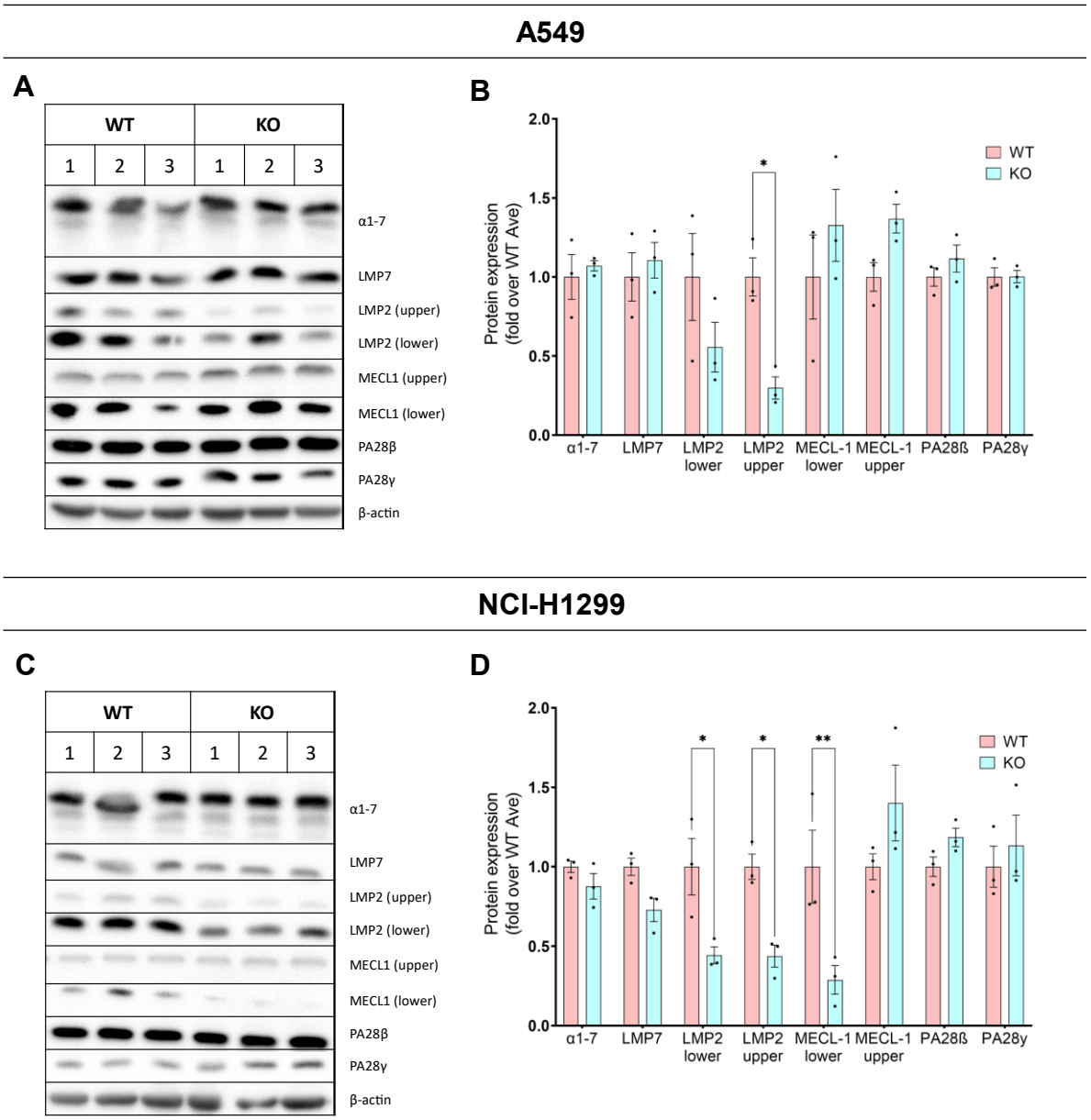

Figure 5.12: Alterations in the immunoproteasome subunits observed on the protein expression level upon PA200 KO. 20S proteasome subunit and immunoproteasome-specific subunit expression levels were compared between the three different WT and KO cell lines of A549 and NCI-H1299 cells. **(A, C)** c20s and i20S protein expression levels were measured by Western Blot analysis of selected clones and **(B, D)** quantified **(A-B)** in A549 and **(C-D)** in NCI-H1299 cell lines. β-actin served as a housekeeping protein to ensure equal protein loading in the Western blotting, and the KOs normalised against WTs (*p < 0.05, **p < 0.01, ***p < 0.001, ordinary two-way ANOVA with Šídák test, n=3, different passages).

According to the protein expression levels, the subunits of c20S and i20S were differentially regulated in the two NSCLC cell lines in response to PA200 depletion. In the Western blot, the upper and lower bands represent the higher and lower molecular weight forms of the subunits, respectively. The upper band corresponds to the precursor form of the immunoproteasome subunits, which is not processed and thus not yet incorporated into the assembled proteasome

complex. In contrast, the lower band represents the mature form of these subunits assembled into active proteasome complexes (Chen & Hochstrasser, 1996; Frentzel et al., 1993; Frentzel et al., 1994; M. Groettrup et al., 1997; Schmidtke et al., 1996). Therefore, these results suggest that mature MECL-1 (PSMB10) protein levels are differentially regulated in A549 and NCI-H1299 cell lines upon PA200 deletion, although the precursor levels were increased in both of them.

5.4.2 PA200 depletion differentially affects immunoproteasome assembly in A549 and NCI-H1299 cells

The aforementioned Nature Cancer paper showed that the immunoproteasome-specific activities involved in the production of the MHC class I antigenic peptide may be negatively regulated by the binding of PA200 to the immunoproteasome (Javitt et al., 2023). Therefore, we analysed the differences in the total protein expression levels in the immunoproteasome-associated proteins. Hence, TSDG lysates were run on native gels to analyze the effect of PA200 on immunoproteasome assembly into mature and active complexes. Once again, an opposite response was observed in PA200 depleted A549 and NCI-H1299 cell lines for all immunoproteasome-specific subunits (Figure 5.13 A and B, respectively). However, the most distinct difference was observed for the MECL-1 subunit. In A549 cells, the MECL-1 recruitment increased in each proteasome complex upon PA200 depletion, whereas in NCI-H1299 cells, the number of immunoproteasome complexes containing MECL-1 decreased. Similarly, LMP2 and LMP7 integration to the immunoproteasome was increased in the PA200 KOs of A549 but decreased in the NCI-H1299 PA200 KOs compared to their WT controls.

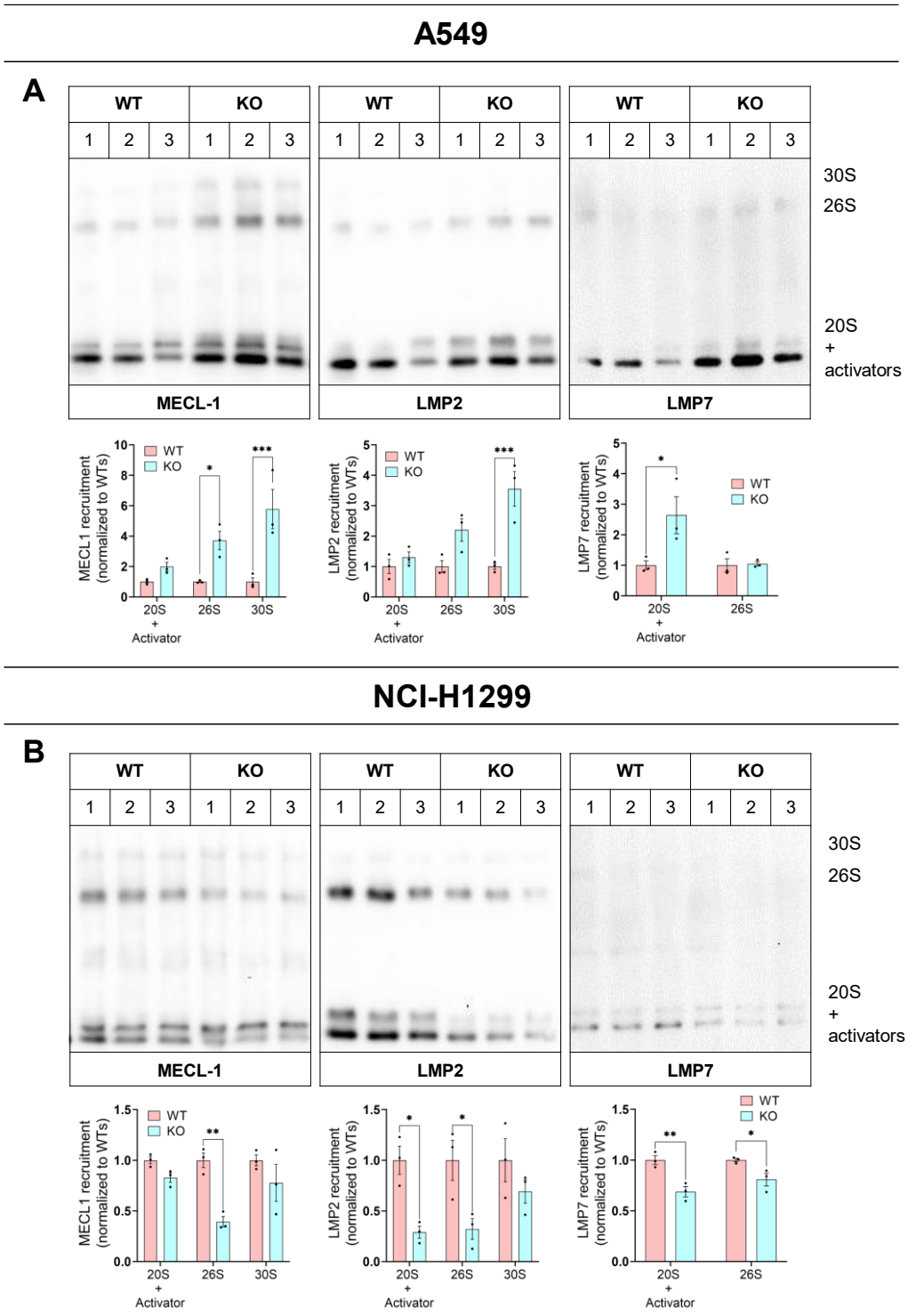

Figure 5.13: i20S is differentially regulated upon PA200 KO in two different NSCLC cell lines. The distribution of the immunoproteasome complexes was compared between the selected WTs and KO cell lines. The gels were blotted after the in-gel proteasome activity of native gels to determine the distribution of the i20s-specific subunits in proteasome complexes of **(A)** A549 cells and **(B)** NCI-H1299 cells. The quantification is shown below the respective image. (*p < 0.05, **p < 0.01, ***p < 0.001, ordinary two-way ANOVA with Šídák test, n=3, different passages).

Considering the differences in the assembly of the immunoproteasome-specific subunits, we next analysed the ATP- and ubiquitin-independent proteasome activators associated mainly with the immunoproteasome. In the A549 cells, more PA28α and PA28β regulators were recruited to the 20S in the absence of PA200 (Figure 5.14 A). However, PA28α recruitment to the 20S was similar in NCI-H1299 WT and KO clones, while PA28β was less recruited to the 20S upon PA200 depletion in NCI-H1299 clones (Figure 5.14 B). In both cell lines, we observed the activators mainly associated with the core unit of the proteasome (the 20S).

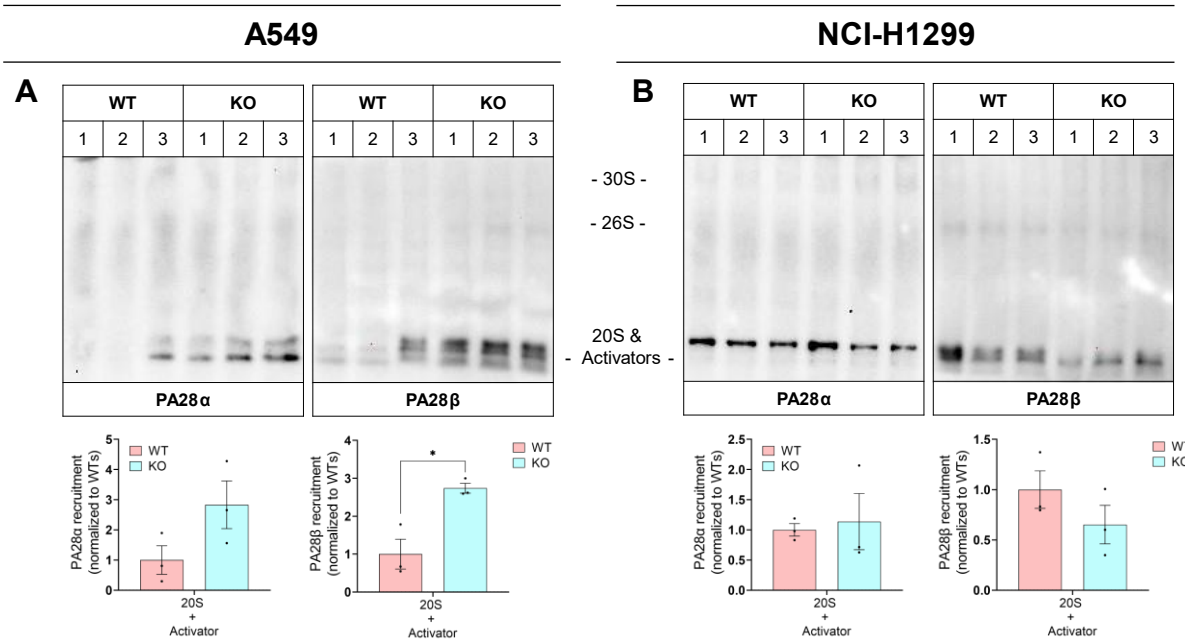

Figure 5.14: PA28α/β are differentially associated with the 20S upon PA200 KO in two different NSCLC cell lines. ATP and ubiquitin-independent proteasome activators PA28α/β compared between the selected WT and KO cell lines. The native gels were blotted after in-gel proteasome activity to observe the distribution in the selected cell lines **(A)** in A549 cells and **(B)** in NCI-H1299 cells. The quantification is shown below the respective image. (Ordinary two-way ANOVA with Šídák test, n=3, different passages).

These results suggest that the immunoproteasome profile in the two different NSCLC cell lines is differentially regulated upon PA200 depletion. Furthermore, PA200 ablation alters the distribution of the proteasome complexes and i20S-specific activators at baseline.

5.4.3 PA200 differentially regulates the expression of interferon-inducible proteasome subunits and activators in lung cancer cell lines

Next, we examined how PA200 depletion might affect immunoproteasomes and activators when the cells were treated with interferons. As explained in the introduction, the expression

of the i20S-specific subunits is upregulated by interferons, and immunoproteasome subunits then assemble into mature and active i20S complexes. First, the mRNA expression levels of the immunoproteasome subunits were analysed in both cell lines upon Type I and Type II interferon treatment.

At baseline, the mRNA levels were similar in WT and PA200 KO A549 cells without significant changes (Figure 5.15 A, B). Upon treatment with Type I or Type II interferons for 24h, all immunoproteasome subunits and the PA28α/PA28β encoding genes PSME1/2 were strongly upregulated in both cells. However, in PA200-depleted cells, PSMB8, PSMB10 and PSME1 mRNA levels were further upregulated by IFN-β and IFN-γ compared to the WT cells. Similarly, an induction was observed on the PSME2 mRNA levels in IFN-β-treated PA200 KO cells (Figure 5.15 B).

In NCI-H1299 cells, immunoproteasome and PA28α and PA28β expression were similar in WT and PA200 KO cells (Figure 5.15 C, D). IFN-β or IFN-γ treatment strongly upregulated these genes in the WT and PA200-depleted cells to a similar extent. Only PSME3 induction by IFN-β was significantly higher upon PA200 KO.

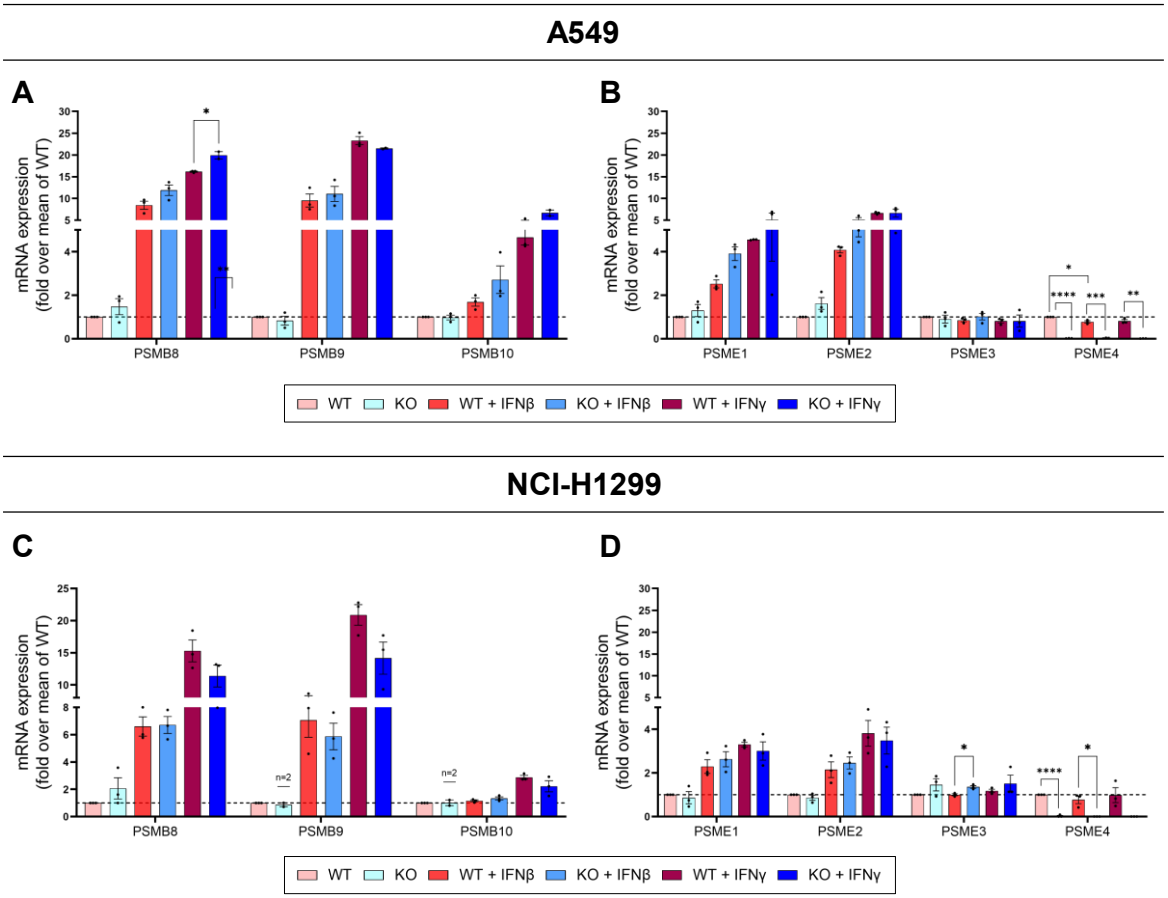

Figure 5.15: Immunoproteasome-specific subunits and proteasome activators are differentially regulated on their mRNA levels upon Type I and Type II interferon treatment in response to PA200 depletion. mRNA levels of **(A, C)** immunoproteasome-specific genes and **(B, D)** proteasome activators were quantified at baseline and after the treatment of IFN-β and IFN-γ in the **(A, B)** A549 cell line and **(C, D)** in the NCI-H1299 cell lines. RPL19 was used as a housekeeping gene; all samples were normalised to the untreated WTs. (*p < 0.05, **p < 0.01, ***p < 0.001, **** p < 0.0001 unpaired t-test, Holm-Šídák method, n=3 unless stated otherwise, different passages).

Next, the protein expression levels of proteasome subunits were analysed at baseline and under interferon treatment conditions to see if any changes in the mRNA levels translated into the protein expression levels after 24h. The baseline protein expression levels of the α-subunits and the immunoproteasome subunits were similar between the WT and KOs according to the Western blot analysis (Figure 5.16 A, B). MECL-1 and LMP2 were detected with two bands (lower: precursor, upper: mature), whereas, for LMP7, the two bands were not consistent. The induction of the immunoproteasome-specific subunits was more pronounced in the IFN-γ treated cells compared to the IFN-β treated cells, but PA200 depletion did not affect it. No significant changes were observed in the PA200 levels between the WTs upon IFN treatments.

Additionally, we again observed differences between the A549 and NCI-H1299 cell lines upon PA200 KOs. At the baseline, only the upper (mature) MECL-1 and LMP7s protein levels were increased in the KOs, while lower (precursor) MECL-1 and LMP2 levels stayed similar (Figure 5.16 B). Yet, the induction of immunoproteasome-specific subunits showed no significant difference between WT and KO cells under the treatment conditions. However, the increase in the lower band of MECL-1 was less pronounced in KOs following IFN-β treatment. Furthermore, PA200 protein levels were elevated in WT cells under both treatment conditions. Similar to A549 cells, the IFN-γ treated cells exhibited a higher induction of immunoproteasome-specific subunits.

The interferon treatments induced baseline mRNA and protein levels of immunoproteasome-specific subunits in both wild-type (WT) and knockout (KO) cells, as expected. However, the induction levels of certain i20S-specific genes varied depending on the presence of PA200 and the type of treatment, while protein levels were similar between WT and KO cells. Notably, these changes were observed at different magnitudes in the two NSCLC cell lines, both at the mRNA and protein levels. This suggests a context-dependent function of PA200 in different NSCLC cell lines. It is worth mentioning that the differences in induction levels between the experiment and the effect on gene expression hindered the statistical test results.

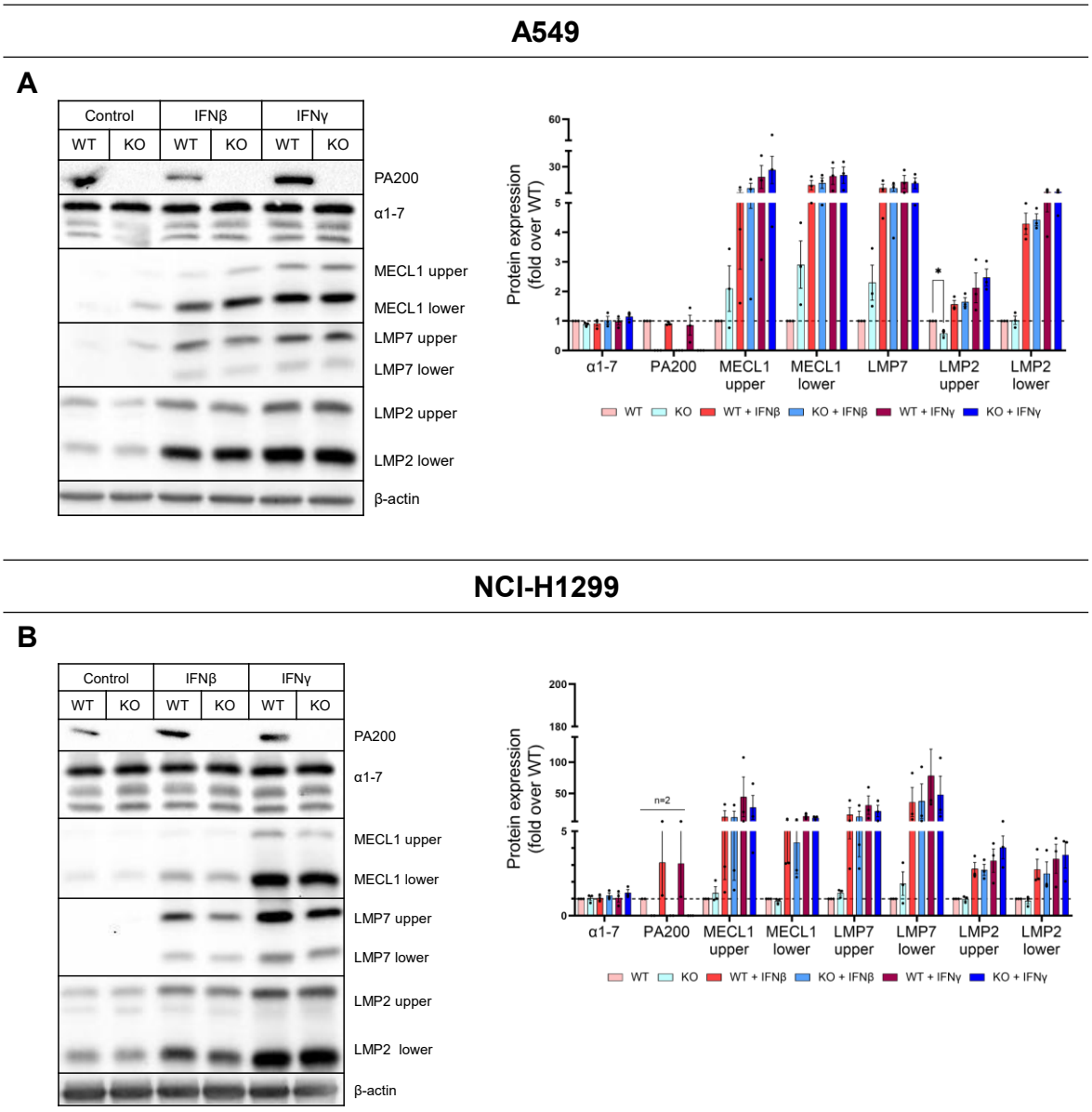

Figure 5.16: Immunoproteasome-specific subunits' and proteasome activators' protein levels are altered differently upon PA200 deletion upon IFN-β and IFN-γ treatments. Protein levels of immunoproteasome-specific subunits, α1-7 and PA200, were quantified after 24h treatment of IFN-β and IFN-γ with the respective antibodies in the **(A) A549** and the **(B)** NCI-H1299 cell lines (unpaired t-test, Holm-Šídák method, n=3 unless stated otherwise, different passages).

5.4.4 Depletion of PA200 differentially affected immunoproteasome assembly upon interferon treatment in NSCLC cell lines

We further analysed the effect of PA200 depletion on the assembly and activity of immunoproteasome complexes upon interferon treatment using in-gel proteasome activity assay and activity-based probes (ABPs).

In A549 cell lines, the in-gel proteasome activity assay with CT-L substrate showed an increase in the 20S+activators in all interferon-treated cells. The overall activity in the 20S+activators was higher in the KOs compared to the WTs; however, no significant change was observed upon interferon treatments (Figure 5.17 A). No changes were observed for 26S and 30S complexes which were less affected by interferon treatment. Next, active proteasome complexes were labelled with activity-based probes (ABPs), which shows how much of the i20S subunits are incorporated into the proteasome complexes. At baseline, the activity of the proteasome complexes with immunoproteasome-specific subunits MECL-1 and LMP7 was significantly higher in the PA200 KOs. In the IFN-β treated PA200 KOs, MECL-1 was again incorporated into the proteasomes, while in the IFN-γ treated PA200 KOs, the incorporation was similar to the corresponding WT cells (Figure 5.17 B).

In NCI-H1299 cell lines, the 20S+activators' CT-L activity was increased in all interferon-treated cells except for IFN-β-treated PA200 KOs. In addition, the increase in CT-L activity of IFN-γ-treated PA200 KOs was less for the 20S+activators (Figure 5.17 C). The activity-based results showed no significant activity changes at the baseline with immunoproteasome-specific subunits (Figure 5.17 D). However, MECL-1 incorporation was less in the IFN-γ treated PA200 KOs compared to its control, IFN-γ treated WTs (Figure 5.17 D).

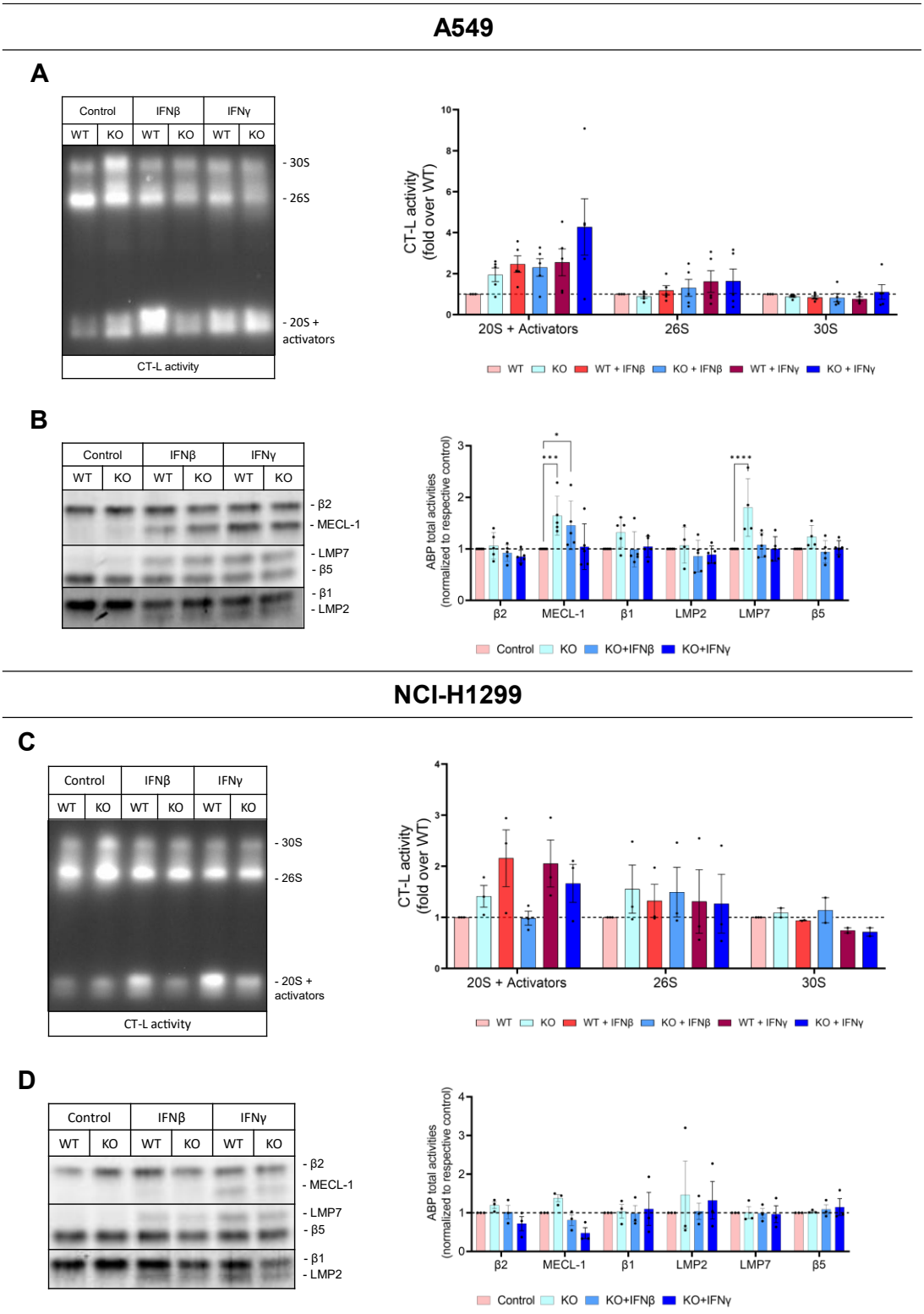

Figure 5.17: Proteasome activities and immunoproteasome-specific subunit integration change with PA200 deletion and IFN-β and IFN-γ treatments. Chymotrypsin-like activity of proteasome subunits was **(A, C)** measured, and the activity of the immunoproteasome-specific subunit proteasomes was monitored with **(B, D)** ABPs in the **(A-B)** A549 cell line and **(C-D)** in the NCI-H1299 cell lines (Two-way ANOVA test, Sídák method, at least n=3, different passages).

Finally, the overall distribution of proteasome complexes and integration of immunoproteasome-specific subunits was studied upon interferon treatments. The proteasome complexes were mainly distributed as 20S+activators and 26S, with only a small portion composed of the 30S (Figure 5.18). The interferon treatments did not change the amount of these complexes but instead induced an increase in the incorporation of immunoproteasome-specific subunits. MECL-1 was incorporated into the proteasomes in both cell lines more upon IFN treatments than the other subunits and was the only subunit within 30S complexes. In the A549 cell line, MECL-1 was observed on the 30S with both interferon treatments (Figure 5.18 A), while it was only observed with IFN-γ treatment in NCI-H1299 cells (Figure 5.18 B). LMP7 (in NCI-H1299, Figure 5.18 B) and LMP2 (in A549, Figure 5.18 A) showed increased integration into the 26S complexes, particularly in WT cells treated with IFN-γ. Due to low baseline levels in the proteasome complexes, no statistical analysis was conducted.

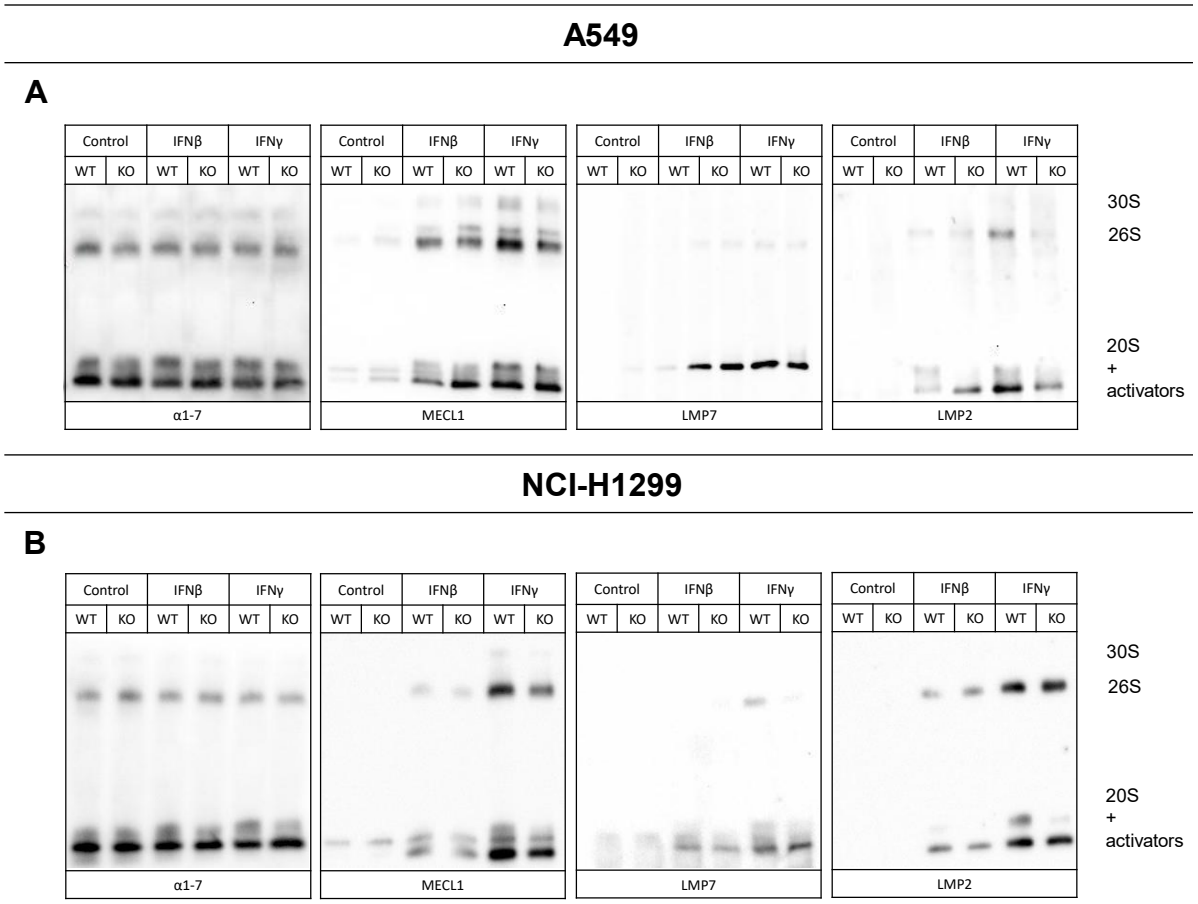

Figure 5.18: The immunoproteasome-specific subunit integration to the proteasome complexes changes with PA200 deletion and IFN-β and IFN-γ treatments. After measuring the activities, the gels were blotted and incubated with different proteasome subunit antibodies. **(A)** A549 cell lines and **(B)** NCI-H1299 cell lines (n=3).

We also analysed whether PA200 is recruited to the proteasome upon interferon treatment and performed native gels and immunoblots for PA200 in WT A549 and NCI-H1299 cells (Figure 5.19). In the A549 cells, the binding of PA200 to the proteasomes increased upon IFN-β and IFN-γ treatments, while in the NCI-H1299 cells, it decreased (Figure 5.19 A, B). Changes were more prominent upon IFN-γ treatment compared to IFN-β treatment.

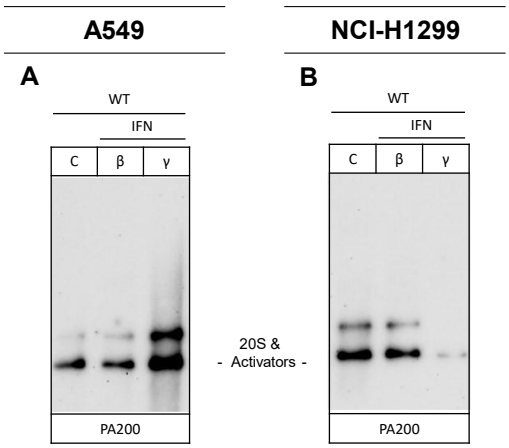

Figure 5.19: Differential incorporation of PA200 to the proteasome complexes upon interferon treatments after 24 hours. Native gels were blotted and incubated with different PA200 antibodies. **(A)** A549 cell lines and **(B)** NCI-H1299 cell lines (n=3).

These results show that the immunoproteasome-specific subunits are induced upon Type I and Type II interferons, and the PA200 status of the cell can alter the response.

5.5 PA200 regulates tumour cell growth in vivo

We observed changes in the proliferation, migration, invasion, and epithelial-mesenchymal transition between the WT and PA200 KO cells in vitro. Based on our data, we hypothesized that these changes could translate to reduced metastatic activities of PA200 KO cells in vivo. Therefore, each corresponding WT and KO cell line pool was injected subcutaneously into the flank of immunodeficient mice to determine tumour growth and metastasis.

The mice injected with A549 cells produced larger primary tumours in WT-injected mice compared to the KO-injected ones (Figure 5.20 A), which was confirmed further by the tumour volume tracked over time (Figure 5.20 B). Accordingly, the primary tumour mass, calculated after the harvesting, was lower in the PA200 KOs (Figure 5.20 C). The body weights of the mice were not altered (Figure 5.20 D). Interestingly, while 80% of the mice formed a primary tumour with the WT cell injection, only 60% of the mice formed a primary tumour with the PA200 KO cell injection (Figure 5.20 E). We determined proliferation in the primary tumour and the lungs using Ki67 staining, but no significant changes were observed between the WT and KO-injected mice (Figure 5.20 F).

Similar to A549 cells injected mice, the mice with NCI-H1299 WT cell injection also produced larger primary tumours than the KOs (Figure 5.20 G, H). The body mass remained similar between the two groups (Figure 5.20 I). In contrast to the A549 results, all mice produced primary tumours with a comparable mass between the WT and KO cells (Figure 5.20 J). We also observed a higher degree of necrosis in the tumours by visual inspection, mainly in those generated by PA200 KO cell injection (60%), while only 20% of the primary tumours formed by WT injection developed necrosis (Figure 5.20 K). Similar to the A549 group, no significant changes in proliferation were observed between the NCI-H1299 WT and KO-injected mice (Figure 5.20 L). In conclusion, PA200 KO cell lines generated smaller primary tumours than those formed from WT cell lines, indicating a difference in proliferation and tumour-forming capacity upon PA200 depletion.

We also investigated the development of metastases into the lung upon harvesting of the animals. However, due to the restrictions imposed by the legal regulations on the maximal tumour burden and the well-being of the mice, we had to sacrifice the mice earlier. The mice were sacrificed, and the samples were collected when the tumour reached the size of 150 mm^3 or had necrosis before macrometastases developed. We also performed histological analyses of the lungs for micrometastases but detected only one animal with NCI-H1299 WT-injected cells having micrometastasis in the lungs. Due to the above-mentioned limitations, we were

thus unable to obtain meaningful data on how the presence of PA200 affects tumour invasion and metastasis.

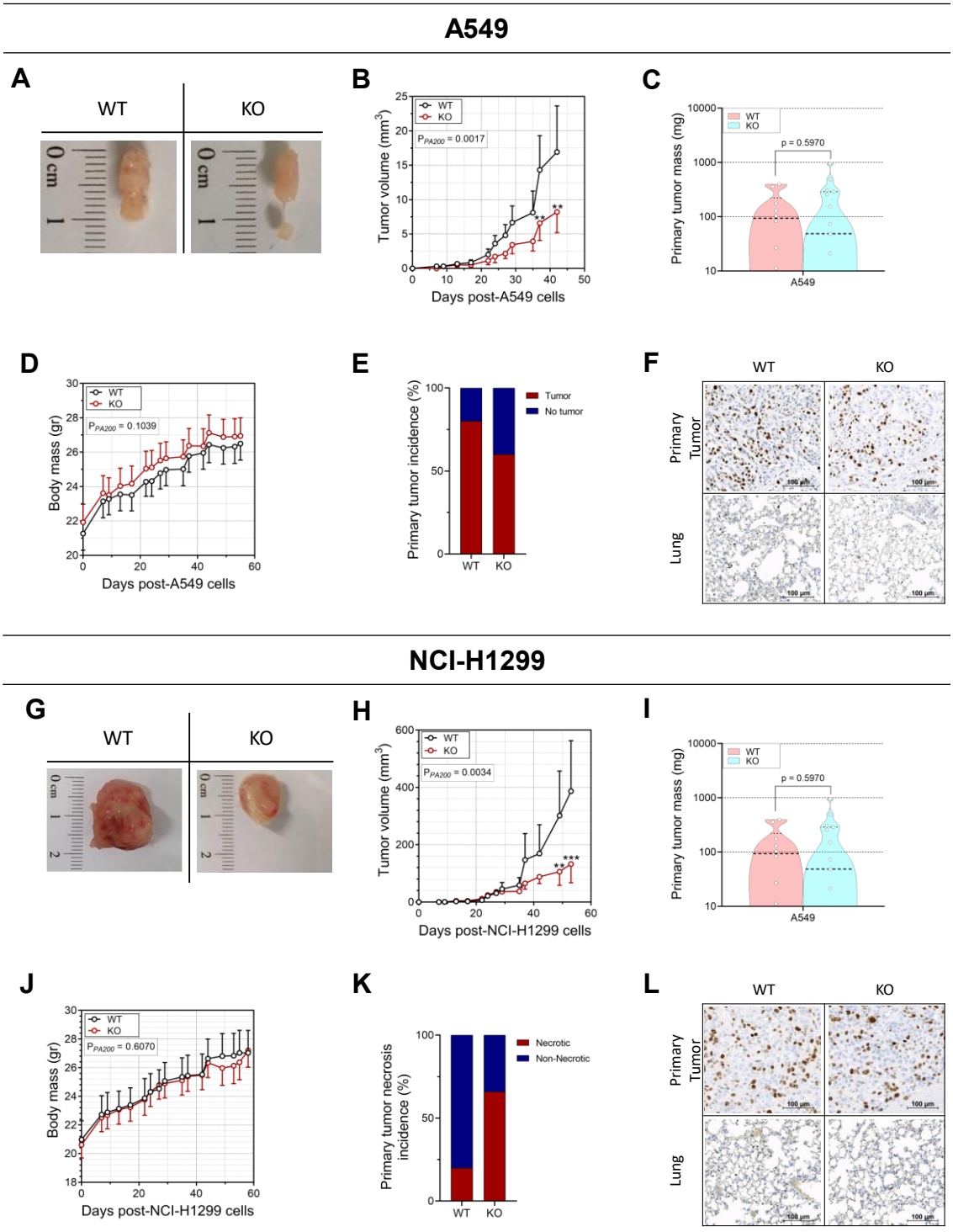

Figure 5.20: Tumour volume decreased upon PA200 depletion in vivo. A549 and NCI-H1299 WT and PA200 KO cell lines were injected subcutaneously into SCID mice. Primary tumours were monitored over time and **(A, G)** photographed after dissection. **(B, H)** Tumour volume, **(C, I)** primary tumour mass and **(D, J)** body mass were measured in WT or PA200 KO–injected **(A-F)** A549 and **(F-L)** NCI-H1299 mice. The primary tumour incidence is shown in **(E)** A549. **(J)** The necrosis incidence on primary tumours in the NCI-H1299 cells-injected mice was calculated by visual inspection. (*p < 0.05, **p < 0.01, ***p < 0.001, **(B-C, H-I)** ordinary two-way ANOVA **(D, J)** unpaired t-test, Holm-Šídák method, WT n=10, PA200 KO n=15 for each cell line)

5.6 Differential transcriptomic changes upon PA200 depletion in the two NSCLC cell lines

5.6.1 RNA-sequencing analysis reveals a differential response of the two lung cancer cell lines to the deletion of PA200

As we observed several differences (metabolism, proteasome regulation, and EMT) and similarities (migration, invasion, and in vivo) between our two cancer cell lines, we studied their RNA signature to identify transcriptomic regulation in selected WT and PA200 KO cell lines in an unbiased way.

In the A549 PA200 KO cell line, 419 genes were upregulated, and 345 genes were downregulated compared to the WTs (Figure 5.21 A) as shown in a volcano plot (Figure 5.21 B, $|FC| \geq 2$, $p \leq 0.05$, $FDR \leq 0.05$, upregulated in orange, downregulated in blue). To confirm the specificity of the RNA-seq, six of the highly regulated genes were selected, and their mRNA expression level was analyzed by qRT-PCR. The mRNA expression of Prickle1, BMP4, and LGR6 increased in PA200 KOs, while ADAM23, PA200, and ITGB3 decreased in the PA200 KOs, respectively corresponding to the RNA-seq results (Figure 5.21 B).

The number of dysregulated genes was lower in the NCI-H1299 PA200 KO cell lines when compared to the A549 PA200 KOs. In this cell lines, 196 genes were upregulated, and 288 genes were downregulated compared to the WTs (Figure 5.21 C) as seen in the volcano plot (Figure 5.21 D, $|FC| \geq 2$, $p \leq 0.05$, $FDR \leq 0.05$, upregulated in orange, downregulated in blue). Similarly, six of the highly regulated genes were chosen, and the level of mRNA expression was assessed with qRT-PCR to confirm the specificity of the RNA-seq. From the selected target genes, the mRNA expression of LINC01127 increased in PA200 KOs, while EPAS1, NPAS2, TGFA, and PA200 mRNA expressions decreased in PA200 KOs, corresponding to the RNA-seq results (Figure 5.21 D).

When the two PA200 KO cell line RNA-seq datasets were compared, only a small part of the genes was regulated in a similar way (Figure 5.21 E). Upon PA200 deletion, 12 genes were downregulated (FIBCD1, KCNIP3, BICDL1, PREX1, GPC1, PSME4, AC016738.1, HES2, ANKRD33B, ITGB3, AC106760.1, ADGRB1) and only 4 genes were upregulated in both NSCLC cell lines (ADAMTS16, EFHC2, GLRB, FAM160A1). Of note, 23 genes were counter-regulated: 13 genes were upregulated in A549 but downregulated in the NCI-H1299 KOs (TGFA, TSPAN1, TBC1D2, GRAMD2B, RAET1E, LIPG, THBS1, ANK1, CORO2A,

SYTL5, ADRB2, SHROOM3, COL13A1) and 10 genes were upregulated in NCI-H1299 but downregulated in the A549 KOs (ADAM23, SIX3, STON1, TRIM9, GPR63, PIANP, FNDC4, F2RL2, AC022506.2, GEM).

In conclusion, the transcriptomic analysis revealed more differences than similarities. These data suggest that PA200 depletion in the two NSCLC cell lines results in rather cell-specific effects on the transcriptome level. This might also explain the observed differences in proliferation, invasion and EMT that we observed before.

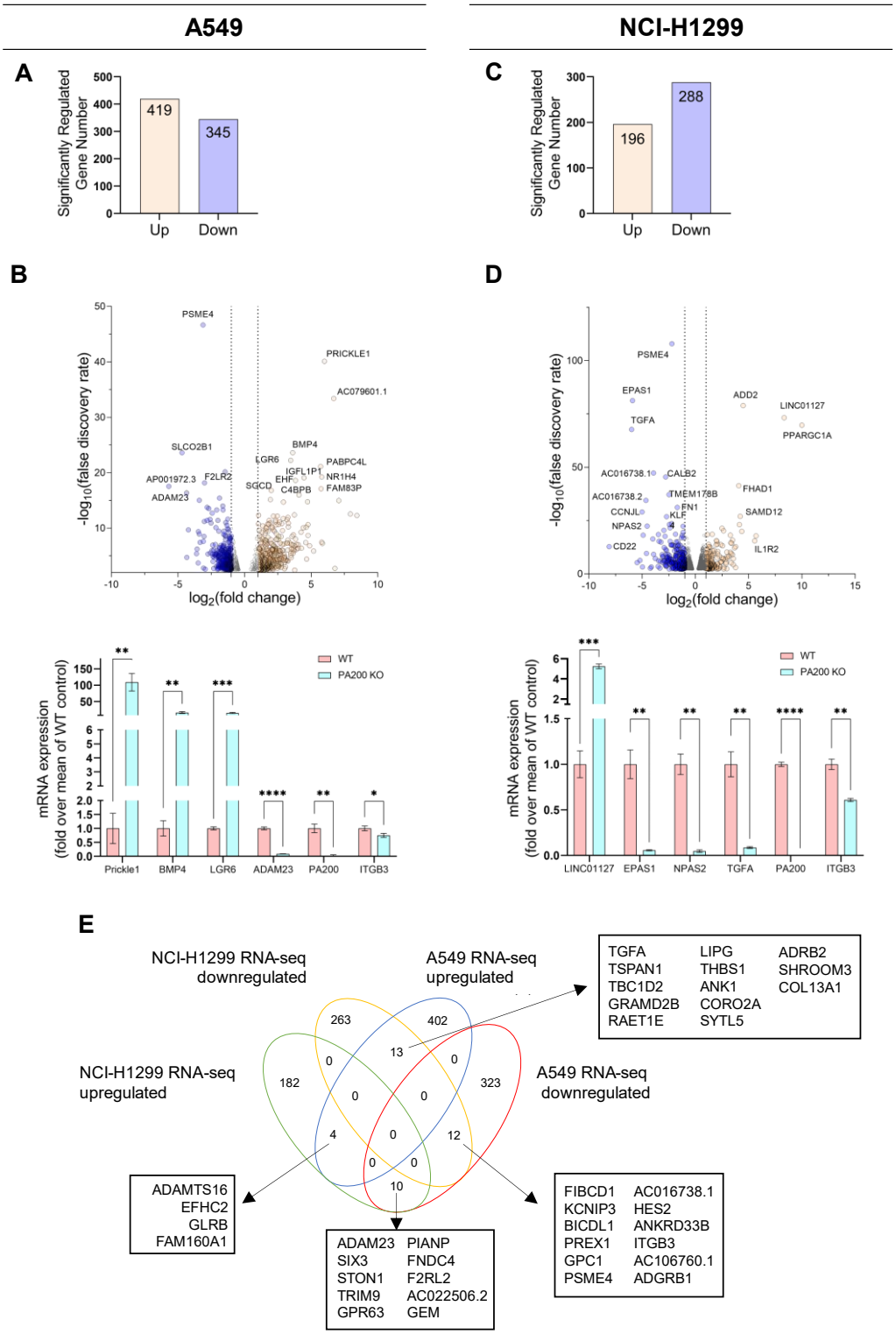

Figure 5.21: RNA-sequencing analysis of PA200 KO in NSCLC cell lines indicates differential regulation of the transcriptome upon PA200 depletion. NSCLC KOs of PA200 were examined for gene regulation by RNA sequencing. The results were filtered, and the **(A, C)** regulated genes **(|FC| ≥ 2, p ≤ 0.05, FDR ≤ 0.05)** were plotted in volcano plots for **(B)** A549 and **(D)** NCI-H1299 cell lines. **(E)** A Venn diagram was used to show the co-regulated and counter-regulated genes. RNA sequencing was performed in the Genomics Core Facility, HMGU. (n=3, selected cell lines, WT and KO)

To understand the roles of the dysregulated genes in the dataset, additional analysis was performed. Molecular signature database (MsigDB), GO Biological Process (GO BP) and GO Molecular Function (GO MF) functions of the Enrichr web tool were used for the analysis. The Reactome database (version 81) was used to analyse the pathways involved. The signatures were analysed separately for the upregulated and downregulated genes for two cell lines (Figure 5.22 and Figure 5.23). The top 10 of each category are shown in the tables unless the category has less.

In A549 PA200 KOs, the upregulated genes mainly contributed to the molecular signatures of epithelial-mesenchymal transition (EMT), KRAS Signalling (up), interferon (α and γ) response, inflammatory response, and IL-6/JAK/STAT3 signalling (Figure 5.22 A, left panel). Downregulated genes were associated with EMT and glycolysis (Figure 5.22 A, right panel). The molecular signatures affected in the NCI-H1299 PA200 KOs differed from the A549 PA200 KOs. The upregulated genes contributed to the molecular signatures of estrogen response (early and late), IL-2/STAT5 signalling, and hedgehog signalling (Figure 5.23 A, left panel). Like the A549 PA200 KO cells, the downregulated genes were enriched in the EMT molecular signature. In addition, inflammatory response, apical junction, and KRAS signalling (down) signatures were also observed in the downregulated gene dataset (Figure 5.23 A, right panel).

Gene ontology analysis for biological processes of upregulated genes was assigned to the glucuronidation processes, positive regulation of cell proliferation, and extracellular structure organization (Figure 5.22 B, left panel). In contrast, downregulated genes were involved in different biological processes such as extracellular structure organization, ion transport, Wnt signalling pathway and extracellular matrix organization (Figure 5.22 B, right panel). In NCI-H1299 PA200 KOs, the upregulated genes were involved mainly in the endodermal cell fate and development, fatty acid oxidation, regulation of the natural killer cell activation, and interferon-gamma production (Figure 5.23 B, left panel), while the downregulated genes grouped under extracellular matrix/structure organization, chemotaxis, cell proliferation and differentiation (Figure 5.23 B, right panel).

Go Molecular Function (GO MF) was analysed for both cell lines to better understand the dysregulated genes' molecular functions. In the A549 PA200 KOs, the upregulated genes allocated to various molecular functions, including retinoic acid, retinoid, and epidermal growth factor receptor binding, whereas the downregulated genes distributed to channel activities, phospholipase C activities, and phosphatase activities (Figure 5.22 C, left and right panel, respectively). In the NCI-H1299 PA200 KOs, the upregulated genes were involved in

DNA and alpha-actinin binding. Contrary to A549, the phospholipase C and phosphatase activities were associated with the upregulated genes in the NCI-H1299 PA200 KOs (Figure 5.23 C, left panel). The downregulated genes in the NCI-H1299 were primarily associated with the platelet-derived growth receptor, protease, growth factor, and receptor binding (Figure 5.23 C, right panel).

The Reactome pathway analysis shared a few common pathways for upregulated and downregulated genes. For instance, the upregulated genes found in the beta-cell regulations and extracellular matrix degradation pathways and the downregulated genes associated with the integrin cell surface interactions and non-integrin membrane-ECM interactions (Figure 5.22 D and Figure 5.23 D). However, most of the top 10 hits differed in both cell lines.

Although the commonly up- and downregulated genes are a small portion in the A549 and NCI-H1299 PA200 KOs, these results suggest that PA200 depletion results in similar dysregulation of biological processes, molecular functions, and pathways. It is important to note that even though there are shared pathways, in one cell line, it comprised upregulated genes, while in the other cell line, it comprised downregulated genes.

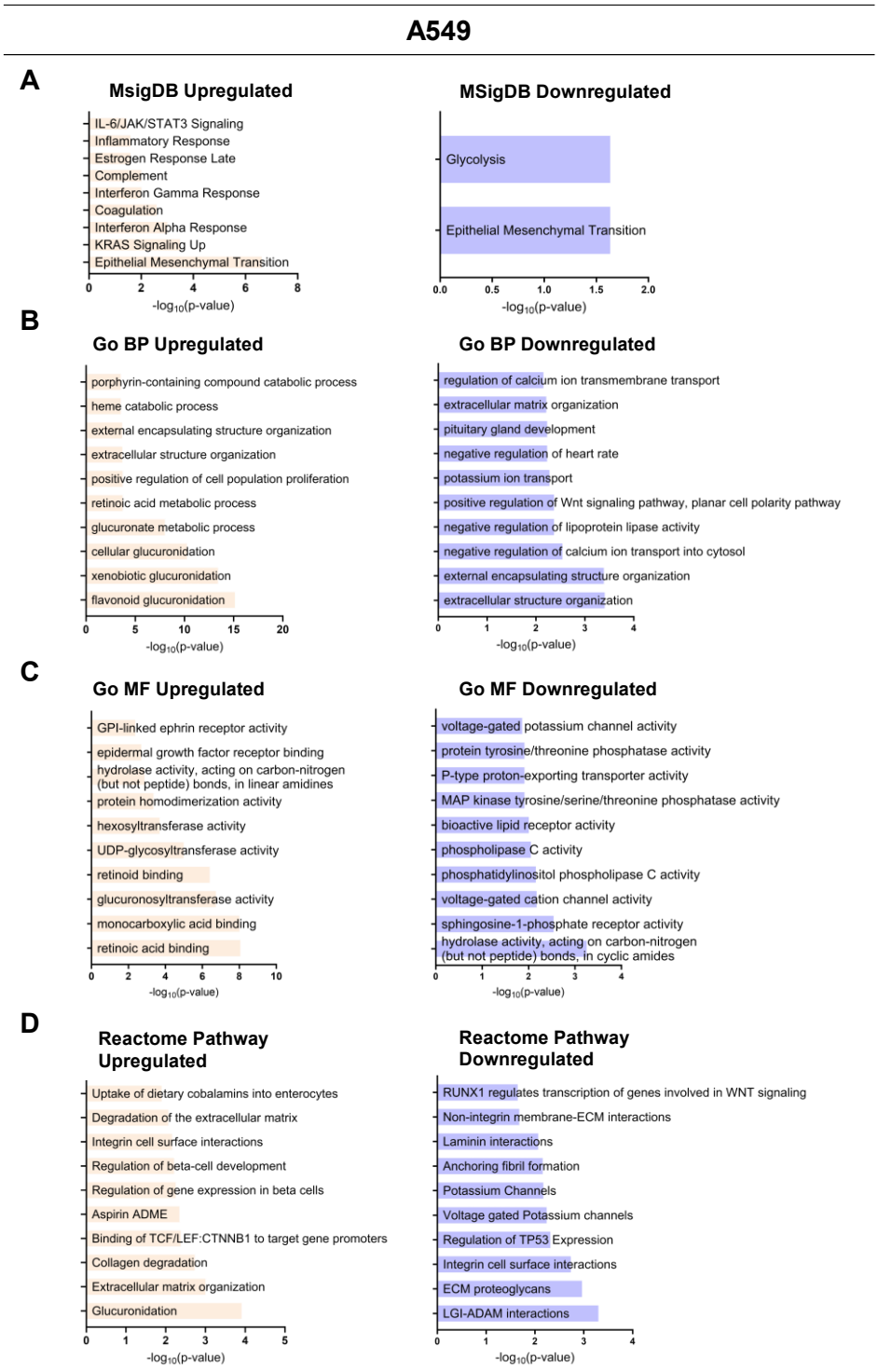

Figure 5.22: PA200 depletion affected multiple biological processes, molecular functions, and pathways in A549 cells. Transcriptome regulation was determined by RNA sequencing of PA200 KO A549 cells. Significantly up- or down-regulated genes were used for further analysis, and only the top 10 results are shown in the graphs **(FC ≥ 2, p ≤ 0.05, FDR ≤ 0.05).** The left panel shows how the upregulated genes affected (yellow) **(A)** molecular signature, the gene ontology (GO) of **(B)** biological process (BP), **(C)** molecular function (MF), and **(D)** Reactome pathways, while the right panel shows the terms associated with downregulated genes (purple).

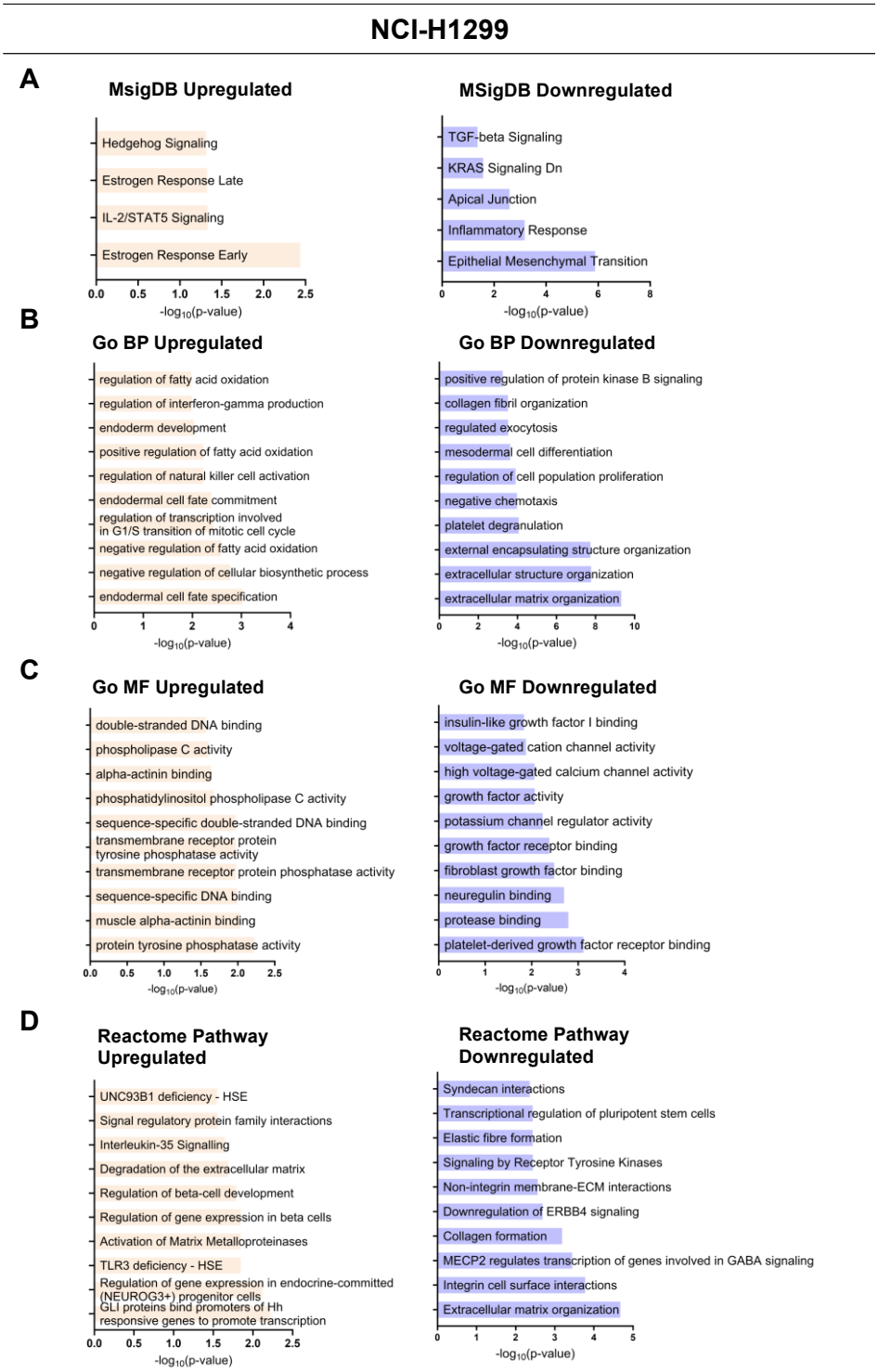

Figure 5.23: PA200 depletion affected multiple biological processes, molecular functions, and pathways in NCI-H1299 cells. Transcriptome regulation was determined by RNA sequencing of PA200 KO NCI-H1299 cells. Significantly up- or down-regulated genes were used for further analysis, and only the top 10 results are shown in the graphs (FC ≥ 2, $p \leq 0.05$, FDR ≤ 0.05). The left panel shows how the upregulated genes affected (yellow) **(A)** molecular signature, the gene ontology (GO) of **(B)** biological process (BP), **(C)** molecular function **(MF)**, and **(D)** Reactome pathways, while the right panel shows the terms associated with downregulated genes (purple).

5.6.2 Non-coding RNAs are a significant part of the regulated RNAs in PA200-depleted cells

In the volcano plot, which shows the most significantly regulated genes, we detected several non-coding RNAs dysregulated in both cell lines upon PA200 depletion (Figure 5.21 B, D). Therefore, the results were further analysed to determine whether there is a comprehensive alteration in the expression of non-coding RNAs. Interestingly, the non-coding RNAs contributed to 32% of the altered transcriptome in A549 PA200 KOs with 124 upregulated and 120 downregulated non-coding RNA genes (Figure 5.24 A, B). Similarly, in NCI-H1299 PA200 KOs, 27% of the RNA dysregulation was related to non-coding RNAs with 57 upregulated and 75 downregulated genes (Figure 5.24 D, E). To visualize the non-coding RNAs in the overall transcriptomic changes, we coloured them in green in the volcano plots (Figure 5.24 C, F). This figure thus demonstrates that the deletion of PA200 results in a concerted and prominent dysregulation of PA200 in both NSCLC cell lines. It is important to note that these genes are also included in the downstream analysis. However, due to less knowledge in this area, they are not found in GO BP, GO MF, Reactome pathways, and molecular signature database.

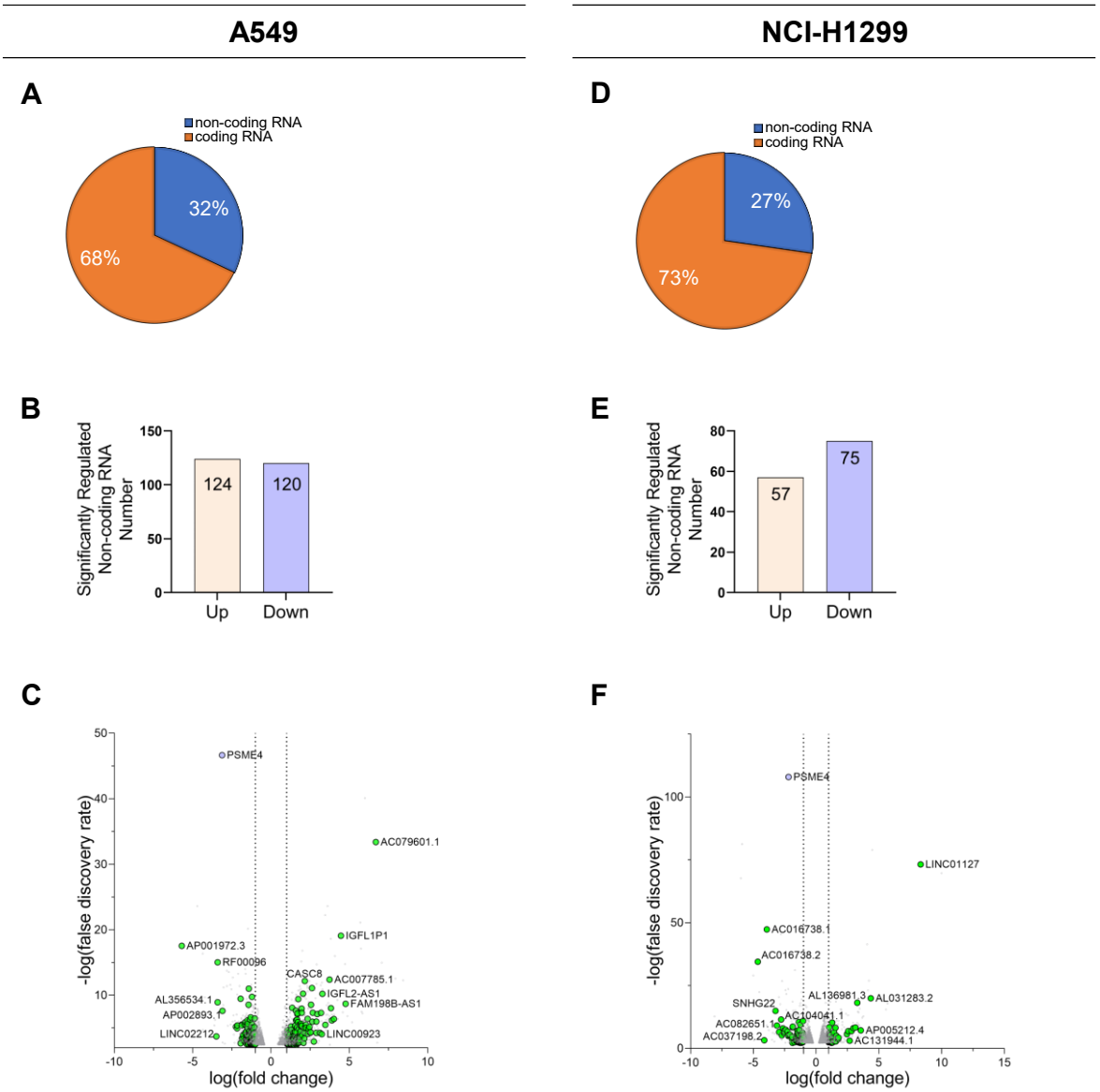

Figure 5.24: The non-coding RNA genes are affected by PA200 depletion. (A, D) The pie chart shows the percentage changes in coding (orange) and non-coding (blue) dysregulated genes. **(B, E)** Bar graphs show how many non-coding RNA genes are up- or down-regulated in the PA200 KOs. **(C, F)** Volcano plots show all the significantly changed non-coding RNA genes (green) ($|FC| \geq 2$, $p \leq 0.05$, $FDR \leq 0.05$, **(A-C)** A549 and **(D-F)** NCI-H1299).

5.7 Differential Interactome of PA200 in the two NSCLC cell lines

5.7.1 Mass Spectrometry reveals proteasome-independent PA200 interactors

The common denominator of PA200 depletion in the two NSCLC cancer cell lines was that the two cell lines responded differently to the genetic deletion of PA200. These cell-specific effects lead us to the assumption that PA200 has differential roles in the two cell lines, which might be revealed by its interactome. To determine the PA200 interactors, PA200 was immunoprecipitated from both WT cell lines and analysed by mass spectrometry. As a control for specific interactions, we used protein lysates from the respective PA200 KO cells. PA200 was specifically precipitated at high intensity, as shown in the volcano plot (Figure 5.25 A, B). Surprisingly, when taking into account all significantly interacting proteins of the three technical replicates of two different NSCLC lines, the interactome lacked proteasome subunits.

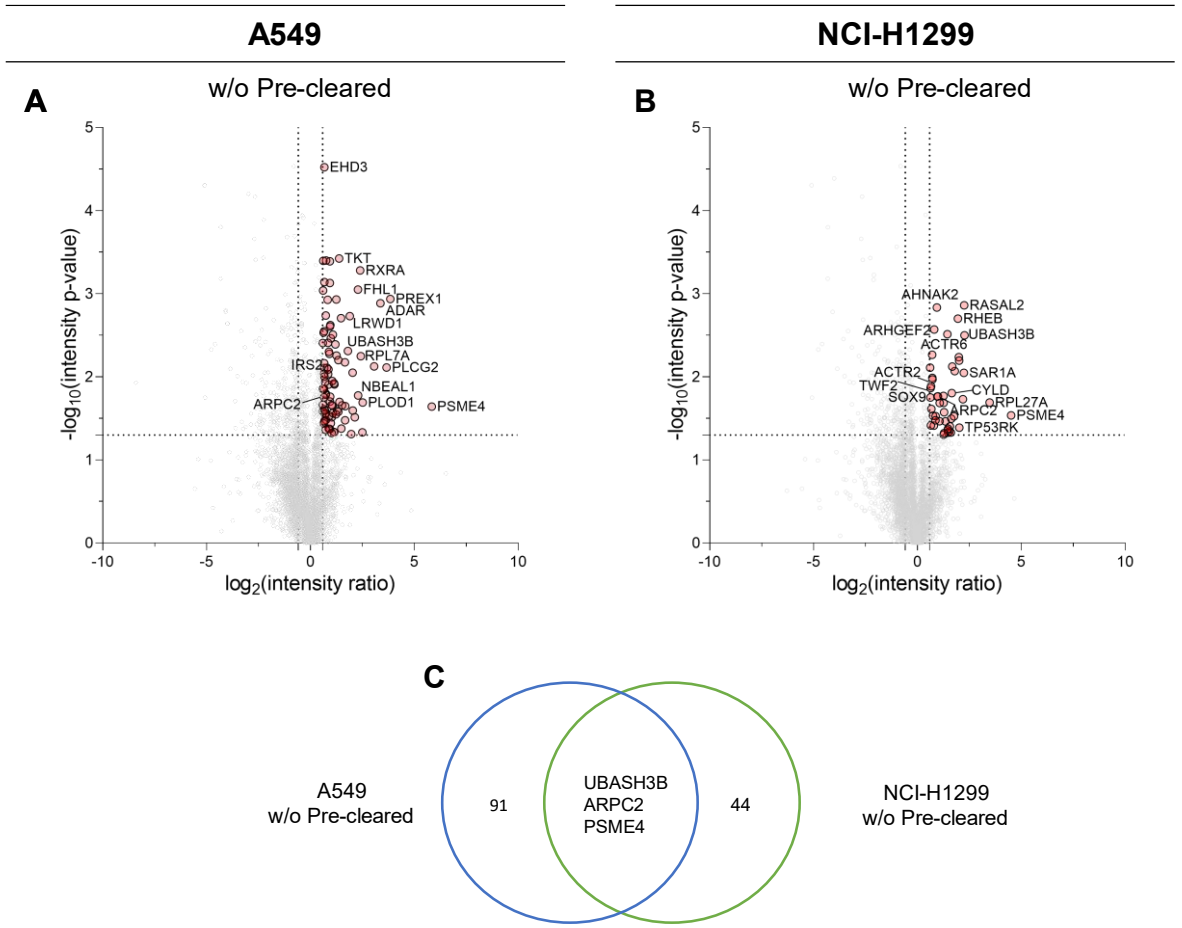

Figure 5.25: PA200 interactors are different in NSCLC cell lines. Interactors of PA200 were captured by PA200 immunoprecipitation and analysed by mass spectrometry. PA200 KO cell lines were used as the control lysates. All significantly enriched interacting proteins of PA200 compared to control lysates for **(A)** A549 and **(B)** NCI-H1299 cells showed light pink circles ($FC \geq 1.5$, $p \leq 0.05$). **(C)** Venn diagram shows the significantly enriched proteins in immunoprecipitation of PA200 (PSME4) in two NSCLC cell lines. LC-MS/MS was performed by Dr J. Merl-Pham, Research Unit Protein Science and Metabolomics and Proteomics Core Facility (HMGU). (n=3, different passages)

The interacting proteins were analysed with Enrichr and Reactome databases to understand the functions and pathways of the PA200 interactors. In the A549 w/o pre-cleared lysates, the interactors of PA200 were mainly related to the E2F and Myc targets (Figure 5.26 A). In addition, reactive oxygen species, ultraviolet (UV) response, glycolysis, and G2-M checkpoint were also found to be enriched (Figure 5.26 A). The Reactome pathway analysis showed that the PA200 interactors were mainly involved in the DNA process (Figure 5.26 B). In accordance with that, the gene ontology (GO) molecular functions (MF) of these interactors were related to the DNA binding processes (Figure 5.26 C) and multiple DNA-related GO biological processes (BP) (Figure 5.26 D).

The PA200 interactors proteins in the NCI-H1299 w/o pre-cleared lysates, however, were related to the molecular signatures of the mitotic spindle, UV response, mTORC1 and PI3K/AKT/mTOR signalling (Figure 5.26 E). Unlike A549 cells, PA200-interactors in NCI-H1299 were found in Reactome pathways such as Rho GTPase signalling and regulation of transcription pathways (Figure 5.26 F). The interacting proteins showed characteristics of DNA binding and methyltransferases, amongst others (Figure 5.26 G). The biological processes of these interactors were related to nucleation, regulation of lamellipodium organization, and canonical Wnt signalling (Figure 5.26 H).

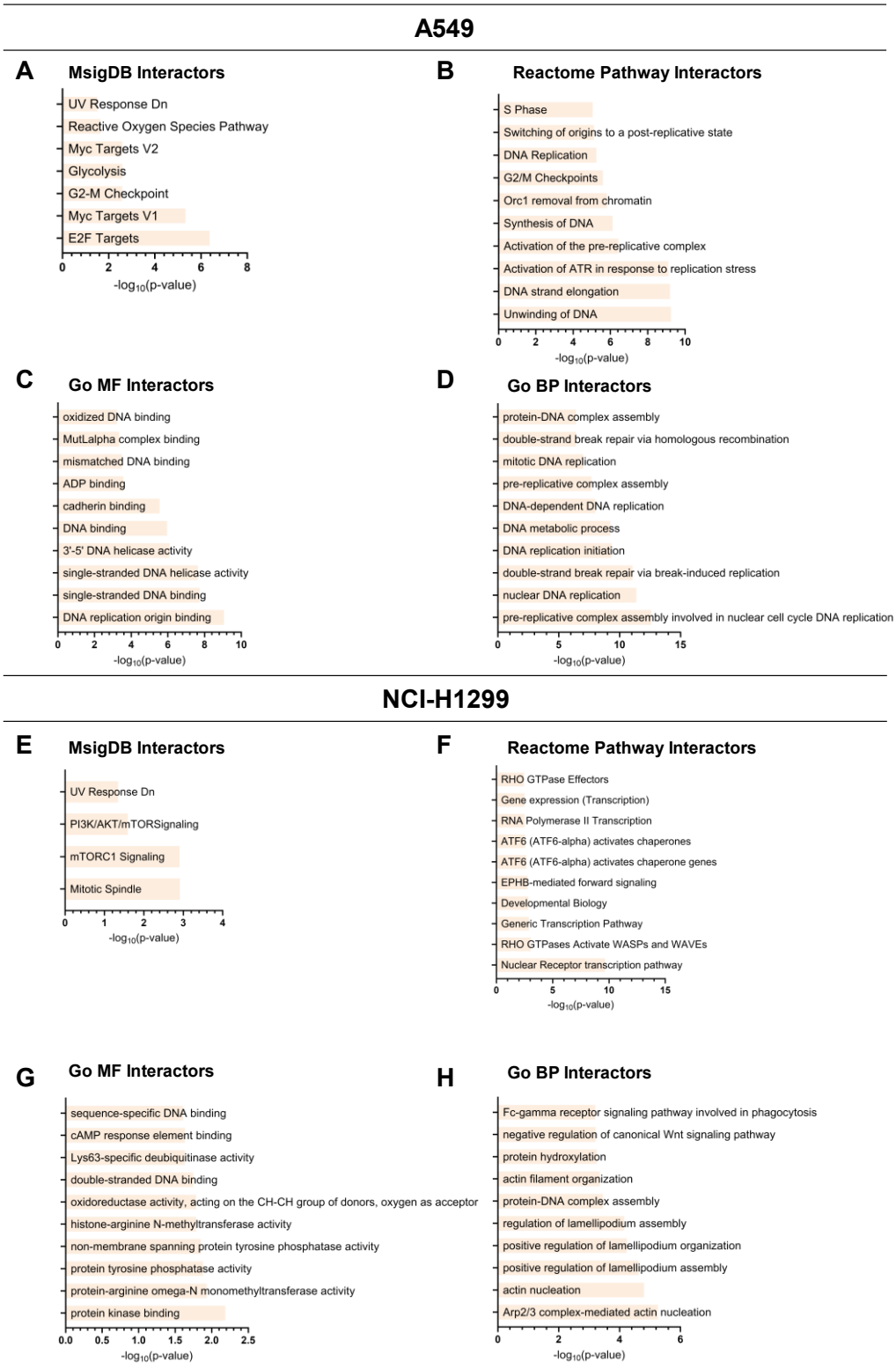

Figure 5.26: Different sets of proteins interact with PA200 in the two NSCLC cell lines. The PA200 interactors in the w7o pre-cleared lysates were analysed with EnrichR and Reactome database (FC ≥ 2, p ≤ 0.05, FDR ≤ 0.05). **(A, E)** The molecular signature (MsigDB), **(B, F)** Reactome pathways, gene ontology (GO), **(C, G)** molecular functions (MF), and **(D, H)** biological processes (BP) of the PA200 interactors were analysed in **(A-D)** w/o pre-cleared A549 lysates and **(E-H)** NCI-H1299 cell lysates.

5.7.2 Pre-cleared lysates have different proteasome-independent PA200 interactors than w/o Pre-cleared lysates

We were surprised by the lack of proteasome-binding proteins in our immunoprecipitation analysis and hypothesized that some of the interactions with PA200 might be due to unspecific bindings. Therefore, to enhance the specificity of our immunoprecipitation analysis and investigate potential unspecific bindings, we performed pre-clearing of lysates by incubating them with protein A-coupled beads at room temperature for 20 minutes. The pre-cleared lysates were then separated from the beads using a magnetic rack and subsequently incubated with the protein A-antibody complex. Following washing with TSDG buffer + 0.2% IPEGAL, the bead-antibody-PA200-interactor complexes were washed with TSDG alone to reduce detergent levels. Elution of interacting proteins was achieved by denaturing the fractions with Laemmli buffer for 10 minutes at 95°C using a magnetic bead rack. The resulting fractions containing PA200 and its interactors were then subjected to mass spectrometry analysis in both cell lines. The PA200 KO cell lysates did not have PA200 peptides, while the WT lysates had enriched LFQ intensity ratios of PA200 compared to w/o pre-cleared lysates (approximately 15-fold in A549 and 3.5-fold in NCI-H1299) confirming the specificity of immunoprecipitation of PA200 proteins. However, we were surprised to find that the interactome of PA200, even after pre-clearing, did not include peptides from the core 20S proteasome subunits, similar to the non-precleared lysates (Figure 5.27 A, B).

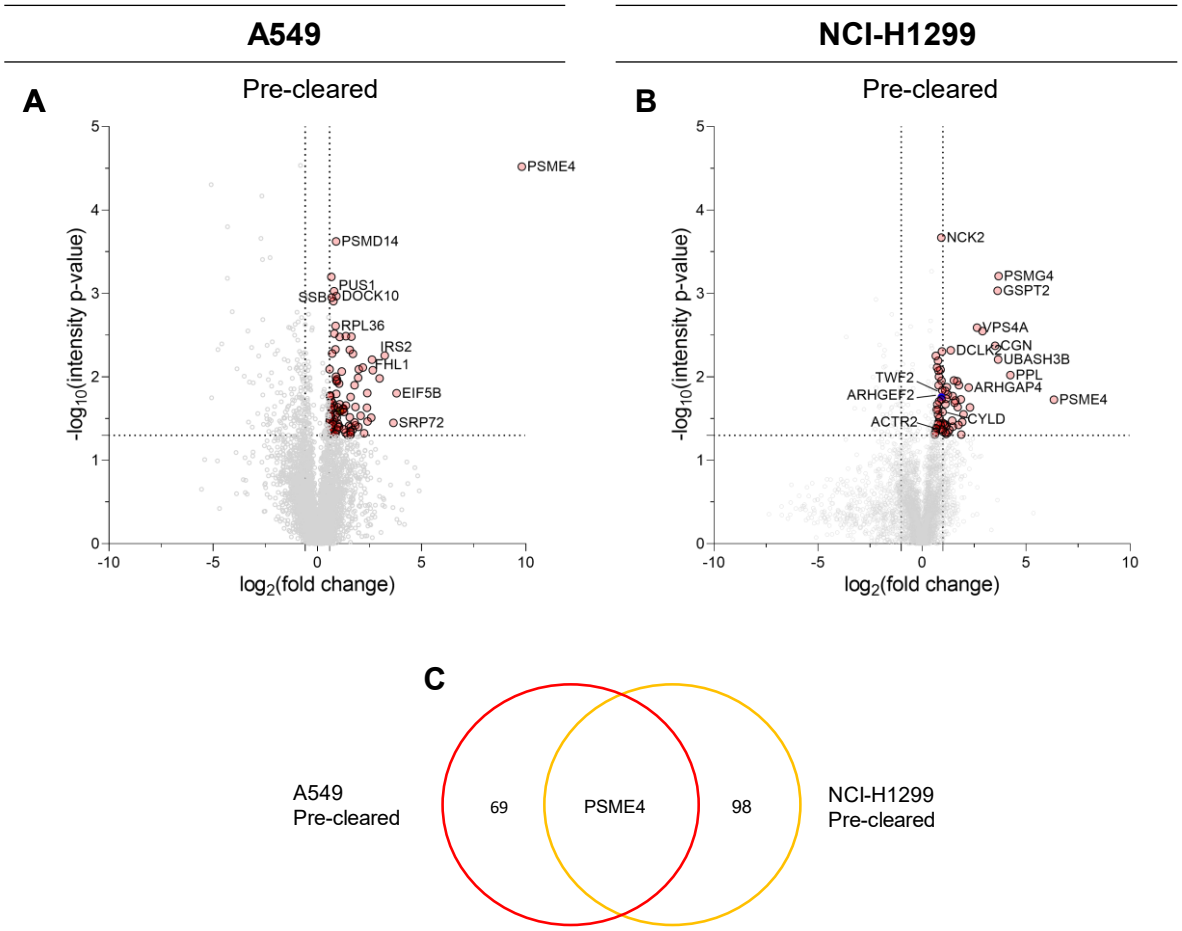

Figure 5.27: PA200 interactors are different in pre-cleared NSCLC cell lysates. Interactors of PA200 were captured by PA200 immunoprecipitation of pre-cleared protein lysates and analysed by mass spectrometry. PA200 KO cell lines were used as the control lysates. All significantly enriched interacting proteins of PA200 compared to control lysates for **(A)** A549 and **(B)** NCI-H1299 cells ($FC \geq 1.5$, $p \leq 0.05$) showed in light pink circles. **(C)** Venn diagram shows the significantly enriched proteins in immunoprecipitation of PA200 (PSME4) in A549 and NCI-H1299. LC-MS/MS was performed by Dr J. Merl-Pham, Research Unit Protein Science and Metabolomics and Proteomics Core Facility (HMGU). (n=3, different passages)

We performed a similar GO and pathway analysis for the PA200 interacting proteins in the two cell lines as above. In the A549 pre-cleared lysates, the interactors of PA200 were mainly related to the molecular signatures of Myc targets, hypoxia, G2-M checkpoint, and adipogenesis (Figure 5.28 A). The Reactome pathway analysis showed that the PA200 interactors were involved in the translation initiation processes, the 40S/60S ribosomal subunits formations, and the nonsense-mediated decay (NMD) process (Figure 5.28 B). The molecular functions of these interactors are related to the RNA binding process and multiple RNA-related biological processes (Figure 5.28 B). In contrast, the PA200 interactors proteins in the NCI-H1299 pre-cleared lysates were enriched in molecular signatures of the mitotic spindle, heme

metabolism, and mTORC1 and hedgehog signalling (Figure 5.28 E). The only common signature between A549 and NCI-H1299 PA200-interactome was the G2-M checkpoint. The Reactome pathway analysis revealed that PA200-interactors in NCI-H1299 were involved in pathways related to Rho GTPase signalling, cellular responses, and mRNA stability (Figure 5.28 F). On the other hand, similar to A549, the interactors were involved in NMD processes. In addition to RNA binding, the interactors also participate in the binding of the microtubule, tubulin, protein kinase C, cadherin, and phosphatase (Figure 5.28 G). The biological processes of these interactors were related to depolymerization, assemblies, and signal transduction (Figure 5.28 H).

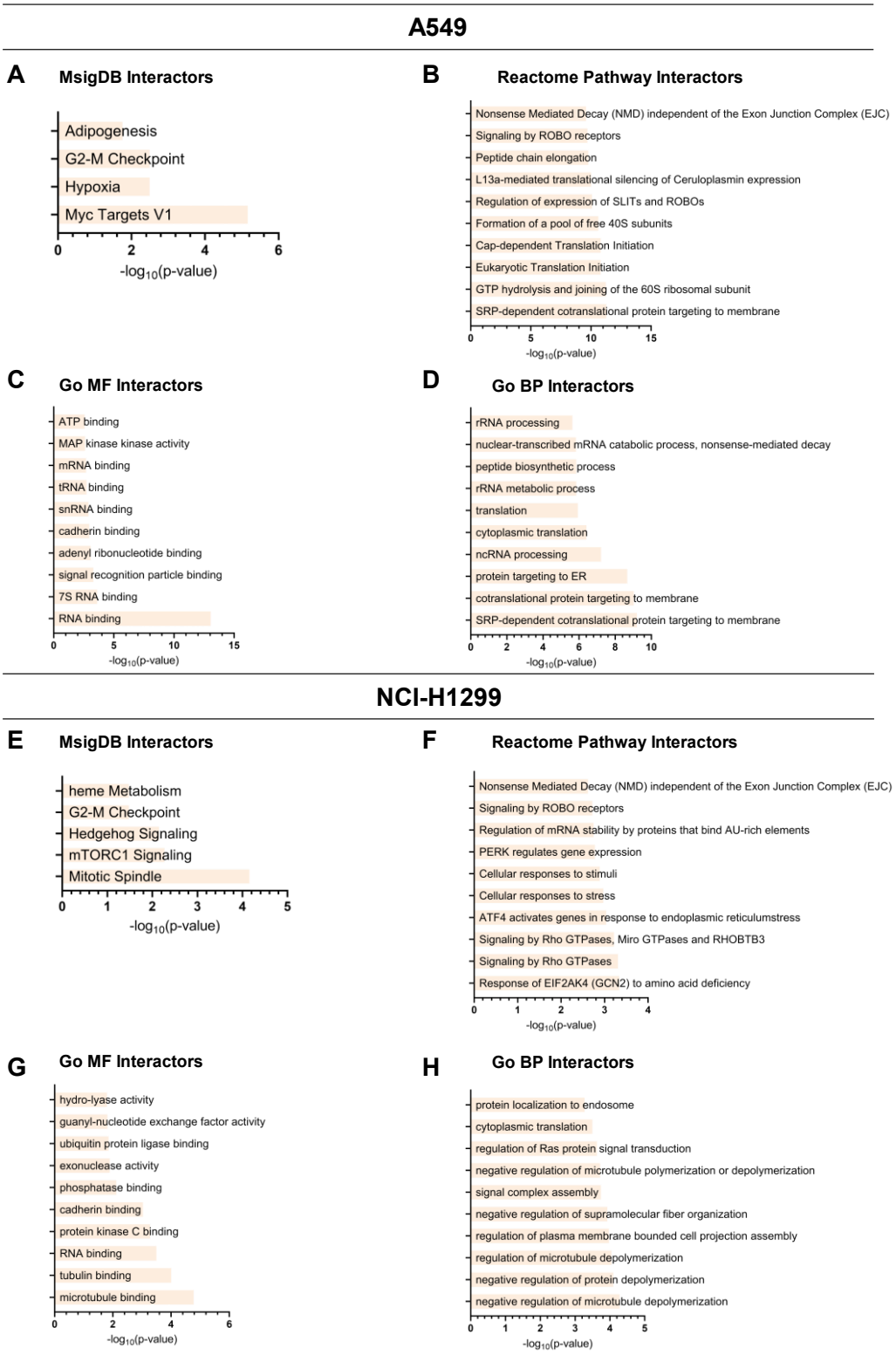

Figure 5.28: The PA200 interactors from the pre-cleared lysates of NSCLC cell lines exhibited distinct molecular signatures. EnrichR and the Reactome database were employed to identify the functions of these interactors. **(**FC ≥ 2, p ≤ 0.05, FDR ≤ 0.05)**. (A, E)** The molecular signature (MsigDB), **(B, F)** Reactome pathways, gene ontology (GO), **(C, G)** molecular functions **(MF)**, and **(D, H)** biological processes (BP) of the PA200 interactors were analysed in **(A-D)** w/o pre-cleared A549 lysates and **(E-H)** NCI-H1299 cell lysates.

5.7.3 Pre-clearing of the protein lysates alters the interactome of PA200

The interactome data analysis showed apparent differences between the PA200 interactors of A549 and NCI-H1299 cell lysates that depended on the pre-clearing of the lysates, as shown by a Venn diagram (Figure 5.29 A). A549 lysates shared only 7 interactors, while NCI-H1299 lysates shared five interactors (excluding PA200). While no proteins were common to each group (except PA200 or PSME4), UBASH3B protein co-immunoprecipitated with three groups of protein (Figure 5.29 A). To understand the lack of proteasome subunits as PA200 interacting proteins, we blotted the eluted proteins from our different conditions for α1-7 to detect proteasome subunits (Figure 5.29 B). We noted strong and similar enrichment of PA200 in our immunoprecipitation experiments using the WT A549 and NCI-H1299 cells which were absent in the respective KO cells, confirming the specificity of the pulldown. Of note, we detected alpha subunits of the proteasome in both WT and KO pulldowns, indicating that the anti-PA200 antibody non-specifically binds to the proteasome under our experimental conditions. In pre-cleared lysates, this interaction was clearly reduced (Figure 5.29 B). These data indicate that our rather non-stringent conditions of PA200 pulldown, which were designed to stabilize the interaction with the proteasome, resulted in unspecific binding to the antibody in PA200-depleted cells. As we compared the enrichment of interacting proteins compared to KO controls, we sort of “lost” our proteasome subunits as interacting proteins. Our data thus reveal two main points: 1. The interaction of PA200 with the proteasome is not very strong in the NSCLC cancer cell lines, and 2. The detected interacting proteins bind PA200 in a proteasome-independent manner. Overall, these results indicate a possible presence and function of proteasome-free PA200 in the cells, which might interact with various proteins depending on the cellular context.

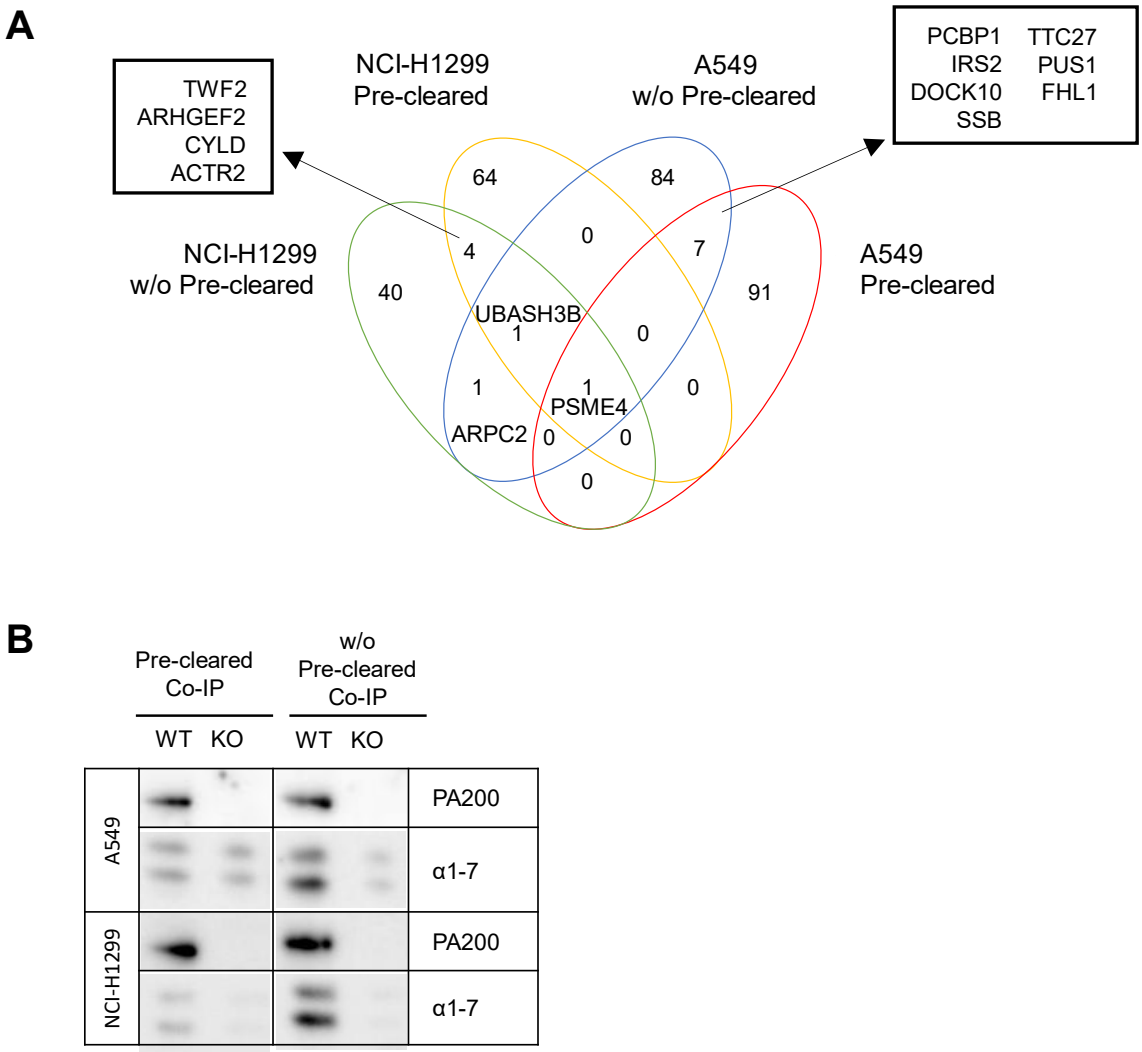

Figure 5.29: Immunoprecipitation of PA200 from pre-cleared or w/o pre-cleared cell lysates reveals distinct interactors. (A) A Venn diagram was generated with the list of PA200 interactors in A549 and NCI-H1299 cells generated from the pre-cleared or w/o pre-cleared lysate. **(B)** Western blot analysis of the PA200 immunoprecipitation with A549 and NCI-H1299 cell lysates, with α1-7 and PA200 antibodies. (n=1, different cell lines)

5.8 Proteasome-independent PA200 in the cell

To test the hypothesis of free non-proteasome bound PA200 in the cell, we ran our non-pre-cleared lysates on a native gel, cut it into six horizontal stripes for each sample and analysed the fractions by mass spectrometry (Figure 1.30 A). The results showed that the first three fractions contain most of the proteasome subunits, while most of the subunits are not present in fractions 4-6. Furthermore, PA200 (PSME4) was detected in all fractions in WT cells, whereas no PA200 peptide was found in the KO cells, confirming the specificity of the experiment. According to the LC-MS/MS results, PA200 is mainly found in fractions 2 and 3, which roughly corresponds to the 26S and 20S complexes. Interestingly, PA200 was also found in the fractions where no other core proteasome was present (Figure 5.30 B). Next, we tested if PA200 is also present in insoluble cellular compartments. Therefore, cells were lysed under mild native lysis conditions with TSDG buffer, and the insoluble pellet was further lysed under strong denaturing conditions using urea. Upon Western blotting, we observed that most of the cellular PA200 could be detected in the soluble fraction of the cell but that a small proportion of PA200 was found in the insoluble fraction (Figure 5.30 B). These results thus strongly suggest the presence of a subfraction of PA200, which can interact with DNA and RNA-binding proteins and become insoluble.

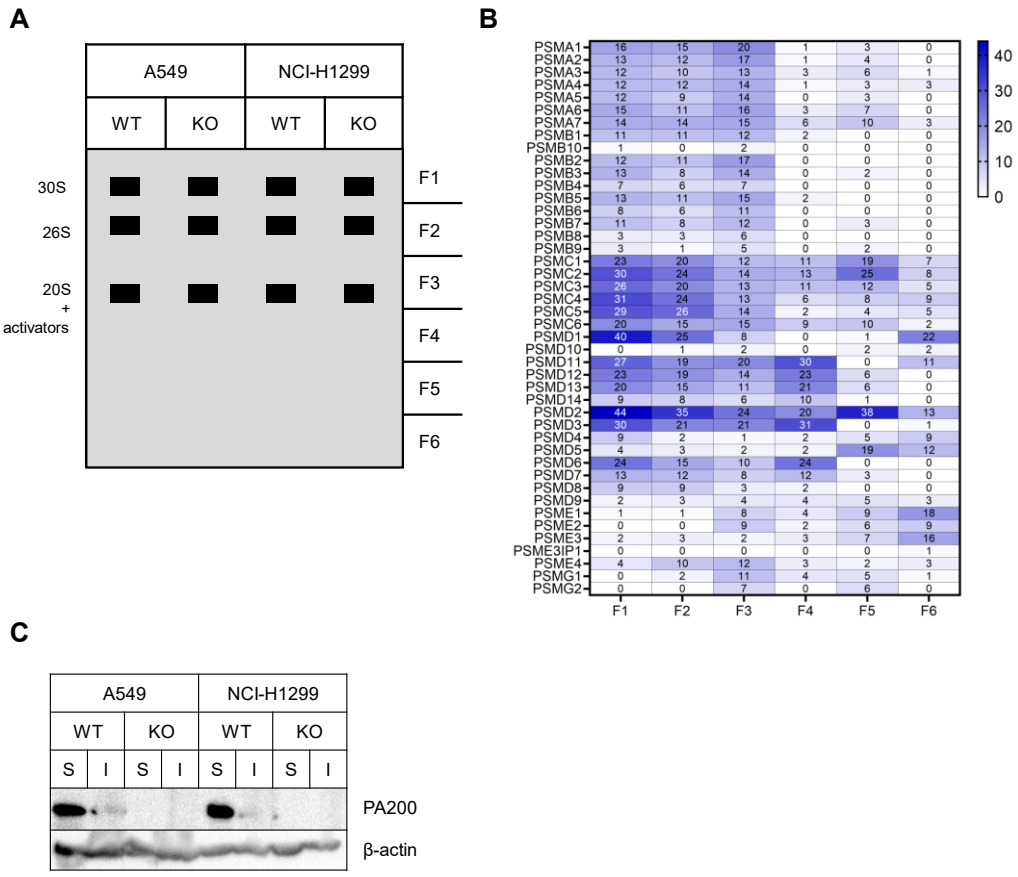

Figure 5.30: PA200 is found without complexing to catalytically active proteasomes in both NSCLC cell lines. The TSDG of the w/o pre-cleared lysates were run on a native gel cut into six different fractions and analysed with LC-MS/MS (performed by Dr J. Merl-Pham, Research Unit Protein Science and Metabolomics and Proteomics Core Facility, HMGU). **(A)** The figure illustrates the fractions of each sample. **(B)** Fractions analysed for proteasome subunit peptides. The numbers indicate the unique peptides found in each fraction. **(C)** Western blot of TSDG (S, soluble) and urea lysates (I, insoluble) of TSDG lysed pellets.

6 Discussion

Since PA200 has been identified as a proteasome activator, the focus was to understand its function (Ustrell et al., 2002). Recent advances in genomics, proteomics and structural biology have paved the way to identify new roles of PA200, as discussed in the recent review (Yazgili et al., 2022). In this study, the function of PA200 in NSCLC was studied *in vitro* and *in vivo*. PA200 was found to have different functional roles in two distinct NSCLC cell lines. These include metabolic adaptation, invasion and migration, immunoproteasome regulation, and tumour cell growth. Additionally, a significant amount of non-coding RNAs (ncRNAs) were detected to be dysregulated upon PA200 knock-out. Interestingly, interactome analysis revealed novel PA200 interactors in NSCLC and suggested a potential proteasome-free PA200 fraction in the cell. The data of this thesis indicate that PA200 plays a distinct oncogenic role in tumour cell growth, differentiation, migration and in the regulation of interferon responses which strongly depends on the cellular context. We were, however, unable to mechanistically delineate the activity of PA200 in NSCLC cell lines.

6.1 PA200 regulates NSCLC in a cell context-dependent manner

The regulation of PA200 in a disease context was initially discovered in a previous study conducted by our group (Welk, 2018; Welk et al., 2019). Notably, elevated PA200 protein levels were observed in the fibrotic lungs of patients with idiopathic pulmonary fibrosis (Welk et al., 2019). Further investigations revealed that PA200 functions as a negative regulator of myofibroblast development in human cells but not in mouse cells, as demonstrated through transient silencing and overexpression experiments. Subsequently, increased levels of PA200 protein were detected in the tumour tissues of lung cancer patients compared to their healthy lung tissues (Welk, 2018). However, the role of PA200 was not analysed in detail.

To elucidate the functional role of PA200 in non-small cell lung cancer (NSCLC), PA200 knock-out cell lines were generated using CRISPR/Cas9 technology. A549 and NCI-H1299 cell lines were selected as numerous studies have used these cell lines successfully before to study hallmarks of cancer. With the use of two distinct NSCLC cell lines as biological replicates, we aimed to elucidate a conserved function of PA200 in NSCLC (Lu et al., 2018; Prasad et al., 2022; Sun et al., 2018).

Although the two cell lines are commonly used as biological replicates to study NSCLC, several studies also reported differential responses with regard to other proteins (Li et al., 2017; Shankar et al., 2015; Ugrinova & Pasheva, 2017; Xu et al., 2014). One of the key differences between the two NSCLC cell lines is that A549 has a K-Ras (oncogene) mutation, while NCI-H1299 contains p53 (tumour suppressor) deletion. Downstream Ras proteins target mainly cell-cycle progression, survival, and transcription, while p53 targets senescence, apoptosis and DNA repair (Downward, 2003; Vousden & Prives, 2009). Furthermore, while A549 was isolated from the primary site of the tumour, the NCI-H1299 cell line is derived from a metastatic site. Primary tumour cells and metastatic tumour cells may have various genetic and epigenetic changes, which might affect their behaviour and response to treatment (Vanharanta & Massagué, 2013). Metastatic cells, for example, may have additional alterations that improve their propensity to invade and migrate to other organs and escape from immunosurveillance. Therefore, it is important to keep the key differences (Table 6.1) between the two cell lines in mind for further discussion.

Table 6.1: Key differences between the two NSCLC cell lines

	A549 (Cellosaurus, 2012a)	**NCI-H1299** (Cellosaurus, 2012b)
Disease	Lung adenocarcinoma	Lung large cell carcinoma
Derived from	Primary site	Metastatic site (Lymph node)
Variations	KRAS and STK11 mutation	TP53 deletion, NRAS mutation
Characteristics (Li et al., 2017)	Non-invasive	Invasive
Phenotype	Epithelial (Sundararajan et al., 2014)	Mesenchymal (Tripathi et al., 2016)

To our surprise, these two NSCLC cell lines responded very differently to PA200 depletion on their transcriptome level and functionally, as determined in multiple biological assays. As our Western blots revealed higher baseline expression of PA200 in NCI-H1299 WT cells, its deletion might have a greater impact on the cellular processes in this cell line. Our data thus suggest a cell context-dependent effect of PA200.

6.1.1 PA200 depletion differentially regulates proteasome activity and composition in two NSCLC cell lines

Knowing that PA200 is a proteasome activator, we first analysed whether PA200 depletion results in the inhibition of the catalytical activities of the proteasome. Surprisingly, total CT-L and C-L activities decreased in A549 but increased in NCI-H1299 cell lines upon PA200 knock-out. When the CT-L activities for each proteasome complex were analysed (20S+activators, 26S, and 30S) using native gel analysis, the results showed an increase in the activities of 20S+activators in A549 KOs while the activity of these complexes was decreased in NCI-H1299 KOs. The difference between the two results might result from the two different methods applied: The first method identifies the changes in the total proteasome activity in cell extracts, whereas the latter identifies the changes in the different proteasome complexes in a native gel analysis. The total proteasome activity assay does not show the activity levels of each proteasome complex but rather shows overall activity change. Therefore, these results might indicate that the activity of the 30S contributes to a larger extent to the overall CT-L activity in the extracts compared to the 20S+activators.

Additionally, when we analysed the in vitro effects of recombinant PA200 added to purified constitutive 20S proteasomes, we did not observe any significant change in the activities of all three active sites using a chemiluminescence activity assay. These data are thus in contrast to the original description of PA200 as a proteasome activator. The first report on PA200 showed an increase primarily in the C-L activity of PA200-20S complexes isolated from bovine testes (Ustrell et al., 2002). A later study reported an increased C-L activity that related to cellular PA200 expression (Blickwedehl et al., 2008). In contrast to these earlier results, Toste Rego et al. showed that the T-L active site was activated in an in vitro reconstituted PA200/20S complex while the C-L and CT-L activities decreased (Toste Rego & da Fonseca, 2019). Another recent paper from Guan et al. found 3-4-fold increased CT-L activity using purified human 20S and recombinant human PA200 (Guan et al., 2020). The recent study revealed activation of the C-L and suppression of the T-L activities when recombinant human PA200 was added to cell extracts (Javitt et al., 2023). Lastly, Zivkovic et al. found increased CT-L, T-L and C-L activities when recombinant human PA200 was added to bovine proteasomes, 50% of them spermatoproteasome (Zivkovic et al., 2022). Our activity assay results with purified proteasomes have added further diversity to the published activity results, suggesting that the differences in proteasome activation capacity of PA200 may stem from experimental variations. Factors such as the origin of PA200 or c20S/i20S, different substrates and detection

methods employed, as well as differences in incubation time and temperature could contribute to these discrepancies. For instance, in a comparative analysis of human c20S activity with recombinant human PA200, we observed that the use of chemiluminescent substrates failed to detect early kinetic activity changes induced by PA200 addition. It is important to note that these differences were reported across multiple independent labs, highlighting the diverse actions of PA200 under various cellular conditions.

A recent study also proposed that PA200 regulated the function of the immunoproteasome by reducing its activity in lung cancer (Javitt et al., 2023). Therefore, we further extended our analysis of PA200-depleted cells to the composition of the active site of proteasome complexes. Both precursor and mature LMP2 levels were decreased in both KO cell lines at baseline, while the mature MECL-1 protein levels were decreased significantly only in NCI-H1299 PA200 KOs. The incorporation of immunoproteasome subunits revealed an elevated assembly of immunoproteasomes in A549 KOs but diminished assembly in NCI-H1299 at baseline. Interestingly, when treated with IFN-β or IFN-γ for 24 hours, no major changes were observed with regard to induced immunoproteasome expression and activity in both cell lines. Yet, MECL-1 incorporation was higher in IFN-β treated A549 PA200 KOs, according to the ABP results. Interestingly, our native gel results showed that only MECL-1 was found within the 30S complexes after interferon treatments but mainly in the WT cells.

Cells that express both the immunoproteasome and constitutive proteasome subunit genes may create a hybrid proteasome that combines the two as intermediate proteasomes (Cascio et al., 2002; Kopp et al., 2001; Wang et al., 2020). An intermediate proteasome was discovered to be made up of only one (LMP7) subunit or two (LMP7 and LMP2) subunits added in place of the constitutive subunits. However, our data suggest that in NSCLC cell lines, MECL-1 can be present in the 30S proteasome complexes without the presence of LMP7 and LMP2. Our A549 cell line results are in line with Javitt et al., showing that when PA200 is low, then the immunoproteasomes are active. However, in NCI-H1299 cell lines, our results show the opposite. This might indicate that the absence of PA200 affects the cells depending on their cellular context. This difference might come from the different epithelial/mesenchymal status of the two cell lines. Furthermore, as NCI-H1299 cell lines are isolated from the metastatic site, whereas A549 was isolated from the primary cell line, the basal immune regulation might differ between the two cells. This notion is supported by our finding that PA200 recruitment to 20S complexes increased with IFN-γ in A549 WT cells while it was decreased in NCI-H1299 WT cells, indicating a differential response to type II interferon between the two cell lines.

6.1.2 PA200 regulates several hallmarks of cancer

Owing to increased PA200 protein levels in the cancerous tissues of NSCLC patients, we hypothesized a potential regulatory function of PA200 as an oncogenic regulator and investigated its activity in the regulation of several hallmarks of cancer. Based on previous studies both on PA200 and other proteasome activators, we hypothesized PA200 might be involved in metabolism, invasion, EMT, tumour growth and immunosurveillance and thus focused our analysis on these hallmarks of cancer (Blickwedehl et al., 2008; Blickwedehl et al., 2012; Javitt et al., 2021; Javitt et al., 2023; Tong et al., 2020)

6.1.2.1 PA200 differentially regulates NSCLC cell metabolism

Firstly, proliferation and metabolism were studied. Although the MTT assay is frequently used as a proliferation assay, it rather assays mitochondrial activity. Therefore, MTT assays should not be regarded as a direct indicator of cell proliferation. For this reason, we measured the doubling time of the cells as a proliferation rate indicator and used an MTT assay to assess metabolic activity. Our results showed that PA200 differentially regulates proliferation and metabolism depending on the cellular context. While the proliferation rate was decreased in A549 PA200 KOs, their metabolic activity was higher under several conditions. Of note, the opposite was observed for NCI-H1299 cells.

In a previous study conducted on the HeLa cell line, it was observed that the knockdown of PA200 led to heightened sensitivity to glutamine (Blickwedehl et al., 2012). Glutamine plays a crucial role as a precursor for the synthesis of various amino acids, proteins, nucleotides, and other biologically important molecules. Additionally, glutamine is involved in the generation of NADPH (nicotinamide adenine dinucleotide phosphate) and GSH (glutathione), which are essential components for maintaining a balanced redox environment (Mohamed et al., 2014). Therefore, glutamine plays an important role in cell development, proliferation and metabolic homeostasis (Lian Chen & Hengmin Cui, 2015). Accordingly, limiting glutamine supply and inhibiting its metabolism has been shown to reduce the proliferation of cancer cells, whereas depending on the type of cell, glutamine supplementation can either stimulate or inhibit cell death (Fuchs & Bode, 2006). Numerous pathways, including Ras and p53, play a significant role in the regulation of glutamine metabolism in malignancies. This modulation contributes to carcinogenesis and maintains the growth of cancer. When Ras is activated, glutamine has been found to be the main carbon source for the TCA cycle (Ying et al., 2012). When K-Ras and Akt pathways are activated in transformed cells, it results in the synthesis of around 60% of

the total FADH2 and NADH2 molecules from glutamine, whereas only about 30% of these molecules are generated from glucose. (Fan et al., 2013). Similarly, in cells with K-Ras mutations, there is an increase in the rate of oxygen consumption and ATP generation when exposed to glutamine. This enhanced utilization of glutamine contributes to the development of tumours (Weinberg et al., 2010). K-Ras renders cells more sensitive to glutamine deprivation. When K-Ras expression is reduced, cells are rescued from apoptosis triggered by low levels of glutamine (Gwinn et al., 2018). In addition, glutamine deprivation can cause K-Ras-transformed cells to stop proliferating (Gaglio et al., 2009). On the other hand, glutamine metabolism is regulated by p53 in a number of ways. For instance, p53 inhibits carcinogenesis by increasing GSH levels upon upregulation of GLS2 and decreasing ROS levels (Hu et al., 2010; Suzuki et al., 2010). A crucial part of the cysteine/glutamate antiporter, which mediates the conversion of extracellular cysteine to intracellular glutamate and is overexpressed in a number of human malignancies, has been reported to be suppressed by p53 (Jiang et al., 2015; Lo et al., 2008). Additionally, p53 can block the PI3K-AKT-mTOR and GLUT1-GLUT4 and suppress the GLUT1 and GLUT4 glucose transporter genes. These p53-related activities suppress cell proliferation, which in turn reverses the cancer phenotype (Levine & Puzio-Kuter, 2010).

We here observed that PA200 regulated the L-glutamine sensitivity of NSCLC cancer cells depending on the cellular context. Under normal supply conditions (10% FBS, +L-glutamine), A549 PA200 KOs showed higher metabolic activity compared to their respective WT controls, while in NCI-H1299 PA200 KOs, it was reduced. When either the L-glutamine or FBS supply was reduced, PA200-depleted A549 cells showed less sensitivity. Interestingly, according to our transcriptome data, several glycolysis-related genes were downregulated upon PA200 depletion in A549 cells according to the MsigDB. Speculatively, a decrease in the glycolysis pathway but an increase in the NADPH-driven metabolic activity assay might indicate that oxidative phosphorylation is favoured upon PA200 deletion in A549. NCI-H1299 PA200 KO cells, however, were sensitised to L-glutamine or FBS deficiency. Again, these differences might be coming from the different p53 and Kras mutational status of these cells as well as from their origins and to identify the mechanisms behind them, further studies are needed.

6.1.2.2 PA200 regulates tumour cell invasion *in vitro* and *in vivo*

The invasion and epithelial-to-mesenchymal transition (EMT) capacity were studied as they are critical in cancer biology and reflect the metastatic properties (Mittal, 2018). Here, the

absence of PA200 decreased the invasiveness of both A549 and NCI-H1299 cells, yet this effect was observed mainly in the more invasive NCI-H1299 cells (Li et al., 2017). Because of the changes in the invasiveness, we analysed if PA200 regulates the epithelial/mesenchymal differentiation state of the cells, e.g., epithelial or mesenchymal. On the protein level, both E-cadherin and N-cadherin levels were increased, while ITGB3 levels decreased upon PA200 knockout in both cell lines at baseline. Considering the role of E-cadherin and N-cadherin as EMT regulator, we hypothesised that in the absence of PA200 EMT could be altered. Therefore, we treated cells with TGFβ which induces EMT in the cancer cells (Hao et al., 2019). However, our results did not show major differences in EMT marker gene expression upon TGFβ treatment. Yet, while TGFβ increased ITGB3 protein levels both in A549 WT and KOs, it failed to increase it in the NCI-H1299PA200 KOs. Of note, while ZEB2 transcription increased in the A549 it was decreased in NCI-H1299 KOs.

ITGB3, a prognostic marker associated with poor survival, is observed to be upregulated in various cancers, including non-small cell lung cancer (Cosset et al., 2017; Gruber et al., 2005; Hosotani et al., 2002; Kong et al., 2017; Noh et al., 2018; Taherian et al., 2011). Its expression increases during EMT, promoting metastasis in breast cancer cells, while its silencing prevents metastasis and EMT (Galliher & Schiemann, 2006; Mamuya & Duncan, 2012; Parvani et al., 2015). Moreover, increased ITGB3 expression in tumour cells correlates with tumour-initiating cell characteristics and confers resistance against EGFR inhibition by forming a complex with KRAS and RalB, leading to the activation of TBK1 and NF-κB (Lo et al., 2012; Seguin et al., 2014). The transcriptional level elevation of αvβ3 integrin expression is promoted by TGFβ1 and subsequently causes auto-stimulation of the type II TGF- receptor via SRC and the stimulation of MAPK, thereby influencing the progression of EMT (Galliher & Schiemann, 2006; Pechkovsky et al., 2008; Scaffidi et al., 2004). Furthermore, ITGB3 knockdown enhances sensitivity to the DNA-targeting agent temozolomide by impairing DNA repair (Christmann et al., 2017). All of this data points to ITGB3 as a promising marker and modulator that keeps tumours stem-like (Zhu et al., 2019). In our RNA-seq result, we again observed ITGB3 downregulation and integrin cell surface interactions and non-integrin membrane interactions were downregulated. However, our MS-based PA200 interactome analysis did not show ITGB3 as a direct PA200 interactor which indicates that the dysregulation of ITGB3 might be indirect. In order to identify such regulator, we checked the RNA-seq and MS data rigorously. None of the co- or counter-regulated genes were found to function as regulators of ITGB3 and no regulator was found to interact with PA200. It is worth highlighting that such

ITGB3 regulator might be a PA200 target rather than a direct interactor which our MS data might not uncover. While it is speculative, there is a possibility that such regulator might be differentially involved in the p53 or Ras pathways as ITGB3 was only recovered in A549 cells with TGFβ treatment but not in NCI-H1299.

The decrease in invasion and the regulation of EMT upon PA200 depletion in vitro provoked thought on the possible decrease in tumour growth upon PA200 depletion in vivo. Therefore, we injected WT and PA200 KOs cells into the flanks of immune-deficient mice and monitored tumour growth. PA200-depleted cells developed smaller primary tumours compared to their respective WT cells. Notably, tumours developed from NCI-H1299 cell lines were larger compared to the A549 cell lines regardless of PA200 status, which adds to the differences between the two NSCLC lines. Due to the early termination of the experiments related to ethical reasons, we only observed lung metastasis in one mouse (NCI-H1299 WT injected). Importantly, primary tumour incidence was higher in A549 WT cells, while all NCI-H1299 injected mice developed tumours. This result is in line with our in vitro data on the highly invasive nature of NCI-H1299 cells and A549 WT cells compared to their PA200-depleted cells.

Altogether, our results indicate a relation between the PA200 and integrin pathway and tumour growth regulation in vivo. Notably, the downregulation of ITGB3 was observed as a common factor in both A549 and NCI-H1299 cell lines at baseline. Given the established association between integrin signalling and tumour growth in cancer, it is plausible that the interplay between ITGB3 and PA200 might contribute to the effects on invasion and tumour growth (Desgrosellier & Cheresh, 2010). However, the underlying mechanism remains to be elucidated. Understanding this relationship could potentially identify a promising targeted treatment, as demonstrated by Seguin et al., who showed that a combination of bortezomib (a proteasome inhibitor) and erlotinib (an EGFR tyrosine kinase inhibitor) overcame therapeutic resistance mediated by the αvβ3 pathway in cancer cells both in vitro and in vivo (Seguin et al., 2014).

6.1.2.3 Immunoproteasome regulation is affected by PA200 depletion and is different in epithelial and mesenchymal NSCLC cells

The immunoproteasome is an integral part of the MHC class I antigen presentation machinery as it produces peptides of 13–25 residues and hydrophobic C-termini that fit well into the MHC class I peptide binding cleft (Aki et al., 1994; Boes et al., 1994; Gaczynska et al., 1993;

Goldberg et al., 2002; Rock & Goldberg, 1999). Immunoproteasomes, characterized by significantly different catalytic activities, including higher trypsin- and chymotrypsin-like activity and lower caspase-like activity, are involved in the degradation of protein substrates in the MHC class I restricted antigen processing pathway (Goldberg et al., 2002; Rock & Goldberg, 1999; Tanaka, 2009). Hypotheses from various labs suggest that the altered catalytic activity of the immunoproteasome plays important roles in inflammation, autoimmune diseases, cancer, cell-mediated immunity, protein homeostasis, cell differentiation, cytokine release, and cell signalling (Cui et al., 2014; Gutcher & Becher, 2007; K. W. Kalim et al., 2012; Tripathi et al., 2021). Tumours dynamically express immunoproteasome subunits, which may be associated with disease prognosis and survival (Dytfeld et al., 2016; Kiuchi et al., 2021; Lee et al., 2019; Lou et al., 2016; Q. Wang et al., 2019).

Recent research has revealed strong correlations between higher levels of immunoproteasome subunits, local production of IFN-, increased tumour-infiltrating lymphocyte abundance, and longer survival in melanoma patients (Hugo et al., 2016; Kalaora et al., 2020; Leister et al., 2022; Leister et al., 2021). These discoveries have enabled the classification of the tumour microenvironment (TME) based on the production of proinflammatory cytokines and the infiltration of T cells, resulting in the distinction between cold tumours (non-T cell inflamed) and hot tumours (T cell inflamed) (Gajewski, 2015). Hot tumours, characterized by the presence of T cell infiltration and indications of immunological activity, have demonstrated a more positive response to immunotherapy, including treatments targeting programmed death ligand 1 (PD-L1) and programmed cell death protein 1 (PD-1) (Zemek et al., 2019). As a result, strategies have focused on the "heat up" of noninflamed cold tumours aiming to improve their response to immunotherapy (Gajewski, 2015; Liu et al., 2020). Notably, the expression of immunoproteasomes in tumour cells has been found to impact the responsiveness to immunotherapy in non-small cell lung cancer (NSCLC) patients (Tripathi et al., 2016). The presence of a more diverse tumour antigen pool is thought to be efficiently recognized by cytotoxic CD8 T lymphocytes (CTLs), leading to a better prognosis of the disease due to increased immunoproteasome activity in tumour cells. Consequently, a lack of immunoproteasome expression has been linked to poor outcomes in NSCLC patients. Overall, solid tumours with high immunoproteasome levels, such as melanoma and NSCLC, are associated with a wider variety of tumour antigens, improved responsiveness to immune-checkpoint therapy, and most crucially, improved patient survival.

In this study, we investigated the impact of PA200 knockout on immunoproteasome expression and assembly in A549 and NCI-H1299 cell lines. Interestingly, we observed distinct regulatory

patterns for immunoproteasome subunits and active complexes in these cell lines. Specifically, MECL-1 protein levels were significantly reduced in NCI-H1299 PA200 KOs while showing an increase in A549 cells. Both precursor and mature LMP2 levels were decreased in both KOs. The integration of LMP2 is crucial for incorporating the MECL-1 subunit, and the presence of LMP7 aids in the development of immunoproteasomes by cleaving pro-peptides from LMP2 and MECL-1 (Marcus Groettrup et al., 1997; Kingsbury et al., 2000; Marques et al., 2009). The differences in LMP7 incorporation in NCI-H1299 PA200 KO cells might explain the lower level of integrated MECL-1 in the same cell line, while the opposite trend was observed in the A549 cell line. Overall, our findings suggest that PA200 depletion leads to an increase in immunoproteasome complexes in A549 cells but a decrease in NCI-H1299 cells.

A recently published study made a significant discovery regarding the role of PA200 in relation to the immunoproteasome (Javitt et al., 2023). It was found that PA200 binds to the immunoproteasome and exerts inhibitory effects on all functions associated with it. Intriguingly, the study also unveiled that PA200-restricted proteasome activity leads to a reduction in the variety of MHC I-presented antigens and enhanced PSME4 degradation and presentation influence nuclear antigens. Furthermore, the study identified a link between PA200 expression and cold tumours, which are known to exhibit resistance to immunotherapy, as described above. The presence of PA200 appears to decrease the susceptibility of these tumours to immunotherapy. Importantly, unlike other markers that indicate responsiveness to immune checkpoint inhibitors (ICI), PA200 was identified as one of the rare indicators of resistance to ICI treatment.

Compared to Javitt et al., we here observe differential effects of PA200 on the immunoproteasome, perhaps due to different experimental settings. Javitt et al. used short hairpin RNAs (shRNAs) to repress the expression of PA200 mRNA in A549 cells. However, even with highly effective shRNAs, some residual expression of the target gene remains as also seen in their data sets. This is because shRNAs act at the post-transcriptional level by targeting mRNA for degradation, and cellular processes like RNA turnover and translation can contribute to residual gene expression (Mittal, 2004). On the other hand, the CRISPR/Cas9 technology we have used results in a permanent and full loss of gene expression compared to shRNA-mediated knockdown. These differences between the shRNA targeted PA200 knockdown (0.5-fold) and PA200 total knock-out (no mRNA detected) might explain the differences observed in the RNA-seq data sets generated by Javitt et al. and us with only a few mRNAs regulated similarly. This indicates that even a small amount of PA200 expression can have quite a different effect on the mRNA regulation compared to the total PA200 ablation.

Furthermore, the animal models used between the two studies have some differences. While Javitt et al. used KP1.9 cells (isolated from a male C57BL/6 KrasLSL-G12D/WT;p53Flox/Flox mouse), we injected human cells with different mutational status as outlined in Table 6.1. As we injected human cells into mice, we used NOD SCID mice, which have impaired T and B cell lymphocyte development and are deficient in natural killer (NK) cell function to avoid rejection of human cells in a mouse host. Similarly, to avoid rejection, Javitt et al. used only male C57Bl/6J mice, as the KP1.9 cells isolated from male mice are rejected when injected into female mice. Yet, they observed the effect of PA200 status with an orthotopic mouse model. They saw an increase in the tumour lesion number and lesion area in the lungs of mice that had been injected with PA200 overexpressing KP1.9 cells, while tumour size was lower in cells with shRNA-mediated knockdown of PA200. PA200 OE-injected mice had decreased tumour inflammation and exhibited reduced inflammation and T-cell activation. To confirm the PA200 and its relevance to immunity, they also used RAG1−/− mice which lack mature B and T lymphocytes, and they did not observe aberrant changes related to PA200 expression. However, we observed decreased tumour volume of the primary tumour when PA200 KO cells were injected into the flank of mice. Additionally, during the course of our mouse experiments, we noticed an unexpected development of necrosis at the primary tumour site, especially in the NCI-H1299 cell line and notably in KO-injected mice. The reason behind this phenomenon is unknown and requires further in-depth analysis and investigation.

In conclusion, our study sheds light on the differential regulation of immunoproteasome complexes upon PA200 knockout in A549 and NCI-H1299 cell lines. The contrasting effects on immunoproteasome assembly in these cell lines provide valuable insights into the role of PA200 in modulating immunoproteasome activity and potentially impacting tumour biology. However, the observation of necrosis in the NCI-H1299 cell line warrants further exploration to fully understand its underlying mechanisms and implications. Together with the study by Javitt et al., our research provides additional evidence regarding the intricate role of PA200 in regulating proteasome function and antigen presentation. Importantly, our results indicate that the absence of PA200 has varying effects on the immunoproteasomes, depending on the specific cellular context. Understanding these complex mechanisms is of utmost significance to advance our comprehension of tumour immunogenicity and resistance to immunotherapy. Moreover, it opens possibilities for the identification of potential therapeutic targets for future interventions. Our study contributes to the growing body of knowledge concerning the role of PA200 in the immune response and cancer biology. By shedding light on the modulation of

immunoproteasome activity, our findings may pave the way for the development of novel approaches to enhance immunotherapy responses and improve cancer treatment outcomes.

6.1.3 Transcriptomic differences are observed in PA200 KO NSCLC lines

To obtain an overall idea of the transcriptomic changes in the cell in the absence of PA200, both cell lines (WT and KOs) were subjected to RNA-seq. Strikingly, the transcriptomes were quite different between the two cell lines upon PA200 depletion. A549 cells showed significantly more genes to be regulated upon PA200 depletion. When analysed in detail, we observed only 16 of the genes to be regulated in a similar pattern (up- or down-regulated), while 23 genes were counter-regulated (upregulated in one and downregulated in the other, and vice versa). Although different genes were regulated by PA200 KO in the two cell lines, some of the regulated pathways overlapped, e.g., degradation of ECM, regulation of beta-cell development and gene expression in beta cells were enriched in both KOs, while integrin cell surface interactions and non-integrin membrane interactions were downregulated. Interestingly, genes related to glycolysis (such as ISG20, CHPF, GPC1, MXI1, ANGPTL4, MERTK, SLC16A3, and PPFIA4) decreased in the A549 KOs while inflammatory responses genes were counter-regulated in the two cell lines, i.e., upregulated in A549 (RNF144B, PTPRE, IL6, TNFSF15, CYBB, NMI, F3, RASGRP1, TLR3) and downregulated in NCI-H1299 KOs (LYN, BST2, GNA15, CD82, ITGB3, PCDH7, NLRP3, TNFRSF1B, ICOSLG, KCNJ2).

There is limited knowledge of the shared upregulated genes in both KO cell lines (ADAMTS16, EFHC2, GLRB, and FAM160A1). The ADAMTS family of metalloproteinases, which consists of 19 members, is involved in a wide range of biological processes, including spermatogenesis and fertilization, neurogenesis, inflammatory reactions, and cancer (Reiss & Saftig, 2009; Sun et al., 2015). It has been demonstrated that ADAMTS16 plays a role in the control of blood pressure, cardiac fibrosis, premature ovarian failure, and male genitourinary system dysfunction (Abdul-Majeed et al., 2014; Gopalakrishnan et al., 2012; Gunes et al., 2016; Joe et al., 2009; Pyun et al., 2014; Sakamoto et al., 2010; Yao et al., 2019). Our current knowledge of EFHC2, GLRB, and FAM160A1 indicates that they are involved in cognitive abilities, neurological processes, and Natural-killer/T-cell lymphoma (NKTL), respectively (Chan et al., 2018; Schaefer et al., 2018; Startin et al., 2015). Similarly, the co-downregulated genes are not well studied. However, some of these genes include the regulation of tumour growth, vascularization, tumour progression and tumour microenvironments such as GPC1,

PREX1, and ITGB3 (Lund et al., 2020; Ye, 2020; Zhu et al., 2019). From the counter-regulated genes, SIX3, which is downregulated in A549 and upregulated in NCI-H1299, was found to play a role in NSCLC by inhibiting the Wnt pathway (Ma et al., 2022). The downregulated SIX3 gene might translate into low levels of the protein, which leads to less inhibition of WNT. Indeed, in the A549 cells, we saw upregulation of WNT-related genes such as PRICKLE1, BMP4, and LGR6 but not in NCI-H1299.

Of note, in NCI-H1299 KOs, we observed downregulation of genes involved in B-cell receptor and development (CD22, PIK3AP1) and costimulatory genes of T-cell proliferation and T-cell adhesion genes (CD200, ICOSLG, CYFIP2), a tyrosine-protein kinase (LYN) which might involve in the regulation of innate and adaptive immune responses and finally an upregulation of a negative regulator of T-cell receptor (PTPN22) (Aiba et al., 2008; Brian & Freedman, 2021; Iwata et al., 2020; Mayne et al., 2004; Nitschke et al., 1997; Vathiotis et al., 2021; Zhang et al., 2020). All these genes indicate a decreased capability of B-cell and T-cell regulation in NCI-H1299 PA200 KO cells. However, in A549 KOs, we observed an increase in IL6 gene expression (required for Th17 generation), DPP4 (positive regulator of T-cell activation), and TOX, which is involved in T-cell development (Korn & Hiltensperger, 2021; Ohnuma et al., 2006; X. Wang et al., 2019). The changes in A549 KO, therefore, suggest an increased capacity for T-cell activation. As previously discussed, Javitt et al. showed differences in the hot and cold tumours where the abundance of PA200 affected antigen representation. When they injected PA200 silenced mice cells into mice, they observed that cytotoxic T cell and regulatory T cell (Treg) populations were higher in these mice compared to controls (Javitt et al., 2023). While these results accord with the RNA signature of A549 KOs, they do not fit our NCI-H1299 PA200 KO RNA signatures, which might strengthen the context-dependent regulation of PA200, as discussed previously. Furthermore, the differences might also be related to the differences in immunoproteasome regulation in the absence of PA200 in the two NSCLC cell lines.

Additionally, we observed that almost 27-32% of the regulated RNAs were identified as non-coding RNA in both lines. These include a variety of subsets such as long-intergenic non-coding RNA (lincRNA), long non-coding RNA (lncRNA), and microRNA (miRNA). However, due to a lack of knowledge on the non-coding RNAs that we detected, we currently do not know how this dysregulation affects the cells or why PA200 depletion affects the expression of these ncRNAs. Yet, the dysregulation might be related to the changes in the protein levels of RNA regulatory proteins, as PA200's absence might alter the degradation levels of some of these proteins.

6.1.4 PA200 has a diverse interactome

To investigate whether the observed differences in gene regulation between the two cell lines were due to a differential interactome of PA200, we performed immunoprecipitation (IP) experiments using a PA200 antibody. We employed a previously optimized IP method used in our laboratory, which had been successfully applied in primary human lung fibroblasts (Welk, 2018). The pulldown of PA200 in PA200-depleted cells served as a control, while Welk used an IgG-negative control. Surprisingly, in the cancer cell lines, we did not identify a significant number of proteasome subunits as PA200 interactors. In NCI-H1299 cells, only PSMB3 showed interaction with a fold change ≥ 1.5, and several subunits were identified as minor interactors (1.5 ≥ fold change ≥ 1; A549: PSMA7, PSMB3, PSMB5, PSMA4, PSMB1, and PSMA6; NCI-H1299: PSMA6, PSMB2). This might be due to the use of PA200-depleted cells as a control where proteasome subunits might unspecifically bind to the PA200 antibody.

Upon further analysis of the interactors, we observed that the majority of these interactors were DNA-binding proteins, particularly in A549 cells, but also in NCI-H1299. Notably, only two proteins, UBASH3B and ARPC2, were consistently identified as PA200 interactors in both cell lines. Interestingly, several genes (PREX1, OPLAH, PLCG2, HS1BP3) were found to be downregulated in A549 knockout cells on the RNA level, yet they were identified as PA200 interactors. Similarly, the gene PLOD2 was downregulated in NCI-H1299 knockout cells and identified as a PA200 interactor. One may speculate that the respective gene products may not only interact with PA200 but serve as substrates of PA200-capped proteasome complexes leading to their degradation. In the absence of PA200 in the cells, protein turnover rates might decrease, potentially resulting in decreased/increased gene expression of these proteins depending on the requirement of the cells. However, this hypothesis requires further analysis for validation. These findings highlight the intricate interplay between PA200, proteasome subunits, and DNA-binding proteins, suggesting potential regulatory mechanisms that warrant further investigation.

One possible explanation for the lack of enrichment of proteasome subunits as PA200 interactors could be attributed to the non-specific binding of proteins to the beads or antibody used in the immunoprecipitation (IP) assay. To address this, we performed a pre-clearing step by incubating the lysates with beads without antibodies prior to the IP with the PA200-bead complex. Surprisingly, even the pre-cleared lysates did not reveal a significant number of PA200-proteasome subunit interactions. In A549 cells, we identified PSMA5 and PSMD14 as PA200 interactors, while PSMG4 was identified in NCI-H1299 cells, with fold changes ≥ 1.5.

Only PSMB3, PSMC4, and PSMC3 showed interactions with a fold change ranging from 1.5 to 1 in A549 cells. Interestingly, the pre-cleared lysates of both A549 and NCI-H1299 cells did not exhibit any similar interactors using a cut-off of 1.5-fold enrichment. In A549 cells, the pre-cleared lysates revealed CAVIN2, FBXO2, HPCAL1, and GATA6 as PA200 interactors. Notably, the gene expression of the first three proteins was found to be decreased, while that of GATA6 was increased in A549 knockout cells based on RNA-seq results. In the pre-cleared lysates of NCI-H1299 cells, we only identified PPL as a PA200 interactor, which showed altered RNA regulation (downregulated). To further check the non-specific binding interactors, we used the Contaminant Repository for Affinity Purification (CRAPome) database, which was developed to identify unspecific binders (contaminants) in mass spectrometry data (Mellacheruvu et al., 2013). When screening all PA200 protein interactors (with or without pre-clearing) for potential contaminants, only 19 proteins were identified in more than 50% of the 716 experimental entries used for the database. This corresponds to approximately 6% of the total PA200 interactors. Interestingly, 41 of the PA200 interactors have never been identified as unspecific binders in the CRAPome database Table 6.2. These proteins, therefore, are potential unique PA200 interactors.

Table 6.2: Potential unique PA200 interactors that are not found in any of the experiment entries uploaded to the CRAPome database

	w/o Pre-cleared	Pre-cleared
A549	RECK, NBEAL1, TEX30, PARVB, H1-10, PDE1C, ABHD4, SEPTIN10, TUT7, IRS1, RHPN2, OPLAH, AVL9, TARS3, TKTL1	AGAP1, NEIL2, HPCAL1, ANKRD9, DARS1, CZIB, OTUD6B, ERRFI1, FGD6
NCI-H1299	BLOC1S1, MAGEA12, HOXB4, UBE2H, DLC1	PSMG4, FAM216A, TBC1D17, EPDR1, DCLK2, ATOH1, H3-3A, SEPTIN8, TRPC4AP, MEAK7, SCNM1, ZNF511

These findings suggest that the specific interactions between PA200 and proteasome subunits may be influenced by cell type-specific factors or other regulatory mechanisms. Further investigation is needed to elucidate the functional implications of these interactions and their potential role in cellular processes.

6.2 PA200 exists independent from proteasome in the NSCLC cell lines

In our IP results, we observed that the interactors of PA200 were predominantly DNA and RNA binding proteins across different experimental settings rather than proteasome subunits. These results raise the intriguing possibility of proteasome-independent PA200 existence in cancer cells. To explore this further, we analysed whether there are PA200 complexes that are not associated with active proteasomes. Our mass spectrometry (MS) results from native gel analysis revealed the presence of PA200 protein in fractions where active proteasome complexes were absent.

To maintain the integrity of PA200-bound proteasome complexes during our immunoprecipitation protocol, we employed a mild protein isolation method using a TSDG buffer. However, we hypothesized that there might be residual insoluble PA200 present upon TSDG cell lysis, specifically associated with DNA, as suggested by Blickwedehl et al. (Blickwedehl et al., 2008). To investigate this further, we introduced a stronger protein denaturant, urea, which is known to disrupt hydrogen bonds and other non-covalent interactions in proteins, leading to the loss of their structural integrity (Zangi et al., 2009). While urea is commonly utilized for cell lysis and protein extraction, it is important to note that it has the potential to degrade RNA, DNA, and other biomolecules (Raghunathan et al., 2020). This property of urea leads to the dissociation of protein complexes from nucleic acids. By subjecting the TSDG-lysed cell pellets to urea lysis, we confirmed our hypothesis that PA200 is present in the insoluble fractions of TSDG-lysed cells. Importantly, this was observed only in wild-type cells upon urea lysis of the previously TSDG-lysed pellets. These results provide further support for the existence of proteasome-independent PA200, which might be associated with DNA and RNA binding proteins tightly bound to insoluble cellular components. Our data are in line with a previous report from Welk et al., who demonstrated that upon bortezomib treatment, PA200 was rapidly recruited to proteasomes in the absence of transcriptional activation, indicating the existence of non-proteasome bound PA200 in the cell ready for recruitment to the proteasome (Welk et al., 2016). However, the specific function of such proteasome-independent PA200 has not been investigated to date. The functional implications of these interactions in the cell remain unclear and require further investigation for a comprehensive understanding of the function of PA200 in NSCLC.

7 Limitations and Outlook

Throughout the course of this PhD thesis, I encountered several limitations while investigating the role of PA200 in lung cancer. Initially, I attempted to overexpress the PA200 protein in HEK-293 and A549 cell lines using standard transfection reagents like Lipofectamine or PEI. However, the high molecular weight of the PA200 plasmid (approximately 11 kb) with the pcDNA3.1 backbone posed a significant obstacle to successful transfection. As a result, achieving efficient transfection with this large plasmid became a limiting factor in these experiments. Subsequently, we explored viral transfection methods, utilizing the CRISPR knock-out cell lines that I generated. Unfortunately, our collaborators also failed to generate PA200 overexpressing cell lines. It appears that the large PA200 containing plasmid size in both the standard and the lentiviral transfer plasmid hindered successful overexpression in my experiments. It is worth noting that even in up-to-date results from different laboratories, overexpression of PA200 was achieved only up to moderate levels of around 2-3-fold (Javitt et al., 2023; Fu Wang et al., 2017; Welk et al., 2019). It seems that surpassing this limit in overexpression studies may continue to be challenging due to the constraints imposed by the vector size.

We acknowledge that using an immunodeficient animal model had certain limitations, especially when investigating the tumour microenvironment. Despite these limitations, we chose this model based on our in vitro observations and its relevance to studying the role of PA200 in metastasis. However, the rapid growth of the primary tumour after subcutaneous injection necessitated the early sacrifice of mice due to ethical concerns. Unfortunately, this early termination may have limited metastasis development. To address this concern in future studies, alternative injection methods like orthotopic transplantation or tail vein injection could be explored, as they may offer a more comprehensive representation of the metastatic process.

Another limitation we encountered was finding a suitable working PA200 antibody. This issue has been previously raised (Welk et al., 2019; Yazgili et al., 2022). While the main antibody we used worked well for Western blots, it failed to do so with immunofluorescence in our experiments. Despite using the same antibody previously used for immunofluorescence, we still obtained an unspecific background signal when testing our PA200 knockout cell lines (Aladdin et al., 2020). Considering that we observed no PA200 at the RNA or protein level with any of the methods we employed, we believe this antibody is unsuitable for immunofluorescence purposes, at least in human lung cancer cell lines. To overcome this

problem, we attempted to generate monoclonal antibodies; however, the completion of this task remains pending as none of the generated antibodies worked with immunofluorescence so far.

In light of these limitations, we recognize the importance of addressing these issues in future research to enhance the validity and accuracy of our findings. Addressing the limitations of the animal model and finding appropriate and reliable antibodies for PA200 detection are critical steps to further advance our understanding of the role of PA200 in cancer progression and metastasis. We believe that by addressing these challenges, future studies will make significant contributions to the field of cancer research and aid in the development of potential therapeutic strategies targeting PA200 and its associated pathways.

References

Abdueva, D., Wing, M., Schaub, B., Triche, T., & Davicioni, E. (2010). Quantitative expression profiling in formalin-fixed paraffin-embedded samples by affymetrix microarrays. *J Mol Diagn*, *12*(4), 409-417. https://doi.org/10.2353/jmoldx.2010.090155

Abdul-Majeed, S., Mell, B., Nauli, S. M., & Joe, B. (2014). Cryptorchidism and infertility in rats with targeted disruption of the Adamts16 locus. *PLoS One*, *9*(7), e100967.

Abi Habib, J., De Plaen, E., Stroobant, V., Zivkovic, D., Bousquet, M.-P., Guillaume, B., Wahni, K., Messens, J., Busse, A., & Vigneron, N. (2020). Efficiency of the four proteasome subtypes to degrade ubiquitinated or oxidized proteins. *Scientific reports*, *10*(1), 1-17.

Adamczyk-Gruszka, O., Horecka-Lewitowicz, A., Gruszka, J., Wawszczak-Kasza, M., Strzelecka, A., & Lewitowicz, P. (2022). FGFR-2 and Epithelial–Mesenchymal Transition in Endometrial Cancer. *Journal of Clinical Medicine*, *11*(18), 5416. https://www.mdpi.com/2077-0383/11/18/5416

Aguado, C., Chara, L., Antonanzas, M., Matilla Gonzalez, J. M., Jimenez, U., Hernanz, R., Mielgo-Rubio, X., Trujillo-Reyes, J. C., & Counago, F. (2022). Neoadjuvant treatment in non-small cell lung cancer: New perspectives with the incorporation of immunotherapy. *World J Clin Oncol*, *13*(5), 314-322. https://doi.org/10.5306/wjco.v13.i5.314

Aiba, Y., Kameyama, M., Yamazaki, T., Tedder, T. F., & Kurosaki, T. (2008). Regulation of B-cell development by BCAP and CD19 through their binding to phosphoinositide 3-kinase. *Blood*, *111*(3), 1497-1503. https://doi.org/10.1182/blood-2007-08-109769

Aiken, C. T., Kaake, R. M., Wang, X., & Huang, L. (2011). Oxidative stress-mediated regulation of proteasome complexes. *Mol Cell Proteomics*, *10*(5), R110.006924. https://doi.org/10.1074/mcp.M110.006924

Aki, M., Shimbara, N., Takashina, M., Akiyama, K., Kagawa, S., Tamura, T., Tanahashi, N., Yoshimura, T., Tanaka, K., & Ichihara, A. (1994). Interferon-gamma induces different subunit organizations and functional diversity of proteasomes. *J Biochem*, *115*(2), 257-269. https://doi.org/10.1093/oxfordjournals.jbchem.a124327

Akiyama, K.-y., Yokota, K.-y., Kagawa, S., Shimbara, N., Tamura, T., Akioka, H., Nothwang, H. G., Noda, C., Tanaka, K., & Ichihara, A. (1994). cDNA Cloning and Interferon γ Down-Regulation of Proteasomal Aubunits X and Y. *Science*, *265*(5176), 1231-1234.

Aladdin, A., Yao, Y., Yang, C., Kahlert, G., Ghani, M., Király, N., Boratkó, A., Uray, K., Dittmar, G., & Tar, K. (2020). The Proteasome Activators Blm10/PA200 Enhance the Proteasomal Degradation of N-Terminal Huntingtin. *Biomolecules*, *10*(11). https://doi.org/10.3390/biom10111581

Alberg, A. J., Brock, M. V., Ford, J. G., Samet, J. M., & Spivack, S. D. (2013). Epidemiology of lung cancer: Diagnosis and management of lung cancer, 3rd ed: American College of Chest Physicians evidence-based clinical practice guidelines. *Chest*, *143*(5 Suppl), e1S-e29S. https://doi.org/10.1378/chest.12-2345

Ali, A., Wang, Z., Fu, J., Ji, L., Liu, J., Li, L., Wang, H., Chen, J., Caulin, C., & Myers, J. N. (2013). Differential regulation of the REGγ–proteasome pathway by p53/TGF-β signalling and mutant p53 in cancer cells. *Nature communications*, *4*(1), 1-16.

American Cancer Society, A. (2019). *What Is Lung Cancer?* https://www.cancer.org/cancer/lung-cancer/about/what-is.html

Angeles, A., Fung, G., & Luo, H. (2012). Immune and non-immune functions of the immunoproteasome. *Front Biosci (Landmark Ed)*, *17*(5), 1904-1916. https://doi.org/10.2741/4027

Arciniega, M., Beck, P., Lange, O. F., Groll, M., & Huber, R. (2014). Differential global structural changes in the core particle of yeast and mouse proteasome induced by ligand binding. *Proc Natl Acad Sci U S A*, *111*(26), 9479-9484. https://doi.org/10.1073/pnas.1408018111

Bard, J. A., Goodall, E. A., Greene, E. R., Jonsson, E., Dong, K. C., & Martin, A. (2018). Structure and function of the 26S proteasome. *Annual review of biochemistry*, *87*, 697.

Barton, L. F., Cruz, M., Rangwala, R., Deepe, G. S., Jr., & Monaco, J. J. (2002). Regulation of immunoproteasome subunit expression in vivo following pathogenic fungal infection. *J Immunol*, *169*(6), 3046-3052. https://doi.org/10.4049/jimmunol.169.6.3046

Basler, M., Moebius, J., Elenich, L., Groettrup, M., & Monaco, J. J. (2006). An altered T cell repertoire in MECL-1-deficient mice. *The Journal of Immunology*, *176*(11), 6665-6672.

Baugh, J. M., Viktorova, E. G., & Pilipenko, E. V. (2009). Proteasomes can degrade a significant proportion of cellular proteins independent of ubiquitination. *J Mol Biol*, *386*(3), 814-827. https://doi.org/10.1016/j.jmb.2008.12.081

Bedford, L., Hay, D., Devoy, A., Paine, S., Powe, D. G., Seth, R., Gray, T., Topham, I., Fone, K., & Rezvani, N. (2008). Depletion of 26S proteasomes in mouse brain neurons causes neurodegeneration and Lewy-like inclusions resembling human pale bodies. *Journal of Neuroscience*, *28*(33), 8189-8198.

Berridge, M. V., & Tan, A. S. (1993). Characterization of the Cellular Reduction of 3-(4,5-dimethylthiazol-2-yl)-2,5-diphenyltetrazolium bromide (MTT): Subcellular Localization, Substrate Dependence, and Involvement of Mitochondrial Electron Transport in MTT Reduction. *Archives of Biochemistry and Biophysics*, *303*(2), 474-482. https://doi.org/https://doi.org/10.1006/abbi.1993.1311

Beyoğlu, D., & Idle, J. R. (2021). Metabolic Rewiring and the Characterization of Oncometabolites. *Cancers*, *13*(12), 2900. https://www.mdpi.com/2072-6694/13/12/2900

Blickwedehl, J., Agarwal, M., Seong, C., Pandita, R. K., Melendy, T., Sung, P., Pandita, T. K., & Bangia, N. (2008). Role for proteasome activator PA200 and postglutamyl proteasome activity in genomic stability. *Proc Natl Acad Sci U S A*, *105*(42), 16165-16170. https://doi.org/10.1073/pnas.0803145105

Blickwedehl, J., McEvoy, S., Wong, I., Kousis, P., Clements, J., Elliott, R., Cresswell, P., Liang, P., & Bangia, N. (2007). Proteasomes and proteasome activator 200 kDa (PA200) accumulate on chromatin in response to ionizing radiation. *Radiat Res*, *167*(6), 663-674. https://doi.org/10.1667/RR0690.1

Blickwedehl, J., Olejniczak, S., Cummings, R., Sarvaiya, N., Mantilla, A., Chanan-Khan, A., Pandita, T. K., Schmidt, M., Thompson, C. B., & Bangia, N. (2012). The proteasome activator PA200 regulates tumor cell responsiveness to glutamine and resistance to ionizing radiation. *Mol Cancer Res*, *10*(7), 937-944. https://doi.org/10.1158/1541-7786.MCR-11-0493-T

Bockstahler, M., Fischer, A., Goetzke, C. C., Neumaier, H. L., Sauter, M., Kespohl, M., Müller, A.-M., Meckes, C., Salbach, C., & Schenk, M. (2020). Heart-specific immune responses in an animal model of autoimmune-related myocarditis mitigated by an immunoproteasome inhibitor and genetic ablation. *Circulation*, *141*(23), 1885-1902.

Boes, B., Hengel, H., Ruppert, T., Multhaup, G., Koszinowski, U. H., & Kloetzel, P. M. (1994). Interferon gamma stimulation modulates the proteolytic activity and cleavage site preference of 20S mouse proteasomes. *J Exp Med*, *179*(3), 901-909. https://doi.org/10.1084/jem.179.3.901

Braselmann, H., Michna, A., Heß, J., & Unger, K. (2015). CFAssay: statistical analysis of the colony formation assay. *Radiation Oncology*, *10*(1), 223. https://doi.org/10.1186/s13014-015-0529-y

Bray, F., Ferlay, J., Laversanne, M., Brewster, D. H., Gombe Mbalawa, C., Kohler, B., Piñeros, M., Steliarova-Foucher, E., Swaminathan, R., Antoni, S., Soerjomataram, I., & Forman, D. (2015). Cancer Incidence in Five Continents: Inclusion criteria, highlights from Volume X and the global status of cancer registration. *Int J Cancer*, *137*(9), 2060-2071. https://doi.org/10.1002/ijc.29670

Brehm, M. A., Schenk, T. M., Zhou, X., Fanick, W., Lin, H., Windhorst, S., Nalaskowski, M. M., Kobras, M., Shears, S. B., & Mayr, G. W. (2007). Intracellular localization of human Ins(1,3,4,5,6)P5 2-kinase. *Biochem J*, *408*(3), 335-345. https://doi.org/10.1042/BJ20070382

Breitling, L. P., Rinke, A., & Gress, T. M. (2020). Recent Survival Trends in High-Grade Neuroendocrine Neoplasms and Lung Cancer. *Neuroendocrinology*, *110*(3-4), 225-233. https://doi.org/10.1159/000500883

Brian, B. F. t., & Freedman, T. S. (2021). The Src-family Kinase Lyn in Immunoreceptor Signaling. *Endocrinology*, *162*(10). https://doi.org/10.1210/endocr/bqab152

Brucet, M., Marqués, L., Sebastián, C., Lloberas, J., & Celada, A. (2004). Regulation of murine Tap1 and Lmp2 genes in macrophages by interferon gamma is mediated by STAT1 and IRF-1. *Genes Immun*, *5*(1), 26-35. https://doi.org/10.1038/sj.gene.6364035

Burgstaller, G., Oehrle, B., Koch, I., Lindner, M., & Eickelberg, O. (2013). Multiplex Profiling of Cellular Invasion in 3D Cell Culture Models. *PLoS One*, *8*(5), e63121. https://doi.org/10.1371/journal.pone.0063121

Byrum, J., Jordan, S., Safrany, S. T., & Rodgers, W. (2004). Visualization of inositol phosphate-dependent mobility of Ku: depletion of the DNA-PK cofactor InsP6 inhibits Ku mobility. *Nucleic Acids Res*, *32*(9), 2776-2784. https://doi.org/10.1093/nar/gkh592

Cancer, I. A. f. R. o. (2020). *Global Cancer Observatory Cancer Fact Sheets: Lung*. World Health Organization. https://gco.iarc.fr/today/data/factsheets/cancers/15-Lung-fact-sheet.pdf

Carpentier G., M. M., Courty J. and Cascone I. (2012). Angiogenesis Analyzer for ImageJ. 4th ImageJ User and Developer Conference proceedings, Mondorf-les-Bains, Luxembourg.

Cascio, P. (2014). PA28αβ: the enigmatic magic ring of the proteasome? *Biomolecules*, *4*(2), 566-584.

Cascio, P., Call, M., Petre, B. M., Walz, T., & Goldberg, A. L. (2002). Properties of the hybrid form of the 26S proteasome containing both 19S and PA28 complexes. *EMBO J*, *21*(11), 2636-2645. https://doi.org/10.1093/emboj/21.11.2636

Cellosaurus. (2012a, 21 Mar 2023). *A-549 (CVCL_0023)*. https://www.cellosaurus.org/CVCL_0023

Cellosaurus. (2012b, 21 Mar 2023). *NCI-H1299 (CVCL_0060)*. https://www.cellosaurus.org/CVCL_0060

Çetin, G., Klafack, S., Studencka-Turski, M., Krüger, E., & Ebstein, F. (2021). The Ubiquitin–Proteasome System in Immune Cells. *Biomolecules*, *11*(1), 60. https://www.mdpi.com/2218-273X/11/1/60

Chan, J. Y., Ng, A. Y. J., Cheng, C. L., Nairismägi, M. L., Venkatesh, B., Cheah, D. M. Z., Li, S. T., Chan, S. H., Ngeow, J., Laurensia, Y., Lim, J. Q., Pang, J. W. L., Nagarajan, S., Song, T., Chia, B., Tan, J., Huang, D., Goh, Y. T., Poon, E., Somasundaram, N., Tao, M., Quek, R. H. H., Farid, M., Khor, C. C., Bei, J. X., Tan, S. Y., Lim, S. T., Ong, C. K., & Tang, T. (2018). Whole exome sequencing identifies recessive germline mutations in FAM160A1 in familial NK/T cell lymphoma. *Blood Cancer J*, *8*(11), 111. https://doi.org/10.1038/s41408-018-0149-5

Chatterjee-Kishore, M., Kishore, R., Hicklin, D. J., Marincola, F. M., & Ferrone, S. (1998). Different requirements for signal transducer and activator of transcription 1alpha and interferon regulatory factor 1 in the regulation of low molecular mass polypeptide 2 and transporter associated with antigen processing 1 gene expression. *J Biol Chem*, *273*(26), 16177-16183. https://doi.org/10.1074/jbc.273.26.16177

Chen, D. S., & Mellman, I. (2017). Elements of cancer immunity and the cancer-immune set point. *Nature*, *541*(7637), 321-330. https://doi.org/10.1038/nature21349

Chen, E. Y., Tan, C. M., Kou, Y., Duan, Q., Wang, Z., Meirelles, G. V., Clark, N. R., & Ma'ayan, A. (2013). Enrichr: interactive and collaborative HTML5 gene list enrichment analysis tool. *BMC Bioinformatics*, *14*, 128. https://doi.org/10.1186/1471-2105-14-128

Chen, L., & Cui, H. (2015). Targeting Glutamine Induces Apoptosis: A Cancer Therapy Approach. *International Journal of Molecular Sciences*, *16*(9), 22830-22855. https://www.mdpi.com/1422-0067/16/9/22830

Chen, L., & Cui, H. (2015). Targeting Glutamine Induces Apoptosis: A Cancer Therapy Approach. *Int J Mol Sci*, *16*(9), 22830-22855. https://doi.org/10.3390/ijms160922830

Chen, P., & Hochstrasser, M. (1996). Autocatalytic subunit processing couples active site formation in the 20S proteasome to completion of assembly. *Cell*, *86*(6), 961-972.

Christmann, M., Diesler, K., Majhen, D., Steigerwald, C., Berte, N., Freund, H., Stojanović, N., Kaina, B., Osmak, M., & Ambriović-Ristov, A. (2017). Integrin αVβ3 silencing sensitizes malignant glioma cells to temozolomide by suppression of homologous recombination repair. *Oncotarget*, *8*(17), 27754.

Ciechanover, A. (2005). Proteolysis: from the lysosome to ubiquitin and the proteasome. *Nature reviews Molecular cell biology*, *6*(1), 79-87.

Cosset, É., Ilmjärv, S., Dutoit, V., Elliott, K., von Schalscha, T., Camargo, M. F., Reiss, A., Moroishi, T., Seguin, L., & Gomez, G. (2017). Glut3 addiction is a druggable vulnerability for a molecularly defined subpopulation of glioblastoma. *Cancer Cell*, *32*(6), 856-868. e855.

Coux, O., Zieba, B. A., & Meiners, S. (2020). The Proteasome System in Health and Disease. *Adv Exp Med Biol*, *1233*, 55-100. https://doi.org/10.1007/978-3-030-38266-7_3

Cui, Z., Hwang, S. M., & Gomes, A. V. (2014). Identification of the immunoproteasome as a novel regulator of skeletal muscle differentiation. *Mol Cell Biol*, *34*(1), 96-109. https://doi.org/10.1128/mcb.00622-13

Dahlmann, B. (2016). Mammalian proteasome subtypes: Their diversity in structure and function. *Arch Biochem Biophys*, *591*, 132-140. https://doi.org/10.1016/j.abb.2015.12.012

de Graaf, N., van Helden, M. J. G., Textoris-Taube, K., Chiba, T., Topham, D. J., Kloetzel, P.-M., Zaiss, D. M. W., & Sijts, A. J. A. M. (2011). PA28 and the proteasome immunosubunits play a central and independent role in the production of MHC class I-binding peptides in vivo. *European journal of immunology*, *41*(4), 926-935. https://doi.org/https://doi.org/10.1002/eji.201041040

de Verteuil, D. A., Rouette, A., Hardy, M.-P., Lavallée, S., Trofimov, A., Gaucher, É., & Perreault, C. (2014). Immunoproteasomes Shape the Transcriptome and Regulate the

Function of Dendritic Cells. *The Journal of Immunology*, *193*(3), 1121-1132. https://doi.org/10.4049/jimmunol.1400871

de Visser, K. E., Eichten, A., & Coussens, L. M. (2006). Paradoxical roles of the immune system during cancer development. *Nat Rev Cancer*, *6*(1), 24-37. https://doi.org/10.1038/nrc1782

DeNardo, D. G., Andreu, P., & Coussens, L. M. (2010). Interactions between lymphocytes and myeloid cells regulate pro- versus anti-tumor immunity. *Cancer Metastasis Rev*, *29*(2), 309-316. https://doi.org/10.1007/s10555-010-9223-6

Desgrosellier, J. S., & Cheresh, D. A. (2010). Integrins in cancer: biological implications and therapeutic opportunities. *Nat Rev Cancer*, *10*(1), 9-22. https://doi.org/10.1038/nrc2748

Dick, T. P., Ruppert, T., Groettrup, M., Kloetzel, P. M., Kuehn, L., Koszinowski, U. H., Stevanovic, S., Schild, H., & Rammensee, H.-G. (1996). Coordinated dual cleavages induced by the proteasome regulator PA28 lead to dominant MHC ligands. *Cell*, *86*(2), 253-262.

Dong, S., Jia, C., Zhang, S., Fan, G., Li, Y., Shan, P., Sun, L., Xiao, W., Li, L., & Zheng, Y. (2013). The REGγ proteasome regulates hepatic lipid metabolism through inhibition of autophagy. *Cell metabolism*, *18*(3), 380-391.

Douida, A., Batista, F., Boto, P., Regdon, Z., Robaszkiewicz, A., & Tar, K. (2021). Cells Lacking PA200 Adapt to Mitochondrial Dysfunction by Enhancing Glycolysis via Distinct Opa1 Processing. *Int J Mol Sci*, *22*(4). https://doi.org/10.3390/ijms22041629

Douida, A., Batista, F., Robaszkiewicz, A., Boto, P., Aladdin, A., Szenykiv, M., Czinege, R., Virag, L., & Tar, K. (2020). The proteasome activator PA200 regulates expression of genes involved in cell survival upon selective mitochondrial inhibition in neuroblastoma cells. *J Cell Mol Med*, *24*(12), 6716-6730. https://doi.org/10.1111/jcmm.15323

Downward, J. (2003). Targeting RAS signalling pathways in cancer therapy. *Nature Reviews Cancer*, *3*(1), 11-22. https://doi.org/10.1038/nrc969

Duma, N., Santana-Davila, R., & Molina, J. R. (2019). Non-Small Cell Lung Cancer: Epidemiology, Screening, Diagnosis, and Treatment. *Mayo Clin Proc*, *94*(8), 1623-1640. https://doi.org/10.1016/j.mayocp.2019.01.013

Dyson, H. J., & Wright, P. E. (2005). Intrinsically unstructured proteins and their functions. *Nat Rev Mol Cell Biol*, *6*(3), 197-208. https://doi.org/10.1038/nrm1589

Dytfeld, D., Luczak, M., Wrobel, T., Usnarska-Zubkiewicz, L., Brzezniakiewicz, K., Jamroziak, K., Giannopoulos, K., Przybylowicz-Chalecka, A., Ratajczak, B., Czerwinska-Rybak, J., Nowicki, A., Joks, M., Czechowska, E., Zawartko, M., Szczepaniak, T., Grzasko, N., Morawska, M., Bochenek, M., Kubicki, T., Morawska, M., Tusznio, K., Jakubowiak, A., & Komarnicki, M. A. (2016). Comparative proteomic profiling of refractory/relapsed multiple myeloma reveals biomarkers involved in resistance to bortezomib-based therapy. *Oncotarget*, *7*(35), 56726-56736. https://doi.org/10.18632/oncotarget.11059

Eisele, M. R., Reed, R. G., Rudack, T., Schweitzer, A., Beck, F., Nagy, I., Pfeifer, G., Plitzko, J. M., Baumeister, W., & Tomko Jr, R. J. (2018). Expanded coverage of the 26S proteasome conformational landscape reveals mechanisms of peptidase gating. *Cell reports*, *24*(5), 1301-1315. e1305.

Fabre, B., Lambour, T., Delobel, J., Amalric, F., Monsarrat, B., Burlet-Schiltz, O., & Bousquet-Dubouch, M. P. (2013). Subcellular distribution and dynamics of active proteasome complexes unraveled by a workflow combining in vivo complex cross-linking and quantitative proteomics. *Mol Cell Proteomics*, *12*(3), 687-699. https://doi.org/10.1074/mcp.M112.023317

Fabre, B., Lambour, T., Garrigues, L., Amalric, F., Vigneron, N., Menneteau, T., Stella, A., Monsarrat, B., Van den Eynde, B., & Burlet‐Schiltz, O. (2015). Deciphering preferential interactions within supramolecular protein complexes: the proteasome case. *Molecular systems biology*, *11*(1), 771.

Fabre, B., Lambour, T., Garrigues, L., Ducoux-Petit, M., Amalric, F., Monsarrat, B., Burlet-Schiltz, O., & Bousquet-Dubouch, M. P. (2014). Label-free quantitative proteomics reveals the dynamics of proteasome complexes composition and stoichiometry in a wide range of human cell lines. *J Proteome Res*, *13*(6), 3027-3037. https://doi.org/10.1021/pr500193k

Fan, J., Kamphorst, J. J., Mathew, R., Chung, M. K., White, E., Shlomi, T., & Rabinowitz, J. D. (2013). Glutamine‐driven oxidative phosphorylation is a major ATP source in transformed mammalian cells in both normoxia and hypoxia. *Molecular systems biology*, *9*(1), 712.

Farah, C. S., Dalley, A. J., Nguyen, P., Batstone, M., Kordbacheh, F., Perry-Keene, J., & Fielding, D. (2016). Improved surgical margin definition by narrow band imaging for resection of oral squamous cell carcinoma: A prospective gene expression profiling study. *Head Neck*, *38*(6), 832-839. https://doi.org/10.1002/hed.23989

Farajihaye Qazvini, F., Samadi, N., Saffari, M., Emami-Razavi, A. N., & Shirkoohi, R. (2019). Fibroblast growth factor-10 and epithelial-mesenchymal transition in colorectal cancer. *Excli j*, *18*, 530-539. https://doi.org/10.17179/excli2018-1784

Fares, J., Fares, M. Y., Khachfe, H. H., Salhab, H. A., & Fares, Y. (2020). Molecular principles of metastasis: a hallmark of cancer revisited. *Signal Transduction and Targeted Therapy*, *5*(1), 28. https://doi.org/10.1038/s41392-020-0134-x

Fehling, H., Swat, W., Laplace, C., Kühn, R., Rajewsky, K., Müller, U., & Von Boehmer, H. (1994). MHC class I expression in mice lacking the proteasome subunit LMP-7. *Science*, *265*(5176), 1234-1237.

Felip, E., Rosell, R., Maestre, J. A., Rodríguez-Paniagua, J. M., Morán, T., Astudillo, J., Alonso, G., Borro, J. M., González-Larriba, J. L., Torres, A., Camps, C., Guijarro, R., Isla, D., Aguiló, R., Alberola, V., Padilla, J., Sánchez-Palencia, A., Sánchez, J. J., Hermosilla, E., & Massuti, B. (2010). Preoperative chemotherapy plus surgery versus surgery plus adjuvant chemotherapy versus surgery alone in early-stage non-small-cell lung cancer. *J Clin Oncol*, *28*(19), 3138-3145. https://doi.org/10.1200/jco.2009.27.6204

Finley, D., Chen, X., & Walters, K. J. (2016). Gates, channels, and switches: elements of the proteasome machine. *Trends in biochemical sciences*, *41*(1), 77-93.

Folkmann, A. W., Noble, K. N., Cole, C. N., & Wente, S. R. (2011). Dbp5, Gle1-IP6 and Nup159: a working model for mRNP export. *Nucleus*, *2*(6), 540-548. https://doi.org/10.4161/nucl.2.6.17881

Fort, P., Kajava, A. V., Delsuc, F., & Coux, O. (2015). Evolution of proteasome regulators in eukaryotes. *Genome Biol Evol*, *7*(5), 1363-1379. https://doi.org/10.1093/gbe/evv068

Foss, G. S., & Prydz, H. (1999). Interferon regulatory factor 1 mediates the interferon-gamma induction of the human immunoproteasome subunit multicatalytic endopeptidase complex-like 1. *J Biol Chem*, *274*(49), 35196-35202. https://doi.org/10.1074/jbc.274.49.35196

Fouad, Y. A., & Aanei, C. (2017). Revisiting the hallmarks of cancer. *Am J Cancer Res*, *7*(5), 1016-1036.

Franken, N. A. P., Rodermond, H. M., Stap, J., Haveman, J., & van Bree, C. (2006). Clonogenic assay of cells in vitro. *Nature Protocols*, *1*(5), 2315-2319. https://doi.org/10.1038/nprot.2006.339

Frentzel, S., Kuhn-Hartmann, I., Gernold, M., Gött, P., Seelig, A., & Kloetzel, P. M. (1993). The major ‐ histocompatibility ‐ complex ‐ encoded β ‐ type proteasome subunits LMP2 and LMP7: Evidence that LMP2 and LMP7 are synthesized as proproteins and that cellular levels of both mRNA and LMP ‐ containing 20S proteasomes are differentially regulated. *European journal of biochemistry*, *216*(1), 119-126.

Frentzel, S., Pesold-Hurt, B., Seelig, A., & Kloetzel, P.-M. (1994). 20 S proteasomes are assembled via distinct precursor complexes processing of LMP2 and LMP7 proproteins takes place in 13–16 S preproteasome complexes. *Journal of molecular biology*, *236*(4), 975-981.

Freudenburg, W., Gautam, M., Chakraborty, P., James, J., Richards, J., Salvatori, A. S., Baldwin, A., Schriewer, J., Buller, R. M., Corbett, J. A., & Skowyra, D. (2013a). Immunoproteasome Activation During Early Antiviral Response in Mouse Pancreatic β-cells: New Insights into Auto-antigen Generation in Type I Diabetes? *J Clin Cell Immunol*, *4*(2). https://doi.org/10.4172/2155-9899.1000141

Freudenburg, W., Gautam, M., Chakraborty, P., James, J., Richards, J., Salvatori, A. S., Baldwin, A., Schriewer, J., Buller, R. M., Corbett, J. A., & Skowyra, D. (2013b). Reduction in ATP levels triggers immunoproteasome activation by the 11S (PA28) regulator during early antiviral response mediated by IFNβ in mouse pancreatic β-cells. *PLoS One*, *8*(2), e52408. https://doi.org/10.1371/journal.pone.0052408

Früh, K., Gossen, M., Wang, K., Bujard, H., Peterson, P. A., & Yang, Y. (1994). Displacement of housekeeping proteasome subunits by MHC ‐ encoded LMPs: a newly discovered mechanism for modulating the multicatalytic proteinase complex. *The EMBO journal*, *13*(14), 3236-3244.

Fuchs, B. C., & Bode, B. P. (2006). Stressing out over survival: glutamine as an apoptotic modulator. *Journal of Surgical Research*, *131*(1), 26-40.

Funakoshi, M., Tomko Jr, R. J., Kobayashi, H., & Hochstrasser, M. (2009). Multiple assembly chaperones govern biogenesis of the proteasome regulatory particle base. *Cell*, *137*(5), 887-899.

Gaczynska, M., Rock, K. L., & Goldberg, A. L. (1993). Gamma-interferon and expression of MHC genes regulate peptide hydrolysis by proteasomes. *Nature*, *365*(6443), 264-267. https://doi.org/10.1038/365264a0

Gaglio, D., Soldati, C., Vanoni, M., Alberghina, L., & Chiaradonna, F. (2009). Glutamine deprivation induces abortive s-phase rescued by deoxyribonucleotides in k-ras transformed fibroblasts. *PLoS One*, *4*(3), e4715.

Gajewski, T. F. (2015). The next hurdle in cancer immunotherapy: overcoming the non–T-cell–inflamed tumor microenvironment. Seminars in oncology,

Galliher, A. J., & Schiemann, W. P. (2006). β3Integrin and Src facilitate transforming growth factor-β mediated induction of epithelial-mesenchymal transition in mammary epithelial cells. *Breast cancer research*, *8*(4), 1-16.

Galluzzi, L., Vitale, I., Aaronson, S. A., Abrams, J. M., Adam, D., Agostinis, P., Alnemri, E. S., Altucci, L., Amelio, I., Andrews, D. W., Annicchiarico-Petruzzelli, M., Antonov, A. V., Arama, E., Baehrecke, E. H., Barlev, N. A., Bazan, N. G., Bernassola, F., Bertrand, M. J. M., Bianchi, K., Blagosklonny, M. V., Blomgren, K., Borner, C., Boya, P., Brenner, C., Campanella, M., Candi, E., Carmona-Gutierrez, D., Cecconi, F., Chan, F. K., Chandel, N. S., Cheng, E. H., Chipuk, J. E., Cidlowski, J. A., Ciechanover, A., Cohen, G. M., Conrad, M., Cubillos-Ruiz, J. R., Czabotar, P. E., D'Angiolella, V., Dawson, T. M., Dawson, V. L., De Laurenzi, V., De Maria, R., Debatin, K. M., DeBerardinis, R. J., Deshmukh, M., Di Daniele, N., Di Virgilio, F., Dixit, V. M., Dixon, S. J., Duckett, C. S., Dynlacht, B. D., El-Deiry, W. S., Elrod, J. W., Fimia, G. M., Fulda, S., García-Sáez, A. J., Garg, A. D., Garrido, C., Gavathiotis,

E., Golstein, P., Gottlieb, E., Green, D. R., Greene, L. A., Gronemeyer, H., Gross, A., Hajnoczky, G., Hardwick, J. M., Harris, I. S., Hengartner, M. O., Hetz, C., Ichijo, H., Jäättelä, M., Joseph, B., Jost, P. J., Juin, P. P., Kaiser, W. J., Karin, M., Kaufmann, T., Kepp, O., Kimchi, A., Kitsis, R. N., Klionsky, D. J., Knight, R. A., Kumar, S., Lee, S. W., Lemasters, J. J., Levine, B., Linkermann, A., Lipton, S. A., Lockshin, R. A., López-Otín, C., Lowe, S. W., Luedde, T., Lugli, E., MacFarlane, M., Madeo, F., Malewicz, M., Malorni, W., Manic, G., Marine, J. C., Martin, S. J., Martinou, J. C., Medema, J. P., Mehlen, P., Meier, P., Melino, S., Miao, E. A., Molkentin, J. D., Moll, U. M., Muñoz-Pinedo, C., Nagata, S., Nuñez, G., Oberst, A., Oren, M., Overholtzer, M., Pagano, M., Panaretakis, T., Pasparakis, M., Penninger, J. M., Pereira, D. M., Pervaiz, S., Peter, M. E., Piacentini, M., Pinton, P., Prehn, J. H. M., Puthalakath, H., Rabinovich, G. A., Rehm, M., Rizzuto, R., Rodrigues, C. M. P., Rubinsztein, D. C., Rudel, T., Ryan, K. M., Sayan, E., Scorrano, L., Shao, F., Shi, Y., Silke, J., Simon, H. U., Sistigu, A., Stockwell, B. R., Strasser, A., Szabadkai, G., Tait, S. W. G., Tang, D., Tavernarakis, N., Thorburn, A., Tsujimoto, Y., Turk, B., Vanden Berghe, T., Vandenabeele, P., Vander Heiden, M. G., Villunger, A., Virgin, H. W., Vousden, K. H., Vucic, D., Wagner, E. F., Walczak, H., Wallach, D., Wang, Y., Wells, J. A., Wood, W., Yuan, J., Zakeri, Z., Zhivotovsky, B., Zitvogel, L., Melino, G., & Kroemer, G. (2018). Molecular mechanisms of cell death: recommendations of the Nomenclature Committee on Cell Death 2018. *Cell Death Differ*, *25*(3), 486-541. https://doi.org/10.1038/s41418-017-0012-4

Ge, S., Huang, H., Huang, W., Ji, R., Chen, J., Wu, S., Wang, L., Huang, T., Sheng, Y., Yan, H., Lu, C., & Ma, L. (2022). PSME4 Activates mTOR Signaling and Promotes the Malignant Progression of Hepatocellular Carcinoma. *Int J Gen Med*, *15*, 885-895. https://doi.org/10.2147/IJGM.S344360

George, J., Lim, J. S., Jang, S. J., Cun, Y., Ozretić, L., Kong, G., Leenders, F., Lu, X., Fernández-Cuesta, L., Bosco, G., Müller, C., Dahmen, I., Jahchan, N. S., Park, K. S., Yang, D., Karnezis, A. N., Vaka, D., Torres, A., Wang, M. S., Korbel, J. O., Menon, R., Chun, S. M., Kim, D., Wilkerson, M., Hayes, N., Engelmann, D., Pützer, B., Bos, M., Michels, S., Vlasic, I., Seidel, D., Pinther, B., Schaub, P., Becker, C., Altmüller, J., Yokota, J., Kohno, T., Iwakawa, R., Tsuta, K., Noguchi, M., Muley, T., Hoffmann, H., Schnabel, P. A., Petersen, I., Chen, Y., Soltermann, A., Tischler, V., Choi, C. M., Kim, Y. H., Massion, P. P., Zou, Y., Jovanovic, D., Kontic, M., Wright, G. M., Russell, P. A., Solomon, B., Koch, I., Lindner, M., Muscarella, L. A., la Torre, A., Field, J. K., Jakopovic, M., Knezevic, J., Castaños-Vélez, E., Roz, L., Pastorino, U., Brustugun, O. T., Lund-Iversen, M., Thunnissen, E., Köhler, J., Schuler, M., Botling, J., Sandelin, M., Sanchez-Cespedes, M., Salvesen, H. B., Achter, V., Lang, U., Bogus, M., Schneider, P. M., Zander, T., Ansén, S., Hallek, M., Wolf, J., Vingron, M., Yatabe, Y., Travis, W. D., Nürnberg, P., Reinhardt, C., Perner, S., Heukamp, L., Büttner, R., Haas, S. A., Brambilla, E., Peifer, M., Sage, J., & Thomas, R. K. (2015). Comprehensive genomic profiles of small cell lung cancer. *Nature*, *524*(7563), 47-53. https://doi.org/10.1038/nature14664

Gerckens, M., Schorpp, K., Pelizza, F., Wögrath, M., Reichau, K., Ma, H., Dworsky, A.-M., Sengupta, A., Stoleriu, M. G., Heinzelmann, K., Merl-Pham, J., Irmler, M., Alsafadi, H. N., Trenkenschuh, E., Sarnova, L., Jirouskova, M., Frieß, W., Hauck, S. M., Beckers, J., Kneidinger, N., Behr, J., Hilgendorff, A., Hadian, K., Lindner, M., Königshoff, M., Eickelberg, O., Gregor, M., Plettenburg, O., Yildirim, A. Ö., & Burgstaller, G. (2021). Phenotypic drug screening in a human fibrosis model identified a novel class of antifibrotic therapeutics. *Science Advances*, *7*(52), eabb3673. https://doi.org/doi:10.1126/sciadv.abb3673

Gillespie, M., Jassal, B., Stephan, R., Milacic, M., Rothfels, K., Senff-Ribeiro, A., Griss, J., Sevilla, C., Matthews, L., Gong, C., Deng, C., Varusai, T., Ragueneau, E., Haider, Y., May, B., Shamovsky, V., Weiser, J., Brunson, T., Sanati, N., Beckman, L., Shao, X., Fabregat, A., Sidiropoulos, K., Murillo, J., Viteri, G., Cook, J., Shorser, S., Bader, G., Demir, E., Sander, C., Haw, R., Wu, G., Stein, L., Hermjakob, H., & D'Eustachio, P. (2021). The reactome pathway knowledgebase 2022. *Nucleic Acids Research*, *50*(D1), D687-D692. https://doi.org/10.1093/nar/gkab1028

Gilligan, D., Nicolson, M., Smith, I., Groen, H., Dalesio, O., Goldstraw, P., Hatton, M., Hopwood, P., Manegold, C., Schramel, F., Smit, H., van Meerbeeck, J., Nankivell, M., Parmar, M., Pugh, C., & Stephens, R. (2007). Preoperative chemotherapy in patients with resectable non-small cell lung cancer: results of the MRC LU22/NVALT 2/EORTC 08012 multicentre randomised trial and update of systematic review. *Lancet*, *369*(9577), 1929-1937. https://doi.org/10.1016/s0140-6736(07)60714-4

Giopanou, I., Lilis, I., Papaleonidopoulos, V., Agalioti, T., Kanellakis, N. I., Spiropoulou, N., Spella, M., & Stathopoulos, G. T. (2017). Tumor-derived osteopontin isoforms cooperate with TRP53 and CCL2 to promote lung metastasis. *Oncoimmunology*, *6*(1), e1256528. https://doi.org/10.1080/2162402x.2016.1256528

Goetzke, C. C., Althof, N., Neumaier, H. L., Heuser, A., Kaya, Z., Kespohl, M., Klingel, K., & Beling, A. (2021). Mitigated viral myocarditis in A/J mice by the immunoproteasome inhibitor ONX 0914 depends on inhibition of systemic inflammatory responses in CoxsackievirusB3 infection. *Basic Research in Cardiology*, *116*(1), 1-16.

Goldberg, A. L., Cascio, P., Saric, T., & Rock, K. L. (2002). The importance of the proteasome and subsequent proteolytic steps in the generation of antigenic peptides. *Mol Immunol*, *39*(3-4), 147-164. https://doi.org/10.1016/s0161-5890(02)00098-6

Gopalakrishnan, K., Kumarasamy, S., Abdul-Majeed, S., Kalinoski, A. L., Morgan, E. E., Gohara, A. F., Nauli, S. M., Filipiak, W. E., Saunders, T. L., & Joe, B. (2012). Targeted disruption of Adamts16 gene in a rat genetic model of hypertension. *Proceedings of the National Academy of Sciences*, *109*(50), 20555-20559. https://doi.org/doi:10.1073/pnas.1211290109

Goss, G. D., O'Callaghan, C., Lorimer, I., Tsao, M. S., Masters, G. A., Jett, J., Edelman, M. J., Lilenbaum, R., Choy, H., Khuri, F., Pisters, K., Gandara, D., Kernstine, K., Butts, C., Noble, J., Hensing, T. A., Rowland, K., Schiller, J., Ding, K., & Shepherd, F. A. (2013). Gefitinib versus placebo in completely resected non-small-cell lung cancer: results of the NCIC CTG BR19 study. *J Clin Oncol*, *31*(27), 3320-3326. https://doi.org/10.1200/jco.2013.51.1816

Greten, F. R., & Grivennikov, S. I. (2019). Inflammation and Cancer: Triggers, Mechanisms, and Consequences. *Immunity*, *51*(1), 27-41. https://doi.org/10.1016/j.immuni.2019.06.025

Gridelli, C., Rossi, A., Carbone, D. P., Guarize, J., Karachaliou, N., Mok, T., Petrella, F., Spaggiari, L., & Rosell, R. (2015). Non-small-cell lung cancer. *Nat Rev Dis Primers*, *1*, 15009. https://doi.org/10.1038/nrdp.2015.9

Grivennikov, S. I., Greten, F. R., & Karin, M. (2010). Immunity, inflammation, and cancer. *Cell*, *140*(6), 883-899. https://doi.org/10.1016/j.cell.2010.01.025

Groettrup, M., Khan, S., Schwarz, K., & Schmidtke, G. (2001). Interferon-gamma inducible exchanges of 20S proteasome active site subunits: why? *Biochimie*, *83*(3-4), 367-372. https://doi.org/10.1016/s0300-9084(01)01251-2

Groettrup, M., Kirk, C. J., & Basler, M. (2010). Proteasomes in immune cells: more than peptide producers? *Nat Rev Immunol*, *10*(1), 73-78. https://doi.org/10.1038/nri2687

Groettrup, M., Kraft, R., Kostka, S., Standera, S., Stohwasser, R., & Kloetzel, P. M. (1996). A third interferon - γ - induced subunit exchange in the 20S proteasome. *European journal of immunology*, *26*(4), 863-869.

Groettrup, M., Soza, A., Eggers, M., Kuehn, L., Dick, T. P., Schild, H., Rammensee, H.-G., Koszinowski, U. H., & Kloetzel, P.-M. (1996). A role for the proteasome regulator PA28α in antigen presentation. *Nature*, *381*(6578), 166-168.

Groettrup, M., Standera, S., Stohwasser, R., & Kloetzel, P. M. (1997). The subunits MECL-1 and LMP2 are mutually required for incorporation into the 20S proteasome. *Proc Natl Acad Sci U S A*, *94*(17), 8970-8975. https://doi.org/10.1073/pnas.94.17.8970

Groettrup, M., Standera, S., Stohwasser, R., & Kloetzel, P. M. (1997). The subunits MECL-1 and LMP2 are mutually required for incorporation into the 20S proteasome. *Proceedings of the National Academy of Sciences*, *94*(17), 8970-8975. https://doi.org/doi:10.1073/pnas.94.17.8970

Groll, M., Bajorek, M., Köhler, A., Moroder, L., Rubin, D. M., Huber, R., Glickman, M. H., & Finley, D. (2000). A gated channel into the proteasome core particle. *Nat Struct Biol*, *7*(11), 1062-1067. https://doi.org/10.1038/80992

Groll, M., Ditzel, L., Löwe, J., Stock, D., Bochtler, M., Bartunik, H. D., & Huber, R. (1997). Structure of 20S proteasome from yeast at 2.4Å resolution. *Nature*, *386*(6624), 463-471. https://doi.org/10.1038/386463a0

Grosche, A., Hauser, A., Lepper, M. F., Mayo, R., von Toerne, C., Merl-Pham, J., & Hauck, S. M. (2016). The Proteome of Native Adult Müller Glial Cells From Murine Retina. *Mol Cell Proteomics*, *15*(2), 462-480. https://doi.org/10.1074/mcp.M115.052183

Gruber, G., Hess, J., Stiefel, C., Aebersold, D., Zimmer, Y., Greiner, R., Studer, U., Altermatt, H., Hlushchuk, R., & Djonov, V. (2005). Correlation between the tumoral expression of β3-integrin and outcome in cervical cancer patients who had undergone radiotherapy. *British Journal of Cancer*, *92*(1), 41-46.

Gstraunthaler, G. (2003). Alternatives to the use of fetal bovine serum: Serum-free cell culture. *ALTEX - Alternatives to animal experimentation*, *20*(4), 275-281. https://doi.org/10.14573/altex.2003.4.257

Guan, H., Wang, Y., Yu, T., Huang, Y., Li, M., Saeed, A., Perculija, V., Li, D., Xiao, J., Wang, D., Zhu, P., & Ouyang, S. (2020). Cryo-EM structures of the human PA200 and PA200-20S complex reveal regulation of proteasome gate opening and two PA200 apertures. *PLoS Biol*, *18*(3), e3000654. https://doi.org/10.1371/journal.pbio.3000654

Gunes, M. F., Akpinar, M. B., Comertoglu, I., Akyol, S., Demirçelik, B., Gurel, O. M., Aynekin, B., Erdemli, H. K., Ates, M., & Eryonucu, B. (2016). The investigation of a disintegrin and metalloproteinase with thrombospondin motifs (ADAMTS) 1, 5 and 16 in thoracic aortic aneurysms and dissections. *Clin Lab*, *62*(3), 425-433.

Guo, Y., Dong, X., Jin, J., & He, Y. (2021). The Expression Patterns and Prognostic Value of the Proteasome Activator Subunit Gene Family in Gastric Cancer Based on Integrated Analysis. *Front Cell Dev Biol*, *9*, 663001. https://doi.org/10.3389/fcell.2021.663001

Gutcher, I., & Becher, B. (2007). APC-derived cytokines and T cell polarization in autoimmune inflammation. *J Clin Invest*, *117*(5), 1119-1127. https://doi.org/10.1172/jci31720

Gwinn, D. M., Lee, A. G., Briones-Martin-del-Campo, M., Conn, C. S., Simpson, D. R., Scott, A. I., Le, A., Cowan, T. M., Ruggero, D., & Sweet-Cordero, E. A. (2018). Oncogenic KRAS regulates amino acid homeostasis and asparagine biosynthesis via ATF4 and alters sensitivity to L-asparaginase. *Cancer Cell*, *33*(1), 91-107. e106.

Hanahan, D. (2022). Hallmarks of Cancer: New Dimensions. *Cancer Discov*, *12*(1), 31-46. https://doi.org/10.1158/2159-8290.CD-21-1059

Hanahan, D., & Weinberg, R. A. (2000). The hallmarks of cancer. *Cell*, *100*(1), 57-70. https://doi.org/10.1016/s0092-8674(00)81683-9

Hanahan, D., & Weinberg, R. A. (2011). Hallmarks of cancer: the next generation. *Cell*, *144*(5), 646-674. https://doi.org/10.1016/j.cell.2011.02.013

Hanakahi, L. A., & West, S. C. (2002). Specific interaction of IP6 with human Ku70/80, the DNA-binding subunit of DNA-PK. *EMBO J*, *21*(8), 2038-2044. https://doi.org/10.1093/emboj/21.8.2038

Hao, Y., Baker, D., & Ten Dijke, P. (2019). TGF-β-Mediated Epithelial-Mesenchymal Transition and Cancer Metastasis. *Int J Mol Sci*, *20*(11). https://doi.org/10.3390/ijms20112767

Hauck, S. M., Dietter, J., Kramer, R. L., Hofmaier, F., Zipplies, J. K., Amann, B., Feuchtinger, A., Deeg, C. A., & Ueffing, M. (2010). Deciphering membrane-associated molecular processes in target tissue of autoimmune uveitis by label-free quantitative mass spectrometry. *Molecular & Cellular Proteomics*, *9*(10), 2292-2305.

Havel, J. J., Chowell, D., & Chan, T. A. (2019). The evolving landscape of biomarkers for checkpoint inhibitor immunotherapy. *Nat Rev Cancer*, *19*(3), 133-150. https://doi.org/10.1038/s41568-019-0116-x

Hodgkinson, C. L., Morrow, C. J., Li, Y., Metcalf, R. L., Rothwell, D. G., Trapani, F., Polanski, R., Burt, D. J., Simpson, K. L., Morris, K., Pepper, S. D., Nonaka, D., Greystoke, A., Kelly, P., Bola, B., Krebs, M. G., Antonello, J., Ayub, M., Faulkner, S., Priest, L., Carter, L., Tate, C., Miller, C. J., Blackhall, F., Brady, G., & Dive, C. (2014). Tumorigenicity and genetic profiling of circulating tumor cells in small-cell lung cancer. *Nat Med*, *20*(8), 897-903. https://doi.org/10.1038/nm.3600

Hosotani, R., Kawaguchi, M., Masui, T., Koshiba, T., Ida, J., Fujimoto, K., Wada, M., Doi, R., & Imamura, M. (2002). Expression of integrin αvβ3 in pancreatic carcinoma: relation to MMP-2 activation and lymph node metastasis. *Pancreas*, *25*(2), e30-e35.

Hou, J. M., Krebs, M. G., Lancashire, L., Sloane, R., Backen, A., Swain, R. K., Priest, L. J., Greystoke, A., Zhou, C., Morris, K., Ward, T., Blackhall, F. H., & Dive, C. (2012). Clinical significance and molecular characteristics of circulating tumor cells and circulating tumor microemboli in patients with small-cell lung cancer. *J Clin Oncol*, *30*(5), 525-532. https://doi.org/10.1200/jco.2010.33.3716

Howlader, N., Forjaz, G., Mooradian, M. J., Meza, R., Kong, C. Y., Cronin, K. A., Mariotto, A. B., Lowy, D. R., & Feuer, E. J. (2020). The Effect of Advances in Lung-Cancer Treatment on Population Mortality. *N Engl J Med*, *383*(7), 640-649. https://doi.org/10.1056/NEJMoa1916623

Hu, W., Zhang, C., Wu, R., Sun, Y., Levine, A., & Feng, Z. (2010). Glutaminase 2, a novel p53 target gene regulating energy metabolism and antioxidant function. *Proceedings of the National Academy of Sciences*, *107*(16), 7455-7460.

Huang, R., Wei, Y., Hung, R. J., Liu, G., Su, L., Zhang, R., Zong, X., Zhang, Z. F., Morgenstern, H., Brüske, I., Heinrich, J., Hong, Y. C., Kim, J. H., Cote, M., Wenzlaff, A., Schwartz, A. G., Stucker, I., McLaughlin, J., Marcus, M. W., Davies, M. P., Liloglou, T., Field, J. K., Matsuo, K., Barnett, M., Thornquist, M., Goodman, G., Wang, Y., Chen, S., Yang, P., Duell, E. J., Andrew, A. S., Lazarus, P., Muscat, J., Woll, P., Horsman, J., Teare, M. D., Flugelman, A., Rennert, G., Zhang, Y., Brenner, H., Stegmaier, C., van der Heijden, E. H., Aben, K., Kiemeney, L., Barros-Dios, J., Pérez-Ríos, M., Ruano-Ravina, A., Caporaso, N. E., Bertazzi, P. A., Landi, M. T., Dai, J., Hongbing Shen, H., Fernandez-Tardon, G., Rodriguez-Suarez, M., Tardon, A., & Christiani, D. C. (2015). Associated Links Among Smoking, Chronic Obstructive Pulmonary Disease, and Small Cell Lung Cancer: A Pooled Analysis in

the International Lung Cancer Consortium. *EBioMedicine*, *2*(11), 1677-1685. https://doi.org/10.1016/j.ebiom.2015.09.031

Huber, E. M., Basler, M., Schwab, R., Heinemeyer, W., Kirk, C. J., Groettrup, M., & Groll, M. (2012). Immuno- and constitutive proteasome crystal structures reveal differences in substrate and inhibitor specificity. *Cell*, *148*(4), 727-738. https://doi.org/10.1016/j.cell.2011.12.030

Huber, E. M., & Groll, M. (2017). The mammalian proteasome activator PA28 forms an asymmetric α4β3 complex. *Structure*, *25*(10), 1473-1480. e1473.

Hugo, W., Zaretsky, J. M., Sun, L., Song, C., Moreno, B. H., Hu-Lieskovan, S., Berent-Maoz, B., Pang, J., Chmielowski, B., & Cherry, G. (2016). Genomic and transcriptomic features of response to anti-PD-1 therapy in metastatic melanoma. *Cell*, *165*(1), 35-44.

ICE Analysis. In. (2019). (Version v3.0) Synthego.

Iwata, R., Hyoung Lee, J., Hayashi, M., Dianzani, U., Ofune, K., Maruyama, M., Oe, S., Ito, T., Hashiba, T., Yoshimura, K., Nonaka, M., Nakano, Y., Norian, L., Nakano, I., & Asai, A. (2020). ICOSLG-mediated regulatory T-cell expansion and IL-10 production promote progression of glioblastoma. *Neuro Oncol*, *22*(3), 333-344. https://doi.org/10.1093/neuonc/noz204

Jagannathan, S., Vad, N., Vallabhapurapu, S., Vallabhapurapu, S., Anderson, K. C., & Driscoll, J. J. (2015). MiR-29b replacement inhibits proteasomes and disrupts aggresome+autophagosome formation to enhance the antimyeloma benefit of bortezomib. *Leukemia*, *29*(3), 727-738. https://doi.org/10.1038/leu.2014.279

Javitt, A., Shmueli, M. D., Kramer, M. P., Kolodziejczyk, A. A., Cohen, I. J., Kamer, I., Litchfield, K., Bab-Dinitz, E., Zadok, O., & Neiens, V. (2021). The proteasome regulator PSME4 drives immune evasion and abrogates anti-tumor immunity in NSCLC. *bioRxiv*.

Javitt, A., Shmueli, M. D., Kramer, M. P., Kolodziejczyk, A. A., Cohen, I. J., Radomir, L., Sheban, D., Kamer, I., Litchfield, K., Bab-Dinitz, E., Zadok, O., Neiens, V., Ulman, A., Wolf-Levy, H., Eisenberg-Lerner, A., Kacen, A., Alon, M., Rêgo, A. T., Stacher-Priehse, E., Lindner, M., Koch, I., Bar, J., Swanton, C., Samuels, Y., Levin, Y., da Fonseca, P. C. A., Elinav, E., Friedman, N., Meiners, S., & Merbl, Y. (2023). The proteasome regulator PSME4 modulates proteasome activity and antigen diversity to abrogate antitumor immunity in NSCLC. *Nature Cancer*, *4*(5), 629-647. https://doi.org/10.1038/s43018-023-00557-4

Jemal, A., Center, M. M., DeSantis, C., & Ward, E. M. (2010). Global patterns of cancer incidence and mortality rates and trends. *Cancer Epidemiol Biomarkers Prev*, *19*(8), 1893-1907. https://doi.org/10.1158/1055-9965.Epi-10-0437

Jiang, L., Kon, N., Li, T., Wang, S.-J., Su, T., Hibshoosh, H., Baer, R., & Gu, W. (2015). Ferroptosis as a p53-mediated activity during tumour suppression. *Nature*, *520*(7545), 57-62.

Jiang, T.-X., Zou, J.-B., Zhu, Q.-Q., Liu, C. H., Wang, G.-F., Du, T.-T., Luo, Z.-Y., Guo, F., Zhou, L.-M., & Liu, J.-J. (2019). SIP/CacyBP promotes autophagy by regulating levels of BRUCE/Apollon, which stimulates LC3-I degradation. *Proceedings of the National Academy of Sciences*, *116*(27), 13404-13413.

Jiang, T. X., Ma, S., Han, X., Luo, Z. Y., Zhu, Q. Q., Chiba, T., Xie, W., Lin, K., & Qiu, X. B. (2021). Proteasome activator PA200 maintains stability of histone marks during transcription and aging. *Theranostics*, *11*(3), 1458-1472. https://doi.org/10.7150/thno.48744

Jiao, C., Li, L., Zhang, P., Zhang, L., Li, K., Fang, R., Yuan, L., Shi, K., Pan, L., & Guo, Q. (2020). REGγ ablation impedes dedifferentiation of anaplastic thyroid carcinoma and

accentuates radio-therapeutic response by regulating the Smad7-TGF-β pathway. *Cell Death & Differentiation*, *27*(2), 497-508.

Joe, B., Saad, Y., Lee, N. H., Frank, B. C., Achinike, O. H., Luu, T. V., Gopalakrishnan, K., Toland, E. J., Farms, P., Yerga-Woolwine, S., Manickavasagam, E., Rapp, J. P., Garrett, M. R., Coe, D., Apte, S. S., Rankinen, T., Pérusse, L., Ehret, G. B., Ganesh, S. K., Cooper, R. S., O'Connor, A., Rice, T., Weder, A. B., Chakravarti, A., Rao, D. C., & Bouchard, C. (2009). Positional identification of variants of Adamts16 linked to inherited hypertension. *Human Molecular Genetics*, *18*(15), 2825-2838. https://doi.org/10.1093/hmg/ddp218

Jones, J., Otu, H., Spentzos, D., Kolia, S., Inan, M., Beecken, W. D., Fellbaum, C., Gu, X., Joseph, M., Pantuck, A. J., Jonas, D., & Libermann, T. A. (2005). Gene signatures of progression and metastasis in renal cell cancer. *Clin Cancer Res*, *11*(16), 5730-5739. https://doi.org/10.1158/1078-0432.CCR-04-2225

Jones, K. B., Salah, Z., Del Mare, S., Galasso, M., Gaudio, E., Nuovo, G. J., Lovat, F., LeBlanc, K., Palatini, J., Randall, R. L., Volinia, S., Stein, G. S., Croce, C. M., Lian, J. B., & Aqeilan, R. I. (2012). miRNA signatures associate with pathogenesis and progression of osteosarcoma. *Cancer Res*, *72*(7), 1865-1877. https://doi.org/10.1158/0008-5472.CAN-11-2663

Kalaora, S., Lee, J. S., Barnea, E., Levy, R., Greenberg, P., Alon, M., Yagel, G., Bar Eli, G., Oren, R., & Peri, A. (2020). Immunoproteasome expression is associated with better prognosis and response to checkpoint therapies in melanoma. *Nature communications*, *11*(1), 896.

Kalim, K. W., Basler, M., Kirk, C. J., & Groettrup, M. (2012). Immunoproteasome subunit LMP7 deficiency and inhibition suppresses Th1 and Th17 but enhances regulatory T cell differentiation. *The Journal of Immunology*, *189*(8), 4182-4193.

Kalim, K. W., Basler, M., Kirk, C. J., & Groettrup, M. (2012). Immunoproteasome subunit LMP7 deficiency and inhibition suppresses Th1 and Th17 but enhances regulatory T cell differentiation. *J Immunol*, *189*(8), 4182-4193. https://doi.org/10.4049/jimmunol.1201183

Kalluri, R., & Weinberg, R. A. (2009). The basics of epithelial-mesenchymal transition. *J Clin Invest*, *119*(6), 1420-1428. https://doi.org/10.1172/jci39104

Kaneko, T., Hamazaki, J., Iemura, S.-i., Sasaki, K., Furuyama, K., Natsume, T., Tanaka, K., & Murata, S. (2009). Assembly pathway of the Mammalian proteasome base subcomplex is mediated by multiple specific chaperones. *Cell*, *137*(5), 914-925.

Kelly, K., Altorki, N. K., Eberhardt, W. E., O'Brien, M. E., Spigel, D. R., Crinò, L., Tsai, C. M., Kim, J. H., Cho, E. K., Hoffman, P. C., Orlov, S. V., Serwatowski, P., Wang, J., Foley, M. A., Horan, J. D., & Shepherd, F. A. (2015). Adjuvant Erlotinib Versus Placebo in Patients With Stage IB-IIIA Non-Small-Cell Lung Cancer (RADIANT): A Randomized, Double-Blind, Phase III Trial. *J Clin Oncol*, *33*(34), 4007-4014. https://doi.org/10.1200/jco.2015.61.8918

Khor, B., Bredemeyer, A. L., Huang, C. Y., Turnbull, I. R., Evans, R., Maggi, L. B., Jr., White, J. M., Walker, L. M., Carnes, K., Hess, R. A., & Sleckman, B. P. (2006). Proteasome activator PA200 is required for normal spermatogenesis. *Mol Cell Biol*, *26*(8), 2999-3007. https://doi.org/10.1128/MCB.26.8.2999-3007.2006

Kim, J. M., & Chen, D. S. (2016). Immune escape to PD-L1/PD-1 blockade: seven steps to success (or failure). *Ann Oncol*, *27*(8), 1492-1504. https://doi.org/10.1093/annonc/mdw217

Kim, S. K., & Cho, S. W. (2022). The Evasion Mechanisms of Cancer Immunity and Drug Intervention in the Tumor Microenvironment. *Front Pharmacol*, *13*, 868695. https://doi.org/10.3389/fphar.2022.868695

Kincaid, E. Z., Che, J. W., York, I., Escobar, H., Reyes-Vargas, E., Delgado, J. C., Welsh, R. M., Karow, M. L., Murphy, A. J., & Valenzuela, D. M. (2012). Mice completely lacking immunoproteasomes show major changes in antigen presentation. *Nature immunology*, *13*(2), 129-135.

Kincaid, E. Z., Che, J. W., York, I., Escobar, H., Reyes-Vargas, E., Delgado, J. C., Welsh, R. M., Karow, M. L., Murphy, A. J., Valenzuela, D. M., Yancopoulos, G. D., & Rock, K. L. (2012). Mice completely lacking immunoproteasomes show major changes in antigen presentation. *Nature immunology*, *13*(2), 129-135. https://doi.org/10.1038/ni.2203

Kingsbury, D. J., Griffin, T. A., & Colbert, R. A. (2000). Novel propeptide function in 20 S proteasome assembly influences beta subunit composition. *J Biol Chem*, *275*(31), 24156-24162. https://doi.org/10.1074/jbc.M001742200

Kish-Trier, E., & Hill, C. P. (2013). Structural biology of the proteasome. *Annu Rev Biophys*, *42*, 29-49. https://doi.org/10.1146/annurev-biophys-083012-130417

Kiuchi, T., Tomaru, U., Ishizu, A., Imagawa, M., Iwasaki, S., Suzuki, A., Otsuka, N., Ohhara, Y., Kinoshita, I., Matsuno, Y., Dosaka-Akita, H., & Kasahara, M. (2021). Expression of the immunoproteasome subunit β5i in non-small cell lung carcinomas. *J Clin Pathol*, *74*(5), 300-306. https://doi.org/10.1136/jclinpath-2020-206618

Kniepert, A., & Groettrup, M. (2014). The unique functions of tissue-specific proteasomes. *Trends Biochem Sci*, *39*(1), 17-24. https://doi.org/10.1016/j.tibs.2013.10.004

Kong, Q.-L., An, X.-Z., Guan, X.-M., Ma, Y.-M., Li, P.-F., Liang, S.-Y., Hu, Y.-N., Cui, Y.-H., & Yu, J. (2017). Expression of β-integrin family members in children with T-cell acute lymphoblastic leukemia. *Zhongguo Dang dai er ke za zhi= Chinese Journal of Contemporary Pediatrics*, *19*(6), 620-626.

Kopp, F., Dahlmann, B., & Kuehn, L. (2001). Reconstitution of hybrid proteasomes from purified PA700-20 S complexes and PA28alphabeta activator: ultrastructure and peptidase activities. *J Mol Biol*, *313*(3), 465-471. https://doi.org/10.1006/jmbi.2001.5063

Korn, T., & Hiltensperger, M. (2021). Role of IL-6 in the commitment of T cell subsets. *Cytokine*, *146*, 155654. https://doi.org/10.1016/j.cyto.2021.155654

Kuleshov, M. V., Jones, M. R., Rouillard, A. D., Fernandez, N. F., Duan, Q., Wang, Z., Koplev, S., Jenkins, S. L., Jagodnik, K. M., Lachmann, A., McDermott, M. G., Monteiro, C. D., Gundersen, G. W., & Ma'ayan, A. (2016). Enrichr: a comprehensive gene set enrichment analysis web server 2016 update. *Nucleic Acids Res*, *44*(W1), W90-97. https://doi.org/10.1093/nar/gkw377

Kumar Deshmukh, F., Yaffe, D., Olshina, M. A., Ben-Nissan, G., & Sharon, M. (2019). The Contribution of the 20S Proteasome to Proteostasis. *Biomolecules*, *9*(5). https://doi.org/10.3390/biom9050190

Lamichhane, D. K., Kim, H. C., Choi, C. M., Shin, M. H., Shim, Y. M., Leem, J. H., Ryu, J. S., Nam, H. S., & Park, S. M. (2017). Lung Cancer Risk and Residential Exposure to Air Pollution: A Korean Population-Based Case-Control Study. *Yonsei Med J*, *58*(6), 1111-1118. https://doi.org/10.3349/ymj.2017.58.6.1111

Lander, G. C., Martin, A., & Nogales, E. (2013). The proteasome under the microscope: the regulatory particle in focus. *Current opinion in structural biology*, *23*(2), 243-251.

Lee, C. K., Gimeno, R., & Levy, D. E. (1999). Differential regulation of constitutive major histocompatibility complex class I expression in T and B lymphocytes. *J Exp Med*, *190*(10), 1451-1464. https://doi.org/10.1084/jem.190.10.1451

Lee, M., Song, I. H., Heo, S. H., Kim, Y. A., Park, I. A., Bang, W. S., Park, H. S., Gong, G., & Lee, H. J. (2019). Expression of Immunoproteasome Subunit LMP7 in Breast

Cancer and Its Association with Immune-Related Markers. *Cancer Res Treat*, *51*(1), 80-89. https://doi.org/10.4143/crt.2017.500

Leister, H., Krause, F. F., Mahdavi, R., Steinhoff, U., & Visekruna, A. (2022). The Role of Immunoproteasomes in Tumor-Immune Cell Interactions in Melanoma and Colon Cancer. *Archivum Immunologiae et Therapiae Experimentalis*, *70*(1), 5. https://doi.org/10.1007/s00005-022-00644-x

Leister, H., Luu, M., Staudenraus, D., Lopez Krol, A., Mollenkopf, H.-J., Sharma, A., Schmerer, N., Schulte, L. N., Bertrams, W., & Schmeck, B. (2021). Pro-and antitumorigenic capacity of immunoproteasomes in shaping the tumor microenvironment. *Cancer immunology research*, *9*(6), 682-692.

Levin, A., Minis, A., Lalazar, G., Rodriguez, J., & Steller, H. (2018). PSMD5 Inactivation Promotes 26S Proteasome Assembly during Colorectal Tumor ProgressionEnhanced Proteasome Assembly Mediates Tumor Proteostasis. *Cancer research*, *78*(13), 3458-3468.

Levine, A. J., & Puzio-Kuter, A. M. (2010). The control of the metabolic switch in cancers by oncogenes and tumor suppressor genes. *Science*, *330*(6009), 1340-1344.

Levy-Barda, A., Lerenthal, Y., Davis, A. J., Chung, Y. M., Essers, J., Shao, Z., Van Vliet, N., Chen, D. J., Hu, M. C., & Kanaar, R. (2011). Involvement of the nuclear proteasome activator PA28γ in the cellular response to DNA double-strand breaks. *Cell cycle*, *10*(24), 4300-4310.

Li, C.-H., Liu, C.-W., Tsai, C.-H., Peng, Y.-J., Yang, Y.-H., Liao, P.-L., Lee, C.-C., Cheng, Y.-W., & Kang, J.-J. (2017). Cytoplasmic aryl hydrocarbon receptor regulates glycogen synthase kinase 3 beta, accelerates vimentin degradation, and suppresses epithelial–mesenchymal transition in non-small cell lung cancer cells. *Archives of Toxicology*, *91*(5), 2165-2178. https://doi.org/10.1007/s00204-016-1870-0

Liberzon, A., Subramanian, A., Pinchback, R., Thorvaldsdóttir, H., Tamayo, P., & Mesirov, J. P. (2011). Molecular signatures database (MSigDB) 3.0. *Bioinformatics*, *27*(12), 1739-1740. https://doi.org/10.1093/bioinformatics/btr260

Lieu, E. L., Nguyen, T., Rhyne, S., & Kim, J. (2020). Amino acids in cancer. *Experimental & Molecular Medicine*, *52*(1), 15-30. https://doi.org/10.1038/s12276-020-0375-3

Lin, H., Zhang, X., Liu, L., Fu, Q., Zang, C., Ding, Y., Su, Y., Xu, Z., He, S., Yang, X., Wei, X., Mao, H., Cui, Y., Wei, Y., Zhou, C., Du, L., Huang, N., Zheng, N., Wang, T., & Rao, F. (2020). Basis for metabolite-dependent Cullin-RING ligase deneddylation by the COP9 signalosome. *Proc Natl Acad Sci U S A*, *117*(8), 4117-4124. https://doi.org/10.1073/pnas.1911998117

Lindeman, N. I., Cagle, P. T., Aisner, D. L., Arcila, M. E., Beasley, M. B., Bernicker, E. H., Colasacco, C., Dacic, S., Hirsch, F. R., Kerr, K., Kwiatkowski, D. J., Ladanyi, M., Nowak, J. A., Sholl, L., Temple-Smolkin, R., Solomon, B., Souter, L. H., Thunnissen, E., Tsao, M. S., Ventura, C. B., Wynes, M. W., & Yatabe, Y. (2018). Updated Molecular Testing Guideline for the Selection of Lung Cancer Patients for Treatment With Targeted Tyrosine Kinase Inhibitors: Guideline From the College of American Pathologists, the International Association for the Study of Lung Cancer, and the Association for Molecular Pathology. *Arch Pathol Lab Med*, *142*(3), 321-346. https://doi.org/10.5858/arpa.2017-0388-CP

Lindeman, N. I., Cagle, P. T., Beasley, M. B., Chitale, D. A., Dacic, S., Giaccone, G., Jenkins, R. B., Kwiatkowski, D. J., Saldivar, J. S., Squire, J., Thunnissen, E., & Ladanyi, M. (2013). Molecular testing guideline for selection of lung cancer patients for EGFR and ALK tyrosine kinase inhibitors: guideline from the College of American Pathologists, International Association for the Study of Lung Cancer, and

Association for Molecular Pathology. *J Thorac Oncol*, *8*(7), 823-859. https://doi.org/10.1097/JTO.0b013e318290868f

Liu, F., Song, S., Yi, Z., Zhang, M., Li, J., Yang, F., Yin, H., Yu, X., Guan, C., Liu, Y., Liu, Z., Wang, J., & Zhu, D. (2017). HGF induces EMT in non-small-cell lung cancer through the hBVR pathway. *Eur J Pharmacol*, *811*, 180-190. https://doi.org/10.1016/j.ejphar.2017.05.040

Liu, Z., Han, C., & Fu, Y.-X. (2020). Targeting innate sensing in the tumor microenvironment to improve immunotherapy. *Cellular & molecular immunology*, *17*(1), 13-26.

Livnat-Levanon, N., Kevei, É., Kleifeld, O., Krutauz, D., Segref, A., Rinaldi, T., Erpapazoglou, Z., Cohen, M., Reis, N., Hoppe, T., & Glickman, M. H. (2014). Reversible 26S proteasome disassembly upon mitochondrial stress. *Cell Rep*, *7*(5), 1371-1380. https://doi.org/10.1016/j.celrep.2014.04.030

Lo, M., Wang, Y. Z., & Gout, P. W. (2008). The x cystine/glutamate antiporter: a potential target for therapy of cancer and other diseases. *Journal of cellular physiology*, *215*(3), 593-602.

Lo, P.-K., Kanojia, D., Liu, X., Singh, U. P., Berger, F. G., Wang, Q., & Chen, H. (2012). CD49f and CD61 identify Her2/neu-induced mammary tumor-initiating cells that are potentially derived from luminal progenitors and maintained by the integrin–TGFβ signaling. *Oncogene*, *31*(21), 2614-2626.

Lou, S., Cleven, A. H., Balluff, B., de Graaff, M., Kostine, M., Briaire-de Bruijn, I., McDonnell, L. A., & Bovée, J. V. (2016). High nuclear expression of proteasome activator complex subunit 1 predicts poor survival in soft tissue leiomyosarcomas. *Clin Sarcoma Res*, *6*, 17. https://doi.org/10.1186/s13569-016-0057-z

Lu, X., Gao, J., Zhang, Y., Zhao, T., Cai, H., & Zhang, T. (2018). CTEN induces epithelial-mesenchymal transition (EMT) and metastasis in non small cell lung cancer cells. *PLoS One*, *13*(7), e0198823. https://doi.org/10.1371/journal.pone.0198823

Lu, Y., Wu, J., Dong, Y., Chen, S., Sun, S., Ma, Y.-B., Ouyang, Q., Finley, D., Kirschner, M. W., & Mao, Y. (2017). Conformational landscape of the p28-bound human proteasome regulatory particle. *Molecular cell*, *67*(2), 322-333. e326.

Lund, M. E., Campbell, D. H., & Walsh, B. J. (2020). The Role of Glypican-1 in the Tumour Microenvironment. In A. Birbrair (Ed.), *Tumor Microenvironment: Extracellular Matrix Components – Part A* (pp. 163-176). Springer International Publishing. https://doi.org/10.1007/978-3-030-40146-7_8

Ma, T.-L., Zhu, P., Chen, J.-X., Hu, Y.-H., & Xie, J. (2022). SIX3 function in cancer: progression and comprehensive analysis. *Cancer Gene Therapy*, *29*(11), 1542-1549. https://doi.org/10.1038/s41417-022-00488-9

Maag, J. L. V., Fisher, O. M., Levert-Mignon, A., Kaczorowski, D. C., Thomas, M. L., Hussey, D. J., Watson, D. I., Wettstein, A., Bobryshev, Y. V., Edwards, M., Dinger, M. E., & Lord, R. V. (2017). Novel Aberrations Uncovered in Barrett's Esophagus and Esophageal Adenocarcinoma Using Whole Transcriptome Sequencing. *Mol Cancer Res*, *15*(11), 1558-1569. https://doi.org/10.1158/1541-7786.MCR-17-0332

Macbeth, M. R., Schubert, H. L., Vandemark, A. P., Lingam, A. T., Hill, C. P., & Bass, B. L. (2005). Inositol hexakisphosphate is bound in the ADAR2 core and required for RNA editing. *Science*, *309*(5740), 1534-1539. https://doi.org/10.1126/science.1113150

Maitra, A. (2019). Molecular envoys pave the way for pancreatic cancer to invade the liver. *Nature*, *567*(7747), 181-182. https://doi.org/10.1038/d41586-019-00710-z

Mamuya, F. A., & Duncan, M. K. (2012). aV integrins and TGF‐β‐induced EMT: a circle of regulation. *Journal of cellular and molecular medicine*, *16*(3), 445-455.

Manasanch, E. E., & Orlowski, R. Z. (2017). Proteasome inhibitors in cancer therapy. *Nat Rev Clin Oncol*, *14*(7), 417-433. https://doi.org/10.1038/nrclinonc.2016.206

Mandemaker, I. K., Geijer, M. E., Kik, I., Bezstarosti, K., Rijkers, E., Raams, A., Janssens, R. C., Lans, H., Hoeijmakers, J. H., Demmers, J. A., Vermeulen, W., & Marteijn, J. A. (2018). DNA damage-induced replication stress results in PA200-proteasome-mediated degradation of acetylated histones. *EMBO Rep*, *19*(10). https://doi.org/10.15252/embr.201745566

Marcum, R. D., & Radhakrishnan, I. (2019). Inositol phosphates and core subunits of the Sin3L/Rpd3L histone deacetylase (HDAC) complex up-regulate deacetylase activity. *J Biol Chem*, *294*(38), 13928-13938. https://doi.org/10.1074/jbc.RA119.009780

Marques, A. J., Palanimurugan, R., Matias, A. C., Ramos, P. C., & Dohmen, R. J. (2009). Catalytic Mechanism and Assembly of the Proteasome. *Chemical Reviews*, *109*(4), 1509-1536. https://doi.org/10.1021/cr8004857

Massagué, J., & Obenauf, A. C. (2016). Metastatic colonization by circulating tumour cells. *Nature*, *529*(7586), 298-306. https://doi.org/10.1038/nature17038

Matyskiela, M. E., Lander, G. C., & Martin, A. (2013). Conformational switching of the 26S proteasome enables substrate degradation. *Nature structural & molecular biology*, *20*(7), 781-788.

Mayne, M., Moffatt, T., Kong, H., McLaren, P. J., Fowke, K. R., Becker, K. G., Namaka, M., Schenck, A., Bardoni, B., Bernstein, C. N., & Melanson, M. (2004). CYFIP2 is highly abundant in CD4+ cells from multiple sclerosis patients and is involved in T cell adhesion. *Eur J Immunol*, *34*(4), 1217-1227. https://doi.org/10.1002/eji.200324726

McCarthy, M. K., & Weinberg, J. B. (2015). The immunoproteasome and viral infection: a complex regulator of inflammation. *Front Microbiol*, *6*, 21. https://doi.org/10.3389/fmicb.2015.00021

McGranahan, N., Furness, A. J., Rosenthal, R., Ramskov, S., Lyngaa, R., Saini, S. K., Jamal-Hanjani, M., Wilson, G. A., Birkbak, N. J., Hiley, C. T., Watkins, T. B., Shafi, S., Murugaesu, N., Mitter, R., Akarca, A. U., Linares, J., Marafioti, T., Henry, J. Y., Van Allen, E. M., Miao, D., Schilling, B., Schadendorf, D., Garraway, L. A., Makarov, V., Rizvi, N. A., Snyder, A., Hellmann, M. D., Merghoub, T., Wolchok, J. D., Shukla, S. A., Wu, C. J., Peggs, K. S., Chan, T. A., Hadrup, S. R., Quezada, S. A., & Swanton, C. (2016). Clonal neoantigens elicit T cell immunoreactivity and sensitivity to immune checkpoint blockade. *Science*, *351*(6280), 1463-1469. https://doi.org/10.1126/science.aaf1490

Meiners, S., Heyken, D., Weller, A., Ludwig, A., Stangl, K., Kloetzel, P. M., & Kruger, E. (2003). Inhibition of proteasome activity induces concerted expression of proteasome genes and de novo formation of Mammalian proteasomes. *J Biol Chem*, *278*(24), 21517-21525. https://doi.org/10.1074/jbc.M301032200

Meiners, S., Keller, I. E., Semren, N., & Caniard, A. (2014). Regulation of the proteasome: evaluating the lung proteasome as a new therapeutic target. *Antioxid Redox Signal*, *21*(17), 2364-2382. https://doi.org/10.1089/ars.2013.5798

Meiners, S., Ludwig, A., Stangl, V., & Stangl, K. (2008). Proteasome inhibitors: poisons and remedies. *Med Res Rev*, *28*(2), 309-327. https://doi.org/10.1002/med.20111

Mellacheruvu, D., Wright, Z., Couzens, A. L., Lambert, J. P., St-Denis, N. A., Li, T., Miteva, Y. V., Hauri, S., Sardiu, M. E., Low, T. Y., Halim, V. A., Bagshaw, R. D., Hubner, N. C., Al-Hakim, A., Bouchard, A., Faubert, D., Fermin, D., Dunham, W. H., Goudreault, M., Lin, Z. Y., Badillo, B. G., Pawson, T., Durocher, D., Coulombe, B., Aebersold, R., Superti-Furga, G., Colinge, J., Heck, A. J., Choi, H., Gstaiger, M., Mohammed, S., Cristea, I. M., Bennett, K. L., Washburn, M. P., Raught, B., Ewing, R. M., Gingras, A. C., & Nesvizhskii, A. I. (2013). The CRAPome: a contaminant

repository for affinity purification-mass spectrometry data. *Nat Methods*, *10*(8), 730-736. https://doi.org/10.1038/nmeth.2557

Merl, J., Ueffing, M., Hauck, S. M., & von Toerne, C. (2012). Direct comparison of MS‐based label‐free and SILAC quantitative proteome profiling strategies in primary retinal M üller cells. *Proteomics*, *12*(12), 1902-1911.

Meul, T. (2021). *Adaptive mitochondrial regulation of the proteasome* [Dissertation, LMU Munich].

Meul, T., Berschneider, K., Schmitt, S., Mayr, C. H., Mattner, L. F., Schiller, H. B., Yazgili, A. S., Wang, X., Lukas, C., Schlesser, C., Prehn, C., Adamski, J., Graf, E., Schwarzmayr, T., Perocchi, F., Kukat, A., Trifunovic, A., Kremer, L., Prokisch, H., Popper, B., von Toerne, C., Hauck, S. M., Zischka, H., & Meiners, S. (2020). Mitochondrial Regulation of the 26S Proteasome. *Cell Reports*, *32*(8). https://doi.org/10.1016/j.celrep.2020.108059

Mi, H., Muruganujan, A., Ebert, D., Huang, X., & Thomas, P. D. (2018). PANTHER version 14: more genomes, a new PANTHER GO-slim and improvements in enrichment analysis tools. *Nucleic Acids Research*, *47*(D1), D419-D426. https://doi.org/10.1093/nar/gky1038

Mittal, V. (2004). Improving the efficiency of RNA interference in mammals. *Nature reviews genetics*, *5*(5), 355-365.

Mittal, V. (2018). Epithelial Mesenchymal Transition in Tumor Metastasis. *Annu Rev Pathol*, *13*, 395-412. https://doi.org/10.1146/annurev-pathol-020117-043854

Mohamed, A., Deng, X., Khuri, F. R., & Owonikoko, T. K. (2014). Altered glutamine metabolism and therapeutic opportunities for lung cancer. *Clinical lung cancer*, *15*(1), 7-15.

Morozov, A. V., & Karpov, V. L. (2018). Biological consequences of structural and functional proteasome diversity. *Heliyon*, *4*(10), e00894. https://doi.org/10.1016/j.heliyon.2018.e00894

Mosmann, T. (1983). Rapid colorimetric assay for cellular growth and survival: application to proliferation and cytotoxicity assays. *J Immunol Methods*, *65*(1-2), 55-63. https://doi.org/10.1016/0022-1759(83)90303-4

Muchamuel, T., Basler, M., Aujay, M. A., Suzuki, E., Kalim, K. W., Lauer, C., Sylvain, C., Ring, E. R., Shields, J., & Jiang, J. (2009). A selective inhibitor of the immunoproteasome subunit LMP7 blocks cytokine production and attenuates progression of experimental arthritis. *Nature medicine*, *15*(7), 781-787.

Murata, S., Kawahara, H., Tohma, S., Yamamoto, K., Kasahara, M., Nabeshima, Y.-i., Tanaka, K., & Chiba, T. (1999). Growth retardation in mice lacking the proteasome activator PA28γ. *Journal of Biological Chemistry*, *274*(53), 38211-38215.

Murata, S., Sasaki, K., Kishimoto, T., Niwa, S., Hayashi, H., Takahama, Y., & Tanaka, K. (2007). Regulation of CD8+ T cell development by thymus-specific proteasomes. *Science*, *316*(5829), 1349-1353. https://doi.org/10.1126/science.1141915

Murata, S., Udono, H., Tanahashi, N., Hamada, N., Watanabe, K., Adachi, K., Yamano, T., Yui, K., Kobayashi, N., & Kasahara, M. (2001). Immunoproteasome assembly and antigen presentation in mice lacking both PA28α and PA28β. *The EMBO journal*, *20*(21), 5898-5907.

Murata, S., Yashiroda, H., & Tanaka, K. (2009). Molecular mechanisms of proteasome assembly. *Nature reviews Molecular cell biology*, *10*(2), 104-115.

Namiki, S., Nakamura, T., Oshima, S., Yamazaki, M., Sekine, Y., Tsuchiya, K., Okamoto, R., Kanai, T., & Watanabe, M. (2005). IRF-1 mediates upregulation of LMP7 by IFN-gamma and concerted expression of immunosubunits of the proteasome. *FEBS Lett*, *579*(13), 2781-2787. https://doi.org/10.1016/j.febslet.2005.04.012

Navon, A., & Goldberg, A. L. (2001). Proteins are unfolded on the surface of the ATPase ring before transport into the proteasome. *Molecular cell*, *8*(6), 1339-1349.

Nawshad, A., Lagamba, D., Polad, A., & Hay, E. D. (2005). Transforming growth factor-beta signaling during epithelial-mesenchymal transformation: implications for embryogenesis and tumor metastasis. *Cells Tissues Organs*, *179*(1-2), 11-23. https://doi.org/10.1159/000084505

Ng, M., Freeman, M. K., Fleming, T. D., Robinson, M., Dwyer-Lindgren, L., Thomson, B., Wollum, A., Sanman, E., Wulf, S., Lopez, A. D., Murray, C. J., & Gakidou, E. (2014). Smoking prevalence and cigarette consumption in 187 countries, 1980-2012. *Jama*, *311*(2), 183-192. https://doi.org/10.1001/jama.2013.284692

Nitschke, L., Carsetti, R., Ocker, B., Köhler, G., & Lamers, M. C. (1997). CD22 is a negative regulator of B-cell receptor signalling. *Current Biology*, *7*(2), 133-143.

Nitta, T., Murata, S., Sasaki, K., Fujii, H., Ripen, A. M., Ishimaru, N., Koyasu, S., Tanaka, K., & Takahama, Y. (2010). Thymoproteasome shapes immunocompetent repertoire of CD8+ T cells. *Immunity*, *32*(1), 29-40. https://doi.org/10.1016/j.immuni.2009.10.009

Noh, K.-W., Sohn, I., Song, J.-Y., Shin, H.-T., Kim, Y.-J., Jung, K., Sung, M., Kim, M., An, S., & Han, J. (2018). Integrin β3 inhibition enhances the antitumor activity of ALK inhibitor in ALK-rearranged NSCLC. *Clinical Cancer Research*, *24*(17), 4162-4174.

Ohnuma, K., Inoue, H., Uchiyama, M., Yamochi, T., Hosono, O., Dang, N. H., & Morimoto, C. (2006). T-cell activation via CD26 and caveolin-1 in rheumatoid synovium. *Mod Rheumatol*, *16*(1), 3-13. https://doi.org/10.1007/s10165-005-0452-4

Okamura, M., Yamanaka, Y., Shigemoto, M., Kitadani, Y., Kobayashi, Y., Kambe, T., Nagao, M., Kobayashi, I., Okumura, K., & Masuda, S. (2018). Depletion of mRNA export regulator DBP5/DDX19, GLE1 or IPPK that is a key enzyme for the production of IP6, resulting in differentially altered cytoplasmic mRNA expression and specific cell defect. *PLoS One*, *13*(5), e0197165. https://doi.org/10.1371/journal.pone.0197165

Ortega, J., Heymann, J. B., Kajava, A. V., Ustrell, V., Rechsteiner, M., & Steven, A. C. (2005). The axial channel of the 20S proteasome opens upon binding of the PA200 activator. *J Mol Biol*, *346*(5), 1221-1227. https://doi.org/10.1016/j.jmb.2004.12.049

Ortiz-Navarrete, V., Seelig, A., Gernold, M., Frentzel, S., Kloetzel, P. M., & Hämmerling, G. J. (1991). Subunit of the'20S'proteasome (multicatalytic proteinase) encoded by the major histocompatibility complex. *Nature*, *353*(6345), 662-664.

Paradigms, E. (2017). *Diagnosis, Staging, and Testing for Nonsquamous NSCLC*. Retrieved November 1, 2022 from https://www.targetedonc.com/view/diagnosis-staging-and-testing-for-nonsquamous-nsclc

Park, Y., Hwang, Y.-P., Lee, J.-S., Seo, S.-H., Yoon, S. K., & Yoon, J.-B. (2005). Proteasomal ATPase-associated factor 1 negatively regulates proteasome activity by interacting with proteasomal ATPases. *Molecular and cellular biology*, *25*(9), 3842-3853.

Parvani, J. G., Gujrati, M. D., Mack, M. A., Schiemann, W. P., & Lu, Z.-R. (2015). Silencing β3 integrin by targeted ECO/siRNA nanoparticles inhibits EMT and metastasis of triple-negative breast cancer. *Cancer research*, *75*(11), 2316-2325.

Pechkovsky, D. V., Scaffidi, A. K., Hackett, T. L., Ballard, J., Shaheen, F., Thompson, P. J., Thannickal, V. J., & Knight, D. A. (2008). Transforming growth factor β1 induces αvβ3 integrin expression in human lung fibroblasts via a β3 integrin-, c-Src-, and p38 MAPK-dependent pathway. *Journal of Biological Chemistry*, *283*(19), 12898-12908.

Peifer, M., Fernández-Cuesta, L., Sos, M. L., George, J., Seidel, D., Kasper, L. H., Plenker, D., Leenders, F., Sun, R., Zander, T., Menon, R., Koker, M., Dahmen, I., Müller, C.,

Di Cerbo, V., Schildhaus, H. U., Altmüller, J., Baessmann, I., Becker, C., de Wilde, B., Vandesompele, J., Böhm, D., Ansén, S., Gabler, F., Wilkening, I., Heynck, S., Heuckmann, J. M., Lu, X., Carter, S. L., Cibulskis, K., Banerji, S., Getz, G., Park, K. S., Rauh, D., Grütter, C., Fischer, M., Pasqualucci, L., Wright, G., Wainer, Z., Russell, P., Petersen, I., Chen, Y., Stoelben, E., Ludwig, C., Schnabel, P., Hoffmann, H., Muley, T., Brockmann, M., Engel-Riedel, W., Muscarella, L. A., Fazio, V. M., Groen, H., Timens, W., Sietsma, H., Thunnissen, E., Smit, E., Heideman, D. A., Snijders, P. J., Cappuzzo, F., Ligorio, C., Damiani, S., Field, J., Solberg, S., Brustugun, O. T., Lund-Iversen, M., Sänger, J., Clement, J. H., Soltermann, A., Moch, H., Weder, W., Solomon, B., Soria, J. C., Validire, P., Besse, B., Brambilla, E., Brambilla, C., Lantuejoul, S., Lorimier, P., Schneider, P. M., Hallek, M., Pao, W., Meyerson, M., Sage, J., Shendure, J., Schneider, R., Büttner, R., Wolf, J., Nürnberg, P., Perner, S., Heukamp, L. C., Brindle, P. K., Haas, S., & Thomas, R. K. (2012). Integrative genome analyses identify key somatic driver mutations of small-cell lung cancer. *Nat Genet*, *44*(10), 1104-1110. https://doi.org/10.1038/ng.2396

Pickering, A. M., Koop, A. L., Teoh, C. Y., Ermak, G., Grune, T., & Davies, K. J. (2010). The immunoproteasome, the 20S proteasome and the PA28αβ proteasome regulator are oxidative-stress-adaptive proteolytic complexes. *Biochemical Journal*, *432*(3), 585-595.

Prasad, R. R., Mishra, D. K., Kumar, M., & Yadava, P. K. (2022). Human telomerase reverse transcriptase promotes the epithelial to mesenchymal transition in lung cancer cells by enhancing c-MET upregulation. *Heliyon*, *8*(1), e08673. https://doi.org/10.1016/j.heliyon.2021.e08673

Preckel, T., Fung-Leung, W.-P., Cai, Z., Vitiello, A., Salter-Cid, L., Winqvist, O., Wolfe, T. G., Herrath, M. V., Angulo, A., & Ghazal, P. (1999). Impaired immunoproteasome assembly and immune responses in PA28−/− mice. *Science*, *286*(5447), 2162-2165.

Pyun, J.-A., Kim, S., & Kwack, K. (2014). Interaction between thyroglobulin and ADAMTS16 in premature ovarian failure. *Clinical and experimental reproductive medicine*, *41*(3), 120.

Qian, B. Z., & Pollard, J. W. (2010). Macrophage diversity enhances tumor progression and metastasis. *Cell*, *141*(1), 39-51. https://doi.org/10.1016/j.cell.2010.03.014

Qian, M. X., Pang, Y., Liu, C. H., Haratake, K., Du, B. Y., Ji, D. Y., Wang, G. F., Zhu, Q. Q., Song, W., Yu, Y., Zhang, X. X., Huang, H. T., Miao, S., Chen, L. B., Zhang, Z. H., Liang, Y. N., Liu, S., Cha, H., Yang, D., Zhai, Y., Komatsu, T., Tsuruta, F., Li, H., Cao, C., Li, W., Li, G. H., Cheng, Y., Chiba, T., Wang, L., Goldberg, A. L., Shen, Y., & Qiu, X. B. (2013). Acetylation-mediated proteasomal degradation of core histones during DNA repair and spermatogenesis. *Cell*, *153*(5), 1012-1024. https://doi.org/10.1016/j.cell.2013.04.032

Qing, G., Li, B., Vu, A., Skuli, N., Walton, Z. E., Liu, X., Mayes, P. A., Wise, D. R., Thompson, C. B., Maris, J. M., Hogarty, M. D., & Simon, M. C. (2012). ATF4 regulates MYC-mediated neuroblastoma cell death upon glutamine deprivation. *Cancer Cell*, *22*(5), 631-644. https://doi.org/10.1016/j.ccr.2012.09.021

Raghunathan, S., Jaganade, T., & Priyakumar, U. D. (2020). Urea-aromatic interactions in biology. *Biophys Rev*, *12*(1), 65-84. https://doi.org/10.1007/s12551-020-00620-9

Raskov, H., Orhan, A., Christensen, J. P., & Gögenur, I. (2021). Cytotoxic CD8+ T cells in cancer and cancer immunotherapy. *British Journal of Cancer*, *124*(2), 359-367. https://doi.org/10.1038/s41416-020-01048-4

Realini, C., Jensen, C. C., Zhang, Z.-g., Johnston, S. C., Knowlton, J. R., Hill, C. P., & Rechsteiner, M. (1997). Characterization of recombinant REGα, REGβ, and REGγ proteasome activators. *Journal of Biological Chemistry*, *272*(41), 25483-25492.

Rechsteiner, M., Realini, C., & Ustrell, V. (2000). The proteasome activator 11 S REG (PA28) and class I antigen presentation. *Biochemical Journal*, *345*(1), 1-15.

Reiss, K., & Saftig, P. (2009). The "a disintegrin and metalloprotease"(ADAM) family of sheddases: physiological and cellular functions. Seminars in cell & developmental biology,

Respondek, D., Voss, M., Kühlewindt, I., Klingel, K., Krüger, E., & Beling, A. (2017). PA28 modulates antigen processing and viral replication during coxsackievirus B3 infection. *PLoS One*, *12*(3), e0173259.

Rock, K. L., & Goldberg, A. L. (1999). Degradation of cell proteins and the generation of MHC class I-presented peptides. *Annu Rev Immunol*, *17*, 739-779. https://doi.org/10.1146/annurev.immunol.17.1.739

Rodríguez-Martínez, Á., Ruano-Ravina, A., Torres-Durán, M., Provencio, M., Parente-Lamelas, I., Vidal-García, I., Martínez, C., Hernández-Hernández, J., Abdulkader-Nallib, I., Castro-Añón, O., Varela-Lema, L., Piñeiro-Lamas, M., Fidalgo, P. S., Fernández-Villar, A., Barros-Dios, J., & Pérez-Ríos, M. (2022). Residential Radon and Small Cell Lung Cancer. Final Results of the Small Cell Study. *Arch Bronconeumol*, *58*(7), 542-546. https://doi.org/10.1016/j.arbres.2021.01.027

Roelofs, J., Park, S., Haas, W., Tian, G., McAllister, F. E., Huo, Y., Lee, B.-H., Zhang, F., Shi, Y., & Gygi, S. P. (2009). Chaperone-mediated pathway of proteasome regulatory particle assembly. *Nature*, *459*(7248), 861-865.

Rudin, C. M., Brambilla, E., Faivre-Finn, C., & Sage, J. (2021). Small-cell lung cancer. *Nature Reviews Disease Primers*, *7*(1), 3. https://doi.org/10.1038/s41572-020-00235-0

Sakamoto, N., Oue, N., Noguchi, T., Sentani, K., Anami, K., Sanada, Y., Yoshida, K., & Yasui, W. (2010). Serial analysis of gene expression of esophageal squamous cell carcinoma: ADAMTS16 is upregulated in esophageal squamous cell carcinoma. *Cancer science*, *101*(4), 1038-1044.

Sanchez-Palencia, A., Gomez-Morales, M., Gomez-Capilla, J. A., Pedraza, V., Boyero, L., Rosell, R., & Farez-Vidal, M. E. (2011). Gene expression profiling reveals novel biomarkers in nonsmall cell lung cancer. *Int J Cancer*, *129*(2), 355-364. https://doi.org/10.1002/ijc.25704

Savulescu, A. F., & Glickman, M. H. (2011). Proteasome activator 200: the heat is on. *Mol Cell Proteomics*, *10*(5), R110 006890. https://doi.org/10.1074/mcp.R110.006890

Scaffidi, A. K., Petrovic, N., Moodley, Y. P., Fogel-Petrovic, M., Kroeger, K. M., Seeber, R. M., Eidne, K. A., Thompson, P. J., & Knight, D. A. (2004). αvβ3 Integrin interacts with the transforming growth factor β (TGFβ) type II receptor to potentiate the proliferative effects of TGFβ1 in living human lung fibroblasts. *Journal of Biological Chemistry*, *279*(36), 37726-37733.

Scaiola, A., Mangia, F., Imseng, S., Boehringer, D., Berneiser, K., Shimobayashi, M., Stuttfeld, E., Hall, M. N., Ban, N., & Maier, T. (2020). The 3.2-A resolution structure of human mTORC2. *Sci Adv*, *6*(45). https://doi.org/10.1126/sciadv.abc1251

Schaefer, N., Roemer, V., Janzen, D., & Villmann, C. (2018). Impaired Glycine Receptor Trafficking in Neurological Diseases. *Front Mol Neurosci*, *11*, 291. https://doi.org/10.3389/fnmol.2018.00291

Schmidtke, G., Kraft, R., Kostka, S., Henklein, P., Frömmel, C., Löwe, J., Huber, R., Kloetzel, P.-M., & Schmidt, M. (1996). Analysis of mammalian 20S proteasome biogenesis: the maturation of beta‐subunits is an ordered two‐step mechanism involving autocatalysis. *The EMBO journal*, *15*(24), 6887-6898.

Schrader, J., Henneberg, F., Mata, R. A., Tittmann, K., Schneider, T. R., Stark, H., Bourenkov, G., & Chari, A. (2016). The inhibition mechanism of human 20S

proteasomes enables next-generation inhibitor design. *Science*, *353*(6299), 594-598. https://doi.org/10.1126/science.aaf8993

Seguin, L., Kato, S., Franovic, A., Camargo, M. F., Lesperance, J., Elliott, K. C., Yebra, M., Mielgo, A., Lowy, A. M., & Husain, H. (2014). An integrin β3–KRAS–RalB complex drives tumour stemness and resistance to EGFR inhibition. *Nature Cell Biology*, *16*(5), 457-468.

Senichkin, V. V., Kopeina, G. S., Prokhorova, E. A., Zamaraev, A. V., Lavrik, I. N., & Zhivotovsky, B. (2018). Modulation of Mcl-1 transcription by serum deprivation sensitizes cancer cells to cisplatin. *Biochimica et Biophysica Acta (BBA) - General Subjects*, *1862*(3), 557-566. https://doi.org/https://doi.org/10.1016/j.bbagen.2017.11.021

Sha, Z., & Goldberg, A. L. (2014). Proteasome-mediated processing of Nrf1 is essential for coordinate induction of all proteasome subunits and p97. *Curr Biol*, *24*(14), 1573-1583. https://doi.org/10.1016/j.cub.2014.06.004

Shankar, G. M., Antony, J., & Anto, R. J. (2015). Chapter Two - Quercetin and Tryptanthrin: Two Broad Spectrum Anticancer Agents for Future Chemotherapeutic Interventions. In S. Z. Bathaie & F. Tamanoi (Eds.), *The Enzymes* (Vol. 37, pp. 43-72). Academic Press. https://doi.org/https://doi.org/10.1016/bs.enz.2015.05.001

Shim, S. M., Lee, W. J., Kim, Y., Chang, J. W., Song, S., & Jung, Y.-K. (2012). Role of S5b/PSMD5 in proteasome inhibition caused by TNF-α/NFκB in higher eukaryotes. *Cell reports*, *2*(3), 603-615.

Shin, E. C., Seifert, U., Kato, T., Rice, C. M., Feinstone, S. M., Kloetzel, P. M., & Rehermann, B. (2006). Virus-induced type I IFN stimulates generation of immunoproteasomes at the site of infection. *J Clin Invest*, *116*(11), 3006-3014. https://doi.org/10.1172/jci29832

Short, R., & Posch, A. (2011). Stain-Free Approach for Western Blotting: Alternative to the Standard Blot Normalization Process. *Genetic Engineering & Biotechnology News*, *31*(20), 22-23.

Siegel, R. L., Miller, K. D., & Jemal, A. (2020). Cancer statistics, 2020. *CA: A Cancer Journal for Clinicians*, *70*(1), 7-30. https://doi.org/https://doi.org/10.3322/caac.21590

Singal, G., Miller, P. G., Agarwala, V., Li, G., Kaushik, G., Backenroth, D., Gossai, A., Frampton, G. M., Torres, A. Z., Lehnert, E. M., Bourque, D., O'Connell, C., Bowser, B., Caron, T., Baydur, E., Seidl-Rathkopf, K., Ivanov, I., Alpha-Cobb, G., Guria, A., He, J., Frank, S., Nunnally, A. C., Bailey, M., Jaskiw, A., Feuchtbaum, D., Nussbaum, N., Abernethy, A. P., & Miller, V. A. (2019). Association of Patient Characteristics and Tumor Genomics With Clinical Outcomes Among Patients With Non-Small Cell Lung Cancer Using a Clinicogenomic Database. *Jama*, *321*(14), 1391-1399. https://doi.org/10.1001/jama.2019.3241

Sitaraman, S., Na, C.-L., Yang, L., Filuta, A., Bridges, J. P., & Weaver, T. E. (2019). Proteasome dysfunction in alveolar type 2 epithelial cells is associated with acute respiratory distress syndrome. *Scientific reports*, *9*(1), 1-15.

Slater, T. F., Sawyer, B., & Sträuli, U. (1963). Studies on succinate-tetrazolium reductase systems: III. Points of coupling of four different tetrazolium salts III. Points of coupling of four different tetrazolium salts. *Biochimica et Biophysica Acta*, *77*, 383-393. https://doi.org/https://doi.org/10.1016/0006-3002(63)90513-4

Snyder, A. G., Hubbard, N. W., Messmer, M. N., Kofman, S. B., Hagan, C. E., Orozco, S. L., Chiang, K., Daniels, B. P., Baker, D., & Oberst, A. (2019). Intratumoral activation of the necroptotic pathway components RIPK1 and RIPK3 potentiates antitumor immunity. *Sci Immunol*, *4*(36). https://doi.org/10.1126/sciimmunol.aaw2004

Stadtmueller, B. M., & Hill, C. P. (2011). Proteasome activators. *Mol Cell*, *41*(1), 8-19. https://doi.org/10.1016/j.molcel.2010.12.020

Startin, C. M., Fiorentini, C., de Haan, M., & Skuse, D. H. (2015). Variation in the X-linked EFHC2 gene is associated with social cognitive abilities in males. *PLoS One*, *10*(6), e0131604. https://doi.org/10.1371/journal.pone.0131604

Stathopoulos, G. T., Sherrill, T. P., Karabela, S. P., Goleniewska, K., Kalomenidis, I., Roussos, C., Fingleton, B., Yull, F. E., Peebles, R. S., Jr., & Blackwell, T. S. (2010). Host-derived interleukin-5 promotes adenocarcinoma-induced malignant pleural effusion. *Am J Respir Crit Care Med*, *182*(10), 1273-1281. https://doi.org/10.1164/rccm.201001-0001OC

Steeg, P. S. (2006). Tumor metastasis: mechanistic insights and clinical challenges. *Nat Med*, *12*(8), 895-904. https://doi.org/10.1038/nm1469

Steven, A., Fisher, S. A., & Robinson, B. W. (2016). Immunotherapy for lung cancer. *Respirology*, *21*(5), 821-833. https://doi.org/10.1111/resp.12789

Stohwasser, R., Soza, A., Eggers, M., Koszinowski, U. H., & Kloetzel, P.-M. (2000). PA28αβ double and PA28β single transfectant mouse B8 cell lines reveal enhanced presentation of a mouse cytomegalovirus (MCMV) pp89 MHC class I epitope. *Molecular immunology*, *37*(1-2), 13-19.

Sullivan, Lucas B., Gui, Dan Y., Hosios, Aaron M., Bush, Lauren N., Freinkman, E., & Vander Heiden, Matthew G. (2015). Supporting Aspartate Biosynthesis Is an Essential Function of Respiration in Proliferating Cells. *Cell*, *162*(3), 552-563. https://doi.org/10.1016/j.cell.2015.07.017

Sun, J., Luan, Y., Xiang, D., Tan, X., Chen, H., Deng, Q., Zhang, J., Chen, M., Huang, H., & Wang, W. (2016). The 11S proteasome subunit PSME3 is a positive feedforward regulator of NF-κB and important for host defense against bacterial pathogens. *Cell reports*, *14*(4), 737-749.

Sun, W., Feng, J., Yi, Q., Xu, X., Chen, Y., & Tang, L. (2018). SPARC acts as a mediator of TGF-β1 in promoting epithelial-to-mesenchymal transition in A549 and H1299 lung cancer cells. *Biofactors*, *44*(5), 453-464. https://doi.org/10.1002/biof.1442

Sun, Y., Huang, J., & Yang, Z. (2015). The roles of ADAMTS in angiogenesis and cancer. *Tumor Biology*, *36*, 4039-4051.

Sundararajan, R., Salameh, T., Camarillo, I. G., Prabu, R. R., Natarajan, A., & Sankaranarayanan, K. (2014). 10 - Irreversible electroporation: a drug-free cancer treatment. In R. Sundararajan (Ed.), *Electroporation-Based Therapies for Cancer* (pp. 219-243). Woodhead Publishing. https://doi.org/https://doi.org/10.1533/9781908818294.219

Suzuki, S., Tanaka, T., Poyurovsky, M. V., Nagano, H., Mayama, T., Ohkubo, S., Lokshin, M., Hosokawa, H., Nakayama, T., & Suzuki, Y. (2010). Phosphate-activated glutaminase (GLS2), a p53-inducible regulator of glutamine metabolism and reactive oxygen species. *Proceedings of the National Academy of Sciences*, *107*(16), 7461-7466.

Swanton, C., Hill, W., Lim, E., Lee, C., Weeden, C., Augustine, M., Chen, K., Kuan, F.-C., Marongiu, F., & Evans, E. (2022). Non-Small-Cell Lung Cancer Promotion by Air Pollutants.

Taherian, A., Li, X., Liu, Y., & Haas, T. A. (2011). Differences in integrin expression and signaling within human breast cancer cells. *BMC cancer*, *11*, 1-15.

Tanahashi, N., Yokota, K. y., Ahn, J. Y., Chung, C. H., Fujiwara, T., Takahashi, E. i., DeMartino, G. N., Slaughter, C. A., Toyonaga, T., & Yamamura, K. i. (1997). Molecular properties of the proteasome activator PA28 family proteins and γ - interferon regulation. *Genes to Cells*, *2*(3), 195-211.

Tanaka, K. (2009). The proteasome: overview of structure and functions. *Proc Jpn Acad Ser B Phys Biol Sci*, *85*(1), 12-36. https://doi.org/10.2183/pjab.85.12

Tanaka, K., Mizushima, T., & Saeki, Y. (2012). The proteasome: molecular machinery and pathophysiological roles. *Biol Chem*, *393*(4), 217-234. https://doi.org/10.1515/hsz-2011-0285

Thai, A. A., Solomon, B. J., Sequist, L. V., Gainor, J. F., & Heist, R. S. (2021). Lung cancer. *Lancet*, *398*(10299), 535-554. https://doi.org/10.1016/S0140-6736(21)00312-3

Thomas, T. A., & Smith, D. M. (2022). Proteasome activator 28γ (PA28γ) allosterically activates trypsin-like proteolysis by binding to the α-ring of the 20S proteasome. *Journal of Biological Chemistry*, *298*(8).

Tong, L., Shen, S., Huang, Q., Fu, J., Wang, T., Pan, L., Zhang, P., Chen, G., Huang, T., Li, K., Liu, Q., Xie, S., Yang, X., Moses, R. E., Li, X., & Li, L. (2020). Proteasome-dependent degradation of Smad7 is critical for lung cancer metastasis. *Cell Death Differ*, *27*(6), 1795-1806. https://doi.org/10.1038/s41418-019-0459-6

Tong, M., Chan, K. W., Bao, J. Y., Wong, K. Y., Chen, J. N., Kwan, P. S., Tang, K. H., Fu, L., Qin, Y. R., Lok, S., Guan, X. Y., & Ma, S. (2012). Rab25 is a tumor suppressor gene with antiangiogenic and anti-invasive activities in esophageal squamous cell carcinoma. *Cancer Res*, *72*(22), 6024-6035. https://doi.org/10.1158/0008-5472.CAN-12-1269

Toste Rego, A., & da Fonseca, P. C. A. (2019). Characterization of Fully Recombinant Human 20S and 20S-PA200 Proteasome Complexes. *Mol Cell*, *76*(1), 138-147 e135. https://doi.org/10.1016/j.molcel.2019.07.014

Travis, W. D., Brambilla, E., Burke, A. P., Marx, A., & Nicholson, A. G. (2015). Introduction to The 2015 World Health Organization Classification of Tumors of the Lung, Pleura, Thymus, and Heart. *J Thorac Oncol*, *10*(9), 1240-1242. https://doi.org/10.1097/jto.0000000000000663

Travis, W. D., Brambilla, E., Nicholson, A. G., Yatabe, Y., Austin, J. H. M., Beasley, M. B., Chirieac, L. R., Dacic, S., Duhig, E., Flieder, D. B., Geisinger, K., Hirsch, F. R., Ishikawa, Y., Kerr, K. M., Noguchi, M., Pelosi, G., Powell, C. A., Tsao, M. S., & Wistuba, I. (2015). The 2015 World Health Organization Classification of Lung Tumors: Impact of Genetic, Clinical and Radiologic Advances Since the 2004 Classification. *J Thorac Oncol*, *10*(9), 1243-1260. https://doi.org/10.1097/jto.0000000000000630

Tripathi, S. C., Peters, H. L., Taguchi, A., Katayama, H., Wang, H., Momin, A., Jolly, M. K., Celiktas, M., Rodriguez-Canales, J., Liu, H., Behrens, C., Wistuba, II, Ben-Jacob, E., Levine, H., Molldrem, J. J., Hanash, S. M., & Ostrin, E. J. (2016). Immunoproteasome deficiency is a feature of non-small cell lung cancer with a mesenchymal phenotype and is associated with a poor outcome. *Proc Natl Acad Sci U S A*, *113*(11), E1555-1564. https://doi.org/10.1073/pnas.1521812113

Tripathi, S. C., Vedpathak, D., & Ostrin, E. J. (2021). The Functional and Mechanistic Roles of Immunoproteasome Subunits in Cancer. *Cells*, *10*(12). https://doi.org/10.3390/cells10123587

Udagawa, H., Umemura, S., Murakami, I., Mimaki, S., Makinoshima, H., Ishii, G., Miyoshi, T., Kirita, K., Matsumoto, S., Yoh, K., Niho, S., Tsuchihara, K., & Goto, K. (2018). Genetic profiling-based prognostic prediction of patients with advanced small-cell lung cancer in large scale analysis. *Lung Cancer*, *126*, 182-188. https://doi.org/10.1016/j.lungcan.2018.11.014

Uechi, H., Hamazaki, J., & Murata, S. (2014). Characterization of the testis-specific proteasome subunit α4s in mammals. *J Biol Chem*, *289*(18), 12365-12374. https://doi.org/10.1074/jbc.M114.558866

Ugrinova, I., & Pasheva, E. (2017). Chapter Two - HMGB1 Protein: A Therapeutic Target Inside and Outside the Cell. In R. Donev (Ed.), *Advances in Protein Chemistry and Structural Biology* (Vol. 107, pp. 37-76). Academic Press. https://doi.org/https://doi.org/10.1016/bs.apcsb.2016.10.001

Ugun-Klusek, A., Tatham, M. H., Elkharaz, J., Constantin-Teodosiu, D., Lawler, K., Mohamed, H., Paine, S. M., Anderson, G., John Mayer, R., & Lowe, J. (2018). Continued 26S proteasome dysfunction in mouse brain cortical neurons impairs autophagy and the Keap1-Nrf2 oxidative defence pathway. *Cell death & disease*, *8*(1), e2531-e2531.

Ustrell, V., Hoffman, L., Pratt, G., & Rechsteiner, M. (2002). PA200, a nuclear proteasome activator involved in DNA repair. *EMBO J*, *21*(13), 3516-3525. https://doi.org/10.1093/emboj/cdf333

van der Lee, R., Buljan, M., Lang, B., Weatheritt, R. J., Daughdrill, G. W., Dunker, A. K., Fuxreiter, M., Gough, J., Gsponer, J., Jones, D. T., Kim, P. M., Kriwacki, R. W., Oldfield, C. J., Pappu, R. V., Tompa, P., Uversky, V. N., Wright, P. E., & Babu, M. M. (2014). Classification of Intrinsically Disordered Regions and Proteins. *Chemical Reviews*, *114*(13), 6589-6631. https://doi.org/10.1021/cr400525m

Van Kaert, L., Ashton-Rickardt, P. G., Eichelberger, M., Gaczynska, M., Nagashima, K., Rock, K. L., Goldberg, A. L., Doherty, P. C., & Tonegawa, S. (1994). Altered peptidase and viral-specific T cell response in LMP2 mutant mice. *Immunity*, *1*(7), 533-541.

van Rooij, N., van Buuren, M. M., Philips, D., Velds, A., Toebes, M., Heemskerk, B., van Dijk, L. J., Behjati, S., Hilkmann, H., & El Atmioui, D. (2013). Tumor exome analysis reveals neoantigen-specific T-cell reactivity in an ipilimumab-responsive melanoma. *Journal of clinical oncology: official journal of the American Society of Clinical Oncology*, *31*(32).

Vander Heiden, M. G., Cantley, L. C., & Thompson, C. B. (2009). Understanding the Warburg effect: the metabolic requirements of cell proliferation. *Science*, *324*(5930), 1029-1033. https://doi.org/10.1126/science.1160809

Vanharanta, S., & Massagué, J. (2013). Origins of Metastatic Traits. *Cancer Cell*, *24*(4), 410-421. https://doi.org/10.1016/j.ccr.2013.09.007

Varghese, A. M., Zakowski, M. F., Yu, H. A., Won, H. H., Riely, G. J., Krug, L. M., Kris, M. G., Rekhtman, N., Ladanyi, M., Wang, L., Berger, M. F., & Pietanza, M. C. (2014). Small-cell lung cancers in patients who never smoked cigarettes. *J Thorac Oncol*, *9*(6), 892-896. https://doi.org/10.1097/jto.0000000000000142

Vathiotis, I. A., MacNeil, T., Zugazagoitia, J., Syrigos, K. N., Aung, T. N., Gruver, A. M., Vaillancourt, P., Hughes, I., Hinton, S., Driscoll, K., & Rimm, D. L. (2021). Quantitative Assessment of CD200 and CD200R Expression in Lung Cancer. *Cancers*, *13*(5), 1024. https://www.mdpi.com/2072-6694/13/5/1024

Verdoes, M., Florea, B. I., Menendez-Benito, V., Maynard, C. J., Witte, M. D., van der Linden, W. A., van den Nieuwendijk, A. M., Hofmann, T., Berkers, C. R., van Leeuwen, F. W., Groothuis, T. A., Leeuwenburgh, M. A., Ovaa, H., Neefjes, J. J., Filippov, D. V., van der Marel, G. A., Dantuma, N. P., & Overkleeft, H. S. (2006). A fluorescent broad-spectrum proteasome inhibitor for labeling proteasomes in vitro and in vivo. *Chem Biol*, *13*(11), 1217-1226. https://doi.org/10.1016/j.chembiol.2006.09.013

Vousden, K. H., & Prives, C. (2009). Blinded by the Light: The Growing Complexity of p53. *Cell*, *137*(3), 413-431. https://doi.org/10.1016/j.cell.2009.04.037

Waldman, A. D., Fritz, J. M., & Lenardo, M. J. (2020). A guide to cancer immunotherapy: from T cell basic science to clinical practice. *Nature Reviews Immunology*, *20*(11), 651-668. https://doi.org/10.1038/s41577-020-0306-5

Wang, F., Ma, H., Liang, W.-J., Yang, J.-J., Wang, X.-Q., Shan, M.-R., Chen, Y., Jia, M., Yin, Y.-L., Sun, X.-Y., Zhang, J.-N., Peng, Q.-S., Chen, Y.-G., Liu, L.-Y., Li, P., Guo, T., & Wang, S.-X. (2017). Lovastatin upregulates microRNA-29b to reduce oxidative stress in rats with multiple cardiovascular risk factors. *Oncotarget*, *8*(6). https://www.oncotarget.com/article/14462/

Wang, F., Ma, H., Liang, W. J., Yang, J. J., Wang, X. Q., Shan, M. R., Chen, Y., Jia, M., Yin, Y. L., Sun, X. Y., Zhang, J. N., Peng, Q. S., Chen, Y. G., Liu, L. Y., Li, P., Guo, T., & Wang, S. X. (2017). Lovastatin upregulates microRNA-29b to reduce oxidative stress in rats with multiple cardiovascular risk factors. *Oncotarget*, *8*(6), 9021-9034. https://doi.org/10.18632/oncotarget.14462

Wang, Q., Pan, F., Li, S., Huang, R., Wang, X., Wang, S., Liao, X., Li, D., & Zhang, L. (2019). The prognostic value of the proteasome activator subunit gene family in skin cutaneous melanoma. *J Cancer*, *10*(10), 2205-2219. https://doi.org/10.7150/jca.30612

Wang, X., He, Q., Shen, H., Xia, A., Tian, W., Yu, W., & Sun, B. (2019). TOX promotes the exhaustion of antitumor CD8(+) T cells by preventing PD1 degradation in hepatocellular carcinoma. *J Hepatol*, *71*(4), 731-741. https://doi.org/10.1016/j.jhep.2019.05.015

Wang, X., Meul, T., & Meiners, S. (2020). Exploring the proteasome system: a novel concept of proteasome inhibition and regulation. *Pharmacology & Therapeutics*, *211*, 107526.

Warburg, O., Wind, F., & Negelein, E. (1927). THE METABOLISM OF TUMORS IN THE BODY. *J Gen Physiol*, *8*(6), 519-530. https://doi.org/10.1085/jgp.8.6.519

Weinberg, F., Hamanaka, R., Wheaton, W. W., Weinberg, S., Joseph, J., Lopez, M., Kalyanaraman, B., Mutlu, G. M., Budinger, G. S., & Chandel, N. S. (2010). Mitochondrial metabolism and ROS generation are essential for Kras-mediated tumorigenicity. *Proceedings of the National Academy of Sciences*, *107*(19), 8788-8793.

Weinlich, R., Oberst, A., Beere, H. M., & Green, D. R. (2017). Necroptosis in development, inflammation and disease. *Nat Rev Mol Cell Biol*, *18*(2), 127-136. https://doi.org/10.1038/nrm.2016.149

Welk, V. (2018). *Dissecting the role of proteasome activators in lung biology and disease* [Dissertation, LMU Munich].

Welk, V., Coux, O., Kleene, V., Abeza, C., Trumbach, D., Eickelberg, O., & Meiners, S. (2016). Inhibition of Proteasome Activity Induces Formation of Alternative Proteasome Complexes. *J Biol Chem*, *291*(25), 13147-13159. https://doi.org/10.1074/jbc.M116.717652

Welk, V., Meul, T., Lukas, C., Kammerl, I. E., Mulay, S. R., Schamberger, A. C., Semren, N., Fernandez, I. E., Anders, H. J., Gunther, A., Behr, J., Eickelberg, O., Korfei, M., & Meiners, S. (2019). Proteasome activator PA200 regulates myofibroblast differentiation. *Sci Rep*, *9*(1), 15224. https://doi.org/10.1038/s41598-019-51665-0

White, E. Z., Pennant, N. M., Carter, J. R., Hawsawi, O., Odero-Marah, V., & Hinton, C. V. (2020). Serum deprivation initiates adaptation and survival to oxidative stress in prostate cancer cells. *Scientific reports*, *10*(1), 12505. https://doi.org/10.1038/s41598-020-68668-x

Wise, D. R., & Thompson, C. B. (2010). Glutamine addiction: a new therapeutic target in cancer. *Trends Biochem Sci*, *35*(8), 427-433. https://doi.org/10.1016/j.tibs.2010.05.003

Wiśniewski, J. R., Zougman, A., Nagaraj, N., & Mann, M. (2009). Universal sample preparation method for proteome analysis. *Nature Methods*, *6*(5), 359-362. https://doi.org/10.1038/nmeth.1322

Wound Healing Tool. (2022). https://github.com/MontpellierRessourcesImagerie/imagej_macros_and_scripts/wiki/Wound-Healing-Tool

Xie, T., Chen, H., Shen, S., Huang, T., Huang, B., Hu, G., Li, L., & Xu, Y. (2019). Proteasome activator REGγ promotes inflammation in Leydig cells via IkBε signaling. *International Journal of Molecular Medicine*, *43*(5), 1961-1968.

Xie, Z., Bailey, A., Kuleshov, M. V., Clarke, D. J. B., Evangelista, J. E., Jenkins, S. L., Lachmann, A., Wojciechowicz, M. L., Kropiwnicki, E., Jagodnik, K. M., Jeon, M., & Ma'ayan, A. (2021). Gene Set Knowledge Discovery with Enrichr. *Current Protocols*, *1*(3), e90. https://doi.org/https://doi.org/10.1002/cpz1.90

Xu, G., Yu, H., Shi, X., Sun, L., Zhou, Q., Zheng, D., Shi, H., Li, N., Zhang, X., & Shao, G. (2014). Cisplatin sensitivity is enhanced in non-small cell lung cancer cells by regulating epithelial-mesenchymal transition through inhibition of eukaryotic translation initiation factor 5A2. *BMC Pulmonary Medicine*, *14*(1), 174. https://doi.org/10.1186/1471-2466-14-174

Xu, J., Zhou, L., Ji, L., Chen, F., Fortmann, K., Zhang, K., Liu, Q., Li, K., Wang, W., & Wang, H. (2016). The REGγ-proteasome forms a regulatory circuit with IκBε and NFκB in experimental colitis. *Nature communications*, *7*(1), 1-14.

Yamano, T., Sugahara, H., Mizukami, S., Murata, S., Chiba, T., Tanaka, K., Yui, K., & Udono, H. (2008). Allele-selective effect of PA28 in MHC class I antigen processing. *The Journal of Immunology*, *181*(3), 1655-1664.

Yang, Y., Waters, J. B., Früh, K., & Peterson, P. A. (1992). Proteasomes are regulated by interferon gamma: implications for antigen processing. *Proceedings of the National Academy of Sciences*, *89*(11), 4928-4932.

Yao, Y., Hu, C., Song, Q., Li, Y., Da, X., Yu, Y., Li, H., Clark, I. M., Chen, Q., & Wang, Q. K. (2019). ADAMTS16 activates latent TGF-β, accentuating fibrosis and dysfunction of the pressure-overloaded heart. *Cardiovascular Research*, *116*(5), 956-969. https://doi.org/10.1093/cvr/cvz187

Yazgili, A. S., Ebstein, F., & Meiners, S. (2022). The Proteasome Activator PA200/PSME4: An Emerging New Player in Health and Disease. *Biomolecules*, *12*(8), 1150. https://doi.org/10.3390/biom12081150

Yazgili, A. S., Meul, T., Welk, V., Semren, N., Kammerl, I. E., & Meiners, S. (2021). In-gel proteasome assay to determine the activity, amount, and composition of proteasome complexes from mammalian cells or tissues. *STAR Protoc*, *2*(2), 100526. https://doi.org/10.1016/j.xpro.2021.100526

Ye, R. D. (2020). The Rho guanine nucleotide exchange factor P-Rex1 as a potential drug target for cancer metastasis and inflammatory diseases. *Pharmacological Research*, *153*, 104676. https://doi.org/https://doi.org/10.1016/j.phrs.2020.104676

Ye, X., & Weinberg, R. A. (2015). Epithelial-Mesenchymal Plasticity: A Central Regulator of Cancer Progression. *Trends Cell Biol*, *25*(11), 675-686. https://doi.org/10.1016/j.tcb.2015.07.012

Ying, H., Kimmelman, A. C., Lyssiotis, C. A., Hua, S., Chu, G. C., Fletcher-Sananikone, E., Locasale, J. W., Son, J., Zhang, H., & Coloff, J. L. (2012). Oncogenic Kras maintains pancreatic tumors through regulation of anabolic glucose metabolism. *Cell*, *149*(3), 656-670.

Yoo, H. C., Yu, Y. C., Sung, Y., & Han, J. M. (2020). Glutamine reliance in cell metabolism. *Experimental & Molecular Medicine*, *52*(9), 1496-1516. https://doi.org/10.1038/s12276-020-00504-8

Yu, Z., Wei, X., Liu, L., Sun, H., Fang, T., Wang, L., Li, Y., Sui, W., Wang, K., He, Y., Zhao, Y., Huang, W., An, G., Meng, F., Huang, C., Yu, T., Anderson, K. C., Cheng, T., Qiu, L., & Hao, M. (2022). Indirubin-3'-monoxime acts as proteasome inhibitor: Therapeutic application in multiple myeloma. *EBioMedicine*, *78*, 103950. https://doi.org/10.1016/j.ebiom.2022.103950

Zaiss, D. M., de Graaf, N., & Sijts, A. J. (2008). The proteasome immunosubunit multicatalytic endopeptidase complex-like 1 is a T-cell-intrinsic factor influencing homeostatic expansion. *Infection and immunity*, *76*(3), 1207-1213.

Zangi, R., Zhou, R., & Berne, B. J. (2009). Urea's Action on Hydrophobic Interactions. *Journal of the American Chemical Society*, *131*(4), 1535-1541. https://doi.org/10.1021/ja807887g

Zemek, R. M., De Jong, E., Chin, W. L., Schuster, I. S., Fear, V. S., Casey, T. H., Forbes, C., Dart, S. J., Leslie, C., & Zaitouny, A. (2019). Sensitization to immune checkpoint blockade through activation of a STAT1/NK axis in the tumor microenvironment. *Science translational medicine*, *11*(501), eaav7816.

Zhang, J., Pavlova, N. N., & Thompson, C. B. (2017). Cancer cell metabolism: the essential role of the nonessential amino acid, glutamine. *EMBO J*, *36*(10), 1302-1315. https://doi.org/10.15252/embj.201696151

Zhang, X., Yu, Y., Bai, B., Wang, T., Zhao, J., Zhang, N., Zhao, Y., Wang, X., & Wang, B. (2020). PTPN22 interacts with EB1 to regulate T-cell receptor signaling. *Faseb j*, *34*(7), 8959-8974. https://doi.org/10.1096/fj.201902811RR

Zhang, Y., Liu, S., Zuo, Q., Wu, L., Ji, L., Zhai, W., Xiao, J., Chen, J., & Li, X. (2015). Oxidative challenge enhances REGγ–proteasome-dependent protein degradation. *Free Radical Biology and Medicine*, *82*, 42-49.

Zhao, J., Makhija, S., Huang, B., & Cheng, Y. (2021). Efficient tagging and purification of endogenous proteins for structural studies by single particle cryo-EM. *bioRxiv*, 2021.2006.2025.449985. https://doi.org/10.1101/2021.06.25.449985

Zhu, C., Kong, Z., Wang, B., Cheng, W., Wu, A., & Meng, X. (2019). ITGB3/CD61: a hub modulator and target in the tumor microenvironment. *Am J Transl Res*, *11*(12), 7195-7208.

Zivkovic, D., Sanchez Dafun, A., Menneteau, T., Schahl, A., Lise, S., Kervarrec, C., Toste Rego, A., da Fonseca, P. C. A., Chavent, M., Pineau, C., Burlet-Schiltz, O., Marcoux, J., & Bousquet, M. P. (2022). Proteasome complexes experience profound structural and functional rearrangements throughout mammalian spermatogenesis. *Proc Natl Acad Sci U S A*, *119*(15), e2116826119. https://doi.org/10.1073/pnas.2116826119

List of abbreviations

A

ABP	activity-based probe
ANOVA	Analysis of variance
ATP	adenosine triphosphate

B

BCA	bicinchoninic acid
BZ	Bortezomib

C

CAF	cancer-associated fibroblast
cDNA	complementary DNA
C-L	caspase-like
cm	centimeter
cntrl	control
CO2	carbon dioxide
co-IP	
CP	core particle
CPC	Comprehensive Pneumology Center
CPC	Comprehensive Pneumology Center
CT-L	chymotrypsin-like
CT-L	chymotrypsin-like
ctrl	control

D

Da	dalton
°C	degree Celsius
DAPI	4′,6-diamidin-2-phenylindol
DMEM	Dulbecco’s modified Eagle’s medium
DMSO	dimethyl sulfoxide
DNA	deoxyribonucleic acid
DTT	dithiothreitol

E

ECM	extracellular matrix
EDTA	ethylenediaminetetraacetate
EJC	exon junction complex
EM	electron microscopy
EMT	epithelial-mesenchymal transition
ER	endoplasmic reticulum

F

FBS	fetal bovine serum

FDA	Food and Drug Administration
FDR	false discovery rate
FN	fibronectin
FPKM	fragments per kilobase of exon model per million reads mapped
G	
g	gram
GLUT	Glucose transporters
GSH	Glutathione
H	
h	hours
H&E	hematoxylin & eosin
HEAT repeat	huntingtin, elongation factor 3, protein phosphatase 2A and the yeast kinase TOR1 repeat
HEPES	4-(2-hydroxyethyl)-1-piperazineethanesulfonic acid
HMGU	Helmholtz Zentrum München - Deutsches Forschungszentrum für Gesundheit und Umwelt
HRP	horseradish peroxidase
I	
ICC	immunocytochemistry
IDPs	intrinsically disordered proteins
IFNβ	interferon beta
IFNγ	interferon gamma
IHC	immunohistochemistry
ILBD	Institute for Lung Biology and Disease
ILD	interstitial lung disease
IP	immunoprecipitation
IPF	idiopathic pulmonary fibrosis
J	
K	
kDa	kilodalton
kg	kilogram
KO	knockout
L	
LC-MS/MS	liquid chromatography tandem mass spectrometry
LMP	low molecular mass protein
M	
µg	microgram
µL	microliter
µm	micrometer
M	molar
mA	milliampere
MECL-1	multicatalytic endopeptidase complex-like 1

MHC	major histocompatibility complex
min	minute
mL	milliliter
mRNA	messenger ribonucleic acid
ms	milliseconds
ms	milliseconds
mTOR	Mammalian target of rapamycin
MTT	3-(4,5-dimethylthiazol-2-yl)-2,5 diphenyltetrazolium bromide
N	
NADH2	Nicotinamide adenine dinucleotide
NADPH	Nicotinamide adenine dinucleotide phosphate
NF-κB	Nuclear factor kappa-light-chain-enhancer of activated B cells
NMD	nonsense-mediated decay
NRF-1/2	nuclear factor erythroid 2-related factor 1/2
O	
P	
%	percent
PA200	proteasome activator 200 kDa
PA28	proteasome activator 28 kDa
PAGE	polyacrylamide gel electrophoresis
PBS	phosphate buffered saline
PFA	paraformaldehyde
phLF	primary human lung fibroblasts
PI	propidium iodide
PI31	proteasome inhibitor 31 kDa
PI3K	Phosphatidylinositol-3 kinase
PSMA	proteasome subunit alpha type
PSMB	proteasome subunit beta type
PSMC	26S proteasome ATPase regulatory subunit
PSMD	26S proteasome non-ATPase regulatory subunit
PTM	post-translational modification
PVDF	polyvinylidenedifluoride
Q	
qPCR	quantitative polymerase chain reaction
R	
RNAi	ribonucleic acid interference
ROS	reactive oxygen species
RP	regulatory particle
rpm	revolutions per minute
rRNA	ribosmal RNA
RT	room temperature

S

SEM	standard error of the mean
siRNA	small interfering ribonucleic acid

T

TGF-β1	transforming growth factor beta 1
T-L	trypsin-like
TNF	tumour necrosis factor
Tris	Tris(hydroxymethyl)-aminomethane

U

u	unit
UPR	unfolded protein response
UPS	ubiquitin-proteasome system
UTR	untranslated region

V

v	Volt

W

WB	Western blot
WT	wildtype
w/o	without

X

x *g*	times gravity
XL-MS	crosslinking mass spectrometry

Y

Z

List of publications

1. Zambusi, A., Novoselc, K. T., Hutten, S., Kalpazidou, S., Koupourtidou, C., Schieweck, R., Aschenbroich, S., Silva, L., **Yazgili, A. S.**, van Bebber, F., Schmid, B., Möller, G., Tritscher, C., Stigloher, C., Delbridge, C., Sirko, S., Günes, Z. I., Liebscher, S., Schlegel, J., Aliee, H., Theis, F., Meiners, S., Kiebler, M., Dormann, D., & Ninkovic, J. (2022). TDP-43 condensates and lipid droplets regulate the reactivity of microglia and regeneration after traumatic brain injury. Nature Neuroscience. https://doi.org/10.1038/s41593-022-01199-y
2. **Yazgili, A. S.**, Ebstein, F., & Meiners, S. (2022). The Proteasome Activator PA200/PSME4: An Emerging New Player in Health and Disease. Biomolecules, 12(8), 1150. https://www.mdpi.com/2218-273X/12/8/1150
3. **Yazgili, A. S.**, Meul, T., Welk, V., Semren, N., Kammerl, I. E., & Meiners, S. (2021). In-gel proteasome assay to determine the activity, amount, and composition of proteasome complexes from mammalian cells or tissues. STAR Protoc, 2(2), 100526. https://doi.org/10.1016/j.xpro.2021.100526
4. Meul, T., Berschneider, K., Schmitt, S., Mayr, C. H., Mattner, L. F., Schiller, H. B., **Yazgili, A. S.**, Wang, X., Lukas, C., Schlesser, C., Prehn, C., Adamski, J., Graf, E., Schwarzmayr, T., Perocchi, F., Kukat, A., Trifunovic, A., Kremer, L., Prokisch, H., Meiners, S. (2020). Mitochondrial Regulation of the 26S Proteasome. Cell Rep, 32(8), 108059. https://doi.org/10.1016/j.celrep.2020.108059

Acknowledgement

First and foremost, I would like to express my heartfelt gratitude my supervisor, Prof. Silke Meiners, whose expertise, mentorship, and patience have been invaluable throughout my PhD study. Her insightful feedback and dedication to my academic growth have been instrumental in shaping this thesis. I feel lucky to have a supervisor who has strong scientific ethic, open-door policy, and giving advice whenever I needed.

My special gratitude goes to Dr. Georgios Stathopoulos, who generously offered access to his lab during our lab transition, greatly aiding my final PhD year. His mentorship and dedication to my academic growth have been pivotal.

My heartfelt appreciation extends to the members of my Thesis Advisory Committee (TAC), PD Dr. habil. med. Claudia A. Staab-Weijnitz and Dr. Georgios Stathopoulos. Their invaluable input, constructive critique, and dedication to upholding the quality of this work have been instrumental.

I further wish to express my appreciation to the lab members, Dr. Thomas Meul, Dr. Xinyuan Wang, Dr. Ilona Kammerl, Camilla Schlesser, Yuqin Wang, Fatima Mourtada, Alex Sailer, and Lex Kaiser for the intellectual exchange that enriched my research experience and their friendship. I feel lucky to have teaching experience in the lab to brilliant medicine and master's students Lena Gambarte and Amina Orlavic who help me grow my supervision skills and have their friendship. My heartfelt thanks extend to Aydan Sardogan, Ceylan Onursal, Ashesh Chakraborty, Georgia Giotopoulou and Anna Dmitrieva for their support and friendship.

I am thankful for the productive collaborations with Dr. Kamyar Hadian, Dr. Grzegorz Popowicz, Dr. Marijke Jansma, Dr. Stefanie Anne Weiss, Dr. Georgia Giotopoulou, and Dr. Sabine Behrend, with whom I have enjoyed numerous stimulating scientific discussions.

My heartfelt thanks go to my parents, Vesile Yazgili and Ismail Yazgili, my sister, Dr. Neslihan Gokce Yazgili-Kahveci, and my brother in-law, Dr. Ahmet Kahveci for their support, encouragement, and understanding during the challenging phases. I also extend my gratitude to my little nieces Zeynep Meryem Kahveci and Ayse Melek Kahveci who always manage to put a smile on my face and warmth to my heart even in the bad days.

Finally, I want to convey my deepest appreciation to my husband, Mustafa Oguzhan Karakaya. His unwavering presence and steadfast support have been invaluable through the highs and lows of my PhD journey. I cherish his enduring friendship and profoundly positive support on both my scientific career and daily life.